

Aus dem Bereich Biophysik
Theoretische Medizin und Biowissenschaften
der Medizinischen Fakultät
der Universität des Saarlandes, Homburg/Saar

**Functional and morphological adaptations
in *tafazzin*-deficient pancreatic islets
in the context of Barth syndrome**

Dissertation

zur Erlangung des akademischen Grades
eines Doktors der Naturwissenschaften
der Medizinischen Fakultät
der UNIVERSITÄT DES SAARLANDES

2024

vorgelegt von: Christopher Carlein

geb. am: 30.11.1994 in Mannheim-Neckarau

I. Table of contents

I.	Table of contents	ii
II.	Zusammenfassung	vii
III.	Abstract	ix
IV.	Abbreviations.....	xi
1	Introduction	1
1.1	Barth syndrome: Pathophysiology and symptoms.....	1
1.1.1	Etiology of Barth syndrome	1
1.1.1	Cardiolipin: <i>Taz</i> -mediated remodelling and cellular role	2
1.1.2	Metabolic abnormalities in Barth syndrome.....	7
1.1.3	Management of Barth syndrome patients.....	10
1.1.4	Animal models of Barth syndrome	12
1.2	Role and function of the endocrine pancreas	18
1.2.1	Pancreatic islet architecture	18
1.2.2	Pancreatic islet function	20
1.2.3	Redox regulations in pancreatic islets	26
1.3	Aim and motivation of this thesis.....	30
2	Materials.....	32
2.1	Substances	32
2.2	Consumables and kits	34
2.3	Buffers and culture media	36
2.4	Devices and software	38
2.5	Animal preparation equipment	40
2.6	Antibodies	40
3	Methods	42
3.1	Animal experiments	42
3.1.1	Used mouse models.....	43
3.1.2	<i>In vitro</i> doxycycline <i>Taz</i> -KD model.....	45

3.1.3	Genotyping	46
3.1.4	Glucose tolerance test (GTT).....	48
3.2	Handling of mouse islets of Langerhans	49
3.2.1	Isolation and culturing of pancreatic islets	49
3.2.2	Dispersion of pancreatic islets	51
3.2.3	Homogenisation of pancreatic islets	51
3.3	Immunohistochemistry	51
3.4	Western Blot experiments	53
3.4.1	Protein determination	54
3.5	Insulin and glucagon secretion experiments	54
3.6	Ca ²⁺ experiments	56
3.7	Glucose metabolism	60
3.7.1	Glucose uptake measurement	60
3.7.2	Enzymatic activity assays	60
3.7.3	ATP assay	61
3.8	Assessing mitochondrial function in pancreatic islets.....	62
3.8.1	Mitochondrial membrane potential measurement	62
3.8.2	NADH/NADPH autofluorescence measurement	63
3.8.3	OCR and ECAR using Seahorse XFe96 analyser	64
3.9	Redox analysis using genetically-encoded probes.....	66
3.9.1	H ₂ O ₂ measurements.....	67
3.9.2	Redox histology	69
3.10	Morphological analysis of mitochondria	71
3.10.1	Mitochondrial volume determination with Mitotracker and roGFP	71
3.10.2	Confocal and STED microscopy	71
3.11	Lipidomics	74
3.12	Quantitative RT-PCR and RNA sequencing	76
3.12.1	RNA isolation.....	76

3.12.2	Quantitative RT-PCR	76
3.12.3	RNA Sequencing.....	76
3.13	Data analysis and statistics	77
4	Results	79
4.1	Characterisation of <i>Taz</i> -KD in pancreatic islets.....	79
4.2	Whole-body metabolism.....	82
4.3	Immunohistochemistry.....	85
4.3.1	Pancreatic islet composition	85
4.3.2	Proliferation and apoptosis markers	88
4.4	Investigation of pancreatic islet function in <i>Taz</i> -KD	89
4.4.1	Glycolysis as the first step of glucose metabolism	89
4.4.2	Oxygen consumption rate and mitochondrial membrane potential.....	92
4.4.3	ATP production.....	98
4.4.4	Ca ²⁺ handling in <i>Taz</i> -KD pancreatic islets	100
4.4.5	Insulin and glucagon secretion	105
4.4.6	Extracellular acidification rate and pH measurement.....	108
4.5	Redox experiments.....	110
4.5.1	Real-time H ₂ O ₂ analysis.....	111
4.5.2	Redox histology	114
4.5.3	Western blot analysis of relevant redox proteins.....	117
4.6	Analysis of mitochondrial morphology in <i>Taz</i> -KD islets	118
4.6.1	Confocal and STED imaging.....	119
4.6.2	Western blot analysis of relevant morphology and autophagy proteins ...	124
4.7	Omics analysis of <i>Taz</i> -KD islets.....	126
4.7.1	Lipidomics.....	126
4.7.2	RNA sequencing	128
4.8	Post-translational modification: O-Glycosylation	131
4.9	Direct consequences of <i>Taz</i> -KD - <i>in vitro</i> model	132

4.9.1	Characterisation of shTaz - <i>in vitro</i> model	132
4.9.2	Immunohistochemistry - <i>in vitro</i> model	134
4.9.3	Pancreatic islet function <i>in vitro</i> model	136
4.9.4	Lipidomics - <i>in vitro</i> model.....	138
4.9.5	RNA sequencing - <i>in vitro</i> model	140
5	Discussion	141
5.1	Characterisation of the shTaz mouse model	141
5.2	Pancreatic islet composition and function	143
5.3	Metabolic and whole-body phenotype in BTHS	151
5.4	<i>Taz</i> -KD mitochondria of pancreatic islet cells	155
5.5	O-GlcNAc in <i>Taz</i> -KD pancreatic islets	162
5.6	Comparison shTaz <i>in vivo</i> and <i>in vitro</i> model	164
5.7	Pancreatic islet adaption processes.....	168
5.8	Conclusion and outlook	172
6	References	174
7	Supplements	215
7.1	Supplementary data and figures	215
7.1.1	Genotyping	215
7.1.2	Characterisation of <i>Taz</i> -KD in pancreatic islets.....	217
7.1.3	Whole-body metabolism.....	218
7.1.4	Immunohistochemistry	219
7.1.5	Investigation of pancreatic islet function in <i>Taz</i> -KD.....	220
7.1.6	Redox experiments	224
7.1.7	Confocal and STED imaging.....	226
7.1.8	Lipidomics.....	228
7.1.9	RNA sequencing	233
7.1.10	Post-translational modification: O-Glycosylation	235
7.1.11	Characterisation of the shTaz <i>in vitro</i> model	236

7.2	List of Figures	237
7.3	List of Tables	241
7.4	Acknowledgements	242
7.5	CV: Christopher Carlein (includes the publication list)	243

II. Zusammenfassung

Das Barth Syndrom (BTHS) ist eine X-chromosomale Multisystem Erkrankung, die durch Mutationen in dem Gen verursacht wird, das für das mitochondriale Enzym *Tafazzin* (*Taz*) kodiert. Die Transacylase Tafazzin katalysiert den finalen Schritt in der Biosynthese von Cardiolipin (CL) und beeinflusst dadurch entscheidend die Phospholipid-Zusammensetzung in der inneren Mitochondrienmembran. BTHS-Patienten leiden unter einer Vielzahl schwer-wiegender Symptome, darunter Herzversagen, Muskelschwäche und systemischer Stoffwechselstörungen, einschließlich Hypoglykämie. Die Rolle von dysfunktionaler CL-Zusammensetzung in pankreatischen Inseln ist bisher weitgehend unerforscht.

Im Rahmen dieser Arbeit wurde ein shRNA-basiertes, Doxycyclin-induzierbares *Tafazzin*-Knockdown (*Taz*-KD) Maus Modell, bekannt als shTaz, verwendet, um die Eigenschaften und Funktionalität von Pankreasinseln im Zusammenhang mit BTHS zu untersuchen. Nach einer anfänglichen Charakterisierung des *Taz*-KD Modells mittels qPCR-Messung des *Taz* Gens und Lipidomik-Analyse bei *Taz*-KD Pankreasinseln, wurden die 20 Wochen alten *Taz*-KD Mäuse systemisch über das Körpergewicht und mithilfe eines Glukose-Toleranz-Tests mit Wildtyp (WT) Wurfgeschwister Mäusen verglichen. Anschließend wurden Pankreasschnitte mittels Immunfärbung zunächst nach der zellulären Zusammensetzung der Pankreasinseln (α -, β - oder δ -Zellen) und dann nach Apoptose- oder Proliferation-Markern untersucht. Danach wurde eine umfassende biochemische und funktionelle Analyse der isolierten *Taz*-KD Pankreasinseln durchgeführt. Außerdem wurde der Einfluss von Redox Veränderungen über Redox-Histologie und Western Blot bei *Taz*-KD Pankreasinseln analysiert. Da BTHS primär eine Schädigung der Mitochondrien verursacht, wurde die Funktion und Morphologie der Mitochondrien über einen Seahorse XFe96 Analysator und über konfokale Mikroskopie bei isolierten intakten und vereinzelter *Taz*-KD pankreatischen Inseln untersucht. Des Weiteren wurde die Zusammensetzung des RNA- und Lipid-Profiles mittels RNA-Sequenzierung und Lipidomik-Analyse von WT und *Taz*-KD Pankreasinseln verglichen. Abschließend wurden ein neues *Taz*-KD *in vitro* Modell mit einer Woche Doxycyclin Gabe im Kulturmedium etabliert und mechanistisch untersucht. Diese Ergebnisse wurden mit den zuvor gewonnenen Daten der funktionellen Analyse von *Taz*-KD Pankreasinseln bei lebenslanger Doxycyclin Gabe im Futter verglichen, was ein umfassendes Verständnis der Biologie der Pankreasinseln bei der BTHS-Entwicklung ermöglicht.

In den Ergebnissen wurde zunächst die Effizienz des *Taz*-KD mit ca. 65% für Pankreasinseln und ca. 85% bei Herzen festgestellt. Trotz abgeschwächter Effizienz des *Taz*-KD bei Pankreasinseln kam es zu einer Abnahme der CL-Konzentration sowie einer geänderten CL-Spezies-Zusammensetzung. Zusätzlich, wurden ebenfalls andere Phospholipidklassen, insbesondere Phosphatidyl-ethanolamin, -cholin, -glycerol durch den *Taz*-KD signifikant beeinflusst. Die *Taz*-KD Mäuse zeigten ein verringertes Körpergewicht und eine verbesserte Glukose-Toleranz mit unveränderten Insulin- und Glukagon-Plasma-Werten gegenüber den WT-Kontrollen. *Taz*-KD Pankreasinseln zeigten eine vermehrte Anzahl an α -Zellen verbunden mit einer erhöhten Glukagon-Sekretion und unveränderter Insulin-Sekretion. Weitere funktionelle Experimente ergaben einen beschleunigten, zytosolischen Ca^{2+} -Einstrom, eine unveränderte ATP-Produktion und eine erhöhte Glukose-Aufnahme der *Taz*-KD Pankreasinseln. Eine mitochondriale Redox-Analyse ergab einen leicht reduzierten *in vivo* sowie einen geringfügig oxidierten *ex vivo* Redox-Status, verbunden mit einer gesteigerten NOX4 Aktivität und einer erhöhten Menge an Prx3 bei *Taz*-KD Pankreasinseln. Die Mitochondrien von *Taz*-KD Pankreasinseln hatten ein vergrößertes Volumen und einen leicht erhöhten Sauerstoffverbrauch bei niedrigen Glukosemengen. Des Weiteren ergab eine Reactome Analyse der RNA-Sequenzierungsdaten, dass mehrere Gene die an der post-translationalen Modifikation der O-Glykosylierung beteiligt sind, in den *Taz*-KD Pankreas-inseln erhöht waren. Dieser Anstieg konnte auf Proteinebene durch Western Blot und Immunfärbung bestätigt werden. Abschließend wurde beim *Taz*-KD *in vitro* Modell im Vergleich zu gleich behandelten Kontrollen ebenfalls eine Abnahme um 65% der *Taz* RNA und ein geändertes CL-Profil beobachtet. Außerdem konnte eine verminderte ATP-Menge und Insulin Sekretion beim *in vitro* *Taz*-KD Modell gemessen werden.

Die Ergebnisse dieser Arbeit zeigen, dass die Funktionalität der *Taz*-KD Pankreasinseln *in vivo* erhalten bleibt. Dies wird über verschiedene kompensatorische Wege einschließlich vergrößertes Mitochondrien-Volumen, erhöhter Glukoseaufnahme und amplifizierter O-Glykosylierung gewährleistet. Außerdem könnte die erhöhte Menge an α -Zellen und die gesteigerte Glukagon-Sekretion, die Insulin-Sekretion über parakrine Signalwirkung positiv beeinflussen. Diese adaptiven Mechanismen sind vielversprechende Ansatzpunkte für die Behandlung von Pankreasinseln bei metabolischen Defekten. Im Gegensatz dazu hat das *Taz*-KD *in vitro* Modell gezeigt, dass eine Reduktion der *Taz* RNA bei ausbleibenden adaptiven Mechanismen, eine direkte Störung der Pankreasinseln zur Folge hat. Dies verdeutlicht die wichtige Rolle von CL für die Funktion von Pankreasinseln.

III. Abstract

Barth syndrome (BTHS) is an X-linked multisystem disorder caused by mutations in the gene encoding the mitochondrial enzyme tafazzin (*Taz*). The transacylase tafazzin catalyses the final step in the biosynthesis of cardiolipin (CL), thereby decisively influencing the phospholipid composition in the inner mitochondrial membrane. BTHS patients suffer from a variety of severe symptoms, including heart failure, muscle weakness, and systemic metabolic disturbances, including hypoglycemia. The role of dysfunctional CL composition in pancreatic islets is mostly unexplored.

In this thesis, a shRNA-based doxycycline-inducible *tafazzin* knockdown (*Taz*-KD) mouse model, known as shTaz, was used to investigate the properties and functionality of pancreatic islets in the context of BTHS. After initial characterisation of the *Taz*-KD model using qPCR measurements of the *Taz* gene and lipidomics analysis of *Taz*-KD pancreatic islets, 20-week-old *Taz*-KD mice were compared systemically by body weight and using a glucose tolerance test with wildtype (WT) littermate mice. Subsequently, pancreas tissue slices were analysed, first for the cellular composition of the pancreatic islets (α -, β - or δ -cells) and then for apoptosis or proliferation markers. Subsequently, comprehensive biochemical and functional analyses of the isolated *Taz*-KD pancreatic islets were performed. In addition, the influence of redox changes on *Taz*-KD pancreatic islets was analysed using redox histology and western blotting. Since BTHS primarily causes mitochondrial damage, the function and morphology of mitochondria were examined using a Seahorse XFe96 analyser and confocal microscopy in isolated intact and dispersed *Taz*-KD pancreatic islets. Furthermore, the RNA and lipid profiles of WT and *Taz*-KD pancreatic islets were compared by RNA sequencing and lipidomics analysis. Finally, a new *Taz*-KD *in vitro* model with one week of doxycycline administration into the culture medium of isolated islets was established and mechanistically investigated. These results were compared with the earlier obtained data from the functional analyses of the *Taz*-KD pancreatic islets of mice receiving a lifelong doxycycline diet. Together these results provide a comprehensive understanding of pancreatic islet physiology during BTHS development.

The efficiency of doxycycline-induced *Taz*-KD was approximately 65% for pancreatic islets and 85% for hearts. Despite the attenuated efficiency of *Taz*-KD in pancreatic islets, it still resulted in a decreased concentration of CL and a significantly altered CL species composition. *Taz*-KD in pancreatic islets also significantly affected other phospholipid

classes, specifically phosphatidyl-ethanolamine, -choline, and -glycerol. The *Taz*-KD mice displayed reduced body weight and improved glucose tolerance with unchanged plasma insulin and glucagon levels compared to WT controls. *Taz*-KD pancreatic islets had more α -cells, which was associated with enhanced glucagon but unchanged insulin secretion. Further functional experiments revealed a faster cytosolic Ca^{2+} influx upon glucose stimulation, an unchanged ATP production, and an increased glucose uptake of *Taz*-KD compared to WT pancreatic islets. Mitochondrial redox analysis revealed a slightly reduced *in vivo* and an oxidised *ex vivo* redox state, which was connected with increased NOX4 activity and a higher amount of Prx3 in *Taz*-KD compared to WT pancreatic islets. The mitochondria of *Taz*-KD pancreatic islets had a larger volume than control islets and a slightly increased oxygen consumption rate at low glucose levels. Moreover, Reactome analysis of RNA sequencing data revealed that several genes involved in the post-translational modification of O-glycosylation were increased in *Taz*-KD pancreatic islets. This increase was confirmed at the protein level by western blotting and immunostaining. Finally, using the *Taz*-KD *in vitro* model, a 65% decrease in *Taz* RNA and an altered CL profile were observed, when compared to doxycycline-cultured controls. Additionally, decreased ATP levels and impaired insulin secretion were measured in *Taz*-KD pancreatic islets from the *in vitro* model.

The results of this thesis show that the functionality of *Taz*-KD pancreatic islets is maintained *in vivo*. This is ensured via several compensatory mechanisms, including enhanced mitochondrial volume, increased glucose uptake, and amplified O-glycosylation. In addition, the increased number of α -cells and the higher glucagon secretion could positively influence insulin secretion via paracrine signalling. These adaptive mechanisms are promising targets for the treatment of pancreatic islets in metabolic disorders. On the other hand, the *Taz*-KD *in vitro* model has shown that a reduction of *Taz* RNA in the absence of compensatory mechanisms results in a direct defect of pancreatic islets. This highlights the vital role of CL remodelling in pancreatic islet functionality.

IV. Abbreviations

List of general abbreviations

2DG	2-deoxyglucose
Ant A	antimycin A
ATP	adenosintriphosphat
AUC	area under the curve
bp	base pair
BCA	bicinchoninic acid
BS	beam splitter
BSA	bovine serum albumin
BTHS	Barth syndrome
CLD1	cardiolipin-specific deacylase 1
CD7	cell discoverer 7 Zeiss microscope
Ctrl	control
CL	cardiolipin
CoA	coenzyme A
CPT1	carnitine palmitoyl-transferase 1
CT	cycle threshold
DAPI	diamidin-2-phenylindol
DNA	deoxyribonucleic acid
Doxy	doxycycline
DPBS	Dulbecco's phosphate buffered saline
DTT	dithiothreitol
ddH₂O	double distilled water

ECAR	extracellular acidification rate
ECL	enhanced chemiluminescence
EDTA	ethylenediaminetetraacetic acid
ER	endoplasmic reticulum
ETC	electron transport chain
FA	fatty acids
FBS	fetal bovine serum
FCCP	carbonyl cyanide-p-trifluoromethoxyphenylhydrazone
FRET	Förster resonance energy transfer
G6P	glucose-6-phosphate
G6PDH	glucose-6-phosphate dehydrogenase
GAPDH	glyceraldehyde-3-phosphate dehydrogenase
Gck	glucokinase
GFP	green fluorescent protein
GIPR	gastric inhibitory polypeptide receptor
Gln	glutamine
GLP-1R	glucagon-like peptide-1 receptor
Glu	glucose
GPI	glucose-6-phosphate isomerase
GSIS	glucose-stimulated insulin secretion
GTT	glucose tolerance test
GV-SOLAS	Gesellschaft für Versuchstierkunde / Society of Laboratory Animal Science
H₂O₂	hydrogen peroxide
HK	hexokinase
HRP	horseradish peroxidase

HTRF	homogeneous time-resolved fluorescence
IHC	immunohistochemistry
IP injection	intraperitoneal injection
IVC	individually ventilated cages
KD	knockdown
KHB	Krebs-Henseleit buffer
Laser	light amplification by stimulated emission of radiation
LAMP1	lysosomal-associated membrane protein 1
LAMP2	lysosomal-associated membrane protein 2
LC3B	microtubule associated protein 1 light chain 3 β
LVF	linear variable filter
MCU	mitochondrial Ca^{2+} uniporter
MEF	mouse embryonic fibroblasts
Mito	mitochondria
MLCL	monolysocardiolipin
MLCLAT	monolysocardiolipin acyltransferase
MSMS	tandem mass spectrometry
NEFA	non-esterified fatty acids
NEM	N-ethylmaleimide
NNT	nicotinamide nucleotide transhydrogenase
Nox	NADPH oxidase
ns	not significant
$\text{O}_2^{\bullet-}$	superoxide
OCR	oxygen consumption rate
OPA1	GTPase optic atrophy 1

Orp1	oxidant receptor peroxidase 1
OXPHOS	oxidative phosphorylation
PBS	phosphate buffered saline
PCR	polymerase chain reaction
pH	<i>potentia hydrogenii</i>
PMSF	phenylmethylsulfonylfluorid
PPP	pentose phosphate pathway
Prx	peroxiredoxin
PUFA	polyunsaturated fatty acids
PVDF	polyvinylidene difluoride
P/S	penicillin/streptomycin
rcf	relative centrifugal force
RIP	rat insulin promoter
ROI	region of interest
ROS	reactive oxygen species
Rot	rotenone
RPMI	Roswell Park Memorial Institute medium
rpm	revolutions per minute
roGFP	redox-sensitive green fluorescent protein
RT	room temperature
RNA	ribonucleic acid
RNA-Seq	RNA sequencing
SDS-PAGE	sodium dodecylsulfate polyacrylamide gel electrophoresis
SEM	standard error of the mean
SERCA	sarcoplasmic/endoplasmic reticulum Ca^{2+} ATPase

shRNA	short hairpin RNA
SOD	superoxid dismutase
SRC	spare respiratory capacity
STED	stimulated emission depletion
Taz	tafazzin (protein)
<i>Taz</i>	<i>tafazzin</i> (gene)
Taz-KD	<i>tafazzin</i> knockdown
Taz-KO	<i>tafazzin</i> knockout
TCA cycle	tricarboxylic acid cycle / Krebs cycle
TMRM	tetramethylrhodamine methyl ester
TVA	Tierversuchsantrag / Animal experiment approval
WB	western blot
wo	weeks of age
WT	wildtype
λ_{em}	emission wavelength
λ_{ex}	excitation wavelength

List of lipid abbreviations

CE	cholesterol esters
Cer	ceramide
CL	cardiolipin
DAG	diacylglycerol
HexCer	hexosylceramide
LPA	lyso-phosphatidate
LPC (O-)	lyso-phosphatidylcholine (-ether)
LPE (O-)	lyso-phosphatidylethanolamine (-ether)
LPG	lyso-phosphatidylglycerol
LPI	lyso-phosphatidylinositol
LPS	lyso-phosphatidylserine
MLCL	monolysocardiolipin
PA	phosphatidate
PC (O-)	phosphatidylcholine (-ether)
PE (O-)	phosphatidylethanolamine (-ether)
PG	phosphatidylglycerol
PI	phosphatidylinositol
PS	phosphatidylserine
SM	sphingomyelin
TAG	triacylglycerol

1 Introduction

1.1 Barth syndrome: Pathophysiology and symptoms

1.1.1 Etiology of Barth syndrome

Barth syndrome (BTHS) is an X-linked hereditary mitochondrial disorder which Dr. Peter Barth and colleagues first described in 1983.²³ The affected chromosome Xq28 encodes for the highly conserved and ubiquitously expressed mitochondrial transacylase tafazzin (*Taz*), which catalyses the last step of the cardiolipin (CL) remodelling pathway. The pathological cellular consequences of an altered CL remodelling are diverse and tissue-specific but share the restricted energy production.² The multisystem disease BTHS is typically characterised by cardiomyopathy, skeletal myopathy, neutropenia, 3-methylglutaconic aciduria and metabolic alterations.^{38,80} This rare disease almost exclusively affects males, leads to increased child mortality and often requires cardiac transplantation as a treatment.^{195,228} Several loss of function mutations in *Taz* have been described in the literature, the majority being small insertions, deletions and missense mutations.³⁸⁵ The incidence of BTHS is reported to be 1:300,000, but the pediatric prevalence is estimated at about 1 in 1,000,000 male births. The discrepancy of incidence and prevalence suggests that early mortality might result in under-diagnosis of BTHS.²⁵¹ Additionally, in some cases, BTHS was reported to induce miscarriage and stillbirth.¹¹³ Whereas, in the past, 70 - 80% of patients died during infancy and childhood, in recent years, growing percentages of individuals (prognosis of 10 – 20% mortality) successfully survive the toddler years and show stabilisation of early cardiomyopathy.^{113,228} With a rising population of adult BTHS patients as well as increased recognition and knowledge about mitochondrial diseases in general, metabolic diets and treatments of those patients become considerably more important. In the following Chapters, the current knowledge about the underlying cellular mechanisms of BTHS with a focus on the resulting metabolic alterations in patients and available animal models will be summarised. The other clinical features, including the famous triad of cardiomyopathy, skeletal myopathy and neutropenia are not discussed here, but are intensively reviewed in Clarke *et al.*, 2013 and Ferreira *et al.*, 2020.^{80,113}

1.1.1 Cardiolipin: *Taz*-mediated remodelling and cellular role

The function of the mitochondrial membrane-bound transacylase enzyme tafazzin (*Taz*) is to alter the lipid composition by redistributing fatty acids among phospholipids.⁵⁹ Its arguably most crucial substrate is the phospholipid CL, which is enriched in the inner mitochondrial membrane accounting for around 25% of all phospholipids and fulfilling various tasks in mitochondrial energetics, apoptosis and autophagy.^{2,77} Of note, solely the presence of CL in prokaryotes' plasma membrane, while in eukaryotes exclusively located in the mitochondrial membrane supports the endosymbiont theory.⁹⁹ *Taz* mediates the final remodelling step of monolysocardiolipin (MLCL) to the mature CL (**Figure 1.1**).^{324,330} In this reaction, *Taz* acylates MLCL via a coenzyme A (CoA)-independent acyl group transfer from a repertoire of phospholipids, including phosphatidylethanolamine (PE) and phosphatidylcholine (PC).¹²² Two other enzymes offer an alternative remodelling pathway and have been linked with re-acylation of MLCL, namely Acyl-CoA:lysocardiolipin acyltransferase-1 (ALCAT1) and monolysocardiolipin acyltransferase (MLCLAT).¹⁴⁵ ALCAT1 shows in contrast to MLCLAT and *Taz* a low substrate specificity.⁶⁵ The precise biological function of ALCAT1 and MLCLAT is yet to be assessed. However, the accumulation of MLCL in the absence of *Taz* suggests that they are not functionally redundant with *Taz* and cannot compensate for its deficiency.³²⁹ The upstream steps of the complex CL biosynthesis involve many more enzymes and are reviewed in more detail in Houtkooper *et al.*, 2008 and Mejia *et al.*, 2013.^{164,247}

CL (IUPAC name: 1,3-bis(sn-3'-phosphatidyl)-sn-glycerol) consists of two diacylglycerophosphates with a third glycerol backbone (**Figure 1.1**) and has a unique conical shape. The ester-linked fatty acid chains can vary depending on the specific tissue, age of the organism and lipid environment based on diets.⁵⁴ The predominant species is the tetralinoleoyl CL (CL 72:8 (carbonlength:doublebonds)) which is depicted in **Figure 1.1** and consists of four linoleic acid molecules.¹²² The relative abundance of CL 72:8 ranges from around 60% in skeletal muscle to more than 80% in liver and heart tissue.¹⁴³

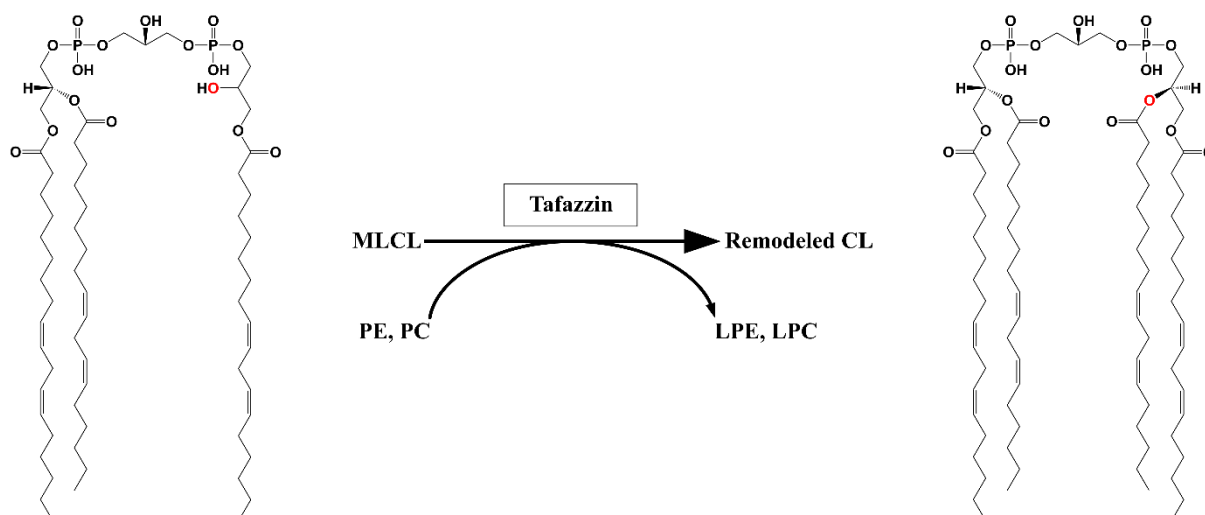


Figure 1.1: CL remodelling mediated by the mitochondrial transacylase Taz

Taz mediates the acyl transfer from various phospholipids (mainly PE and PC) to MLCL, resulting in the formation of mature/remodelled CL. It deprotonates the hydroxyl moiety (oxygen marked in red) of MLCL to facilitate the ester formation. Abbreviations: cardiolipin (CL), tafazzin (Taz), monolyso-cardiolipin (MLCL), phosphatidylethanolamine (PE), lyso-phosphatidylethanolamine (LPE), phosphatidylcholine (PC), lysophosphatidylcholine (LPC). Created with ChemDraw.

Mature CL is a vital component of the cellular homeostasis and it fulfills various roles in mitochondrial functionality, which are listed in **Table 1.1** and introduced in the following paragraphs.^{2,77}

CL is a key player in the structural organisation of the mitochondrial cristae junctions which are membrane structures with high inward-directed curvature. One reason being the cone-shape of CL naturally induces membrane curvature.²⁷ Additionally, CL binds and enhances the GTP hydrolysis activity of the mechanochemical GTPase optic atrophy 1 (OPA1), which catalyses the fusion of the inner mitochondrial membrane.^{21,391} The cristae folding of the membrane greatly increases ATP generating surface and creates concentrated reaction hubs, supporting local proton gradients and limiting ADP diffusion.⁶ CL binds many mitochondrial membrane-bound or associated proteins with high affinity. The translocases of the outer and inner membrane (TOM and TIM, respectively) facilitate protein import into the mitochondria and also require CL for their structural organisation.²⁴⁰ Moreover, the protein-lipid interaction of CL with the proteins of the ETC is depicted in **Figure 1.2**. As illustrated, CL is required for the optimal activity of complex I, complex III, complex IV, and complex V (ATP synthase).^{100,105} Although MLCL can bind several mitochondrial proteins, multiscale molecular dynamics revealed a weaker interaction of proteins of the ETC with MLCL compared to the fully remodelled CL species.⁸⁴ Moreover, supramolecular assembly of the ETC proteins is favoured in the presence

of CL and hence, more enriched in the cristae junctions. The loss of supercomplex formation diminishes ETC efficiency and is often observed when an important part of the cristae junction is missing (e.g. CL, OPA1, mitochondrial contact site and cristae organising system (MICOS complex)).¹³³ Recently, CL has been found to stabilise the mitochondrial Ca^{2+} uniporter (MCU) and hence, being involved in mitochondrial Ca^{2+} homeostasis.²⁰ Ca^{2+} is crucial for the mitochondrial functionality as it regulates the activity of several enzymes of the tricarboxylic acid (TCA) cycle.³³ Furthermore, CL is also directly involved in the stabilisation of TCA cycle proteins. It is necessary for the structural organisation of the α -ketoglutarate and the succinate dehydrogenase complexes.^{70,102} Additionally, CL might facilitate the interaction between pyruvate dehydrogenase and its activating phosphatase.²²⁷ These examples demonstrate that mature CL is vital for both oxidative phosphorylation (OXPHOS) and TCA cycle activity.

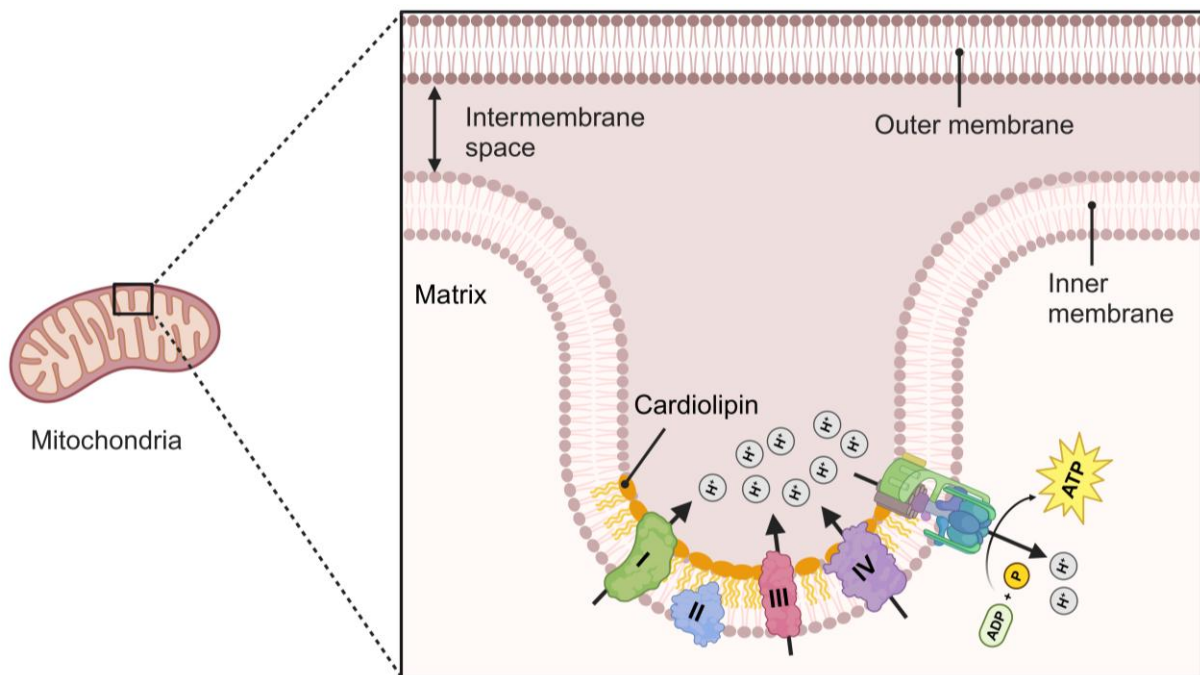


Figure 1.2: CL supports cristae formation and ETC interaction

CL is enriched in the inner mitochondrial membrane and shapes the bending of the cristae structure. The proteins of the ETC are stabilised by mature CL. CL supports supercomplex formation of the ETC proteins and therefore, supports efficient ATP production. The ATP production occurs at the ATP synthase (complex V), using the driving force of the proton gradient, which is buildup by the complexes I, III and IV. Abbreviations: cardiolipin (CL), electron transport chain (ETC). Created with BioRender.com.

Another crucial role of CL is the regulation of apoptosis via its interaction with cytochrome c.^{191,216} During apoptosis and experimental stress conditions achieved by inhibition of complex I (rotenone), kinases (staurosporine), or mitochondrial permeability transition (cyclosporin A), CL is translocated from the inner to the outer leaflet via the Bid, a BH3 proapoptotic member

of the Bcl-2 family, mediated pathway.³⁷⁷ On the outer leaflet of the inner mitochondrial membrane, CL can be oxidised by the peroxidase activity of cytochrome c, which in turn favours the release of cytochrome c into the cytosol, triggering apoptosis signalling cascades.¹⁹¹ Furthermore, investigations in the field of mitophagy, which is the autophagy process specific for mitochondria, showed that CL translocation provides a general signaling platform for the recruitment of autophagic machinery, not only connected to cytochrome c release. Two key proteins, the mitochondrial creatine kinase and the nucleoside diphosphate kinase, have been identified to interact with CL in the process of autophagy-related CL translocation.^{216,331} After externalisation, CL is recognised by Beclin 1 and further recruitment of the autophagosomal membrane is mediated by LC3-2 and LC3B, that specifically interact with externalised CL.¹⁵ Consequently, CL deficient cells have been shown to exhibit diminished mitophagy.⁷⁷

The structure of the mitochondrial network, a vital aspect of cellular health, is a result of the dynamic interplay of mitochondrial fission (controlled separation) and fusion (controlled merging). Both processes are dependent on the availability of CL. On the one hand, CL assists dynamin-related protein 1 in catalysing mitochondrial fission, and on the other hand, phospholipase MitoPLD converts CL to phosphatidic acid to promote Mitofusin-1- and Mitofusin-2-mediated mitochondrial fusion.^{74,350}

An increase in lipid peroxidation can diminish mitochondrial functionality by changing the membrane fluidity and permeability, which directly impacts the mitochondrial membrane potential and OXPHOS efficiency.⁷¹ CL is particularly susceptible to oxidation due to its high levels of unsaturated fatty acids compared to other phospholipids.²⁷⁴ Furthermore, its association with the ETC brings it into close proximity to $O_2^{\bullet-}$, often collectively referred to as one of the reactive oxygen species (ROS), production sites.³⁶² Therefore, CL might play a role in maintaining the balance of redox reactions within the mitochondria.

Overall, efficient mitochondrial functionality highly depends on total CL content, its remodelling process, and the resulting CL species profile. Therefore, defects in CL remodelling have deleterious effects that impact, among others, OXPHOS, apoptosis, autophagy, redox balance, fusion/fission and Ca^{2+} signalling.^{103,128}

Table 1.1: Role of CL in mitochondrial functionality

Adapted from Bertero, 2022.³⁶ Abbreviations: cardiolipin (CL), oxidative phosphorylation (OXPHOS), mitochondrial Ca^{2+} uniporter (MCU), electron transport chain (ETC).

Function	Role of CL	Reference
mitochondrial biogenesis	structural organisation of the mitochondrial translocases mediating protein import and membrane protein complex assembly	Malhotra <i>et al.</i> , 2017 ²⁴⁰
OXPHOS	structural organisation and stabilisation of ETC proteins	Eble <i>et al.</i> , 1990 ¹⁰⁵ Dröse <i>et al.</i> , 2002 ¹⁰⁰
cristae morphology	physical properties of CL promote membrane bending	Beltrán-Heredia <i>et al.</i> , 2019 ²⁷
	structural organisation of the mitochondrial cristae organising system (MICOS) complex	Gottschalk <i>et al.</i> , 2022 ¹³³
Ca^{2+} homeostasis	stabilisation of the MCU	Gosh <i>et al.</i> , 2020 ¹²⁸
mitophagy and apoptosis	cytochrome c peroxidase activity and mitochondrial permeability transition	Lacombe <i>et al.</i> , 2009 ²¹⁶ Schlattner <i>et al.</i> , 2014 ³³¹
	regulation of Beclin 1 and LC3 recruitment to mitochondrial membranes	Tyurin <i>et al.</i> , 2007 ³⁷⁷ Antón <i>et al.</i> , 2016 ¹⁵
intermediary metabolism	structural organisation and activity of succinate and α -ketoglutarate dehydrogenases	Dudek <i>et al.</i> , 2016 ¹⁰² Chatzispyrou <i>et al.</i> , 2018 ⁷⁰
	interaction of pyruvate dehydrogenase with its phosphatase	Li <i>et al.</i> , 2019 ²²⁷
mitochondrial dynamics (fission and fusion)	regulation of the activity of dynamin-related protein 1 mediating mitochondrial fission. Phospholipase MitoPLD promotes CL-dependent Mitofusin-1 and Mitofusin-2 mediated mitochondrial fusion	Choi <i>et al.</i> , 2006 ⁷⁴ Stepanyants <i>et al.</i> , 2015 ³⁵⁰
Mitochondrial redox regulation	Involved in lipid peroxidation and interaction with the peroxidase cytochrome C	Paradies <i>et al.</i> , 2010 ²⁷⁴ Kagan <i>et al.</i> , 2005 ¹⁹¹

1.1.2 Metabolic abnormalities in Barth syndrome

Metabolic abnormality is a broad term, including defects ranging from mitochondrial over cellular to whole-body metabolism. Since mitochondrial diseases affect the main energy-producing system in the cell, they naturally cause metabolic disorders. Along those lines, altered metabolism has been reported multiple times in BTHS for cellular as well as whole-body metabolism and may play an important role in the pathogenesis of BTHS.^{59,75,344} Furthermore, a defective whole-body metabolism is a crucial parameter in the disease progression of this multisystem disorder, especially in stressed or exercise situations.^{60,61} Due to the limited number of patient samples, relatively little is known about the clinical situation, and most molecular studies are performed on cell lines and animal models (further introduced in **Chapter 1.1.4**). Some of the key studies and their main metabolic findings in patients or with patient samples are summarised in the **Table 1.2**. Of interest, female carriers do not display the BTHS-specific biochemical abnormalities and hence, all the summarised studies represent affected male individuals.³⁸⁵ The following paragraphs will combine the clinical metabolic studies together with investigations on cell lines and animal models to introduce the metabolic phenotype in BTHS and *Taz* deficiency.

Table 1.2: Overview of metabolic alterations in BTHS patients and patient samples

Tissue	Main metabolic findings	Reference
plasma	lactic acidemia, low carnitine	Barth <i>et al.</i> , 1983 ²³
plasma	low carnitine, high free fatty acids	Ino <i>et al.</i> , 1988 ¹⁷¹
plasma, urine	3-methylglutaconic aciduria, lactic acidosis, hypoglycemia	Kelly <i>et al.</i> , 1991 ²⁰¹
urine	3-methylglutaconic aciduria, increased ethylhydracrylic acids	Christodoulou <i>et al.</i> , 1994 ⁷⁶
plasma, urine	hypcholesterolemia, decreased low-density lipoprotein cholesterol, low pre-albumin	Spencer <i>et al.</i> , 2006 ³⁴⁴
plasma	hypoglycemia, metabolic acidosis, elevated transaminases, lactic acidosis, mild hyperammonemia	Donati <i>et al.</i> , 2006 ⁹⁸
plasma	metabolic acidosis, lactic acidemia, hyperammonemia, hypoglycemia	Yen <i>et al.</i> , 2008 ⁴²⁰

plasma	increased insulin-stimulated glucose disposal rate, reduced basal and hyperinsulinemic lipolytic rate, higher basal leucine	Cade <i>et al.</i> , 2013 ⁵⁹
plasma	decreased arginine	Rigaud <i>et al.</i> , 2013 ³⁰⁰
plasma	decreased arginine, increased proline, exercise-induced lactic acidemia, low pre-albumin	Vernon <i>et al.</i> , 2014 ³⁸⁵
plasma	decreased serotonin, increased proline and tyrosine, decreased arginine, dysregulated aminoacyl tRNA biosynthesis	Sandlers <i>et al.</i> , 2016 ³²⁰
lymphoblasts	increased glucose uptake and utilisation	Mejia <i>et al.</i> , 2017 ²⁴⁸
skin fibroblasts	preserved TCA cycle flux, destabilisation of the branched-chain ketoacid dehydrogenase	Chatzisprou <i>et al.</i> , 2018 ⁷⁰
plasma	lower creatinine, hypocholesterolemia	Bittel <i>et al.</i> , 2018 ⁴⁰
heart	enhanced glucose metabolism, inability to upregulate fat metabolism in exercise	Cade <i>et al.</i> , 2019 ⁶⁰
heart	increased glucose utilisation, decreased fatty acid uptake, elevated plasma free fatty acids	Cade <i>et al.</i> , 2021 ⁶¹

On a cellular level, metabolic flux analysis of patient skin fibroblasts revealed similar flux through the TCA cycle compared to healthy controls, even though destabilisation of the ETC supercomplexes and the TCA cycle enzyme 2-oxoglutarate dehydrogenase was observed. Moreover, the patient samples showed a destabilisation of the branched-chain ketoacid dehydrogenase which is involved in catabolism of branched-chain amino acids.⁷⁰ It has been suggested that a decrease in cardiac branched-chain amino acid metabolism may lead to rise in keto acids, promoting cardiac insulin resistance and cardiac hypertrophy.³⁹⁴ A recent study investigated the metabolism in BTHS patient lymphoblasts and they observed an increased glucose uptake coupled with higher levels of the glucose transporter GLUT3. GLUT1 levels were unchanged in BTHS compared to control lymphoblasts. Additionally, BTHS patient samples exhibited an enhanced glucose utilisation for triacylglycerol synthesis.²⁴⁸

On systemic level, hypoglycemia is a common symptom in individuals with BTHS and has been attributed to 4% of all hospitalisations in BTHS.³⁶⁹ It has been linked with metabolic decompensation in the infantile period due to prolonged hospitalisation after birth.³⁶⁹ However, the exact reasons and precise age-associated incidence of hypoglycemia remain elusive. Lactic acidosis is often a fundamental symptom in patients with mitochondrial diseases.³⁴⁶

Appropriately, also in some individuals with BTHS, elevated blood lactate levels were reported (**Table 1.2**). Additionally, both lactic acidosis and hypoglycemia are exaggerated during exercise and are commonly observed during neonatal and infant life.^{98,420} 3-methylglutaconic aciduria is a degradation product of the branched-chain amino acid leucine and commonly associated with compromised mitochondrial energy metabolism. It is a key diagnostic marker for BTHS which might result from accumulating acetyl CoA due to decreased metabolic flux through the TCA cycle.¹⁸⁴ However, the precise biochemical reasons remain unknown, but the reported abnormal circulating levels of amino acids can be connected to its increased excretion. In particular, low plasma arginine and possibly related low pre-albumin levels have been reported on several occasions in BTHS patients.^{320,385}

A cross-sectional study with 34 BTHS individuals (age range: 1.2 – 22.6 years) revealed a growth deficiency (mean height percentile: 8%; mean weight percentile: 15%). Additionally, they found hypercholesterolemia in 24% combined with decreased low-density lipoprotein cholesterol in 56% of patients.³⁴⁴ Another group could confirm the reduction in height and weight of BTHS patients versus the normative population. However, they observed a late catch-up in height for a significant percentage of cases.³⁰¹ In 2013, Cade and colleagues published in a study that BTHS patients have a lower fat-free mass and impaired fatty acid, glucose and amino acid metabolism. In detail, they observed an increased insulin-stimulated glucose disposal rate, reduced basal and hyperinsulinemic lipolytic rate and a trend towards increased basal leucine rate.⁵⁹ Metabolic dysregulations were also observed in metabolomics studies on plasma from a cohort of individuals with BTHS.^{320,385} Here, cellular pathways concerning insulin regulation of fatty acid metabolism and inhibition of pancreatic β -cell differentiation and function were the among the most statistically different pathways. One of the metabolites with the highest magnitude of fold change was a decrease in plasma serotonin (8.2-fold). Serotonin is a metabolite with potential mechanistic relevance to BTHS in the peripheral tissue, including cardiomyocyte growth and insulin secretion.³²⁰

Overall, the metabolic phenotype in patients with BTHS is very complex and highly heterogeneous involving several degrees of tissue manifestations. Crucial metabolic symptoms that are recurrent in most BTHS patients include hypoglycemia, enhanced glucose metabolism, lactic acidosis, dysregulated systemic amino acid and fatty acid levels. However, further investigations are necessary to understand the cause and consequences of these metabolic alterations.

1.1.3 Management of Barth syndrome patients

After diagnosis of BTHS, cardiomyopathy needs primary attention as it is the most serious and prominent symptom in patients. Drugs such as β -blockers, vasodilators, angiotensin-converting enzyme inhibitors, angiotensin II type I receptor blockers, or diuretics are most commonly used.³⁶⁹ Based on the recent findings of a decreased mechano-energetic coupling and an impaired MCU complex in BTHS cardiomyocytes, treatment with myosin modulators or SGL2-inhibitors was recommended.^{35,129} Cardiomyopathy, primarily manifested as dilated cardiomyopathy, is the clinical feature that impacts most outcomes, including the potential of severe arrhythmia.³⁶³ Heart transplantation is in some cases the only treatment to avoid serious complications or even sudden death due to cardiac problems.⁵ After a high-risk period for cardiac death in childhood, heart failure can be mitigated in adolescents based on improved and stabilised cardiac function.^{195,300,301} Therefore, the medication can refocus on nutritional and growth-related challenges as well as muscle weaknesses.³⁶³ Additionally, neutropenia needs special alertness as it is clinically relevant in about 18% of BTHS patients and granulocyte colony-stimulating factor treatment has proven to be effective in decreasing infectious complications.⁹¹

Optimisation of nutrition, hydration, and sleep, together with ongoing consultation with a dietitian are crucial managements to tackle metabolic alterations in BTHS patients (summarised in **Chapter 1.1.2**). The recurrent arginine depletion and low pre-albumin levels can limit the synthesis of creatinine, which might be connected to a reduction in plasma creatinine levels observed in BTHS patients.⁴⁰ Therefore, arginine supplementation was suggested to treat growth deficiency and low muscle mass in BTHS.⁸³ In the past, arginine supplementation was shown to be beneficial in other mitochondrial defective conditions including mitochondrial encephalomyopathy, lactic acidosis, and stroke-like episodes (known as MELAS syndrome).²⁰⁸ Of note, arginine supplementation might be linked to upregulation in glucagon secretion which has beneficial systemic effects.²⁴⁴ However, dosing of arginine supplementation is very critical as excess arginine leads to nitric oxide overproduction with consequent vasodilatation and hypotension.¹²⁶ Instead a more general approach with whey protein supplementation combined with resistance exercise training was very successful and resulted in significantly improved skeletal muscle strength and quality of life in individuals with BTHS.⁴³

To prevent hypoglycemic events, patients should avoid long periods without eating and consume a slowly absorbing energy source, such as uncooked cornstarch and a carbohydrate-rich snack before bedtime to prevent muscle mass loss.²⁹⁶ Additionally, since the frequency

and triggers of hypoglycemia in BTHS patients are unknown, blood glucose measurements should be included in all assessments for clinical deterioration. Testing for ongoing symptoms of hypoglycemia was recommended to be part of regular clinic evaluations.³⁶⁹

The current medication of BTHS is symptom-oriented, but this might potentially change in the near future, as two interventional clinical trials, namely CARDIOMAN and TAZPOWER, to treat BTHS are being carried out (intermediate results are published but trials are still ongoing).^{90,292} CARDIOMAN is a placebo-controlled study with 12 patients that investigated the efficacy of bezafibrate, a peroxisome proliferator-activated receptor α (PPAR α) agonist, in improving BTHS conditions. Although, no statistically significant changes were observed, echocardiography data showed tendencies towards improved heart size in BTHS patients treated with bezafibrate. The pharmacological effect of bezafibrate has been documented well before the clinical trial, showing substantial benefits for cardiac diseases and mitochondrial disorder in patients and animal models.²⁰³ In a *Taz-KD* mice model, bezafibrate rescues the left ventricular ejection fraction and upregulates the expression of genes related to mitochondrial fatty acid oxidation.³²⁶ The cardiac ameliorations in both preclinical and clinical studies with bezafibrate suggest that stimulation of myocardial β -oxidation via PPAR α could be beneficial for BTHS patients. On the contrary, other researchers have pointed out potential limitations as systemic activation of PPAR α might also stimulate hepatic fatty acid β -oxidation, resulting in lower circulating lipids and, hence, reducing myocardial fatty acid β -oxidation.¹³⁵

The TAZPOWER study is also a placebo-controlled study with 12 patients that investigated the efficacy of elamipretide, also known as SS-31, in improving BTHS conditions. BTHS patients treated with SS-31 showed improvements in exercise tolerance, strength, and cardiac function when compared to a placebo group or to matched natural history controls.^{161,292} SS-31 treatment even lowered the MLCL/CL ratio, which correlates to important clinical outcomes. Very recently (April of 2024) a journal pre-proof manuscript of the 4 years follow-up with SS-31 therapy was published.³⁷⁰ The long-term therapy with SS-31 resulted in sustained functional improvements regarding exercise capacity and muscle strength, and cardiac function (left-ventricular systolic and diastolic volumes and stroke volume).³⁷⁰ The promising clinical effects of the mitochondria targeted peptide SS-31 arise from its CL binding capacity and the resulting stabilisation of the inner mitochondrial membrane structure.³⁹ The interaction of CL and SS-31 has been linked with enhanced ATP synthesis, reduction of ROS and overall improved mitochondrial function.^{106,315}

Although the cardiac results of SS-31 are promising, no data on the metabolic phenotype, such as altered whole-body glucose, fatty acid and amino acid utilisation were described. Additionally, neither bezafibrate nor SS-31 is currently approved by the FDA and future studies

are necessary to support the data. Moreover, a general problem of rare diseases is the small number of participants, which makes it harder to achieve significant results.

Gene replacement therapy is another approach that could theoretically be used to cure any genetic disorder. Wang *et al.* showed that an AAV-*Taz* gene therapy directed to heart and skeletal muscle effectively restored cardiac function, prevented cardiac fibrosis, and improved muscle contractility in a murine *Taz*-KO model.³⁹⁷ Although, the proof-of-concept AAV-*Taz* gene therapy experiment was successful, before gene therapy can enter the clinical arena, several challenges will need to be addressed, such as tissue-specific efficacy, dosing in humans and public acceptance. Additionally, it is questionable if the AAV gene therapy applied after birth and only directed to specific organs (in the mentioned study: heart and skeletal muscle) would be sufficient to cure the multisystem disorder BTHS.

In summary, a multidisciplinary treatment approach involving cardiologists, nutritionists, hematologists, and genetic counsellors is essential to provide comprehensive care and improve quality of life for individuals with BTHS.

1.1.4 Animal models of Barth syndrome

There are numerous models to study the pathogenesis and underlying mechanisms of BTHS. A common characteristic and prerequisite reported in all models is an abnormal CL composition. Cellular models, including immortalised patient-derived skin fibroblasts or lymphocytes, CRISPR-generated *Taz* knockout in C2C12 myoblasts and inducible pluripotent stem cells-derived cardiac myocytes have helped to uncover critical mechanisms of BTHS.^{101,181,231,381} Those cellular models usually feature the loss in supercomplex formation of the ETC, deformation of mitochondrial morphology and alterations in ROS.²⁸⁷ However, they also face many downsides in translating the results to the human BTHS. Since BTHS is a multisystem disorder, inter-organ communication and whole-body homeostasis are significant factors that are not considered in the cellular models. Additionally, due to the stand-alone system, adaptive and compensatory mechanisms are often under-represented in those models but still are crucial for understanding the nature of the disease. The immaturity of inducible pluripotent stem cells is another essential disadvantage of the model, and their structural and functional properties are rather comparable to fetal or neonatal tissue.²⁸⁷ Animal models overcome some limitations and provide a systematic approach necessary for translational research.

Yeast (*Saccharomyces cerevisiae*) is a eukaryotic, unicellular organism and has been used to study BTHS with mentionable success. In yeast, a phospholipase called cardiolipin-specific deacylase 1 (CLD1) has been found that catalyses the deacylation of CL back to MLCL.³¹ Unfortunately, no corresponding mammalian enzyme has been identified so far. Notably, deletion of *Cld1* could rescue some of the BTHS phenotype in yeast.⁴¹⁹ However, this example illustrates the biggest disadvantage of the model, as it is evolutionary distant to humans.

The fruit fly (*Drosophila*) is an invertebrate model system and has been employed to study BTHS. Like in humans, it expresses several *Taz* transcripts and it allows to study whole organs instead of single cells as in yeast.⁴¹¹ Remarkably, *Taz* mutants demonstrated abnormal cristae which led to muscle weakness and reduced endurance. Even though, the human muscle phenotype was recapitulated well, the heart functioned normally.⁹²

Zebrafish (*Danio rerio*) is a powerful vertebrate system. To investigate the pathogenesis of BTHS, a *Taz* antisense morpholino injection was used in the past, but lately often criticised for being unspecific.²⁰⁹ Exhibiting, abnormal cardiac development, reduced heart rate and contraction, the model could resemble many cardiac aspects of BTHS patients.²⁰² Recently, a new zebrafish mutant line using CRISPR/cas9 targeting *Taz* exon 3 was employed. However, the observed phenotype was completely different from the previous morpholino based model. The homozygous *tafazzin*^{-/-} mutant did not develop cardiac defects but instead recapitulated the prominent neutropenia phenotype.²⁷¹

Mice (*mus musculus*) have some key advantages over other animal model organisms. First, mice are mammals and belong together with humans to clade of euarchontoglires and hence, share a high sequence homology.²⁸⁴ Around 90% of mouse and human genomes can be allocated into regions of conserved synteny (preserved co-localisation of genes on chromosomes).⁵⁶ Next, they provide a tremendous set of investigative tools with already available genetically modified mice strains. Therefore, crossbreeding with genetically modified mice expressing e.g. a biosensor is relatively easy and affordable. Additionally, due to the numerous research already conducted on mice, the reference literature is enormous which helps to design studies and discuss results in a bigger context.²⁸⁷ However, it must be mentioned that mouse is not automatically the best system to study the disease of interest. Genetic variations, sterile laboratory conditions and ethics based on the 3R principle should be considered before choosing the model.¹⁸⁹

In 2013, the inducible short hairpin RNA (shRNA) tafazzin knockdown (*Taz*-KD) model has been introduced. It was the first mammalian model and has become the most applied mouse system to study BTHS.³ The genetically inserted shRNA sequence is encoded on the ROSA26 (Reverse Oriented Splice Acceptor, Clone 26) locus which is widely used for achieving

generalised expression. The inducible RNA interference system works via the tetracycline-controlled Tet-On mechanism. The shRNA expression is normally blocked by the tetracycline repressor protein (tetR) and addition of doxycycline (doxy) allows the transcription by decreasing the affinity of the tetracycline repressor to the tetracycline operator sequence (**Figure 1.3**).²⁸⁰ Therefore, the presence of doxy, which can be administered via drinking water (0.5, 1 or 2 mg/ml)^{166,280,326} or chow (200 or 625 mg/kg)^{3,343}, triggers the expression of the shRNA and consequently, *Taz*-KD.²⁰⁶ Although, the inducible model provides flexibility as the *Taz*-KD is reversible, the lifelong treatment with doxy itself was linked to potential deleterious consequences on mitochondrial function and metabolism. Mice treated with doxy showed reduced OXPHOS capacity, mitochondrial complex I dysfunction, and impaired diastolic cardiac function.⁴⁰⁵ It has been shown that doxy can induce weight gain, disturbs the microbiome and influences the steroidogenesis.¹⁶² Additionally, in some cell lines, doxy exhibited cytotoxic effects in a dose-dependent manner, including generation of oxidative stress and increased apoptosis with a resulting decrease in cell viability.^{306,335,342} On the contrary, other studies show no or even positive effects of doxy application (e.g. protection of β -cell function under high-fat diet).^{305,396} Overall, doxy treatment has various effects on metabolism, ranging from beneficial to deleterious. In cell lines, the harmful effects were occurring in dose-dependent manner. Therefore, doxy side effects must be taken into account while studying BTHS in a *Taz*-KD mouse model. However, as the control group receives the same treatment, the model can still produce meaningful and reliable results.

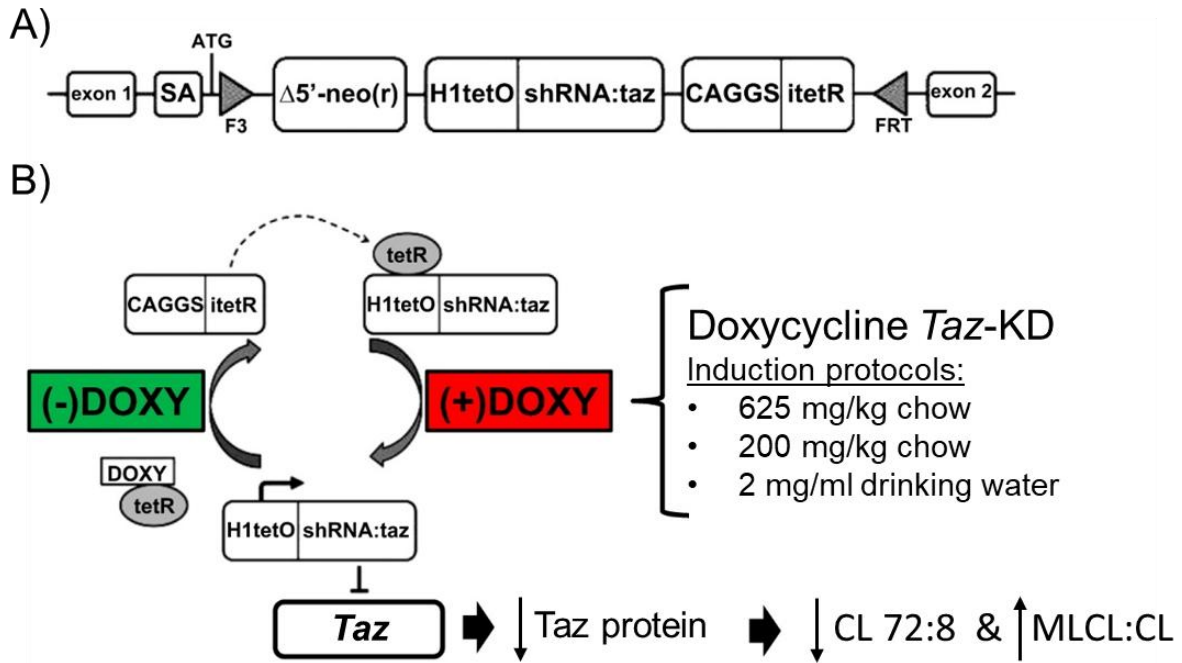


Figure 1.3: Inducible *Taz*-KD mouse model via doxy administration

(A) The F3-FRT cassette contains the shRNA H1-tet-on promoter which is flanked by a tetR and a neomycin selection gene. (B) The tetR inactivates the transcription of the tetO-shRNA promoter until doxy is added. Doxy binds the tetR promoter and allows the transcription of the shRNA. The shRNA decreases *Taz* mRNA levels which ultimately leads to a decrease in *Taz* protein levels and a change in CL profile. Different doxy induction protocols (chow and drinking water) are used to achieve *Taz*-KD. Abbreviations: doxycycline (doxy), *tafazzin* (*Taz*), tafazzin (*Taz*), cardiolipin (CL), monolysocardiolipin (MLCL), flippase recognition target (FRT), tetracycline (tet), tetracycline repressor protein (tetR), tetracycline operator (tetO). Adapted from Ren *et al.*, 2019 and original from Phoon *et al.*, 2012.^{280,294}

The *Taz*-KD in the shRNA model is highly efficient in heart tissue (> 85% of mRNA) and to somewhat varying degrees in other tissues (e.g. liver, skeletal muscle and brain).²⁸⁷ The reasons for the huge KD efficiency differences among various organs are currently unknown (further discussed in **Chapter 5.1**). For example, Cole *et al.* reported only 60% of *Taz* mRNA reduction in the heart, but around 90% in skeletal muscle and liver.⁸¹ The mice exhibited a normal lifespan and studies of cardiac, skeletal and metabolic phenotype could prove that the model recapitulate many human disease characteristics. In most studies, the levels of CL 72:8 were decreased, whereas the MLCL/CL ratio was increased.²⁸⁷ The mice developed cardiac dysfunction with impaired contractility being the most common feature in all studies. Interestingly, the cardiac phenotype was reported to be very heterogeneous, and independent groups observed various cardiomyopathy characteristics.²⁷³ The reason for those differences is unclear and cannot be explained by strain background (all C57BL6/129S6) or administered

doxy concentration (mostly 625 mg/kg food). Metabolically, the model exhibited increased lactate levels during exercise, impaired oxygen utilisation and earlier switch to carbohydrate substrates in heart tissue.²⁸⁵ On whole-body metabolism scale, researchers reported a lean phenotype with decreased body weight and altered glucose tolerance.⁸² In contrast to cellular models, no clear indications for increased ROS levels were found in the *Taz*-KD model.³⁵ One study measured the maximum capacity and rate of $O_2^{\bullet-}/H_2O_2$ formation from each production site in the heart and skeletal muscle mitochondria, but they did not identify alterations in the redox state.¹³⁰

Since the gene depletion was not gender-specific in the described models, it is possible to use both genders in the experiments. Although human BTHS is almost exclusively present in boys, there are also benefits of using male and female mice. Theoretically, it is possible that a female individual manifests symptoms of BTHS due to skewed X-inactivation or genetic disorders on both X-chromosomes. Normally, the healthy X-chromosome compensates for the defect and to date there is only one female patient described in literature which has abnormalities on both X-chromosomes.⁸⁷ However, as it is possible that women have BTHS, it is important to study the disease also in females. One of the main reasons behind using both genders in mouse models is to decrease animal numbers while still having meaningful results. Most mechanistic cellular processes are similar in males and females and hence, studying e.g. mitochondrial metabolism in either gives valid results for research progress. However, it is important to note that whole-body metabolism is notably different in males and females, and that male mice due to hormone levels are the better model to recapitulate the human disease in males. Therefore, if a relevant "N" number could be achieved, some whole-body experiments in this thesis are separated by gender. Of note, the mothers are also the carrier of the disease in humans and only 13% of boys have *de novo* mutations not identified in their mother's somatic DNA.⁸⁰

In 2020, a new constitutive *Taz* knockout (*Taz*-KO) model was generated and characterised.³⁹⁷ In contrast to the shRNA based model, *Taz* is genomically excised via a Cre-LoxP approach. The *Taz* gene on the X chromosome is flanked by LoxP sequences, causing excision upon transient expression of Cre recombinase and achieving targeted deletion of *Taz*. The absence of Taz protein and an increased MLCL/CL ratio were observed. One drawback of the model is that it exhibited high neonatal mortality.³⁹⁷ Even though this reflects the human situation with increased miscarriage and child birth, the burden for the experimental mice is significantly worse. Therefore, experiment planning, achieving statistically relevant animal numbers as well as receiving animal experiment approval is more cumbersome. The main advantage of the *Taz*-KO model is that there is no residual Taz protein left, recapitulating patients with a complete loss-of-function mutation, which usually results in severe symptoms.²³³

Characterisation of the cardiac, skeletal, immune and metabolic phenotype was performed by several groups and showed a similar phenotype to many BTHS patients. *Taz*-KO mice displayed shortened lifespan, progressive dilated cardiomyopathy, reduced endurance on a treadmill, lower neutrophil counts and higher energy expenditure.^{86,371,430}

In 2023, a new BTHS mouse model, called TAZ^{G197V}, was published.⁷⁵ Here, the mice carried a G197V missense point mutation in the *Taz* gene, corresponding to a known patient mutation.¹⁰¹ The characterisation of the model showed that the mutant TAZ^{G197V} protein was absent in western blot (WB) experiments of heart samples. Additionally, some clinical features of BTHS could be observed, including reduced neutrophil count and, cardiac dysfunction. TAZ^{G197V} resulted in a defective mitochondrial functionality, which had been observed in the previous models. The authors also described an altered metabolic phenotype with a metabolic switch from OXPHOS to glycolysis and defective fatty acid regulation. Interestingly, pharmacological AMP kinase rescued cellular metabolism and cardiac defect. However, around 40% of the born TAZ^{G197V} male mice died within 20 days after birth.⁷⁵ This model seems promising but still needs further characterisation by independent research groups.

In summary, cellular and animal models combined with patient studies have already discovered important aspects of the disease and will be necessary in the future to uncover the complete metabolic phenotype and its underlying mechanisms.

1.2 Role and function of the endocrine pancreas

As introduced in the previous Chapters, the unique phospholipid CL is crucial for cristae formation and the stability of the ETC proteins. Glucose serves as one of the primary energy sources, and its oxidative metabolism through glycolysis and TCA cycle fuels the ETC. The hormone-producing pancreatic islets tightly regulate glucose distribution and homeostasis in the body, making them essential for the overall energy supply.²² Furthermore, the production and release of hormones, such as insulin and glucagon, make them highly metabolically active. Accordingly, defects in mitochondria have been linked to impaired insulin secretion and the development of diabetes.²¹⁴ BTHS preferentially affects tissues with high metabolic demand, such as the heart and skeletal muscles.⁸⁰ Therefore, this thesis explores the role of CL on pancreatic islet functionality.

1.2.1 Pancreatic islet architecture

The pancreas is a heterocrine gland with a large exocrine (97 - 99%) and a smaller endocrine (1 - 3%) portion. The acinar cells of the exocrine tissue produce digestive enzymes (e.g. amylase and esterases), which are transported to the intestine system.²²¹ The islets of Langerhans (commonly referred to as pancreatic islets) represent the endocrine gland and contain the hormone-producing cells.^{22,311} A single human pancreatic islet measures an average of approximately 200 μm in diameter with around 1500 cells.¹⁰⁹ However, the size is very heterogeneous and varies from ten to thousands of cells.³⁴⁹ They are a highly vascularised composed cluster of various cell types, all of which are functioning in perfect synergy to regulate blood sugar levels and body homeostasis. The three most abundant cell types are the glucagon-producing α -cells (20 - 40% of total human islet cells), the insulin-producing β -cells (50 - 80%) and the somatostatin-producing δ -cells (1 - 10%).²⁶⁶ Even though the islet size among various species is roughly constant, the islet architecture and composition differ significantly.¹³¹ Human pancreatic islets tend to contain more α -cells and less β -cells compared to rodent islets. Additionally, the cell distribution within the islets differs quite a lot. Whereas, the conformation in human islets is heterogeneous and more randomly distributed, mouse islets have a peripheral layer of α - and δ -cells that surrounds a β -cell core.^{204,266}

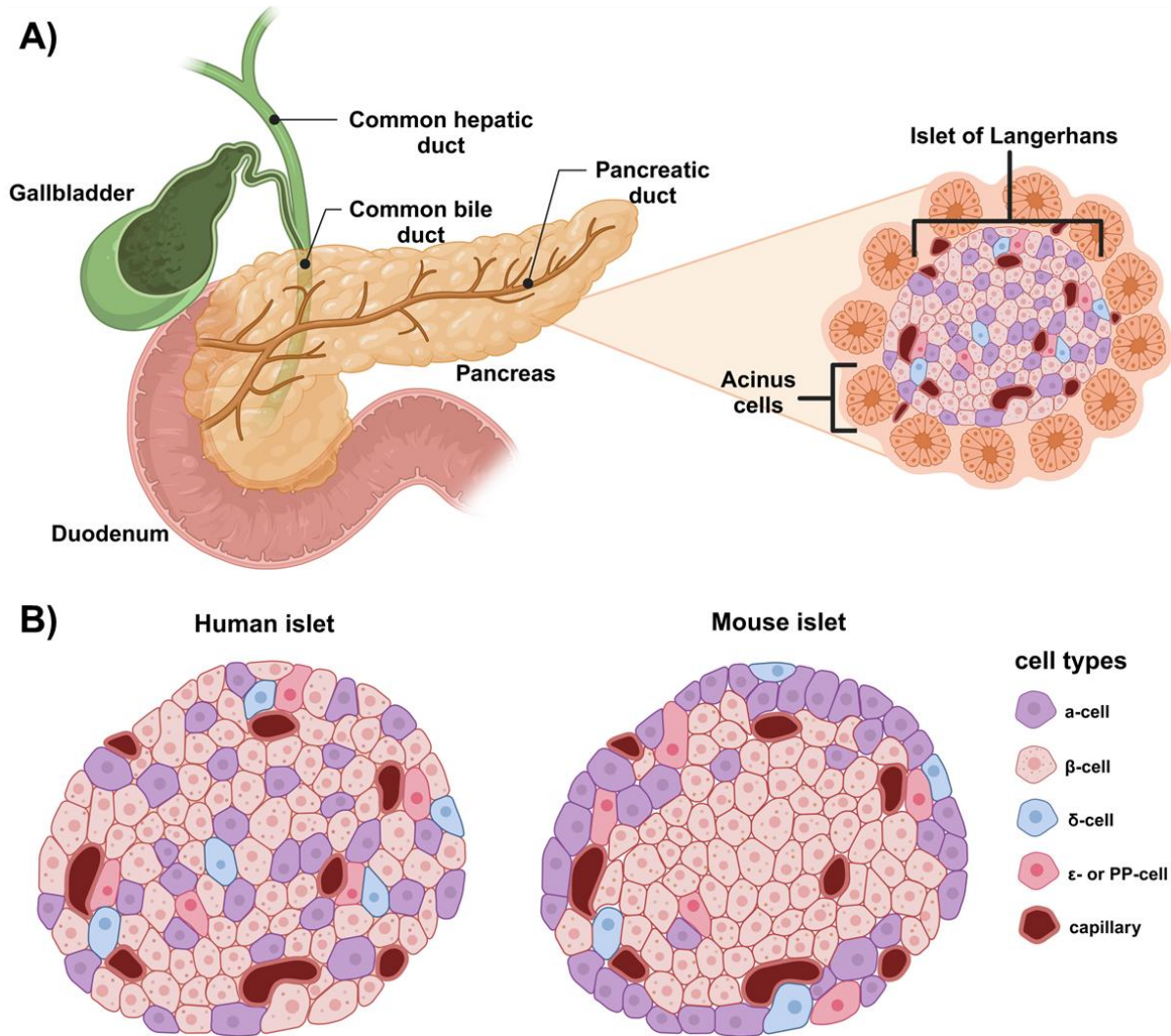


Figure 1.4: Pancreas anatomy and islet of Langerhans

(A) Anatomy of the pancreas. The pancreas is an elongated organ and is traversed by its highly branched main excretory duct, the ductus pancreaticus. The pancreatic duct joins the common bile duct prior to the ampulla of Vater. The pancreas is located in the posterior part of the abdominal cavity transversely behind the stomach between the spleen and duodenum. The endocrine parts of the pancreas are called the islets of Langerhans (pancreatic islets) that are surrounded by the exocrine acinus cells. (B) Pancreatic islets consist of various cell types (α -, β -, δ -, ϵ -, and PP-cells) that are differently arranged among animal species. Comparison of human and mouse islet architecture reveals that while in human islets the cell types are rather randomly distributed, mouse islets have a β -cell core and an α - and δ -cell mantle. Capillaries inside and next to pancreatic islets supply them with oxygen and nutrients. Abbreviations: Pancreatic polypeptide cells (PP cells). Created with BioRender.com.

The composition of the pancreatic islets and the interplay of the various cell types have critical effects on the pancreatic islet function, which is required for optimal fine-tuning of glucose homeostasis inside the body. This received major attention when it was found that β -cells have receptors for glucagon and somatostatin co-regulating their activity. In turn, α -cells also have insulin and somatostatin receptors to enable communication inside the pancreatic islets.²⁵⁵ Therefore, functional experiments on isolated dispersed pancreatic islet cells often provide different results compared to intact pancreatic islets. In single pancreatic islet cells, electrical coupling and paracrine effects are lost. Dispersed β -cells tend to be less responsive to glucose and other nutrients.¹⁷ They exhibit significant heterogeneities regarding sensitivity, transporters, and Ca^{2+} response and show overall altered insulin secretion characteristics.^{17,29} In addition to that, the mechanism of glucagon secretion by the α -cell can only be fully explained by consideration of paracrine effects within the pancreatic islet as a micro-organ.²³⁵

1.2.2 Pancreatic islet function

This Chapter focuses on the functionality of α - and β -cells, arguably the most crucial cell types in pancreatic islets.

Pancreatic β -cell function

The process of glucose-stimulated insulin secretion (GSIS) in β -cells provides marginal insulin secretion at low physiological blood glucose levels ($< 3 \text{ mM}$) as well as a dose-dependent elevation of insulin secretion upon stimulation with increased glucose concentrations.⁴² The insulin secretion upon high glucose stimulation displays a biphasic behaviour. The first peak-shaped phase employs a readily available pool of insulin granules pre-docked at the inside of the plasma membrane, and its cargo is discharged upon secretagogue triggering. By contrast, secondphase secretion includes the mobilisation of intracellular granules to the plasma membrane to evoke insulin exocytosis (**Figure 1.5 A**).³⁹⁸ Therefore, the first phase is a brief spike lasting approximately 10 min that occurs upon rapid depolarisation of all electrically coupled β -cells inside each islet. The long-lasting second phase remains active until physiological glucose levels are restored ($> 30 \text{ min}$) and is characterised by synchronous Ca^{2+} oscillations in all β -cells of an individual islet.^{127,310} In **Figure 1.5 B** the electrical activity upon glucose stimulation is depicted. The graph shows that a short initial phase of enhanced electric activity (burst) is followed by oscillations of the membrane potential between (slow waves).⁵² The electrical activity pattern corresponds to the Ca^{2+} -dependent action potentials and the subsequent pulsatile insulin release.³⁰⁸

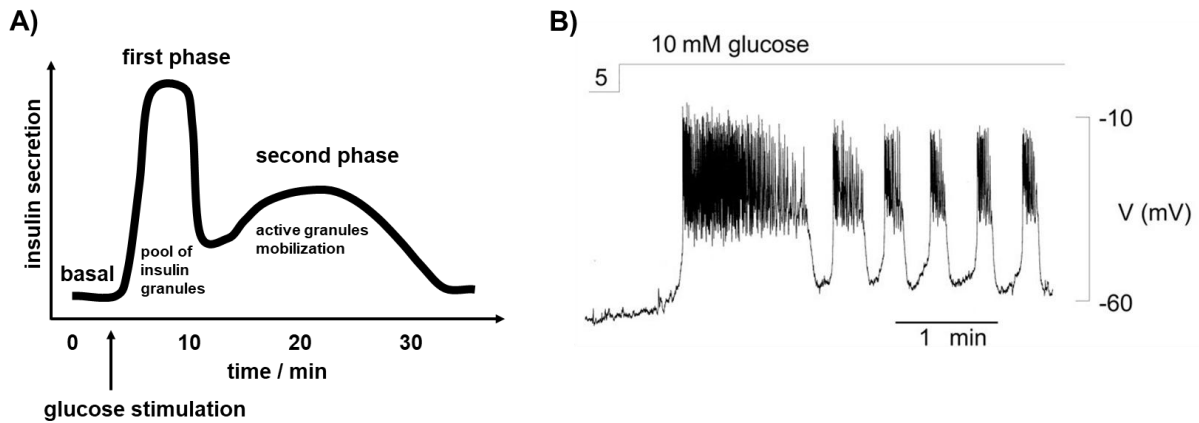


Figure 1.5: Concept of biphasic insulin secretion and electrical activity of pancreatic β -cells stimulated with glucose

(A) Schematic graph of biphasic insulin secretion. The first phase of insulin secretion upon stimulation with glucose is quick (around 5 - 10 min) and corresponds to the release of the readily available pool of insulin granules. The long-lasting second phase (> 20 min) is characterised by active mobilisation of insulin granules to the membrane and their release. (B) Glucose-stimulated electrical activity of a β -cell. Upon increase of the glucose concentration from 5 to 10 mM, electrical activity increases due to a depolarisation of the membrane. The initial burst activity is followed by regular slow waves. (A) was created with Microsoft PowerPoint, but idea was adapted from Meloni *et al.*, 2013.²⁵⁰ (B) was adapted from Rorsman *et al.*, 2000.³⁰⁸

Insulin secretion in response to glucose stimulation arises from an active triggering and an amplifying pathway (**Figure 1.6**).¹⁵² The triggering pathway is initiated via glucose uptake into the β -cell facilitated by GLUT2 (in rodents) or GLUT1 (in humans) uniporters.²⁴⁶ Once inside the cell, the glucose is immediately phosphorylated via the pancreatic specific glucokinase (Gck), which has a lower affinity for glucose compared to other hexokinases. This lower affinity (EC_{50} of around 8 – 10 mM of glucose) allows a glucose-dependent enzymatic rate adaptation across the entire physiological range (3 - 20 mM) of glucose. In contrast, other hexokinases are already saturated at around 5 mM glucose.¹⁹ The resulting glucose-6-phosphate (G6P), which can not leave the cell, can either proceed in further glycolysis steps via the G6P isomerase or is oxidised to 6-phosphogluconolactone. This reaction is the first step of the pentose phosphate pathway (PPP), and it is catalysed by glucose-6-phosphate dehydrogenase (G6PDH), in which nicotinamide adenine dinucleotide phosphate (NADP) is reduced to NADPH.³⁴⁸ Other NADPH production sites are explained in **Chapter 1.2.3**. Following further glycolysis steps, two pyruvate molecules per glucose molecule are produced, and in parallel, two net ATP molecules are gained. Pyruvate is then transported to the mitochondria, and ATP is generated in the process of OXPHOS, increasing the ratio of ATP to ADP. Mitochondrial and glycolytic ATP were both shown to participate in the closure of the

ATP-sensitive K^+ (K_{ATP}) channels. Recently, ATP production during glycolysis was found to happen in close proximity to the plasma membrane and, thus, might significantly accelerate the initial closure of K_{ATP} channels.¹⁵⁸ The closure of the K_{ATP} channels leads to membrane depolarisation due to the decrease in K^+ efflux. When a threshold membrane potential is reached (about -60 to -40 mV), voltage-gated Ca^{2+} (Ca_v) channels open, facilitating cytosolic Ca^{2+} influx. Elevation of intracellular Ca^{2+} levels triggers the release of insulin granules via exocytosis to dispatch insulin into the bloodstream.¹⁵¹ Subsequently, the insulin in the blood mediates glucose transport into other tissues and, in return, reduces the blood glucose levels.¹⁴⁶

The amplifying pathway of insulin secretion is much less understood and, in contrast to the triggering pathway, is independent of K^+ -mediated membrane depolarisation. However, it depends on the initial triggering signal in order to affect insulin secretion under physiological conditions. The amplification pathway is a metabolic way of the β -cell to optimise and fine-tune the insulin secretion.¹⁵² It is involved in both phases of the biphasic insulin secretion and is regulated by the mitochondria as a central hub. Several nutrient secretagogues pathways and metabolic coupling factors, including amino acids, fatty acids, nucleotides, acetyl-CoA and various monosaccharides, contribute to the amplifying pathway. More aspects of the amplifying pathway are intensively reviewed in Maechler, 2013, Kalwat and Cobb, 2017 and Rustenbeck *et al.* 2021.^{194,236,313}

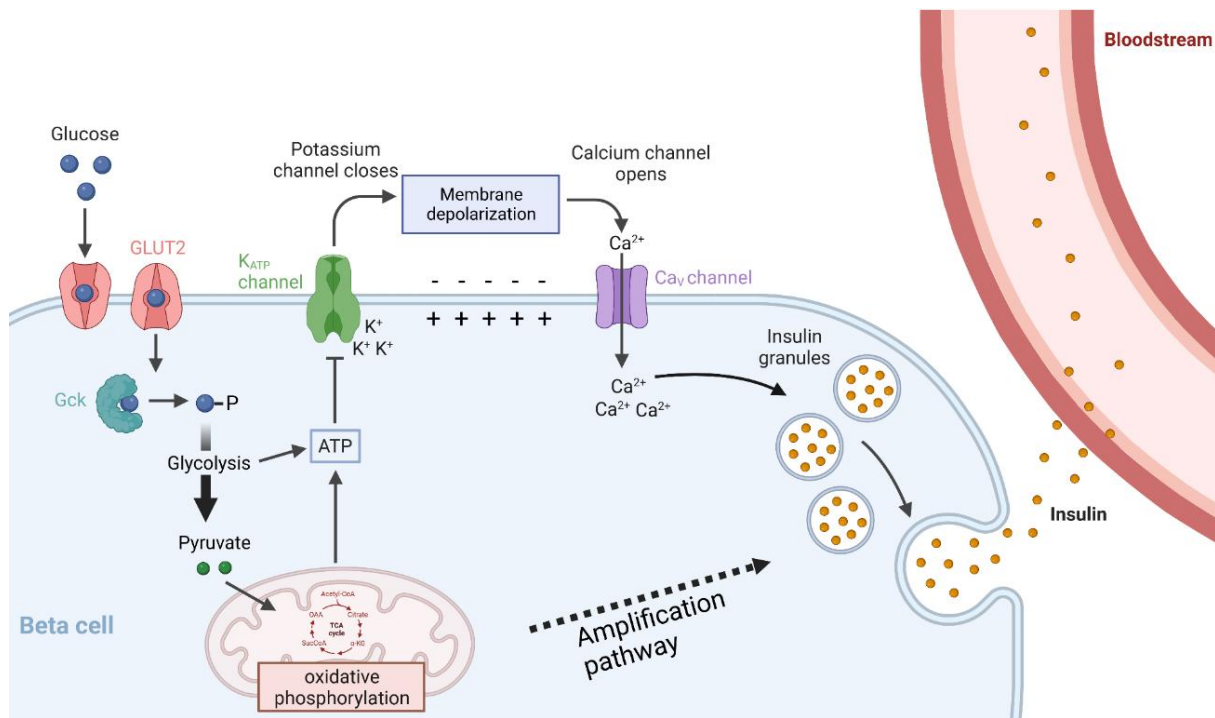


Figure 1.6: Schematic illustration of GSIS

In the process of GSIS, glucose is taken up by the uniporter GLUT2. Once inside the cell, glucose is rapidly phosphorylated to glucose-6-phosphate which is further processed to pyruvate by glycolysis. Pyruvate is taken up by the mitochondria and during OXPHOS, ATP is formed. Increased ATP levels result in the closure of ATP-sensitive K⁺ channels, called K_{ATP} channels. The accumulation of K⁺ inside the cell depolarises the cell membrane and opens Ca_v. The Ca²⁺ influx triggers the release of insulin vesicles. Abbreviations: glucose-stimulated insulin secretion (GSIS), voltage-gated Ca²⁺ channels (Ca_v), glucokinase (Gck), oxaloacetate (OAA), succinyl-CoA (SucCoA), α-ketoglutarate (α-KG), oxidative phosphorylation (OXPHOS). Created with BioRender.com.

Pancreatic α-cell function

Pancreatic α- and β-cells are considered functional antagonists and display opposing effects on whole-body glucose metabolism. Whereas insulin secretion is increased under hyperglycemic conditions to decrease blood sugar levels, glucagon secretion rises in a hypoglycemic environment to maintain or enhance blood sugar levels.¹⁴⁰ Additionally, it has been described that both hormones directly influence each other via glucagon and insulin receptors. Insulin secretion inhibits the release of glucagon.⁶⁴ In contrast, glucagon is an important activator of insulin secretion.⁶⁵ The exact process of glucagon secretion remains an open debate. Especially the role of K_{ATP} channels in low glucose-mediated glucagon secretion is discussed heavily.^{141,235} Here, the model proposed by the group of Rorsman and colleagues is summarised.⁴²⁹ Although the hormones have opposing effects, the proposed initial glucose sensing and secretion machinery seem surprisingly similar to the insulin secretion. However,

there are some key differences which are highlighted in **Figure 1.7 A, B**. Glucose uptake is facilitated by GLUT1, which has a higher glucose affinity than GLUT2 expressed in β -cells. This allows the α -cell to display electrical activity and spontaneous oscillations of Ca^{2+} at low (< 3 mM) glucose concentrations.¹³⁷ The transported glucose is phosphorylated by supposedly the same Gck in α - and β -cells, providing the possibility to adapt to physiological glucose levels.²⁴ Additionally, hexokinases (HK) might play a critical role in α -cells under low glucose conditions due to the higher glucose affinity.⁶⁴ The proceeding glycolysis and OXPHOS increase the ATP levels, leading to a closure of the K_{ATP} in α -cells. α -cell K_{ATP} channels have a > 5 -fold greater ATP sensitivity.²²² Therefore, even under hypoglycemic conditions with low glucose-mediated ATP production, the K_{ATP} channel activity is partly blocked. Another reported possibility is that cytoplasmic ATP is kept high by β -oxidation of non-esterified fatty acids (NEFA).¹⁸ In hyperglycemic conditions with high ATP production, the K_{ATP} channel activity is blocked entirely. Remarkably, the current model suggests a dual role of K_{ATP} channels in regulating insulin and glucagon release. Channel closure can either stimulate (β -cells) or inhibit (α -cells) based on the initial activity at baseline.⁴²⁹ The complete inhibition of K_{ATP} channels leads to a strong membrane depolarisation with resultant inactivation of voltage-dependent Na^+ (Na_v) and Ca^{2+} ($\text{Ca}_{\text{P/Q}}$) channels. The subsequently decreased intracellular Ca^{2+} levels block glucagon secretion (**Figure 1.7 B**).⁶⁴ Furthermore, a reduction in cAMP concentration was found to contribute to the suppression of glucagon secretion in high glucose conditions.⁴²² Conversely if K_{ATP} channels are partially closed, membrane depolarisation is in the activation range of Na_v channels. Na^+ -influx generates an action potential which opens the $\text{Ca}_{\text{P/Q}}$ channels. The resulting influx of Ca^{2+} ions triggers the release of glucagon granules (**Figure 1.7 A**).

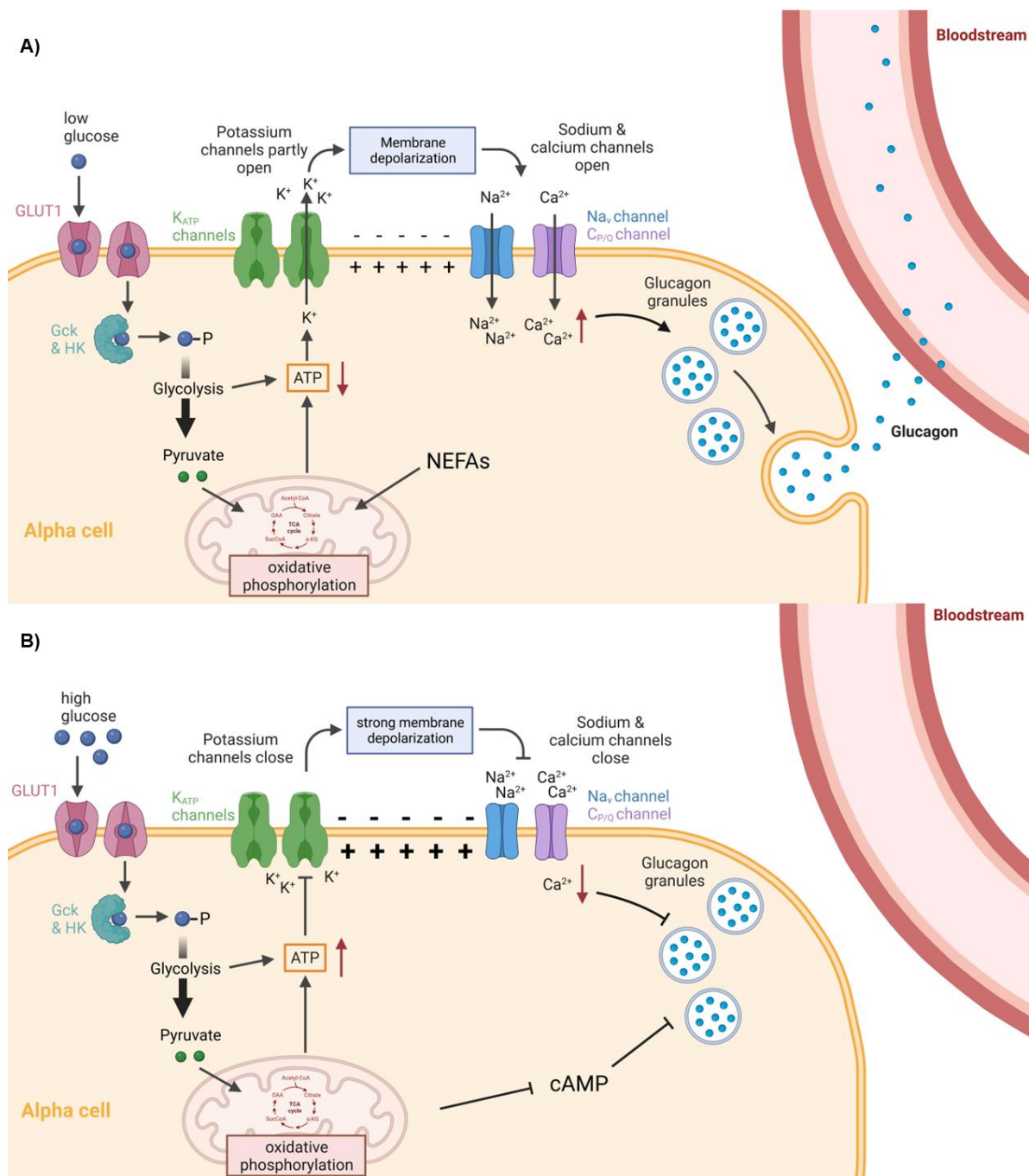


Figure 1.7: Glucose-mediated glucagon secretion

(A) α -cell function in hypoglycemia. Under low glucose conditions (< 3 mM), glucose is taken up by GLUT1 and phosphorylated mainly by the hexokinase (HK). Combined with other factors including non-esterified fatty acids (NEFA), glucose keeps the ATP levels up and partly closes the K_{ATP} channels. The depolarisation originating from the closure of the K_{ATP} channels leads to opening of voltage-gated Na^+ (Na_v) and Ca^{2+} channels ($Ca_{P/Q}$). The Ca^{2+} influx triggers the release of glucagon vesicles. **(B)** α -cell function in hyperglycemia. In high glucose conditions (> 5 mM), glucose is taken up by the GLUT1 transporter and phosphorylated mainly by the glucokinase. The elevated metabolism rate of glucose leads to high ATP levels and completely closes the K_{ATP} channels. The strong depolarisation resulting from the complete closure of K_{ATP} channels leads to a blocking of the voltage-gated Na^+ (Na_v) and Ca^{2+} channels ($Ca_{P/Q}$). Combined with other factors including high cAMP levels the decrease in intracellular Ca^{2+} levels inhibit the release of glucagon vesicles. Created with Biorender.com.

Electrical activity measurements on α -cells and the following action potential shape support the glucagon secretion hypothesis (**Figure 1.8**). An increase in glucose from 1 mM to 6 mM led to reversible membrane depolarisation and a reduction in the action potential voltage.²⁴ Regulation of glucagon secretion by glucose involves additional factors, which are not discussed here. Such factors include intrinsic regulation within the α -cells and paracrine mechanisms. For example, amylin and somatostatin released by β - and δ -cells have been postulated as regulators.⁶⁵ For further details on the function of α -cells, refer to Gromada *et al.*, 2018, MacDonald and Rorsman, 2023 and Hædersdal *et al.*, 2023.^{137,141,235}



Figure 1.8: Pancreatic α -cell electrical activity

(C) Electrical activity of an α -cell recorded as the change in membrane potential (V_m / mV) over time in 1 and 6 mM glucose (left). On the right panel, the corresponding single action potentials at 1 mM (black) and 6 mM (red) are shown. Adapted from Basco *et al.*, 2018.²⁴

1.2.3 Redox regulations in pancreatic islets

In the context of BTHS, the redox state of the mitochondria was believed to play a significant role in the development and manifestation of the disease.²³⁰ However, depending on the used model system and affected tissue, the literature shows contradicting results about ROS.²⁸⁷ Some cellular models of BTHS exhibit higher cytosolic and mitochondrial oxidative stress in samples with *Taz* deficiency.^{287,324} Whereas results from animal studies often do not display a significant rise in ROS that is connected to the BTHS phenotype.^{35,130} Additionally, the role of different ROS sources and their contribution to the mechanistic phenotype remains unknown. The defective ETC is usually the “naïve” explanation in various papers.^{123,316}

Historically, ROS were solely considered unwanted waste products from metabolism and environmental influences that damage cells and need detoxification. Nowadays, the view has changed fundamentally, and ROS species are now considered signalling molecules.²⁵⁹ Furthermore, a precise balance of the redox state is required for the proper function of the cell. Excessive ROS generation, called oxidative stress, contributes to tissue damage by

dysregulating redox-sensitive signalling pathways and oxidative damage to biological structures (e.g. DNA, proteins and lipids). Strongly reduced ROS levels, called reductive stress, also contribute to the imbalance and can have critical consequences on signalling pathways and cellular metabolism.⁴⁰⁸ Redox processes of pancreatic islets are highly compartmentalised and subcellular redox state varies massively within the cell.³⁰⁷ To add more complexity, the subcellular redox state is not limited to membrane-separated regions but rather distinct ROS microdomains are formed within different organelles.⁴⁰⁴ Hydrogen peroxide (H_2O_2) is due to its characteristics recognised as the most important ROS signalling species. H_2O_2 has compared to other ROS molecules (e.g. $\text{O}_2^{\bullet-}$ and hydroxyl radical (OH^\bullet)) a relatively low oxidising potential and therefore, a longer biological half-life. Allowing, H_2O_2 to travel even across membranes via aquaporins and causing redox relays, which are transient oxidation steps of redox-regulated proteins.¹³⁹ In the following paragraphs, the components of the antioxidative system, H_2O_2 production sites, genetically-encoded tools to identify H_2O_2 and the role for pancreatic islet functionality will be summarised. Due to simplicity, the sections will focus on H_2O_2 , which should not underestimate the tremendous role of other oxidants, including nitric oxide, peroxynitrite, singlet oxygen and hypochlorous acid.

Antioxidative system

The antioxidative system is a complex and tightly regulated system that keeps the redox balance inside the cell. It is compartmented among the different organelles and consists of working layers of several proteins and molecules characterised by their affinity to bind H_2O_2 .³⁰⁷ Superoxide dismutase (SOD) has a special role as it acts as an antioxidant enzyme but is at the same time a H_2O_2 production site. SOD accelerates the spontaneous dismutation of $\text{O}_2^{\bullet-}$ to H_2O_2 by a factor of 10^4 .¹³⁹ Several other antioxidative enzymes, including catalase, glutathione peroxidase and peroxiredoxin catalyse the reduction reaction of H_2O_2 to form H_2O . Due to low expression levels of catalase, SOD, and glutathione peroxidase, the pancreatic β -cell was considered vulnerable to oxidative stress, leading to the disease progression of diabetes.²²⁰ However, high expression levels of enzymes in the peroxiredoxin and thioredoxin pathway protect the β -cell and transform the pancreatic islets into a great redox system with high redox signalling activity in key metabolic pathways.¹⁷⁵ NADPH is an essential part of the antioxidative system acting as the major reducing equivalent in cellular redox reactions. NADPH can be directly produced via NAD kinase from NADH but most of the cellular NADPH pool originates from NADP^+ which is reduced to NADPH.²⁶⁹ The nicotinamide nucleotide transhydrogenase (NNT) is a key NADPH biogenesis site in the mitochondria. It uses the mitochondrial protonmotive force and NADH to reduce NADP^+ to NADPH.¹¹⁶ This reaction can also be reversed in pancreatic β -cells and consume NADPH in a state of low mitochondrial

membrane potential.³²¹ However, for most cell types unlike pancreatic β -cells NNT reverse-mode only occurs under pathological conditions.²⁶³ Further important NADPH production sites are the PPP with the G6PDH and the 6-phosphogluconate dehydrogenase, the cytosolic and mitochondrial malic enzymes 1 and 3, and the aldehyde dehydrogenases.⁴⁰⁷ To extend the significance even further, NADPH not only reduces the redox state of cells but it also plays a crucial role in H_2O_2 production via NADPH oxidases (NOX) which will be elaborated on in the next paragraph.

Production of H_2O_2

The main compartments for H_2O_2 production in pancreatic islets are mitochondria, peroxisomes, the endoplasmic reticulum (ER) and the cytosol (**Figure 1.9**). Mitochondria are the major consumer of molecular oxygen (O_2) in the cell, and *in vitro* studies on isolated mitochondria showed that during cellular respiration 1 - 2% of O_2 at the ETC is processed into $\text{O}_2^{\bullet-}$.³⁷⁵ Whereas complex 1 of the ETC solely generates $\text{O}_2^{\bullet-}$ in the mitochondrial matrix, complex 3 is able to produce $\text{O}_2^{\bullet-}$ at its matrix and intermembrane space side. In the intermembrane space, the enzyme SOD1 (also present in the cytosol) and in the matrix, the mitochondrial-specific SOD2 rapidly dismutates $\text{O}_2^{\bullet-}$ to H_2O_2 .³³⁴ Currently, it is still unclear if H_2O_2 production at the ETC accelerates under hyper- or hypoglycemic conditions. It is technically challenging to answer this question as the measured mitochondrial H_2O_2 levels reflect the sum of various combined redox processes. In pancreatic islets, the application of high glucose led to an initial decrease of mitochondrial H_2O_2 due to increased NADPH production.⁹⁶ Additionally, 2-oxoacid dehydrogenase (OGDH) complexes were identified as another crucial H_2O_2 production site in the mitochondrial matrix.²⁸⁹

The cytosol has its own H_2O_2 production sites. One prominent source of cytosolic ROS in pancreatic islets are NOX enzymes that produce $\text{O}_2^{\bullet-}$ or directly H_2O_2 . Rodent and human pancreatic β -cells express NOX1, NOX2 and NOX4.³⁸⁷ Whereas NOX1 and NOX2 are only located in the plasma membrane and produce $\text{O}_2^{\bullet-}$ on the extracellular matrix side, NOX4 was suggested to localise also on the membranes of ER, mitochondria and nucleus. NOX4 has more properties that distinguish it from the others as it produces directly H_2O_2 and is believed to be constitutively active.⁴²⁸ Further often underestimated sources of cytosolic ROS are enzymatic reactions from proteins like xanthine oxidase, lipoxygenase and CYP450.^{46,307} Xanthine oxidase is known to contribute to the pro-inflammatory response during the course of acute pancreatitis.²⁷⁷ Additionally, environmental factors like UV irradiation, nanoparticles and inflammation can lead to a rise in cytosolic ROS levels.⁵⁵

The peroxisomes and the ER are both relatively highly oxidised organelles in the cell. The peroxisomes contain several metabolically active oxidases that consume O_2 and produce H_2O_2 . Due to high catalase expression, the peroxisomes can handle the highly oxidised environment, and show a high ROS scavenging activity.³³² However, in pancreatic β -cells, which have low levels of catalase expression, peroxisomes can significantly contribute to increased cellular ROS levels.¹¹⁰ The ER needs an oxidised environment for protein folding where the formation of disulfide bonds can occur. It has been shown that the oxidative folding of proinsulin significantly increases the H_2O_2 production in the ER of pancreatic β -cells.²⁴⁹

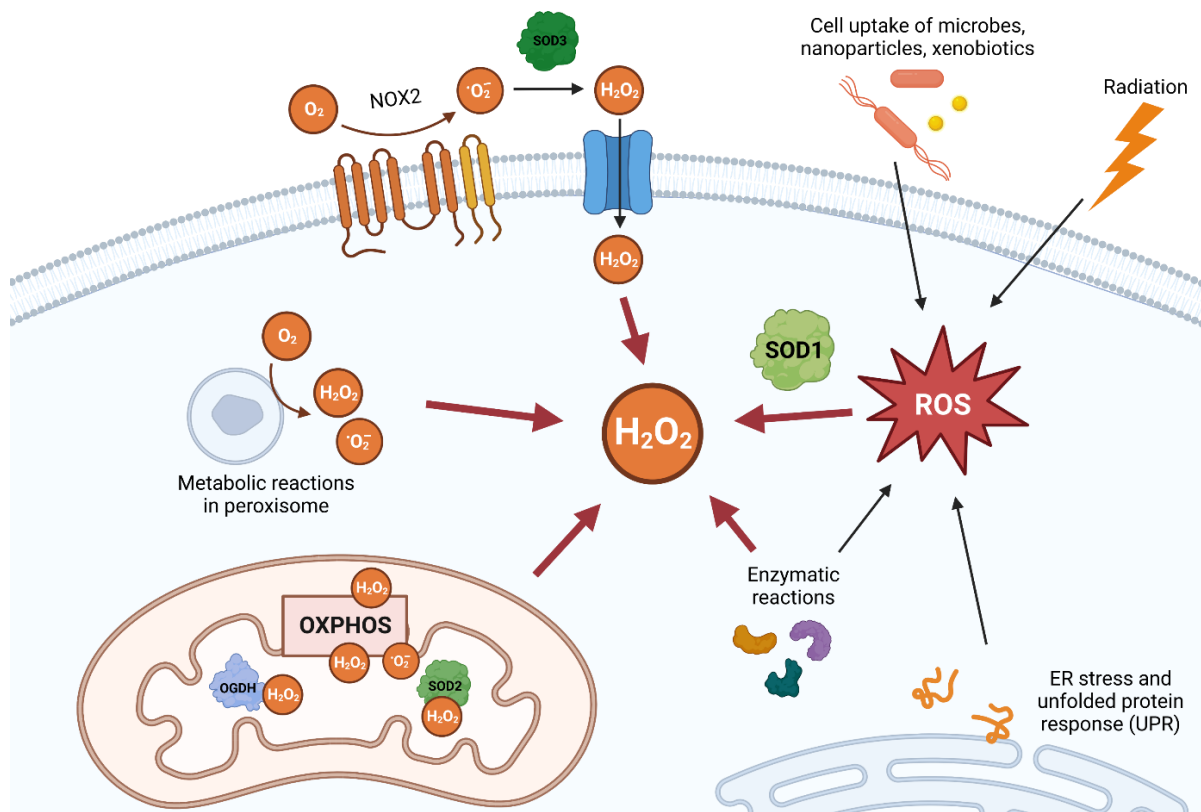


Figure 1.9: H_2O_2 production sites in the cell

ROS originating from the mitochondrial matrix (other than the intermembrane space) do not directly increase cytosolic ROS, but via redox relays and secondary ROS. Peroxisomes and ER are oxidised organelles that can affect H_2O_2 levels and signalling. Enzymatic reactions in the cytosol (e.g. xanthine oxidase and CYP450) are involved in the cellular redox metabolism. Environmental factors like radiation or inflammation can cause cellular ROS. NOX (especially NOX2 in pancreatic islets) are a major source of H_2O_2 that enters the cell via aquaporins. SOD (1-3) enzymes play an important role by catalysing the reaction $O_2^{\bullet -}$ to H_2O_2 . Abbreviations: reactive oxygen species (ROS), NADPH oxidase (NOX), superoxide dismutase (SOD), oxidative phosphorylation (OXPHOS), 2-oxoacid dehydrogenase (OGDH). Created with BioRender.com.

In the past, it has been assumed that increased ROS levels in the cytosol, nucleus or other cellular compartments often originate from mitochondrial sources.⁵ Although, increased mitochondrial oxidation or reductive stress might produce secondary ROS via redox relay and stress responses in other compartments. Recent data using the highly sensitive H₂O₂ sensors HyPer7 showed that the antioxidative system efficiently scavenges ROS from the mitochondrial matrix before it can reach the cytosol.²⁷² Furthermore, another study using the redox-sensitive green fluorescent protein 2 (roGFP2) fused with the H₂O₂-specific oxidant receptor peroxidase 1 (Orp1) to separately investigate redox changes in the mitochondria (mito-roGFP2-Orp1) and cytosol (roGFP2-Orp1), found that cytokine-induced NOX2 activity impacts pancreatic islet function.³⁸⁸ Therefore, using novel H₂O₂ sensors to study the phenotype of BTHS can pinpoint sources of ROS, leading to new and specialised treatment approaches.

1.3 Aim and motivation of this thesis

In recent years, a lot of progress has been made in the field of BTHS, especially in understanding the molecular processes behind this life-threatening disease. Despite advancements in addressing symptoms and decreasing child mortality, individuals with BTHS still express a diminished quality of life, and the condition continues to impose a substantial burden on the body.^{25,205} Most literature focuses on the heart and skeletal muscle as their main research targets. However, as a growing population of adult BTHS patients emerges, treating metabolic problems becomes increasingly relevant.³⁶⁹ Further knowledge of body homeostasis, metabolism and hormone regulation controlled by the pancreas under BTHS conditions is absolutely essential and key for future diets and therapies.

Therefore, this study aims to investigate the alterations in pancreatic islets and their consequences on systemic blood glucose homeostasis in the context of BTHS, using the well established shTaz *tafazzin*-knockdown (*Taz*-KD) mouse model. Additionally, a new mouse model was implemented by crossbreeding the shTaz mice with the mito-roGFP2-Orp1 mice to investigate redox changes and to pinpoint subcellular H₂O₂ production. Furthermore, the thesis delves into cellular adaptation processes that help the cells deal with pathological conditions.

Throughout this thesis, five key questions were addressed:

1. Does BTHS negatively impact pancreatic islet function?
2. Does BTHS lead to oxidative stress, which contributes to the disease manifestation?
3. How do pancreatic islets adapt during the development of BTHS?
4. Are whole-body metabolism changes in BTHS related to a defect in pancreatic islets?
5. What is the role of CL in pancreatic islet function?

Published data and figures

This thesis contains published data, that are part of two publications. The pancreatic islet data presented in this thesis were published in the following manuscript: "Pancreatic islets undergo functional and morphological adaptation during development of Barth syndrome", Carlein *et al.*, 2024, *Preprint bioRxiv*, doi: <https://doi.org/10.1101/2024.06.28.601122>. The data about the redox histology of *Taz*-KD hearts was published in: "Loss of mitochondrial Ca^{2+} uniporter limits inotropic reserve and provides trigger and substrate for arrhythmias in Barth syndrome cardiomyopathy", *Circulation*, Bertero *et al.*, 2021. doi: <https://doi.org/10.1161/CIRCULATIONAHA.121.053755>

2 Materials

The following Chapter lists all the used materials, devices, and software in table form.

2.1 Substances

Table 2.1: Used substances

Abbreviations: Dulbecco's PBS (DPBS), diethyl pyrocarbonate (DEPC), fetal bovine serum (FBS), bovine serum albumin (BSA), dithiothreitol (DTT), enhanced chemiluminescence (ECL), phenylmethylsulfonylfluorid (PMSF).

Substance	Company	Reference number
Agarose	Biozym	840004
Auranofin	Merck/Sigma Aldrich	A6733
BSA, Fraction V	Biomol	1400100
Calcium chloride dihydrate	Merck/Sigma Aldrich	1.02382
Calibrant XF	Agilent	100840-000
Collagenase P	Merck/Sigma Aldrich	11213865001
Dako Fluorescence Mounting Medium	Agilent	S302380
DAPI	Thermo Fisher Scientific	10116287
ddH ₂ O	UdS, Homburg	/
Diamide	Merck/Sigma Aldrich	D3648
Diazoxid	Merck/Sigma Aldrich	D9035-250MG
DMSO	Merck/Sigma Aldrich	D4540
DNA dye Peqlab peqGREEN	Avantor	732-3196
DNA loading dye (6x)	Thermo Fisher Scientific	11541575
Doxycycline hyclate	Merck/Sigma Aldrich	D9891-5G
DPBS	Merck/Sigma Aldrich	D8662
DPBS without magnesium and calcium	Thermo Fisher Scientific	14190094
DTT	Merck/Sigma Aldrich	D9779
ECL Clarity Western Substrate	Bio-Rad	1705060
FBS	Gibco	10270106
Fura-2 AM	Thermo Fisher Scientific	F1221
GeneRuler 100 bp DNA ladder	Thermo Fisher Scientific	SM0241

Glucose XF Seahorse	Agilent	103577-100
Glucose monohydrate	Carl Roth	6780.1
GlutaMAX™ (100x)	Gibco	35050-061
Glutamine	Agilent	103579-100
GLX351322 NOX4 inhibitor	Merck/Sigma Aldrich	SML2546-5MG
Goat serum	Merck/Sigma Aldrich	G9023
GSK2795039 NOX2 inhibitor	MedChemExpress	HY-18950
HCl	Thermo Fisher Scientific	10000180
Helipur®	Braun	18894
Hepatoquick	Diagnostica Stago	00761
HEPES	Merck/Sigma Aldrich	H3375
H ₂ O ₂	Merck/Sigma Aldrich	H1009
Hoechst 33342	Thermo Fisher Scientific	62249
Isoflurane CP®	CP-Pharma (via clinics)	19033194
Image-iT™ TMRM reagent	Thermo Fisher Scientific	I34361
KCl	Merck/Sigma Aldrich	P9333
Ketamine / Ursotamin (10%)	Serumwerk	04-03-9384/22
Lämmli 2x concentrate sample buffer	Merck/Sigma Aldrich	S3401
L-arginine hydrochloride	Merck/Sigma Aldrich	A-5131
L-lysine Monohydrochloride	Merck/Sigma Aldrich	L-5626
MgCl hexahydrate	Merck/Sigma Aldrich	M2670
MitoTracker™ Deep Red FM	Thermo Fisher Scientific	M22426
NaCl	Merck/Sigma Aldrich	137017
NaOH	VWR	28245460
N-ethylmaleimide	Merck/Sigma Aldrich	E3876-25G
Penicillin/Streptomycin	Merck/Sigma Aldrich	P4333-100ML
Platelet poor human plasma	Merck/Sigma Aldrich	P2918
PMSF (100 mM)	Roth	6367.4
Protease/Phosphatase inhibitor cocktail (100x)	Cell Signaling	5872
Protein marker IV (pre-stained), peqGOLD	VWR	27-2110
Poly-L-lysine solution	Merck/Sigma Aldrich	P4707-50ML
Pyruvate	Agilent	103578-100

QuickExtract DNA Extraction Solution, Lucigen	Biozym	101094
Resveratrol	Merck/Sigma Aldrich	R5010
Rompun / Xylazinehydrochlorid (2%)	WDT	04-03-9296/01
Silicone paste KORASILON® medium viscous	Carl Roth	0856.1
SS-31 (MTP 131, elamipretide)	Cayman	33302
TaqMan™ gene expression master mix	Thermo Fisher Scientific	4370048
Taq Polymerase 500U	VWR	733-1301
Tissue-Tek® O.C.T.™ Compound	Science services	SA62550-01
Tolbutamid	Merck/Sigma Aldrich	T0891-25G
Triton X-100	Roth	3051.2
TRIzol™	Thermo Fisher Scientific	15596018
Trypsin-EDTA (0.05%)	Gibco	25300062

Prescription based chemicals (Ketamin, Rompun) were ordered via local animal protection officer (Dr. med. vet. Monika Frings and Dr. med. vet. Christina Körbel) and approved by local authorities (TVA 08/2018, 19/2019).

2.2 Consumables and kits

Table 2.2: Used consumables

Abbreviations: polyvinylidene difluoride (PVDF), homogeneous time-resolved fluorescence (HTRF).

Item	Company	Reference number
Accu-Chek test strips	Aviva	06453970003
BD Microlance™ 3 30G	VWR	613-3942
BD Microlance™ 3 27G	Thermo Fisher Scientific	10204444
Blood lancets Solofix®	Thermo Fisher Scientific	10507554
Doxycycline Food, sterilised (720 ppm Doxy hyclate)	ssniff	A153D70623
Cell culture microplate, 96 well, flat bottom	Greiner	655090

Cover slips Ø25 mm	Orsatec	O2R2515-D
Cryomold Tissue-Tek® (15x15x5mm)	Science Services	SA62534-15
Cryomold Tissue-Tek® (25x20x5mm)	Science Services	SA62534-25
Falcon® 96-well plates, clear round bottom	Corning	353077
Falcon® 6-well plates	VWR	353046
HTRF 96-well low volume plates	Cisbio/Perkin Elmer	66PL96025
Microscope slides, SuperFrost® Plus	VWR	631-0108
Microtome blades – C35	Pfm medical	207500003
Microvette® CB 300 K2E	Sarstedt	16.444
Parafilm	Thermo Fisher Scientific	291-1213
PVDF membrane	Bio-Rad	1620177
Seahorse XFe96 Spheroid Microplates	Agilent	102978-100
Viewseal sealer, clear	Greiner	676070

Not listed materials including e.g. reaction tubes, pipet tips, and petri dishes were purchased in high quality from VWR, Sarstedt, Biozym, Thermo Fisher Scientific or Corning.

Table 2.3: Used Kits

Kit	Company	Reference number
CellTiter-Glo® Luminescent Cell Viability Assay	Promega	G7570
Citrate Synthase Assay Kit	Abcam	ab239712
Crystal Chem Mouse Glucagon ELISA Kit	Crystal Chem	81518
Glucokinase Activity Assay Kit	Abcam	ab273303
Glucose 6 Phosphate Dehydrogenase Activity Assay Kit	Abcam	ab176722
Glucose Uptake-Glo™ Assay	Promega	J1342
HTRF Glucagon kit	Cisbio/Perkin Elmer	62CGLPEG
HTRF Insulin Mouse Serum kit	Cisbio/Perkin Elmer	62IN3PEF
HTRF Insulin ultra-sensitive kit	Cisbio/Perkin Elmer	62IN2PEG
Pico488 dsDNA Quantification Kit	Lumiprobe	NBX-76675
Pierce BCA Protein Assay Kit	Thermo Fisher Scientific	23225

Seahorse XF Cell Mito Stress Test Kit	Agilent	103015-100
Seahorse XF Mito Fuel Flex Test Kit	Agilent	103260-100
Seahorse XFe96 Spheroid-FluxPak	Agilent	102905-100

2.3 Buffers and culture media

All prepared buffers or supplemented media used in this thesis are listed in table form. Krebs-Henseleit buffer (KHB, **Table 2.4**) was diluted in autoclaved ddH₂O and after buffer preparation, the pH was adjusted to 7.4. KHB was used for pancreatic islet isolation and selected measurements on whole and dispersed islets. The glucose concentration was not fixed and varied depending on the experiment. The lysis buffer (**Table 2.5**) was used for WB experiments and the inhibitors PMSF and protease/phosphatase inhibitor cocktail were freshly added right before protein isolation. All used media are listed in **Table 2.6** and the standard islet culture medium was based on RPMI 1640 supplemented with 10% FBS, 1% P/S. However, depending on the experimental needs (e.g. no phenol red, no glucose or sensitive Seahorse assay) variations of the standard RPMI medium were used. The supplements of the media varied depending on the performed experiment and are indicated in the respective method or result section.

Table 2.4: Krebs-Henseleit buffer (KHB)

For some substances the concentration is different in isolation or measurement KHB buffer. Company and reference number of the substances can be found in **Table 2.1**.

Substance	Concentration (islet isolation)	Concentration (measurements)
NaBic	24 mM	"
NaCl	120 mM	"
KCl	4.8 mM	"
MgCl ₂	1.2 mM	"
CaCl ₂	2.5 mM	"
BSA	0.2%*	0.1%
P/S	1%*	0%
HEPES	5 mM	"
Glucose	10 mM*	Variable in each experiment

Table 2.5: Lysis buffer

Company and reference number of the substances can be found in **Table 2.1**. ¹These substances were added freshly right before use.

Substance	Concentration
Tris HCl pH 7.5	10 mM
NaCl	10 mM
EDTA	0.1 mM
Triton-x-100	0.5%
NaN ₃	0.02%
PMSF ¹	200 µM
Protease/Phosphatase inhibitor cocktail ¹	1:100 dilution

Table 2.6: Islet culture and measurement media

*The supplements might be adjusted according to the experimental needs, which is indicated in the respective method or result section.

Medium	Company	Reference number	Supplements*
RPMI 1640	Gibco	21875034	10% FBS, 1% P/S
RPMI 1640 without phenol red	Gibco	11835030	10% FBS, 1% P/S
Seahorse XF RPMI medium	Agilent	103576-100	0.1% FBS
SILAC RPMI Flex medium	Gibco	A2494201	10% FBS, 1% P/S, 2 mM GlutaMAX, 0.174 mM L-lysine, 1.15 mM L-arginine, 1 mM HEPES

2.4 Devices and software

Table 2.7: Used devices provided with company name and serial number

Item	Company	Serial number
Accu-Chek® blood sugar meter	Aviva	06870333001
Axio Observer 7 microscope	Zeiss	3858002144
BeadBath Duo, 2l bath	Biozym	G20001365
CellDiscoverer 7 microscope	Zeiss	4652000063
Centrifuge Universal 32 R	Hettich	1610
Centrifuge Micro Star 17R	VWR	42417784
Centrifuge Z 32 HK	Hermle	67140025
Centrifuge Universal 30 F	Hettich	2568-02
Clariostar plate reader	BMG	430-1113
CO ₂ Incubator Heracell 150i	Thermo Fisher Scientific	40830469
Digital Magnetic Stirrer	Benchmark Scientific	1704-01042
Electrophoresis power supply	Bio-Rad	041BR306599
Gel documentation system	Peqlab	10200388
Gel documentation system (Universal hood 2)	Bio-Rad	76S/07812
Incubator (Non-CO ₂) Heratherm IMC18	Thermo Fisher Scientific	IMC40478529
Ismatec® Reglo ICC Digital peristaltic pump	Cole-Parmer	ISM4412
Isoflurane Luna vaporiser	Norvap	19-16122
Leica CM3050 S Cryostat	Leica	SN7600
Mini-centrifuge Fisherbrand™	Thermo Fisher Scientific	HSD05446
MilliManifold 3->1	Npi electronic	MLF-4
MyBlock Mini Dry Bath	Benchmark Scientific	112002010
NanoDrop One ^C	Thermo Fisher Scientific	AZY1706016
PCR-Thermocycler Primus 96 advanced	Peqlab	15382-02S
Pipetboy acu 2	Integra	155 016
Precision Balance	Kern & Sohn	WB0350037
pH-Electrode Orion Star A211	Thermo Fisher Scientific	X37667
Real-Time PCR Detection System CFX96 C1000 touch	Bio-Rad	785BR06498
Seahorse XFe96 analyser	Agilent	US411582
Slee tissue processor	Slee	MTM 2

Sonic dismembrator model 705	Thermo Fisher Scientific	86853K-09-15
STED microscope	Olympus	/
Stereo microscope 305	Zeiss	3943002384
Stereo microscope Wild M420	Leica	/
Sterile workbench HERAsafe KS	Thermo Fisher Scientific	41984963
Sonicator accessory Cup Horn model #431C2	Thermo Fisher Scientific	2015060595
Trans-Blot® Semi-Dry Transfer Cell	Bio-Rad	221BR57295
Vortex Genie	Scientific Industries	2E5-251618
Water bath Alpha	Lauda	CN21001248

Table 2.8: Microscope accessories

Abbreviations: numerical aperture (NA).

Device	Company	NA
Axio Observer air objective 10x	Zeiss	0.3
Axio Observer air objective 20x	Zeiss	0.75
Axio Observer oil objective 63x	Zeiss	1.4
Axio Observer camera Prime 95B	Photometrics	/
CellDiscoverer 7 air objective 20x	Zeiss	0.95
CellDiscoverer 7 water objective 50x	Zeiss	1.2
Stereo microscope Axiocam 105 color	Zeiss	/
STED microscope oil objective 100x	Olympus	1.4

Table 2.9: Used software versions

Software	Company	Version
BioRender	BioRender	BioRender 2023
ChemDraw	PerkinElmer	19.1.1.21
GraphPad Prism	Dotmatics	9.4
ImageJ	National Institutes of Health, USA	2.3.0
Image Lab	Bio-Rad	3.0.1
Imaris	Oxford Instruments	9.6.0
Imspector	Abberior Instruments	16.3.16118-w2224

Microsoft office: Excel, Word, PowerPoint, OneNote	Microsoft Corporation, USA	2016
OriginPro	OriginLab Corporation, USA	2019b
PyRat	Scionics	v4.5.1
Wave	Agilent Technologies	2.6.3
Zen blue	Zeiss, Germany	2.5 lite, 3.4 pro

2.5 Animal preparation equipment

Table 2.10: Used animal preparation equipment

Item	Company	Reference number
Broome rodent restrainer (15 – 30 g)	Thermo Fisher Scientific	12505846
Castroviejo Micro Needle Holders	FST	12061-01
Graefe Forceps	FST	11051-10
Moria Iris Forceps	FST	11373-12
Mouse restrainer (25 – 70 g)	World precision instruments	II-84XL
Fine Scissors - ToughCut®	FST	14058-11
Pierse Fixation Forceps	FST	18155-13
Surgical Scissors - Sharp-Blunt	FST	14001-14
Vannas Spring Scissors	FST	15000-08

2.6 Antibodies

Table 2.11: Antibodies used for western blot experiments or immunohistochemistry

Abbreviations: Peroxiredoxin 3 (Prx3), lysosomal-associated membrane protein 1 / 2 (LAMP1/LAMP2), PTEN-induced kinase 1 (PINK1), glutathione peroxidase 4 (GPX4), autophagy-related 7 (Atg7), microtubule associated protein 1 light chain 3B (LC3B), immunoglobulin G (IgG)

Antibody	Company	Reference number	Purpose
anti-Atg7	Cell Signaling	2631T	WB
anti-β-actin	proteintech	HRP-66009	WB
anti-Catalase	Cell Signaling	14097	WB

anti-cleaved caspase-3	Cell Signaling	9664	IHC
anti-GFP	Invitrogen	10524234	IHC
anti-Glucagon	abcam	ab10988	IHC
anti-GLUT2	Merck/Sigma Aldrich	07-1402-I	WB
anti-GPX4	abcam	ab125066	WB
anti-Insulin	abcam	ab181547	IHC
anti-Ki67	Cell signaling	12202	IHC
anti-LAMP1	DSHB	1D4B	WB
anti-LAMP2	DSHB	ABL-93	WB
anti-LC3B	Cell Signaling	2775	WB
anti-MCua	Cell Signaling	D2Z3B	WB
anti-Mouse IgG HRP	Agilent Technologies	P044701-2	WB
anti-NOX4	biotechne	NB110-58849	WB
anti-O-GlcNAc (RL2)	Thermo Fisher Scientific	11518842	WB, IHC
anti-PINK1	Thermo Fisher Scientific	11575333	WB
anti-Prk8	Cell Signaling	4211S	WB
anti-Prx3	abcam	ab73349	WB
anti-SOD2	OriGene	TA321189	WB
anti-mouse IgG Alexa Fluor™ 488	Thermo Fisher Scientific	A-21141	IHC
anti-Rabbit IgG Alexa Fluor™ 555	Thermo Fisher Scientific	A-21429	IHC
anti-Rabbit IgG Alexa Fluor™ 594	Thermo Fisher Scientific	A-11012	IHC
anti-Rabbit IgG HRP	R&D Systems	HAF008	WB
anti-Somatostatin	abcam	ab30788	IHC

3 Methods

The method section summarises the techniques, analysis and experimental models used throughout the thesis. The methods are ordered according to the result section and not by the used mouse model. Therefore, at the beginning of the method Chapter, it is important to highlight the differences between the shTaz *in vivo*, *in vitro*, and MiOxTaz models, ensuring that the reader is fully informed about the experimental setup. The specific imaging settings for the techniques are listed in table form at the end of each respective method section. These tables are designed to help the reader replicate the experiment, but it is worth noting that those small tables were not included in the list of tables.

Many of the methods were described similarly to our publication, Carlein *et al.*, 2024: "Pancreatic islets undergo functional and morphological adaptation during development of Barth syndrome" (see **Chapter 1.3**).

3.1 Animal experiments

All animal experiments were approved by the local authorities (animal experiment approval (TVA) 08/2018 and 19/2019) following the Society of Laboratory Animal Science (GV-SOLAS) guidelines. Animal numbers were recorded using the software PyRat and annually reported to local authorities (*Tierschutzbehörde Saarland*, Germany). According to the 3R (replace, reduce, refine) principle, several experiments were combined and performed with the same animal, such as body weight, glucose tolerance test (GTT) and organ isolation. Additionally, some experiments only have the minimum necessary "N" number to perform statistical tests (based on similar experiments found in the literature). Apart from the experiments in **Chapter 4.2**, which includes body weight assessment and GTT, all other measurements were performed after sacrificing the mice and isolating the organs. All mice were kept in individually ventilated cage systems (IVC housing) under 12 h day/night cycles. Based on the limited animal number, in most experiments, no sex-specific analysis was employed while studying the effects of Taz-KD. However, when the sample size was big enough to separate according to gender, as present in body weight and GTT, results from male and female mice were analysed individually.

3.1.1 Used mouse models

In this thesis, the physiological consequences of *Taz* deficiency were studied in the shTaz and shTaz-related mouse models. The shTaz mouse model was chosen for this project due to its ability to recapitulate numerous pathological similarities with BTHS patients (introduced in **Chapter 1.1.4**). The following sections will elaborate on the three used mouse models C57BL/6N, shTaz and MiOxTaz.

C57BL/6N mouse

For initial and establishing experiments, the widely used C57BL/6N mouse strain was selected. The C57BL/6N mice were initially bought from Charles River but, after 2022, had to be received from Janvier-Labs. The change in mouse supplier was requested by the animal facility because all control mice should be exchangeable among working groups. This helps to decrease overall animal numbers in the facility. However, as the C57BL/6N mouse was not crossed with the shTaz mouse and only used in establishing experiments, the change in mouse supplier should not affect the results of this thesis.

shTaz mouse

The main mouse strain investigated in this work is the shRNA *Taz*-KD mouse model, which was obtained from Jackson Laboratories, and the full name is the B6.Cg-Gt(ROSA)26Sor^{tm37(H1/tet0-RNAi:Taz)Arte}/ZkhuJ (stock number: 014648). Due to the specific doxy breeding pattern (**Figure 3.1**), the transgenic mice are heterozygous. The shRNA against *Taz* is located on the ROSA26 locus (more genetic details are provided in **Chapter 1.1.4**). Based on the gene downregulation by an shRNA, this mouse model will be referred to as shTaz. Doxy was administered in a concentration of 625 mg of doxy/kg as part of the food with standard rodent chow.

The shTaz mice had to be bred in a specific manner, which is depicted in **Figure 3.1** and will be referred to as doxy breeding. First, an adult female WT mouse and a male *Taz*-KD mouse were selected, and the female mouse was adjusted to doxy food for one week. After replacing the doxy food with standard chow, the male mouse was added to the breeding cage. The male parent mouse should never be in contact with the doxy food because this would start the transcription of the shRNA against *Taz*, and the resulting *Taz*-KD in male mice leads to infertility. After confirmation of the pregnancy (vaginal plug), the male mouse was removed, and doxy food was again added to the cage. Therefore, the experiment animals already receive doxy during the fetal development which recapitulates the disease in human patients. The weaning is followed by the separation of the mother from her pups. She continues with a

normal chow diet, whereas the pups, which will be used for experiments, continue to receive doxy.

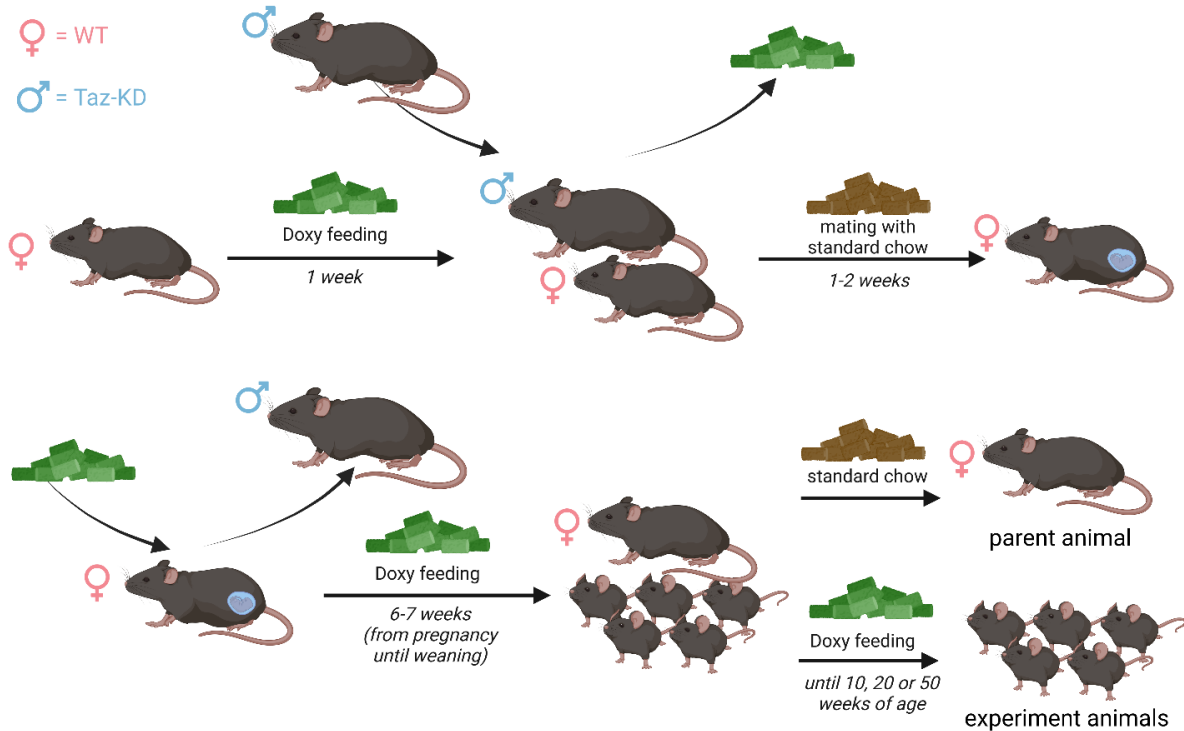


Figure 3.1: Doxy breeding scheme for shTaz mice

A female WT mouse was adjusted for 1-week to doxy food. Then, a male *Taz*-KD mouse was added to the cage, and the food was exchanged for a standard chow. After the detection of pregnancy (vaginal plug), the male mouse was removed from the cage and the female mouse was again fed with doxy food. After weaning, the pups remained on a doxy diet, whereas the mother received standard chow again. Abbreviations: *tafazzin*-knockdown (*Taz*-KD), wildtype (WT), doxycycline (doxy). Created with BioRender.com.

MiOxTaz mouse

Additionally, a new mouse strain was introduced during this project. The mito-roGFP2-Orp1 mouse strain (described by Fujikawa and Roma *et al.* 2016)¹¹⁸ globally expresses a mitochondrial H₂O₂ sensor (ROSA26/CAG-stop^{fl}-mito-roGFP2-Orp1 × CMV-Cre). A female mito-roGFP2-Orp1 mouse was crossbred with a male *Taz*-KD mouse from the shTaz mouse model. The crossbreeding process, depicted in **Figure 3.2**, was conducted in a manner similar to the doxy breeding, allowing a progression of the disease already during fetal development. The only difference to the shTaz breeding (**Figure 3.1**) is that instead of WT female mice, transgenic mito-roGFP2-Orp1 female mice were used. This breeding process resulted in the

creation of the MiOxTaz mouse strain, which was necessary for studying mitochondrial redox changes with high sensitivity (the sensor is further introduced in **Chapter 3.9**).



Figure 3.2: Doxy crossbreeding of shTaz and mito-roGFP2-Orp1 to generate MiOxTaz

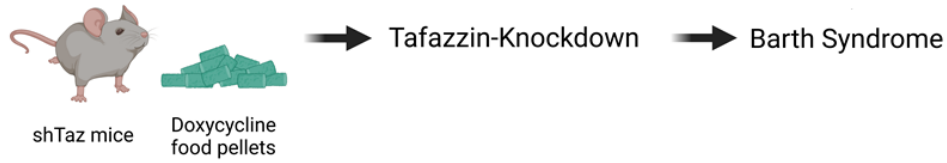
A male *Taz*-KD mouse (shTaz strain) is crossbred with a female mito-roGFP2-Orp1 mouse. The crossbreeding of those two mice strains was performed with a specific doxy protocol depicted in **Figure 3.1** (doxy crossbreeding). The pups resulting from the crossbreeding were fed lifelong with a doxy diet and used for organ isolation experiments. Abbreviations: *tafazzin*-knockdown (*Taz*-KD), wildtype (WT), doxycycline (doxy). Created with BioRender.com.

3.1.2 *In vitro* doxycycline *Taz*-KD model

In addition to the mouse models described earlier, this project established a new method to achieve *Taz*-KD *in vitro*. With this, the shTaz mice were fed with standard chow and did not develop BTHS during their lifetime. Instead, the isolated tissue (pancreatic islets) was treated with doxy added to the petri dish to induce the KD *in vitro* (**Figure 3.3**). Therefore, doxy was dissolved in ddH₂O and 1 µg/ml was added to the standard islet culturing medium (**Chapter 3.2.1**). A prior bachelor thesis project from AG Prates Roma found that 1 µg/ml was enough to induce *Taz*-KD while avoiding doxy deleterious effects in pancreatic islets. The concentration was selected based on assessing islet function via cytosolic Ca²⁺ levels, islet appearance and *Taz* mRNA reduction.²⁰ The culture medium with doxy was renewed daily. To distinguish the *in vitro* experiments from the shTaz mouse model, in all experiments that include *in vitro* model results, the shTaz mice with lifelong doxy administration were termed *in vivo*. Otherwise, if there are no results from the *in vitro* model in the respective section, shTaz always refers to the lifelong doxy model (introduced in **Chapter 3.1.1**).

Of note, although the doxy supplemented in the chow and the doxy added to the medium refer to the same doxycycline hyclate substance, they were ordered from different companies and applied in different concentrations (**Table 2.1** and **Table 2.2**).

In vivo model



In vitro model

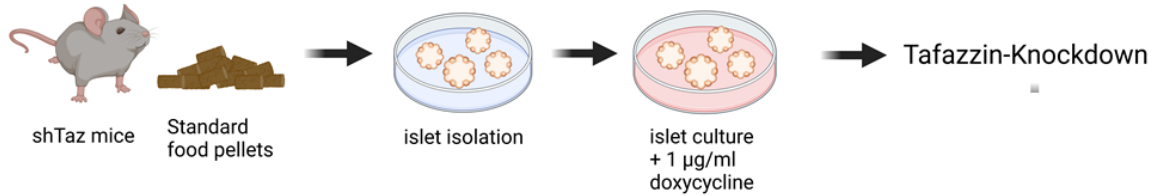


Figure 3.3: Comparison of the *in vivo* and *in vitro* model of *Taz*-KD

In the *in vivo* model, *Taz* levels are reduced during the mice's life through the administration of doxy in the chow. This model mimics the conditions of BTHS patients. In the *in vitro* model, *Taz* levels are unchanged during life as mice are fed with a standard chow. After pancreatic islet isolation, doxy (1 µg/ml) is applied in the culture medium to study the direct effects of *Taz* reduction. Abbreviations: *tafazzin* (*Taz*), *tafazzin*-knockdown (*Taz*-KD), doxycycline (doxy), Barth syndrome (BTHS). Created with BioRender.com.

3.1.3 Genotyping

The genotype of the animals was identified by polymerase chain reaction (PCR). The tissue samples were incubated in a DNA extraction buffer at 65 °C for 15 min and subsequently, mixed and incubated at 98 °C for 2 min. The extracted DNA was amplified using the according primers listed in **Table 3.1**. The primer sequence and the PCR protocols are listed in the supplements (**Chapter 7.1.1**).

Table 3.1: Used primers with the predicted product size

The primer sequence can be found in the supplements (**Chapter 7.1.1**).

Gene of interest	Primers	Predicted product size	Reference
shTaz	JD 72, 73, 74, 75	WT: 144 bp <i>Taz</i> -KD (heterozygous): 144 bp and 381 bp	Acehan <i>et al.</i> , 2011 ³
NNT	E8, E8_rev, E6-12, E6-12_rev	C57BL/6N: 157 bp C57BL/6J: 546 bp	Calculated by Primer-BLAST
mito-roGFP2-Orp1	MS 282, 284, 305	Orp/WT: 603 bp and 388 bp Orp/Orp: 388 bp	Calculated by Primer-BLAST

The PCR products were separated by agarose gel electrophoresis using the DNA dye PeqGREEN. Finally, the gel was visualised by a gel documentation system. The **Figure 3.4** shows representative genotyping results for each of the used genotyping protocols. The shTaz genotyping confirmed the predicted band size of 144 bp for WT and 144 bp + 381 bp for *Taz*-KD (**Figure 3.4 A**). As there are genetic background differences among the used mice strains (described in **Chapter 3.1.1**), the NNT was specifically tested via genotyping. The NNT is a key mitochondrial protein which is known to be one of the major differences among the most commonly used background strains C57BL/6N and C57BL/6J.²⁶³ The presence of the NNT is essential in metabolic and redox homeostasis (described in **Chapter 1.2.3**). Therefore, the testing of the NNT was crucial to properly discuss the obtained results. The genotyping gel confirmed that all used mice strains have the NNT protein (**Figure 3.4 B**). The MiOxTaz genotyping also confirmed the expected band size of the Orp1 genotyping protocol (**Figure 3.4 C**). It is worth mentioning that the Orp/*Taz*-KD displays only a single PCR product at 388 bp, which is consistent with the Orp/Orp homozygous mice strain. This is because the gene sequence in the ROSA26 locus of WT animals was replaced by the shTaz sequence and, therefore, could not be amplified through PCR.

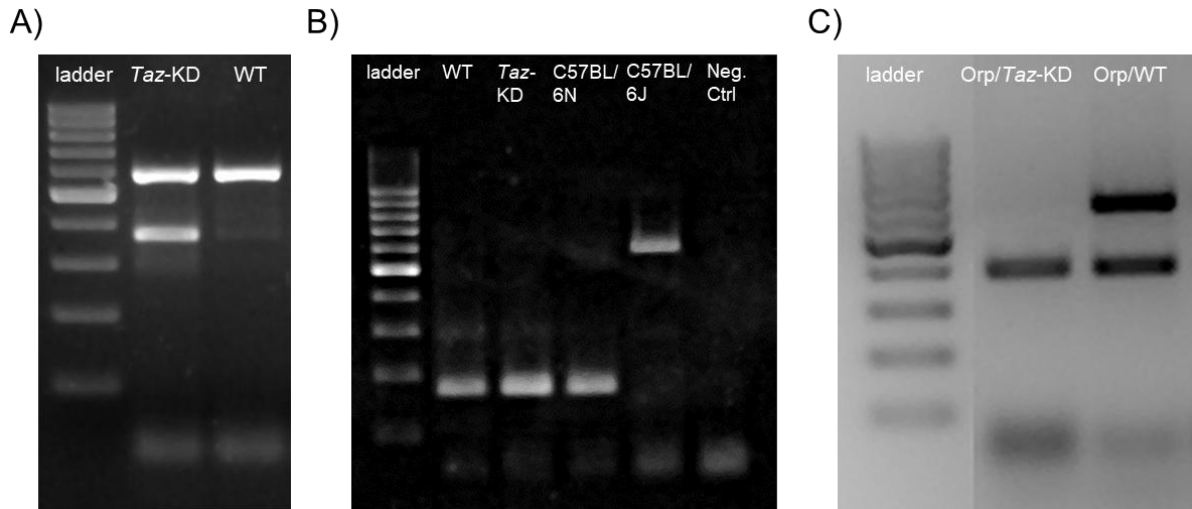


Figure 3.4: Genotyping gels of the used mice models

(A) shTaz genotyping. The *Taz*-KD samples are heterozygous and show two PCR products at predicted band sizes of 144 and 381 bp. **(B)** NNT genotyping. The used shTaz mouse model (WT and *Taz*-KD) was compared with C57BL/6N and C57BL/6J mice. The shTaz model showed the same PCR product present in the C57BL/6N and hence, the used shTaz model the NNT sequence. **(C)** MiOxTaz genotyping. The Orp/*Taz*-KD sample shows only one band as the control sequence in the ROSA26 locus was replaced by the shTaz cassette and the Orp primers cannot bind the shTaz sequence. DNA ladder: 100 bp gene ruler (described in **Figure 7.1**). Abbreviations: *tafazzin* (*Taz*), wildtype (WT), *tafazzin*-knockdown (*Taz*-KD), nicotinamide nucleotide transhydrogenase (NNT), polymerase chain reaction (PCR).

All mice in shTaz and MiOxTAZ strains were genotyped twice for *Taz*. The first genotyping was done using a biopsy of the ear, which was collected during the ear punch identification procedure after weaning of the young mice (biopsy was performed by the animal caretakers). The second genotyping was carried out after sacrificing the mice for the final experiment, using a piece of the tail to double-check the initial genotyping.

3.1.4 Glucose tolerance test (GTT)

The GTT protocol used to measure the systemic response to glucose is depicted in **Figure 3.5**. To enhance reproducibility and minimise animal stress, an initial training phase before each GTT was performed, including acclimating the mice to the mouse restrainer and releasing them without any application. The animals were weighed before the GTT started, and the injection solution was calculated based on an injection volume of 10 μ l PBS solution per gram of body weight. Following a 6 h fasting period, the mice were injected with a prewarmed 2.4 mg glucose per gram body weight solution into the peritoneum (IP injection) using a 27 G needle

and 1 ml syringe. The plasma glucose levels were monitored throughout the experiment (time points: 0, 7, 15, 30, 60 and 120 min) using a blood sugar meter. At each time point, 15 μ l of blood was collected from the tail of the mice by pinching with a 2.9 mm blood lancet and collected in an EDTA-coated tube. A centrifugation step separated the blood plasma at 2,000 relative centrifugal force (rcf) for 15 min at 4 °C. The samples were centrifuged again at 1,000 rcf for 5 min to remove any remaining pellets. The supernatant was frozen at -80 °C. Analysis of plasma glucagon and insulin levels were performed with the corresponding mouse plasma glucagon and insulin kit listed in **Table 2.3**.

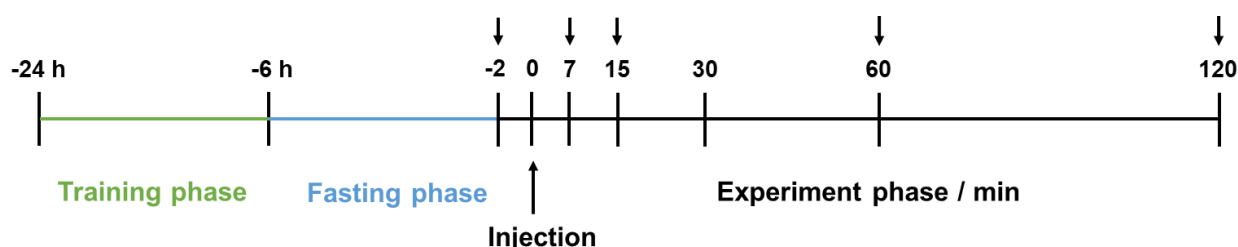


Figure 3.5: Experiment timeline of GTT

The GTT protocol includes a training, fasting and experiment phase. IP glucose injection symbolises time point 0 and the time points during the experiment phase are given in minutes time. Arrows above the timeline indicate the measurement time points at which plasma glucose, insulin and glucagon was evaluated. The time point -2 min was considered the measurement values before glucose injection. Abbreviations: intraperitoneal (IP), glucose tolerance test (GTT).

3.2 Handling of mouse islets of Langerhans

3.2.1 Isolation and culturing of pancreatic islets

The isolation of the mouse pancreatic islets was performed according to established protocols.^{134,224} In detail, the mice were anaesthetised with 2% isoflurane using an isoflurane vaporiser and, subsequently, killed via cervical dislocation. The islet isolation procedure is depicted in **Figure 3.6**, and the equipment used for mice surgery procedures is listed in **Table 2.10**. The body was opened ventrally, and the ampulla (ampulla of Vater) connecting the pancreas and small intestine was clamped. The clamping is necessary to prevent/minimise the flow of collagenase solution into the duodenum. Using a micro-spring scissor, a small incision in the common bile duct was cut directly behind the connection of the hepatic and cystic ducts. A 30 G needle was manually bent and connected to a 5 ml syringe. The needle was carefully inserted into the small incision, and the pancreas was perfused with 5 ml of an ice-cold

collagenase solution (prepared freshly: 0.63 mg/ml in KHB) via the pancreatic duct. The clamping, the cutting with a spring scissor and the perfusion steps were performed under the view of a stereo microscope at room temperature (RT). After perfusion, the pancreas was removed from the connecting tissue and placed into a petridish while using the spleen as an anchor for holding. The spleen and residual fat were cut off. The perfused pancreas was digested for 20 min in a water bath at 37 °C. Following several washing steps in KHB, the pancreatic islets were hand-picked with a pipet under the view of a stereo microscope. Until further use, the pancreatic islets were cultured in RPMI 1640 medium supplemented with 10% FBS and 1% P/S in an incubator at 37 °C and 5% CO₂. Previous studies found that culturing pancreatic islets in RPMI 1640 with 10 mM glucose showed the lowest apoptosis rate and will be referred to as the standard culturing condition throughout this thesis.¹⁸³ Every day in culture, only the pancreatic islets with a healthy and solid appearance were transferred to a new petri dish with fresh medium. Each pancreatic islet transfer (for either culturing or experiments) throughout the thesis was performed under a stereo microscope. Pancreatic islets surrounded by exocrine tissue, partly or fully destroyed, fused with other islets, or with a necrotic centre were removed and excluded from the experiment.

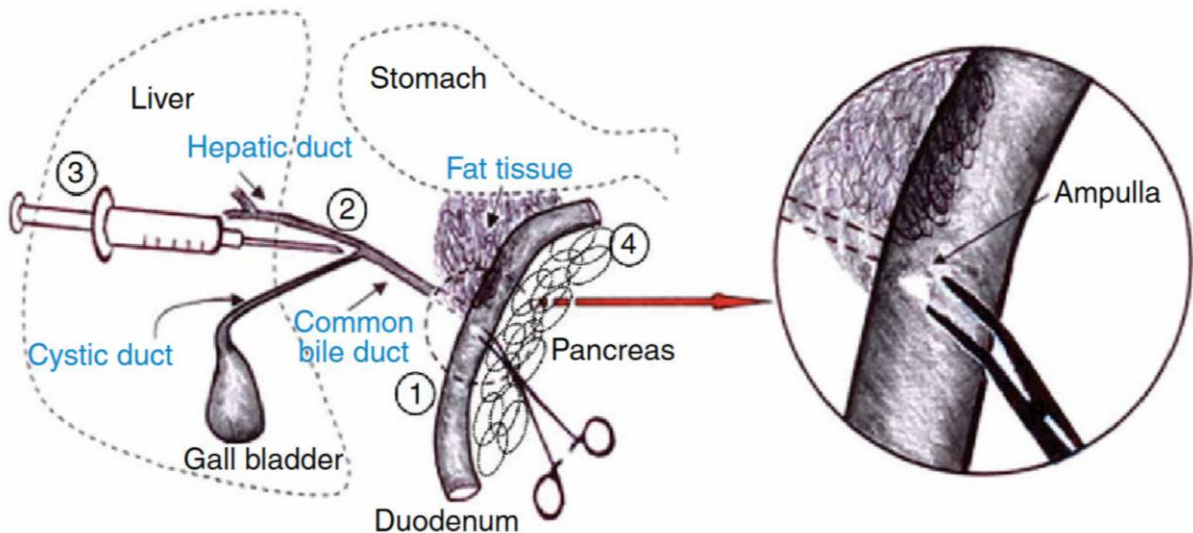


Figure 3.6: Procedure of pancreas perfusion and isolation

The perfusion and isolation of the mouse pancreas can be separated into four steps. 1) The Ampulla of Vater was clamped to block flow of solution into the duodenum. 2) A small incision in the common bile duct was cut. 3) The pancreas was perfused with collagenase solution. 4) The perfused pancreas was removed and fat freed. Adapted from Li *et al.*, 2009.²²⁴

The pancreatic islets isolated from control (C57BL6/N) and shTaz (WT and *Taz*-KD) mice were incubated at least one night and up to a maximum of three days in culture before the

experiments. The pancreatic islets isolated from the *in vitro* doxy model were treated differently and kept in culture for up to 1-week (described in **Chapter 3.1.2**).

3.2.2 Dispersion of pancreatic islets

Pancreatic islets were dispersed by transferring them (50 islets per coverslip) into a 15 ml falcon tube filled with 2.5 ml pancreatic islet medium. Centrifugation at 140 rcf for 3 min was followed by adding 1 ml prewarmed trypsin to the pellet of pancreatic islets. Next, the tube was gently shaken in a water bath at 37 °C for 2 min. After adding 9 ml medium and another centrifugation step (140 rcf, 3 min), the resulting pellet was diluted in 500 µl – 2 ml of medium (or PBS for homogenisation, see below) according to the calculated cell number. Then, the cells were harshly mixed by pipetting 10 times up and down. Finally, the dispersed cells were seeded in 50 - 100 µl volumes on coverslips placed in wells of a 24-well plate. After 3 - 4 h incubation at 37 °C and 5% CO₂, additional medium (2 ml) was added to the attached cells.

3.2.3 Homogenisation of pancreatic islets

Homogenisation of pancreatic islets was necessary for enzymatic assays and sample preparation for lipidomics experiments. First, isolated pancreatic islets were dispersed with trypsin, as described in section 3.2.2. After a final centrifugation step of the dispersed pancreatic islets, the pellet was reconstituted in Dulbecco's phosphate-buffered saline (DPBS), and the solution was sonicated at 50% for 2 min (20 s pulses and 20 s rest time) on ice. Then, the homogenised islets were centrifuged at 10,000 rcf for 10 min at 4 °C (no final centrifugation for lipidomics samples), and the supernatant was frozen at -80 °C.

3.3 Immunohistochemistry

Cryo-slices

Numbers of α -, β - and δ -cells of the *in vivo* Taz-KD model were assessed by immunohistochemistry (IHC). After isolation of the whole pancreas, the tissue was washed in PBS and fixed in 4% paraformaldehyde (PFA) overnight at RT. On the next day, the tissue was washed for 4 h in PBS before transferring it to PBS with 30% sucrose for 3 h.

Subsequently, the whole pancreas was rapidly frozen in Tissue-Tek® O.C.T.™ using liquid nitrogen-cooled isopentane. The frozen tissue was cut at -15 °C using a Leica cryostat into 5 µm thick slices. Pancreas slices were dried for 30 min before being washed with PBS and treated with 3% goat serum for 1 h in a wet chamber. Subsequently, 50 µl of primary anti-insulin together with anti-glucagon or anti-somatostatin antibodies (1:200 diluted) were added (antibodies listed in **Table 2.11**) and incubated overnight in a wet chamber at 4 °C. On the following day, slices were again washed with PBS and 50 µl of secondary antibodies (Alexa 594 and Alexa 488, 1:400 diluted, antibodies listed in **Table 2.11**) were added for 75 min at RT. After a final washing step, slices were dried and mounted with Dako mounting media. Imaging was performed with the Axio Observer 7 system using 10x or 20x air objectives.

Paraffin slices

The whole pancreas of shTaz animals (*in vivo* model) or isolated pancreatic islets (*in vitro* shTaz model) were embedded in paraffin. Freshly isolated pancreatic islets were clotted before PFA fixation. First, the pancreatic islets were incubated in 3 ml RPMI1640 medium on top of 1 ml agarose overnight at 37 °C and 5% CO₂. Subsequently, the pancreatic islets were clotted in a mixture of human platelet-poor plasma, Hepatoquick and 10 % CaCl₂. The clotted pancreatic islets and the whole pancreas were placed for 24 h in a PFA solution and then embedded with an ethanol, xylol and paraffin protocol in a tissue processor. Paraffin blocks were cut with a microtome, and slices were stained against α-, β- or δ-cells, PDX1, Ki67 or cleaved caspase-3. After antibody staining, the slices were treated with DAPI to visualise the nuclei. Imaging was performed with the Axio Observer 7 system using 10x or 20x air objectives. The analysis was performed in ImageJ, and positive stained cells were counted using the cell counter ImageJ plugin.

Spectroscopy	Setup	λ _{ex1}	BS ₁	λ _{em1}	λ _{ex2}	BS ₂	λ _{em2}
Fluorescence	Axio Observer 7	470/40 nm (Alexa488)	505 nm	550/100 nm	340/30 nm (DAPI)	409 nm	510/90 nm
		572/25 nm (Alexa594)	590 nm	629/62 nm			

3.4 Western Blot experiments

Groups of 300 islets were collected in ice-cold PBS and centrifuged at 2000 rcf for 5 min (cooled down to 4 °C). The resulting pellet was snap-frozen in liquid nitrogen and stored at -20 °C until further use. The cell lysis was performed in cell lysis buffer (**Table 2.5**) for 30 min on ice. Subsequently, the samples were centrifuged for 30 min at 14,000 rcf and 4 °C. The supernatant was transferred into a new reaction tube and protein concentration was assessed (**Chapter 3.4.1**). The proteins were separated according to their molecular mass using sodium dodecyl sulfate-polyacrylamide gel electrophoresis (SDS-PAGE). Therefore, the samples were mixed with 2x Lämmli buffer in a 1:1 ratio and denatured for 5 min at 95 °C. Then, the denatured protein samples were added to a 10 or 12.5 % SDS- polyacrylamide gel and separated at 100 V and 30 - 40 mA. The protein marker peqGOLD IV was used to quantify protein size. Before the separated proteins could be visualised with antibodies, they had first to be transferred to a methanol activated polyvinylidene difluoride (PVDF) membrane using the semi-dry approach. Here, the SDS gel and the PVDF membrane were packed between Whatman™ filter papers in a semi dry chamber. After applying 25 V and 1.3 A for 7 min, the membrane was taken out of the chamber and unspecific binding sites were blocked using TBST and 5% BSA for 1 h at RT. The primary antibodies (**Table 2.11**) were diluted 1:500 in TBST with 1% BSA and incubated with the membrane overnight at 4 °C. On the next day, the membrane was washed 3 times for 10 min with TBST before incubation with HRP-conjugated secondary antibody (**Table 2.11**) for 1 h at RT. After another washing step with TBST (3 times for 10 min), the enhanced chemiluminescence (ECL) solution was added to visualise the proteins on the membrane. The WB images were generated with a gel documentation system, analysed using the Image Lab software and normalised to the housekeeping protein β -actin.

Statistical analysis and presentation of WB data were performed in a paired manner (*Taz*-KD sample against corresponding WT sample). All WT samples were set to 100% and do not show an error among them. However, the variation among the samples was displayed in separated Figures in the respective supplementary section (**Chapter 7**). The reason being that depending on the functional experiment, some pancreatic islet samples were frozen after 1 day and others after 2 or 3 days in culture. This maximised the use of the tissue isolated from the animals which is strongly recommended by the animal guidelines following the 3R principle.

3.4.1 Protein determination

A bicinchoninic acid (BCA) protein assay kit was used to measure the protein concentration and to normalise many conducted experiments. A serial dilution of BSA for the standard curve was prepared: 0 – 0.01 – 0.02 – 0.04 – 0.06 – 0.08 – 0.1 mg/ml. If the pancreatic islets were not lysed for the respective measurement, the samples were dispersed and homogenised (according to the protocol in **Chapter 3.2.2**) before protein determination.

Spectroscopy	Detection setup	λ_{ex}
absorbance	Clariostar, discrete wavelength	562 nm

3.5 Insulin and glucagon secretion experiments

Static insulin and glucagon secretion

Static insulin and glucagon secretion was measured in a 24-well plate from pancreatic islets that were isolated one day before the experiment. Initially, all islets of each genotype were pre-incubated together under low glucose conditions (2.8 mM) in KHB for 45 min (37 °C, 5% CO₂). Subsequently, groups of 10 islets each were incubated in KHB with different glucose concentrations (2.8, 5.6, 10, 20 mM) for 1 h at 37 °C and 5% CO₂. After the incubation, the supernatant, which includes the secreted hormones, was collected and frozen at -20 °C. For further assessment of glucagon and insulin content, the remaining islets were dissolved in 74% EtOH and 0.5% HCl, and then, the supernatants of these extracts were frozen at -20 °C.

In another set of experiments, termed stimulatory protocol, glucagon secretion was potentiated by pre-incubation in high instead of low glucose. Therefore, groups of 30 islets were incubated with 20 mM glucose in KHB for 1 h at 37 °C and 5% CO₂. Afterwards, they were transferred to a pre-warmed 24-well plate with 0.5 mM glucose KHB to stimulate glucagon secretion and kept for 1 h at 37 °C and 5% CO₂. The supernatant was frozen at -20 °C. For further assessment of glucagon content, the remaining islets were dissolved in 74% EtOH and 0.5% HCl, and then, the supernatants of these extracts were frozen at -20 °C. Analysis of insulin and glucagon levels in the supernatants was performed using a homogeneous time-resolved fluorescence (HTRF) insulin ultra-sensitive and an HTRF glucagon kit.

Dynamic insulin secretion

Dynamic insulin secretion from pancreatic islets was measured in a new self-made microscope chamber (**Figure 3.7**). The chamber, drafted and designed in collaboration with Markus Hoffmann and Rüdiger Stumpf, facilitates reproducible dynamic insulin secretion experiments that can be combined with parallel microscopic imaging. This allows for the measurement of several signaling molecules, such as H_2O_2 and Ca^{2+} , and their pathways using fluorescent reports (e.g. Fura-2 AM, TMRM, etc.) while assessing the respective insulin levels. The liquid is pumped with a peristaltic flow system into one side of the chamber and due to the closed design of the chamber, the liquid exits on the other side of the chamber (**Figure 3.7 B**). This arrangement ensures a constant flow of the solution that can be collected at different time points.

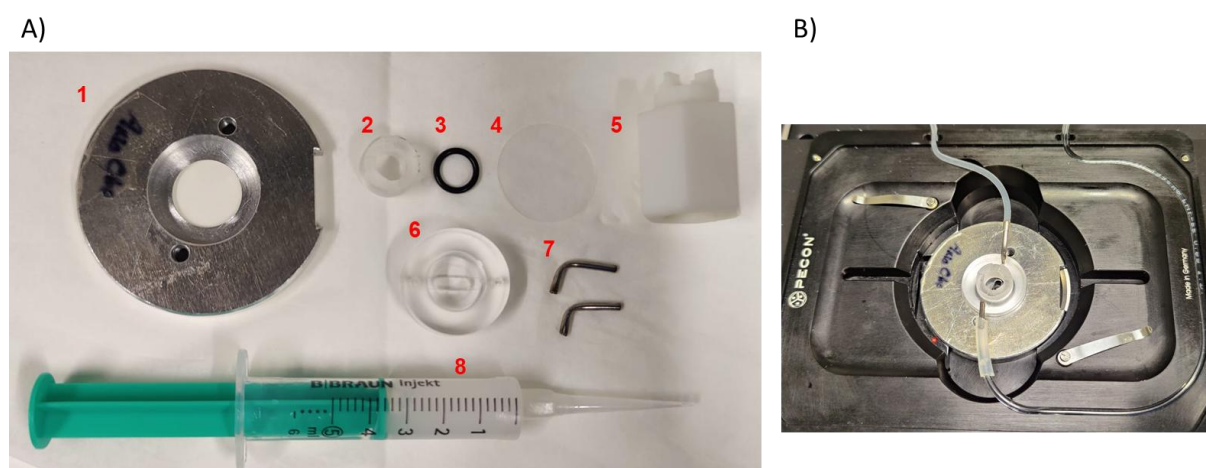


Figure 3.7: Microscope chamber for Ca^{2+} and dynamic insulin measurements

(A) Compartments of the microscope chamber. 1: measurement chamber; 2: tube with thread; 3: O-ring; 4: coverslip; 5: turning device for number 2; 6: solution chamber; 7: connection tubes; 8: silicone paste. (B) Setup of the microscope chamber inbuilt into the temperature unit of the microscope.

Before the dynamic insulin experiments, groups of 10 pancreatic islets were starved in low glucose (2 mM) KHB. Then, the islets were placed inside the chamber, similar to the cytosolic Ca^{2+} experiments (**Chapter 0**). The peristaltic pump system was set to a 1 ml/min flow, and the buffers were kept warm ($37 \pm 2^\circ\text{C}$) with a bead bath. The experiment started with the low glucose (2 mM) solution. The outflowing liquid was collected in ice-cold tubes. The solution of the initial 5 min represented the unstimulated baseline. After that, the outflowing liquid was collected each min in a new reaction tube. After 10 min, a 20 mM glucose KHB solution was pumped into the chamber. After 20 min, the outflowing liquid was collected every 2 min into a

new 2 ml reaction tube before changing to the next reaction tube. After 30 min, a 30 mM KCl solution was pumped into the chamber and the outflowing liquid was again collected every minute. At the end of the experiment, all collected sample solutions were frozen at -20 °C. In addition to that, the pancreatic islets were removed from the chamber and frozen in TE buffer (pH 8) at -20 °C. The insulin secretion levels were assessed using the HTRF insulin ultra-sensitive kit and normalised to DNA content using the Pico488 dsDNA quantification kit. Additionally, the dynamic insulin secretion experiments were also normalised to pancreatic islet size to compare the normalisation with DNA content. The pancreatic islet size was determined under the view of a stereo microscope using a camera adapter (Axio Observer Prime 95B) and analysed via ImageJ.

Spectroscopy	Setup	λ_{ex}	BS	λ_{em1}	λ_{em2}
HTRF	Clariostar, TR-FRET inbuilt filters	TR Ex (BMG inbuilt)	LP TR (BMG inbuilt)	665/10 nm	620/10 nm

3.6 Ca^{2+} experiments

Ca^{2+} experiments have been performed with whole (only cytosolic Ca^{2+}) and dispersed (cytosolic, mitochondrial, and ER Ca^{2+}) pancreatic islets. The mitochondria and ER Ca^{2+} measurements had to be performed on dispersed cells because the adenoviruses used could not penetrate whole pancreatic islets using the established protocol. Furthermore, it was only possible to image the ER and mitochondria separately from other cellular components in dispersed pancreatic islets. The three different Ca^{2+} sensors that have been used to study different cellular compartments are described in **Table 3.2**.

Table 3.2: Kd values of the used Ca^{2+} sensors

Compartment	Dye / sensor	Kd value (reference)
Cytosol	Fura-2 AM	220 nM (Santos <i>et al.</i> , 1991) ³²²
Mitochondria	Mito-Pericam	1.7 μM (Nagai <i>et al.</i> , 2001) ²⁶⁰
ER	D4ER	321 μM (Greotti <i>et al.</i> , 2016) ¹³⁶

Cytosolic Ca^{2+} experiments on whole pancreatic islets

Cytosolic Ca^{2+} levels of whole pancreatic islets were measured using the ratiometric fluorescent dye Fura-2 AM with the fluorescence microscope Axio Observer 7. Groups of 10 similar size WT and *Taz*-KD islets were loaded for 2 h with 5 μM Fura-2 AM under standard culture conditions (culture conditions in **Chapter 3.2.1**). After washing and starvation with 2 mM glucose KHB for 15 min, WT and *Taz*-KD islets were placed carefully next to each other inside the measurement chamber (**Figure 3.7**). An image of the stereo microscope was used to identify the respective genotypes in the measurement chamber of the Axio Observer 7 (**Figure 3.8**). This setup was also used for other experiments (e.g. glucose, tolbutamide and H_2O_2 titration). With this setup, both genotypes could be measured at the same time. Hence, injection time between different experiments does not limit the significance of the results.

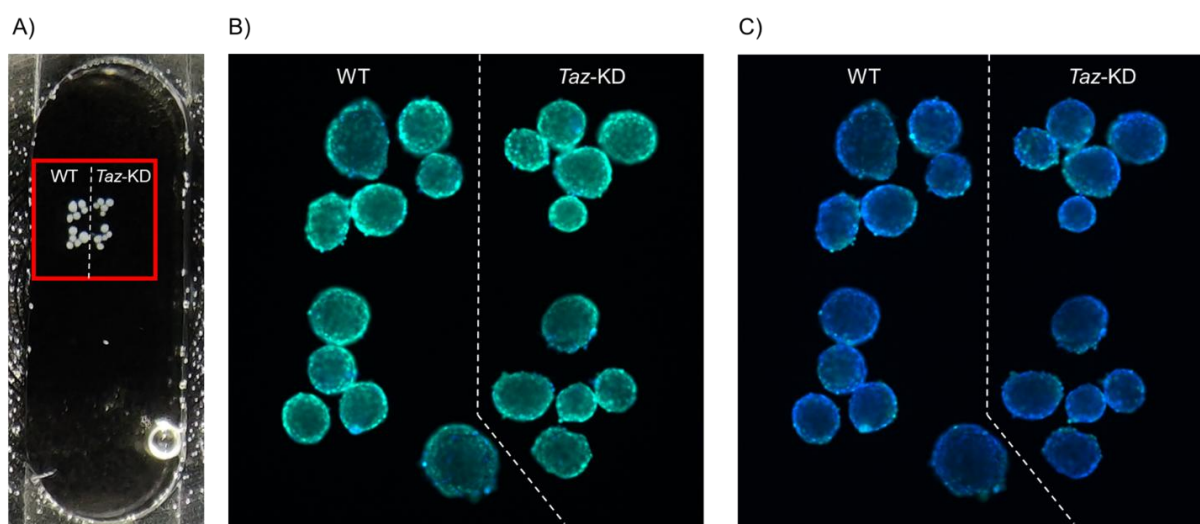


Figure 3.8: Ca^{2+} imaging setup with whole pancreatic islets using Fura-2 AM

(A) Photo of pancreatic islets arrangement inside the microscopy chamber for Ca^{2+} measurement. The photo is taken via a stereo microscope. (B) Image of pancreatic islets stained with Fura-2 AM at the start of a Ca^{2+} experiments. The image is acquired using an epifluorescence microscope with a 10x objective. One of the pancreatic islets moved a bit out of position when compared to (A). The image is false-colored according to the excitation wavelength (blue: $\lambda_{\text{ex1}} = 340/30 \text{ nm}$; green: $\lambda_{\text{ex2}} = 380/10 \text{ nm}$). (C) Image of pancreatic islets stained with Fura-2 AM after addition of high glucose/tolbutamide to stimulate Ca^{2+} influx. This changed the absorption spectra of Fura-2 AM. The image is false coloured according to the excitation wavelength (blue: $\lambda_{\text{ex1}} = 340/30 \text{ nm}$; green: $\lambda_{\text{ex2}} = 380/10 \text{ nm}$), normalised to the display settings of (B).

Before imaging, the pancreatic islets settled for 5 min inside the measurement chamber which was filled with low glucose KHB (2 mM glucose). Afterwards, baseline was recorded for 10 min

and then, glucose concentration was raised to 20 mM glucose. KCl (30 mM) was used to fully depolarise the cells (positive control) at the end of the experiment.

Spectroscopy	Setup	λ_{ex1}	λ_{ex2}	BS	λ_{em}
Fluorescence	Axio Observer 7	340/30 nm	387/15 nm	409 nm	510/90 nm

Titration experiments (tolbutamide and glucose)

To further investigate the cytosolic Ca^{2+} levels in shTaz pancreatic islets, titration experiments were performed by stepwise increasing of the sulfonylurea drug tolbutamide or glucose concentration. Tolbutamide is a K^+ channel blocker that can stimulate insulin secretion independently of the cellular ATP/ADP ratio. It binds to the K_{ATP} channel SUR 1 subunit at a different site than ATP. The resulting closure of the K_{ATP} channels leads to depolarisation of the β -cell plasma membrane from -80 mV to -40 mV, where the voltage-dependent Ca^{2+} channels start to open.⁷³ The stepwise increase of glucose or tolbutamide was achieved by a peristaltic pump system, pumping fresh KHB solution at a rate of 1 ml/min. The pancreatic islets were treated the same way described as in the former section. For the tolbutamide titration experiments, the pancreatic islets were treated with an increasing amount of tolbutamide (1, 5, 10, 30, 50, 100 μM) after measuring the baseline at 2.8 mM glucose KHB. For the glucose titration experiments, the baseline was measured in 0.5 mM glucose KHB. Afterwards, the glucose concentration was stepwise increased (0.5, 2.8, 3.5, 4, 4.5, 5, 5.6, 7, 10, 20 mM), and in the end, a 30 mM KCl solution was used as a positive control.

Mitochondrial Ca^{2+} measurement

The ratiometric mitochondrial Ca^{2+} sensor Mito-Pericam was used to test mitochondrial Ca^{2+} concentration in dispersed pancreatic islets. An increase in Ca^{2+} concentration in the mitochondria causes a spectral shift in the excitation maximum from 410 nm to 490 nm, while the emission remains at 515 nm. A ratiometric increase of 490/410 nm reflects a rise in mitochondrial Ca^{2+} levels. Adenoviral transduction was performed by adding 0.5 μl of Mito-Pericam adenovirus on top of a coverslip with 25 dispersed pancreatic islets in 2 ml RPMI medium (10% FBS, 1% P/S). Islet cells were measured two to three days after transduction using an inverted epifluorescence microscope Axio Observer 7 and a 63x oil objective. The baseline was recorded for 5 min in KHB with 2 mM glucose, before a 20 mM glucose solution

(final concentration) was applied. After 10 - 20 min measurement in high glucose conditions, 30 mM of KCl was applied to have a positive control.

Spectroscopy	Setup	λ_{ex1}	λ_{ex2}	BS	λ_{em}
Fluorescence	Axio Observer 7	405/20 nm	470/40 nm	505 nm	550/100 nm

Ca²⁺ measurement in ER-lumen

The ER-targeted biosensor D4ER was used to measure Ca²⁺ levels in the ER lumen of dispersed pancreatic islets. A rat insulin promoter (RIP) linked to the D4ER gene allowed specific transfection of solely pancreatic β -cells. D4ER was first described by Greotti *et al.*, 2016 and is a low affinity Ca²⁺ probe (K_d value of 321 μ M) based on the Förster resonance energy transfer (FRET) principle.¹³⁶ Meaning, the recorded ratio of the emission wavelengths (540 nm / 475 nm) changed depending on the Ca²⁺ concentration inside the ER. A ratiometric increase of 540 nm / 475 nm reflects a rise in ER Ca²⁺ levels. Groups of 25 dispersed islets were seeded onto coverslips in 2 ml RPMI medium (10% FBS, 1% P/S) and transduced by 0.5 μ l of adenovirus encoding D4ER. Two to three days after transduction, cells were measured using an inverted epifluorescence microscope Axio Observer 7 and a 63x oil objective. The baseline was recorded for 5 min in KHB with 2 mM glucose before a 20 mM glucose solution (final concentration) was applied. At the end of the experiment, 3 μ M thapsigargin was added to empty the ER Ca²⁺ storage.

Spectroscopy	Setup	λ_{ex1}	BS	λ_{em1}	λ_{em2}
Fluorescence	Axio Observer 7	445/25 nm	505 nm	482/18 nm	540/20 nm

Cytosolic Ca²⁺ experiments in dispersed pancreatic islet cells

Cytosolic Ca²⁺ levels of dispersed pancreatic islets were measured in a similar manner to the cytosolic Ca²⁺ experiments in whole pancreatic islets. One day before the experiment, islet dispersion was performed with groups of 25 pancreatic islets. After overnight culture, the dispersed islets were loaded with 2.5 μ M Fura-2 AM for 1 h in islet culturing medium. After washing and starvation with 2 mM glucose KHB for 15 min, cytosolic Ca²⁺ levels of WT and *Taz*-KD dispersed pancreatic islets were measured, according to the protocol described for intact pancreatic islets with the exception that both genotypes could not be measured at the same time.

3.7 Glucose metabolism

3.7.1 Glucose uptake measurement

Using the Glucose Uptake-Glo™ assay kit, glucose uptake into the pancreatic islets was assessed. Groups of 5, 10 and 20 islets were washed in glucose-free SILAC Flex-medium and imaged using a stereo microscope with an AxioCam 105 color (for normalisation). Afterwards, they were incubated for 1 h (37 °C and 5% CO₂) in glucose-free SILAC RPMI Flex medium supplemented with 20 mM of 2-deoxyglucose (2DG) to mimic glucose uptake. Once inside the cells, 2DG is phosphorylated to 2-deoxy-D-glucose-6-phosphate (2DG6P), which cannot be further metabolised. Therefore, the 2DG6P concentration is proportional to the level of glucose uptake into the cell. Pancreatic islets samples without 2DG loading were used as a negative control. After the incubation period, the standard protocol provided by the company was followed.

Spectroscopy	Setup	λ_{em}
Luminescence	Clariostar, LVF	545/50 nm

3.7.2 Enzymatic activity assays

Glucose-6-phosphate dehydrogenase enzymatic assay

Activity of glucose-6-phosphat dehydrogenase (G6PDH) was assessed using a fluorometric kit from abcam. Groups of 50 freshly isolated pancreatic islets were dispersed and homogenised. The protocol was performed according to the guidelines of the manufacturer. Fluorescent intensity was measured using a Clariostar plate reader and normalised for the respective protein concentration assessed via BCA assay.

Spectroscopy	Setup	λ_{ex}	BS	λ_{em}
Fluorescence	Clariostar, LVF	540/20 nm	560 nm	590/20 nm

Glucokinase assay

A fluorometric glucokinase activity assay kit was used to study glucokinase (Gck) activity. If not stated otherwise, the protocol provided by the manufacturer was followed. Groups of

150 freshly isolated pancreatic islets were dispersed and homogenised. For each sample, the background intensity was determined, and the obtained results were normalised for the respective protein concentration assessed via BCA assay.

Spectroscopy	Setup	λ_{ex}	BS	λ_{em}
Fluorescence	Clariostar, LVF	535/20 nm	561 nm	587/20 nm

Citrate synthase assay

A colorimetric citrate synthase assay kit was used to determine citrate synthase activity, which reflects the mitochondrial volume. If not stated otherwise, the protocol provided by the manufacturer was followed. Groups of 150 freshly isolated pancreatic islets were dispersed and homogenised. The citrate synthase activity was normalised for the respective protein concentration assessed via BCA assay.

Spectroscopy	Setup	λ_{ex}
Absorbance	Clariostar, discrete wavelength	412 nm

3.7.3 ATP assay

ATP concentration was determined by the CellTiter-Glo[®] Luminescent Cell Viability Assay Kit. Initially, groups of 5, 10 and 20 pancreatic islets were formed under standard culture conditions and imaged using a stereo microscope with an Axiocam 105 color to select islets with similar sizes. Afterwards, the protocol provided by the manufacturer was followed and the luminescence was recorded with a Clariostar plate reader. The luminescence signal was converted to ATP levels via a standard curve acquired from different concentrations (10 nM – 10 μ M) of adenosine 5'-triphosphate disodium salt hydrate. In some experiments, the pancreatic islets were pretreated for 24 h with various substances, including 100 μ M resveratrol (RSV), 100 nM SS-31, 100 μ M palmitate (complexed 5:1 with BSA, according to the protocol in Yang *et al.*, 2023)⁴¹⁷, 10 μ M GLX, 1 μ M auranofin. In the luminescence experimental settings, no excitation filter or beam splitter was required.

Spectroscopy	Setup	λ_{em}
Luminescence	Clariostar, LVF	545/50 nm

3.8 Assessing mitochondrial function in pancreatic islets

3.8.1 Mitochondrial membrane potential measurement

The dye tetramethylrhodamine methyl ester (TMRM) was used in quenching mode (**Figure 3.9**) to measure the mitochondrial membrane potential of whole pancreatic islets. The islets were incubated at 37 °C for 45 min in low glucose KHB (2 mM glucose) together with 200 nM of TMRM. After loading, the islets were washed and transferred in groups of 25 per well into a 96-well plate filled with low glucose KHB. The baseline was measured for 15 min and then, 20 mM of glucose (or 100 µM of tolbutamide) was applied. As a positive control 25 µM of CCCP was added at the end of each experiment.

Spectroscopy	Setup	λ_{ex}	BS	λ_{em}
Fluorescence	Clariostar, LVF	535/20 nm	557.5 nm	585/30 nm

Quenching mode of TMRM refers to the massive accumulation of TMRM molecules inside the mitochondria. TMRM is positively charged and travels due to hyperpolarisation of mitochondria upon nutrient stimulation into the mitochondrial matrix. Accumulation can lead to changes in the observed spectral properties (**Figure 3.9**) which can be detected with a suitable microscope or plate reader by monitoring the fluorescence. The major changes in the fluorescent properties include a fluorescence quenching and a red shift in the wavelength of maximum excitation and emission energy.³²⁵ These spectral changes are based on self-absorption effects.

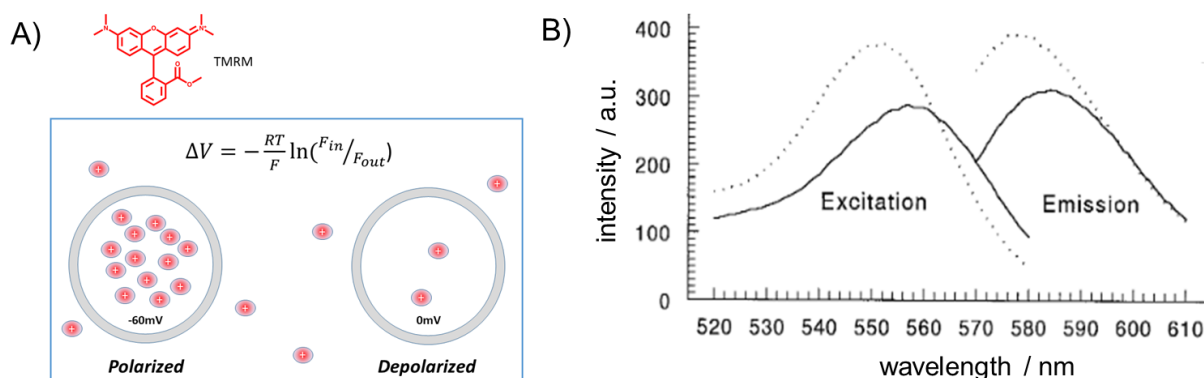


Figure 3.9: Mechanism of the mitochondrial membrane potential dye TMRM

(A) TMRM is positively charged and travels inside the mitochondrial matrix upon hyperpolarisation which can be described by the Nernst equation. (B) The spectral properties of TMRM change when TMRM molecules accumulate. The excitation and emission spectra of TMRM in low concentration (dotted line) decreases and redshifts upon accumulation of TMRM (solid line). (A) was adapted from Potentiometric Probes, University of Connecticut.²⁸⁶ (B) was modified from Scaduto *et al.*, 1999.³²⁵

3.8.2 NADH/NADPH autofluorescence measurement

One way to assess the metabolic state and activity of a cell is by measuring the autofluorescence of cellular NADH/NADPH (NAD(P)H) levels. The technique is based on the fact that upon reduction of NAD or NADP, the molecules become autofluorescent. NADH and NADPH are both essential electron carrier for cellular and mitochondrial energetics and redox homeostasis (introduced in **Chapter 1.2.3**). They have nearly identical emission spectra which is based on their similar structure and hence, cannot be separated by standard autofluorescence (**Figure 3.10**).

The NAD(P)H levels of WT and *Taz*-KD pancreatic islets were acquired in parallel to the H₂O₂ (**Chapter 3.9.1**) and TMRM (**Chapter 3.8.1**) measurements. The cellular autofluorescence reflecting the NAD(P)H levels was monitored over time in a Clariostar plate reader at 37 °C and 5% CO₂.

Spectroscopy	Setup	λ_{ex}	BS	λ_{em}
Fluorescence	Clariostar, Inbuilt filters	340/10 nm	410 nm	450/10 nm

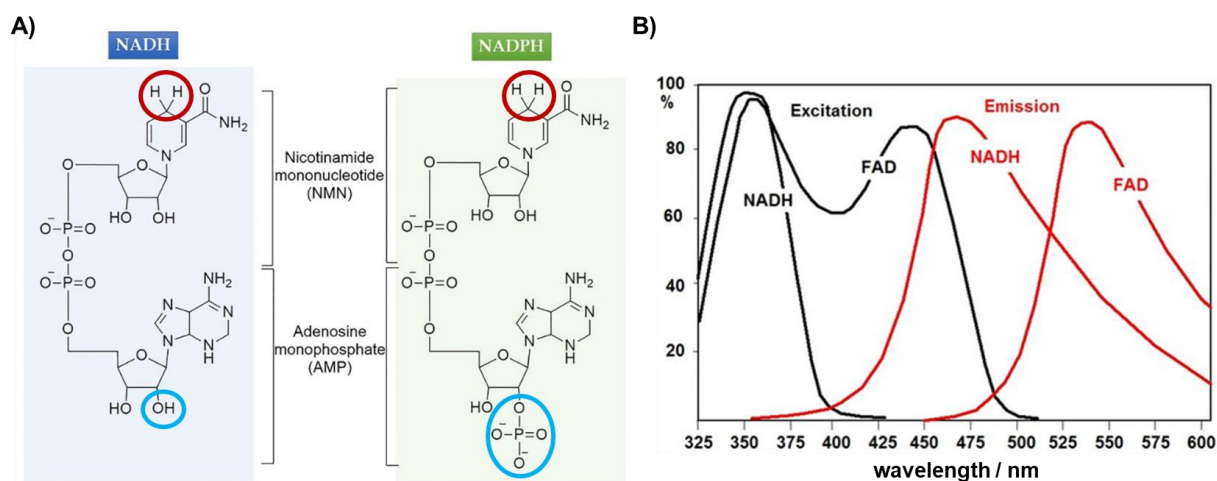


Figure 3.10: NADH/NADPH molecular properties

(A) NADH and NADPH molecular structure. In blue, the structural difference between NADH and NADPH is highlighted. In red, the oxidation site to NAD^+ or NADP^+ is highlighted. (B) Spectral properties of NADH/NADPH and FAD. (A) was adapted from Gao *et al.*, 2020.¹²¹ (B) was adapted from Becker & Hickl webpage.²⁶

3.8.3 OCR and ECAR using Seahorse XFe96 analyser

Oxygen consumption (OCR) and extracellular acidification rate (ECAR) of whole pancreatic islets were assessed using a Seahorse XFe96 analyser. Seahorse is a useful technique to study the metabolic activity of cells and isolated mitochondria.³⁵⁸ The experimental protocol, depicted in **Figure 3.11 A**, was a modified version of the Seahorse XF Cell Mito Stress Test Kit. Glucose was added to enhance cellular respiration. Subsequently, oligomycin was used to block the ATP synthase, and FCCP was used to uncouple the respiration, leading to maximum OCR. In the end, the addition of antimycin A and rotenone blocked mitochondrial respiration. The OCR values with or without the mentioned inhibitors could be used to calculate the metabolic parameters shown in **Figure 3.11 A**.

One day before the experiments, sensor cartridges were prepared by adding calibrant XF and incubating it overnight at 37°C in a non- CO_2 incubator. On the day of the experiment, a spheroid XFe96 microplate was coated with poly-L-lysine, and each well was filled with $175\ \mu\text{l}$ of pre-warmed Seahorse XF RPMI medium supplemented with 0.1% FBS, 2.8 mM glucose, and 2 mM glutamine. Groups of 15 islets were seeded with $5\ \mu\text{l}$ volume into the corresponding detent at the bottom of the wells, and the plate was equilibrated for 1 h in a non- CO_2 incubator. A detailed description of the placing of pancreatic islets inside a Seahorse XFe96 analyser can be found in Taddeo *et al.* 2018.³⁵⁸ After equilibration, the protocol of the Seahorse XF Cell Mito

Stress Test Kit combined with an initial glucose stimulation (2.8, 10, or 20 mM) was conducted. All inhibitor incubation times of the mitochondrial stress test were set to 40 min. The concentrations of the inhibitors were optimised in initial pancreatic islet experiments and set to 4.5 μ M of oligomycin, 1 μ M of FCCP, 5 μ M of antimycin A and rotenone, each. The assay was performed with at least six replicates per condition. Samples with an absolute oxygen concentration outside the range of 130 - 160 mmHg or those that were not stable throughout the assay were excluded from the analysis. The spheroid plate was inspected after the measurement to see if the islets were still inside the small detent of each well. Analysis was done with Wave and Prism software (**Table 2.9**).

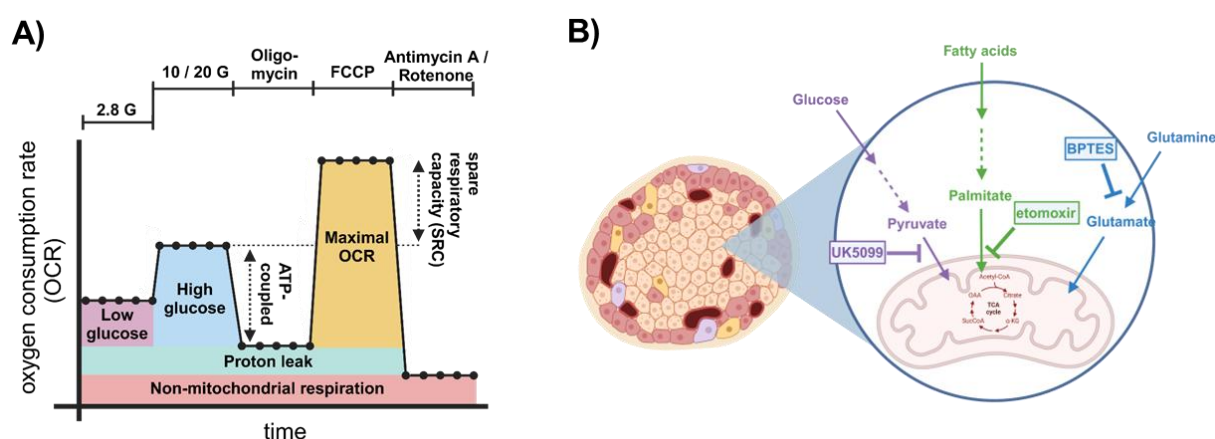


Figure 3.11: Seahorse experiments testing mitochondrial function and nutrient dependencies

(A) Protocol for mitochondrial stress test using a Seahorse analyser combined with inhibitors of the electron transport chain. The oxygen consumption rates were used to calculate the depicted metabolic parameters. (B) Mito Fuel Flex Test for investigation of nutrient dependencies and capacities using a Seahorse analyser combined with the metabolic inhibitors: UK5099, etomoxir and BPTES. (A) was created with Biorender.com. (B) was created with Biorender.com, but the idea was taken from Agilent Technologies user manual.⁷

Nutrient dependencies and capacities were measured using the Seahorse XF Mito Fuel Flex Test Kit. In detail, three inhibitors (2 μ M of UK5099, 4 μ M of Etomoxir and 3 μ M of BPTES) were used to test each genotype's nutrient dependencies and capacities. As displayed in **Figure 3.11 B**, UK5099 is an inhibitor of the glucose utilisation pathway by blocking the mitochondrial pyruvate import via the mitochondrial pyruvate carrier.⁴¹⁶ Etomoxir blocks the lipid β -oxidation because it is an irreversible inhibitor of the carnitine palmitoyl-transferase 1A (CPT1) which is needed for the transport of long chain fatty acids into the mitochondria.³³⁷ BPTES is an inhibitor of the glutamine oxidation pathway. It allosterically inhibits the conversion of glutamine to glutamate, which is catalysed by the glutaminase and normally feeds the TCA cycle via α -ketoglutarate.³⁴¹ After an initial baseline measurement, one of the listed pathways

was blocked by the injection of one inhibitor and subsequently, the other two pathways were blocked together with the next injection. Different combinations of inhibitors could determine the nutrient dependencies and capacities. The Seahorse assay medium for this nutrient dependency test was based on the Seahorse XF RPMI medium supplemented with 10 mM glucose, 2 mM glutamine, 1 mM pyruvate, and 0.1% FBS. The glucose level was set to a concentration of 10 mM as this is comparable to the optimal islet culturing conditions.

The dependency on each substance was calculated percentage-wise using the following formula:

$$(\text{eq. 1}) \text{ Dependency} = \frac{\text{Baseline OCR} - \text{Target inhibitor}}{\text{Baseline OCR} - \text{All inhibitors}} \times 100\%$$

SypHer pH measurements

With the ratiometric SypHer pH sensor cytosolic pH values in dispersed pancreatic islets were determined. Adenoviral transduction was performed by adding 0.5 μl of adenovirus on top of a coverslip with 10 dispersed pancreatic islets in 2 ml RPMI medium (10% FBS, 1% P/S). Two days after transduction, pancreatic islet cells were measured using an inverted epifluorescence microscope Axio Observer 7 and a 20x objective. Glucose in concentrations of 2 mM and then 20 mM was added to the medium, followed by the application of 5 μM oligomycin, 2 μM FCCP and 30 mM NH_4Cl (positive control).

Spectroscopy	Setup	λ_{ex1}	λ_{ex2}	BS	λ_{em}
Fluorescence	Axio Observer 7	405/20 nm	470/40 nm	505 nm	550/100 nm

3.9 Redox analysis using genetically-encoded probes

After the development of the redox-sensitive green fluorescent protein (roGFP), researchers have engineered several variants, with each new one improving sensitivity and specificity. The fusion protein of the redox-sensitive green fluorescent protein 2 (roGFP2) and the oxidant receptor peroxidase 1 (Orp1) is termed roGFP2-Orp1 was introduced in 2016 by Fujikawa *et al.* and was the first redox sensor which is sensitive enough to measure physiological H_2O_2 kinetics in mammalian cells with real-time detection (**Chapter 3.9.1**).¹¹⁸ Additionally, using redox histology (**Chapter 3.9.2**), the sensor can be used to measure *in vivo* redox state. The roGFP2-Orp1 is a fused protein of the roGFP2 biosensor and the thiol peroxidase Orp1. The

process of redox sensing roGFP2-Orp1 is depicted in **Figure 3.12**. The Orp1 thiol groups get specifically oxidised by H_2O_2 which in turn facilitates the roGFP2 oxidation. The resulting conformational change of roGFP2 shifts the excitation spectra from 400 nm (oxidised) to 480 nm (reduced). Therefore, the ratio of oxidised to reduced roGFP2 depends on the local H_2O_2 concentration.

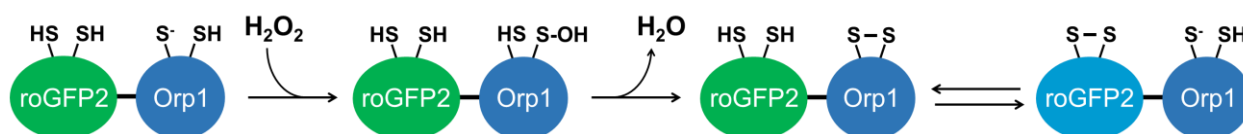


Figure 3.12: Redox sensing using roGFP2-Orp1

The roGFP2-Orp1 biosensor senses an increase in the local H_2O_2 concentration by an initial oxidation of the thiol peroxidase Orp1 and a secondary oxidation of roGFP2. The resulting shift in the excitation spectra of roGFP2 is indicated by a colour change from green to blue. Abbreviations: redox-sensitive GFP 2 (roGFP2), oxidant receptor peroxidase 1 (Orp1). Figure was modified adapted from Fujikawa *et al.*, 2016.¹¹⁸

3.9.1 H_2O_2 measurements

In this thesis, microscope and plate reader experiments have been performed (**Figure 3.13**). Both approaches were used for the redox experiments, and the newly designed microscope system Cell Discoverer 7 (CD7) from Zeiss, which combines the strengths of both methods, was employed. One significant advantage of the plate reader over the microscope is its ability to measure multiple conditions simultaneously. Another advantage is the versatility of spectral techniques, whereas microscopes usually only measure fluorescence. Additionally, the plate reader allows for measurements under long-term incubation conditions, while microscope experiments often stress the samples and are limited to relatively short periods of time. However, microscope imaging generates high-quality images with typically better sensitivity than plate readers. The CD7 combines the benefits of microscopy and plate reader measurements. However, the large amount of data acquired from this automated microscope system needs to be analysed and processed, which requires time and experience.

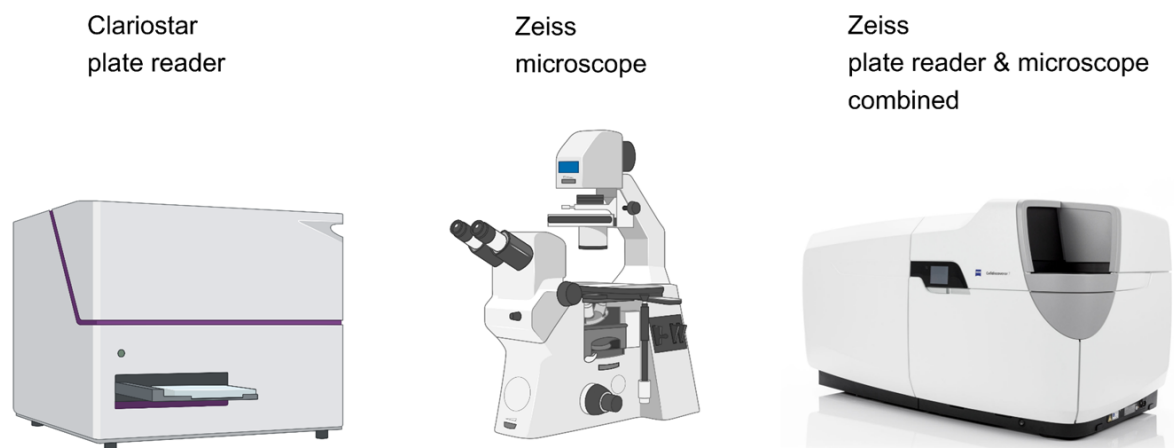


Figure 3.13: Comparison of used plate reader and microscope systems

A Clariostar plate reader from BMG was used for long-term incubation experiments and to combine several conditions. An Axio Observer 7 microscope from Zeiss provided high quality images and with fast image recording. The Cell discoverer 7 microscope from Zeiss allowed long-term incubation and high-quality image capturing. Created with BioRender.com.

Clariostar plate reader H₂O₂ experiments

The long-term redox dynamics of WT and *Taz*-KD pancreatic islets were measured at 37 °C and 5% CO₂ using a Clariostar plate reader. The islets were incubated in phenol-free RPMI medium with or without 10 µM GLX351322 (GLX) or 20 µM GSK2795039 (GSK). Before the experiment, groups of 25 islets were placed in the well centre of U-bottom 96-well plates. For the measurement, the Clariostar was set to None-mode (measures only the center of the well). The focus and gain adjustments were performed before each experiment.

To optimise the measurement process, the beam size (the diameter in focus is 1 mm) was increased to measure all islets simultaneously. This was achieved by setting the beam focus height slightly out of focus (0.5 mm above the recommended focus height), which allowed for a broader coverage of the islets.

Spectroscopy	Setup	λ_{ex1}	λ_{ex2}	BS	λ_{em}
Fluorescence	Clariostar, Inbuilt filters	400/10 nm	482/16 nm	500 nm	530/40 nm

CD7 microscope H₂O₂ experiments

For H₂O₂ live cell imaging using the CD7 microscope islets were measured in phenol-free RPMI medium at 37 °C and 5% CO₂. After culture, islets were collected, and transferred to a black plate with glass bottom (thickness: 170 µm). After an initial baseline measurement, 1 µM auranofin, 100 µM H₂O₂, 10 µM GLX351322 (GLX) or a control (medium with 0.01% DMSO) was added via the automated injection system. After 12 h imaging, the plate was taken out from the CD7, and supernatant was collected for insulin analysis.

Spectroscopy	Setup	λ_{ex1}	λ_{ex2}	BS	λ_{em}
Fluorescence	CD7, LED modules	469/38 nm	423/44 nm	500 nm	530/40 nm

3.9.2 Redox histology

The mito-roGFP2-Orp1 mice crossbred with shTaz mice (MiOxTaz mice, **Chapter 3.1.1**) were sacrificed via an IP ketamin/rompun (1 g/kg Ketavet®/ 100 mg/kg Rompun®) injection. The whole blood system was perfused (protocol shown in **Figure 3.14**) with 25 ml of 50 mM N-ethylmaleimide (NEM) diluted in PBS and afterwards the pancreas was inflated with 5 ml of the same solution. The organs were removed, and fixation was performed overnight at RT with 4% PFA. Next day, the heart samples were washed in PBS, embedded in Tissue Tek OCT Compound and rapidly frozen using liquid nitrogen-cooled isopentane (detailed method description in Bertero *et al.*, 2021).³⁵ To improve cryo-slice quality pancreas samples were additionally treated with 30% sucrose diluted in PBS for 3 h before embedding in Tissue Tek. All samples were cut at 5 µm using a cryostat at -20 °C for heart samples and -15 °C for pancreas samples. The pancreas slices were dried for 30 min, before being washed with PBS and treated with 3% goat serum for 1 h in a wet chamber. Subsequently, 50 µl of primary anti-insulin antibody (1:200 diluted) was added and incubated overnight in wet chamber at 4°C. On the following day, slices were again washed with PBS and 50 µl of secondary antibody (Alexa 594) was added for 1 h 15 min at RT. After a final washing step slices were dried and mounted with Dako mounting media. Imaging was performed with the previously described Axio Observer 7 system using a 20x air objective. Analysis was performed on ImageJ using a self-scripted macro to automate the procedure and minimise risk of bias in setting thresholds.

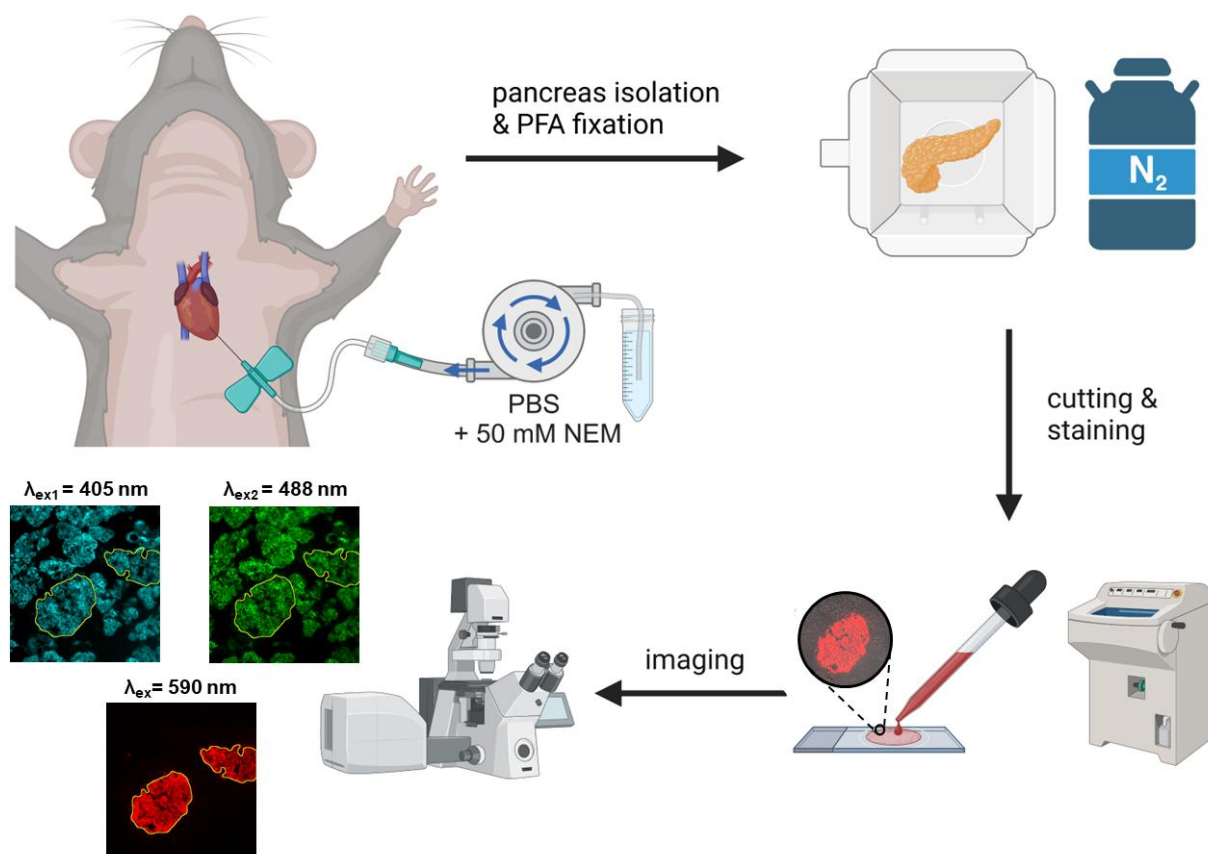


Figure 3.14: Redox histology for *in vivo* redox imaging of pancreatic islets

Schematic protocol of redox histology to measure *in vivo* redox status. Before pancreas isolation, shTaz x Mito-roGFP2-Orp1 mice were perfused with NEM via the cardiovascular system. Isolated pancreas was fixed in PFA and frozen in liquid nitrogen. After cryo-cutting, the cuts were stained against insulin to localise the pancreatic islets. Imaged intensity ratio (excitation: 405/488 nm and emission: 500 – 530 nm) of the mito-roGFP2-Orp1 sensor in pancreatic islets reflects the *in vivo* redox status. Abbreviations: N-ethylmaleimide (NEM), paraformaldehyde (PFA). Created with Biorender.com.

Spectroscopy	Setup	λ_{ex1} (roGFP)	λ_{ex2}	BS	$\lambda_{em1/2}$	λ_{ex3} (insulin)	BS	λ_{em3}
Fluorescence	Axio Observer 7	405/20 nm	470/40 nm	505 nm	550/100 nm	572/25 nm	590 nm	629/62 nm

After calculating the ratio for each image, both genotypes (WT and *Taz*-KD) were compared by calculating the percentage change:

$$(eq2) \text{ change in } \frac{405}{488} nm \text{ ratio} = \frac{(ratio \text{ value} - WT_{mean})}{WT_{mean}} \times 100$$

ratio value: either WT or *Taz*-KD ratio value; WT_{mean} : mean value for all the WT ratio values

3.10 Morphological analysis of mitochondria

3.10.1 Mitochondrial volume determination with Mitotracker and roGFP

MitoTracker™ Deep Red was used to visualise and measure the mitochondrial volume. To quantify the mitochondrial volume, the MitoTracker signal was normalised to the Hoechst 33342 signal. For staining, groups of 50 pancreatic islets were dispersed. The dispersed pancreatic islet cells were washed with KHB and incubated with 50 nM Mitotracker for 30 min at 37 °C in RPMI supplemented with only 0.1% FCS. After two washing steps in KHB, the cells were incubated for 7 min with 5 µg/ml Hoechst dye in KHB (0.1% BSA & 10 mM glucose) at RT protect from light. Before imaging in KHB, the cells were washed three times in KHB (0.1% BSA & 10 mM glucose).

Spectroscopy	Setup	λ_{ex1} (Mitotracker)	BS ₁	λ_{em1}	λ_{ex2} (Hoechst)	BS ₂	λ_{em2}
Fluorescence	Axio Observer 7	620/60 nm	665 nm	700/30 nm	340/30 nm	409 nm	510/90 nm

3.10.2 Confocal and STED microscopy

Stimulated emission depletion (STED) microscopy was used to achieve super-resolution (resolution beyond the Abbe diffraction limit) for studying the mitochondrial morphology of pancreatic islet cells. The diffraction limits the resolution to roughly one-half of the light wavelength and hence, no structures below 200 nm for visible light can be resolved with light microscopy. STED microscopy overcomes this limit by depleting fluorophores around the focus volume (using a TEM01 mode laser beam, also called doughnut mode).³⁸⁶ Only the remaining still excited fluorophores in the complementary region can return to the ground state via

spontaneous fluorescence emission. Therefore, the resulting fluorescence comes from a smaller volume and allows a higher resolution.⁴¹ The STED principle is summarised in **Figure 3.15**.

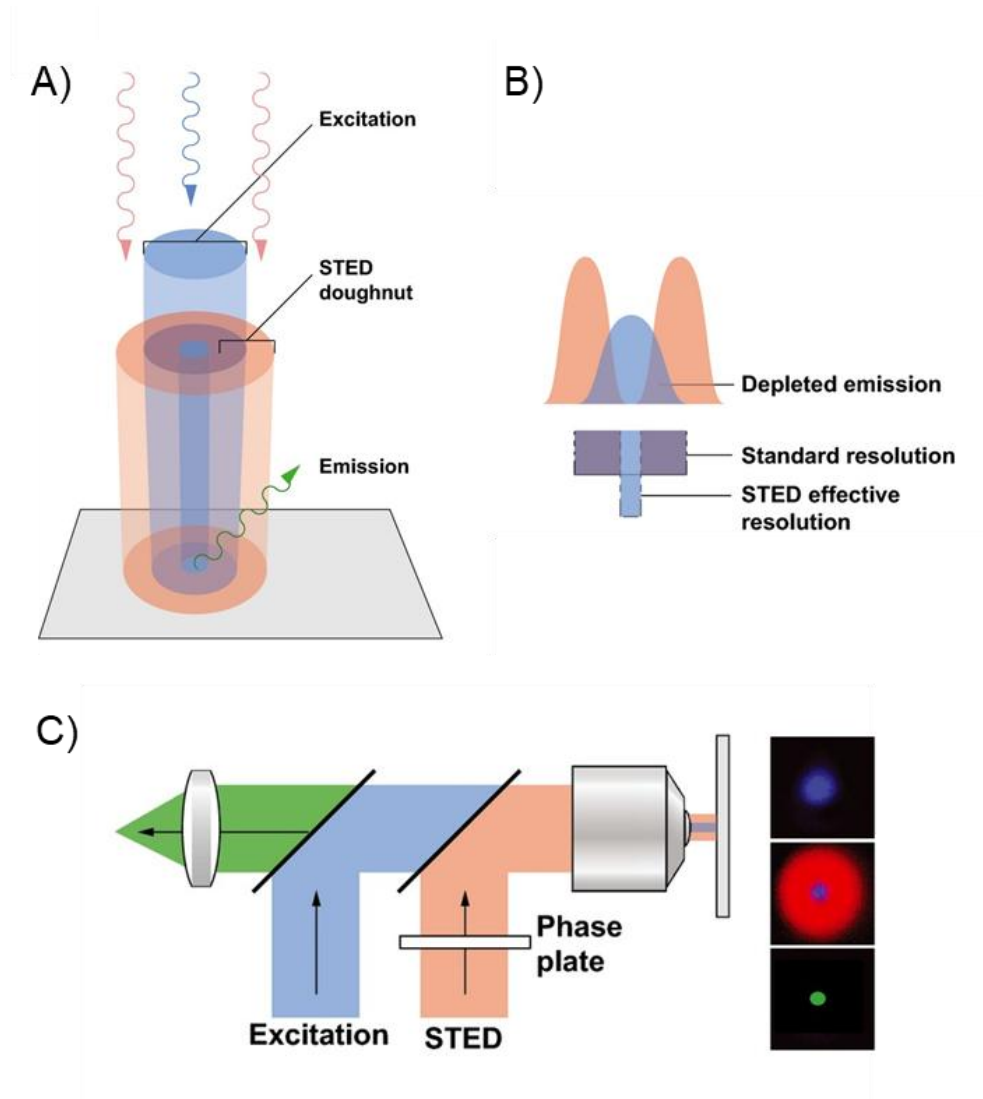


Figure 3.15: STED principle to achieve super-resolution

(A) Excitation volume (blue) and the resulting emission (green) is reduced via stimulated emission depletion using a doughnut laser (orange). (B) The intensity profile of the depletion laser (orange) sharpens the effective focus and increases the effective resolution. (C) STED microscopy setup with a phase plate to form the depletion laser beam (orange) into a "doughnut-shape". The STED beam is overlapped with the excitation beam in the focal plane and the resulting emission fluorescence (green) can be detected. Adapted from Blom and Brismar, 2014.⁴¹

Directly after islet isolation, groups of 50 pancreatic islets were dispersed and seeded on a coverslip (170 μm thickness). On the next day, the dispersed islet cells were washed with 10 mM glucose KHB and stained with 30 nM MitoTracker™ Deep Red in RPMI 1640 (only

0.1% FCS) for 10 min at RT. After three washing steps, the imaging was carried out in 10 mM glucose KHB at RT. The samples were imaged on an inverted STED microscope using the according control software Inspector V16.3. A 100x silicon immersion objective with a numerical aperture 1.4 and a pinhole size of 90 μm (1.08 airy unit) was used. In order to have an overview of the pancreatic islet cells with the labelled mitochondria, single confocal 80 x 80 μm line-interleaved scanning with 200 nm resolution (in XY axis) was performed at excitation of 640 nm. This was followed by another confocal scanning of a randomly selected cell, this time with finer XY pixel size (40 nm) and a Z-stack to generate a 3D image (voxel size: 40 x 40 x 300 nm^3). The detection filter, total pixel dwell time, and excitation laser power was set to 650 – 720 nm, 5 μs , and 30%, respectively. Finally, following the gold nano particle alignment of the STED 640 nm excitation and 775 nm depletion beam, parts of the cellular volume were recorded in STED mode. The STED experiments were performed using rescue settings (Inspector software version 16.3) which reduces the photobleaching of the Mitotracker. The 775 nm depletion laser pulsed at 40% of the maximal power of 1250 mW (corresponding to 75 – 85 mW in the focus, repetition rate of 40 MHz) with no gating and total dwell time of 17.5 μs . The STED images were recorded with a voxel size of 20 x 20 x 300 nm^3 . In addition to confocal and STED image stacks, the residual excitation by the STED beam (so called “re-excitation”) was recorded and later subtracted from the STED recordings after deconvolution.

Data were plane-wise linearly deconvoluted using a Wiener filter with theoretical point spread functions and manually adjusted regularisation parameter. For deconvolution and subtraction of the re-excitation custom-written routines in Matlab were used. Next, all images were preprocessed in ImageJ for feature extraction using smoothing and shot-noise reduction (bilateral filter), background subtraction (rolling-ball algorithm) and sharpening (unsharp mask). Subsequently, threshold-based image segmentation and 3D-rendering was performed in Imaris (version 9.6). The resulting disconnected surfaces were grouped based on their surface area into three classes: Class A = 0.3 - 3 μm^2 , Class B = 3 - 10 μm^2 , and Class C > 10 μm^2 . The morphological parameters, including surface area, volume, number of single mitochondria, sphericity, and bounding boxes were automatically calculated by Imaris software based on each disconnected object. The sphericity describes how spherical an object is and can be calculated via $\frac{1}{\pi^{\frac{1}{3}}} \times \frac{(6 \times \text{volume})^{\frac{2}{3}}}{\text{surface area}}$. The bounding box of a single mitochondria describes the minimal rectangular box which fully encloses the object, and an example is displayed in the supplements (**Figure 7.16**). Furthermore, a nearest neighbor analysis was performed with a custom-written Matlab protocol (collaboration with Marcel Lauterbach) which was adapted for mitochondria network analysis of pancreatic islet cells.

3.11 Lipidomics

In our laboratory at Saarland University (Homburg, Germany), pancreatic islet isolation and sample preparation was performed before the samples were sent to Lipotype GmbH. At Lipotype GmbH, the lipidomic profiles were measured and pre-analysed (extended report). The final data comparison and statistical analysis were conducted in Homburg. WT and *Taz*-KD of three different sample groups were used, namely the lifelong doxy feed shTaz mice (*in vivo* model) with 4 samples per genotype, the 1-week doxy treatment in culture (*in vitro* model) with 3 samples per genotype and a none-doxy receiving control group (0 h group) with 3 samples per genotype.

If no or only one value of a certain species was measured, the species was excluded from species profile analysis. Meaning, if there were at least one or more detection values in each genotype, the species was included in the analysis.

Sample collection for Lipidomics

Groups of 600 islets per Lipidomics sample were collected by pooling 2 - 3 animals with the same genotype and gender. In order to relate the lipidomics results to functional and structural measurements, the pancreatic islets were treated the same way. Meaning, the pancreatic islets of the lifelong doxy feed mice (*in vivo* model) were cultured overnight after isolation. The WT and *Taz*-KD islets of the 1-week *in vitro* model were cultured for one week in doxycycline supplemented RPMI medium (*in vitro* model description in **Chapter 3.1.2**). Subsequently, all samples were homogenised by dispersion in Ca^{2+} - and Mg^{2+} -free PBS with additional sonication (**Chapter 3.2.3**). Then, they were frozen at $-80\text{ }^{\circ}\text{C}$ while a small portion was used for assessing the protein content with a BCA assay.

The protocol of the following three method sections were provided by Lipotype: "Lipid extraction for mass spectrometry", "MS data acquisition", "Lipidomics data analysis and post-processing":

“Lipid extraction for mass spectrometry

Mass spectrometry-based lipid analysis was performed by Lipotype GmbH (Dresden, Germany) as described.³⁵⁵ Lipids were extracted using a chloroform/methanol procedure.¹⁰⁷ Samples were spiked with internal lipid standard mixture containing: cardiolipin 14:0/14:0/14:0/14:0 (CL), ceramide 18:1;2/17:0 (Cer), diacylglycerol 17:0/17:0 (DAG), hexosylceramide 18:1;2/12:0 (HexCer), lyso-phosphatidate 17:0 (LPA), lyso-phosphatidylcholine 12:0 (LPC), lyso-phosphatidylethanolamine 17:1 (LPE), lyso-

phosphatidylglycerol 17:1 (LPG), lyso-phosphatidylinositol 17:1 (LPI), lyso-phosphatidylserine 17:1 (LPS), phosphatidate 17:0/17:0 (PA), phosphatidylcholine 17:0/17:0 (PC), phosphatidylethanolamine 17:0/17:0 (PE), phosphatidylglycerol 17:0/17:0 (PG), phosphatidylinositol 16:0/16:0 (PI), phosphatidylserine 17:0/17:0 (PS), cholesterol ester 16:0 D7 (CE), sphingomyelin 18:1;2/12:0;0 (SM), triacylglycerol 17:0/17:0/17:0 (TAG). After extraction, the organic phase was transferred to an infusion plate and dried in a speed vacuum concentrator. The dry extract was re-suspended in 7.5 mM ammonium formate in chloroform/methanol/propanol (1:2:4; V:V:V). All liquid handling steps were performed using Hamilton Robotics STARlet robotic platform with the Anti Droplet Control feature for organic solvents pipetting.

MS data acquisition

Samples were analysed by direct infusion on a QExactive mass spectrometer (Thermo Scientific) equipped with a TriVersa NanoMate ion source (Advion Biosciences). Samples were analysed in both positive and negative ion modes with a resolution of $R_{m/z=200} = 280000$ for MS and $R_{m/z=200} = 17500$ for MSMS experiments, in a single acquisition. MSMS was triggered by an inclusion list encompassing corresponding MS mass ranges scanned in 1 Da increments.³⁵⁴ Both MS and MSMS data were combined to monitor CE, DAG and TAG ions as ammonium adducts; LPC, LPC O-, PC and PC O- as formate adducts; and CL, LPS, PA, PE, PE O-, PG, PI and PS as deprotonated anions. MS only was used to monitor LPA, LPE, LPE O-, LPG and LPI as deprotonated anions, and Cer, HexCer and SM as formate adducts.

Lipidomics data analysis and post-processing

Data were analysed with in-house developed lipid identification software based on LipidXplorer.^{154,155} Data post-processing and normalisation were performed using an in-house developed data management system. Only lipid identifications with a signal-to-noise ratio > 5, and a signal intensity 5-fold higher than in corresponding blank samples were considered for further data analysis." (protocol sent by Lipotype)

3.12 Quantitative RT-PCR and RNA sequencing

3.12.1 RNA isolation

Pancreatic islets (groups of around 150 per RNA sample) were lysed in ice-cold TRIzol reagent and frozen at -80 °C until further use. RNA extraction was performed by Sandra Janku according to a protocol described in Wenning *et al.*, 2011.⁴⁰³ Thereafter, RNA concentration and purity was measured using a NanoDrop One^C (absorption at 230, 260 and 280 nm). Isolated RNA was either sent for RNA sequencing (RNA-Seq) to Novogene (Cambridge) or reverse transcribed to cDNA.

3.12.2 Quantitative RT-PCR

Quantitative RT-PCR (qPCR) was analysed using the CFX96 C1000 touch thermo cycler with a Taqman protocol and in presence of the mouse specific primers Tafazzin and GAPDH. The assay ID of the used Taqman primers are listed in **Table 3.3**.

Table 3.3: QPCR TaqMan primers

Primer	Company	Assay ID
Tafazzin	Thermo Fisher Scientific	Mm00504978_m1
GAPDH	Thermo Fisher Scientific	Mm99999915_g1

3.12.3 RNA Sequencing

In our laboratory at Saarland University (Homburg, Germany), pancreatic islet isolation, RNA isolation and RNA concentration measurements were performed before the samples were sent to Novogene GmbH. Briefly, RNA samples from WT and *Taz*-KD pancreatic islets (isolation protocol in **Chapter 3.12.1**) were diluted in RNase-free water, and 5 µl of each RNA sample (with a concentration of above 100 ng/µl) were sent for sequencing and analysis to Novogene (Novogene GmbH, Cambridge, UK). Genome assembly “GRCm39” was selected as the reference mouse genome. The final data comparison and statistical analysis were again

conducted in Homburg. WT and *Taz*-KD of two different sample groups were used, namely the lifelong doxy feed sh*Taz* mice (*in vivo* model) and the 1-week doxy treatment in culture (*in vitro* model), each group with 3 samples per genotype.

The following protocol was provided by Novogene:

“Quantity and quality of the RNA samples were assessed as follows. Preliminary quality control was performed in 1% agarose gel electrophoresis to test RNA degradation and potential contamination. Sample purity and preliminary quantity were determined using the Bioanalyser 2100, and it also served to check the RNA integrity and final quantity.

For library preparation, the Novogene NGS RNA Library Prep Set (PT042) was used. The mRNA present in the total RNA sample was isolated with magnetic beads of oligos d(T)25, a method known as polyA-tailed mRNA enrichment. Subsequently, mRNA was randomly fragmented and cDNA synthesis proceeded using random hexamers and the reverse transcriptase enzyme. Once the synthesis of the first chain is finished, the second chain is synthesized with the addition of an Illumina buffer (non-directional library preparation). With this and together with dNTPs, RNase H and polymerase I from *E. coli*, the second chain will be obtained by Nick translation. The resulting products go through purification, end-repair, A-tailing and adapter ligation. Fragments of the appropriate size are enriched by PCR, where indexed P5 and P7 primers are introduced, and final products are purified.

The library was checked with *Qubit 2.0* and real-time PCR for quantification and bioanalyser Agilent 2100 for size distribution detection. Quantified libraries will be pooled and sequenced on the Illumina Novaseq X platform, according to effective library concentration and data amount using the paired-end 150 strategy (PE150).” (protocol sent by Novogene)

3.13 Data analysis and statistics

Most data analysis was performed in OriginPro 2019b and GraphPad Prism Software version 9. GraphPad was also used for the statistical analysis of the data sets. All additional programs are listed in table. This thesis presents the values in mean \pm standard error of the mean (SEM). SEM was preferred over standard deviation as it describes the accuracy of the population mean rather than the biological variation within a measurement. Genetically nearly identical animals (inbreeding) of the same age and grown under controlled normalised conditions were used. Important to note is that the sample size ("n" or "N" number) is given in each Figure legend because the SEM is inversely proportional to the square root of the sample size. Here,

small "n" describes the number of experiments and big "N" represents the number of animals. If not indicated otherwise, the Student's unpaired one-tailed *t*-test was used to compare the mean of two conditions and check for statistical significance via a predefined null hypothesis. P-values < 0.05 were considered to be statistically significant and indicated by *. P-values < 0.01 were indicated by **. P-values < 0.001 were indicated by ***. P-values < 0.0001 were indicated by ****. P-values > 0.05 were indicated in three different ways. Whenever there was no significant difference, the values were not explicitly labelled unless in two specific situations. First, if the results were close to being significant and relevant for the discussion, the exact p-value was provided. Second, if the lack of significance was important for the discussion, the values were indicated as not significant (ns) with ns: $p > 0.05$.

4 Results

The materials and methods described in the previous section were used to investigate the influence of Barth syndrome (BTHS) caused by *Taz*-KD on mouse tissue with a focus on the endocrine pancreas. Each result section starts with a short introduction about the technique and ends with a summary of the main results.

At first, the shTaz *in vivo* mouse model was verified and characterised. Subsequently, the whole-body metabolism was studied. A mechanistic, functional, and structural analysis of pancreatic islet tissue and its mitochondria were performed to understand the observed metabolic alterations. Omics analyses, including lipidomics and RNA-Seq, were conducted to get mechanistic insights into how lipid and gene profiles are affected by *Taz*-KD. These analyses help to link observed functional differences with cellular composition and genetic information, following the principle that structure determines function. Finally, a newly introduced shTaz *in vitro* model was characterised and selected experiments were performed to investigate the direct effects of *Taz*-KD.

Many of the pancreatic islet results are part of our publication Carlein *et al.*, 2024: “Pancreatic islets undergo functional and morphological adaptation during development of Barth syndrome”. The redox histology results of heart tissue are part of our publication Bertero *et al.*, 2021: “Loss of mitochondrial Ca^{2+} uniporter limits inotropic reserve and provides trigger and substrate for arrhythmias in Barth syndrome cardiomyopathy” (see **Chapter 1.3**).

4.1 Characterisation of *Taz*-KD in pancreatic islets

The selected BTHS model for this study was the doxy induced shTaz mice at 20 wo (**Chapter 3.1.1**). The shRNA induced *Taz*-KD efficiency for heart tissue of the shTaz mouse model has already been shown by other groups.²⁸⁷ Nevertheless, as the external (e.g. temperature, food, treatments, and handling) and internal conditions (e.g. genetic mutations, age, body weight, and blood sugar) vary, and to compare the results with pancreatic islet tissue, it is essential to validate a working model at the start of the project. Verification of the *Taz*-KD efficiency was performed by qPCR analysis. In **Figure 4.1**, quantitative analysis of the *Taz* gene expression in 20 wo *Taz*-KD mice showed a significant reduction in *Taz* RNA expression levels in the heart (A1, mean = 13.7% \pm 7.9%) and pancreatic islet (A2, mean = 36.8% \pm 7.4%) tissue compared to WT tissue. The variation among the WT samples of the delta CT

paired analysis is shown in the supplements (**Figure 7.2**). The reduction in *Taz* gene expression resulted in diminished total CL and CL 72:8 (the most abundant CL species) levels when normalised to protein amount (**Figure 4.1 B1, B2**).

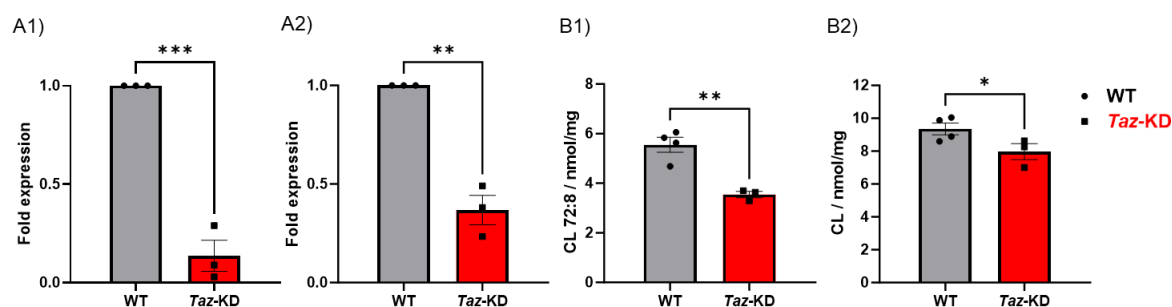


Figure 4.1: *Taz* and CL reduction in *Taz*-KD pancreatic islets

(**A**) *Taz* gene expression levels in heart (A1) and pancreatic islet (A2) tissue from 20 wo WT and *Taz*-KD mice measured by qPCR analysis. N = 3. (**B**) Levels of the main CL 72:8 species (B1) and total CL (B2), analysed by lipidomics analysis and normalised to protein amount. N (WT) = 4, N (*Taz*-KD) = 3. Data = mean \pm SEM; N = number of animals; statistical analysis: paired (A1, A2) and unpaired (B1, B2) *t* test: **p* < 0.05, ***p* < 0.01, ****p* < 0.001. Abbreviations: weeks of age (wo), *tafazzin*-knockdown (*Taz*-KD), wildtype (WT), cardiolipin (CL).

The complete CL species profile of 20 wo sh*Taz* pancreatic islets was normalised to the sum of all lipids measured in each sample (**Figure 4.2**) as recommended by the Lipotype company. The single CL lipid species are notated by the carbon length (e.g. 72) followed by the number of double bonds (e.g. 8). Since not every CL species was detectable in each sample, some replicates are missing in certain CL species.

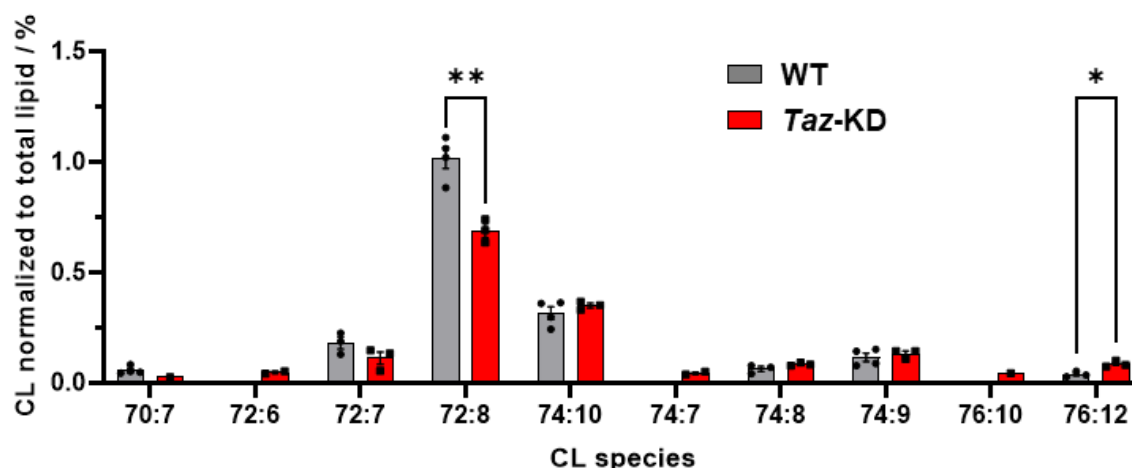


Figure 4.2: Altered CL species profile in *Taz*-KD pancreatic islets

CL species profile of 20 wo WT and *Taz*-KD pancreatic islets measured by lipidomics analysis. The profile was normalised to the sum of all lipids present in each sample. The notation of the lipid species describes the carbon length followed by the number of double bonds. N (WT) = 4, N (*Taz*-KD) = 3, some replicates are missing due to CL levels below the limit of detection. Data = mean \pm SEM; N = number of animals; statistical analysis: unpaired *t* test: **p* < 0.05, ***p* < 0.01. Abbreviations: weeks of age (wo), *tafazzin*-knockdown (*Taz*-KD), wildtype (WT), cardiolipin (CL).

The relative levels of CL compared to all lipids in pancreatic islets were found to be, $CL_{WT} = 1.72 \pm 0.08\%$ and $CL_{Taz-KD} = 1.55 \pm 0.07\%$ (**Figure 4.2** and **Figure 7.3 A**).

As described in the introduction (**Chapter 1.1.1**), CL 72:8 accounts for about 60% of all CL species in skeletal muscle and over 80% in liver and heart tissue.³²⁷ For pancreatic islets, a percentage of $CL_{72:8\ WT} = 59.3 \pm 2.4\%$ for WT and $CL_{72:8\ Taz-KD} = 44.5 \pm 1\%$ for *Taz*-KD was obtained when compared to the total CL amount (**Figure 4.1** and **Figure 4.2**). Therefore, not only were the absolute levels of CL 72:8 in *Taz*-KD mice reduced, but also the relative amount of CL 72:8 compared to the total CL composition in *Taz*-KD was downregulated. Connected to the relative downregulation of CL 72:8, a rise in the other CL species, such as CL 76:12 and a shift towards longer fatty acid chains in CL of *Taz*-KD samples were found (**Figure 4.2** and supplements, **Figure 7.3 B**).

The phenotype of BTHS samples is not only associated with a decrease in CL levels but usually also with an upregulation in MLCL (precursor form of CL, introduced in **Chapter 1.1**).²⁸⁷ MLCL could not be detected in any of the analysed WT and *Taz*-KD pancreatic islet samples. To date, CL and MLCL levels in pancreatic islets were only reported by the group of Grant M Hatch *et al.* in 2021.⁸² They found a concentration of around 0.1 nmol/mg MLCL and 10 nmol/mg CL in control pancreatic islets and approximately 0.35 nmol/mg MLCL and

13 nmol/mg CL in *Taz*-KD samples (values estimated from Figure 1 A & B in Laura Cole *et al.*, 2021).⁸² The concentration of CL in their control pancreatic islets was similar to our tested WT results normalised to nmol/mg: $CL_{WT} = 9.35 \pm 0.36$ nmol/mg (**Figure 4.2**). Although the authors did not observe a reduction in CL levels, the significant increase in MLCL levels in their *Taz*-KD mice led to a rise of about 170% in the MLCL/CL ratio. In contrast, a significant drop in *Taz*-KD CL levels was observed in the presented study: $CL_{Taz-KD} = 7.96 \pm 0.49$ nmol/mg, which was even more pronounced in the main CL species (CL 72:8): $CL_{72:8\ WT} = 5.5 \pm 0.3$ nmol/mg against $CL_{72:8\ Taz-KD} = 3.87 \pm 0.34$ nmol/mg.

The **Chapter 4.7.1** delves deeper into the analysis of other lipid classes and species of the shTaz pancreatic islets. However, since an alteration in the CL profile is one of the principal hallmarks of BTHS, the CL levels are crucial for the shTaz model verification. Consequently, the CL lipidomics results are presented first in the results section to ensure proper presentation and description of the following results.

In summary, *Taz*-KD pancreatic islets show around 65% reduction in *Taz* gene expression which alters CL profile and reduces total CL amount.

4.2 Whole-body metabolism

To assess whole-body metabolism, the *in vivo* parameters, such as body weight, plasma glucose, insulin, and glucagon of shTaz mice were investigated. The body weights of both genotypes were measured at 10, 20 and 50 wo (**Figure 4.3**). Whereas the 10 wo *Taz*-KD mice did not exhibit any alteration in body weight, a weight reduction after 20 wo was observed, which was present in male and female *Taz*-KD mice, when compared to WT mice. The weight reduction persisted after 50 wo, but the limited sample size at 10 and 50 wo prevented gender-specific analysis (gender-specific analysis is described in **Chapter 3.1**). Furthermore, the *Taz*-KD mice were noticeable smaller in size compared to WT littermates (not quantified, **Figure 4.3 C**).

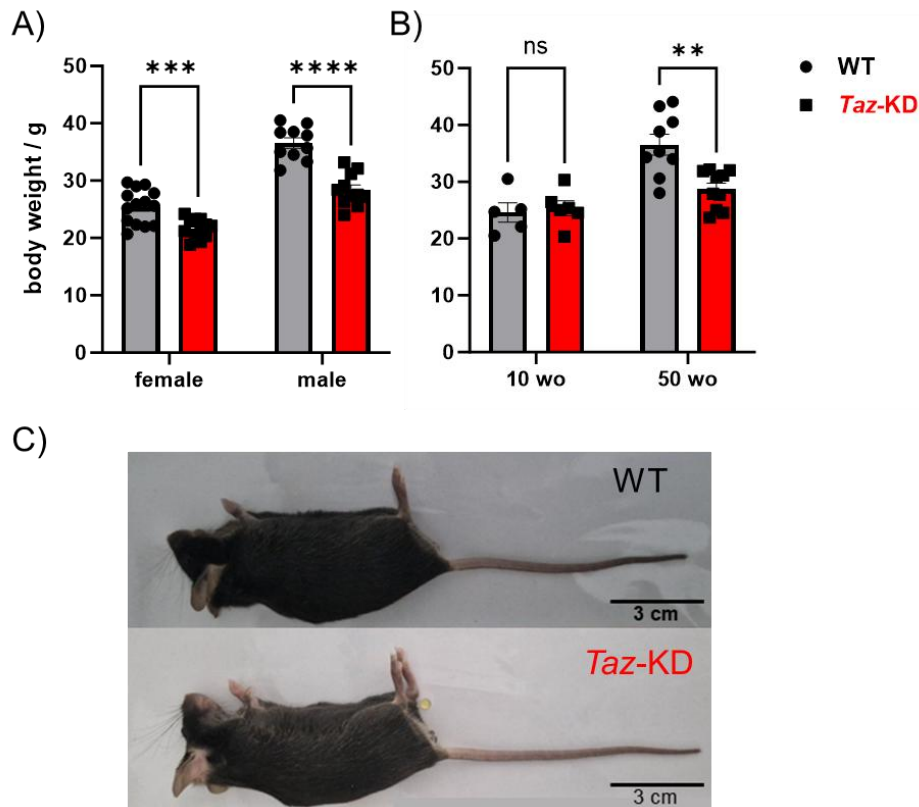


Figure 4.3: Body weight reduction of *Taz*-KD mice after 20 and 50 wo

(A) Quantification of body weight of 20 wo female and male mice. N (WT, female) = 14, N (*Taz*-KD, female) = 10, N (WT, male) = 12, N (*Taz*-KD, male) = 11. (B) Quantification of body weight of 10 and 50 wo mice. N (WT, 10 wo) = 5, N (*Taz*-KD, 10 wo) = 6, N (WT, 50 wo) = 9, N (*Taz*-KD, 50 wo) = 10. (C) Representative size comparison of male WT (upper image) and *Taz*-KD (bottom image) mice at 20 wo. Scale bar: 3 cm. Data = mean \pm SEM; N = number of animals; statistical analysis: unpaired *t* test: ***p* < 0.01, ****p* < 0.001, *****p* < 0.0001. Abbreviations: weeks of age (wo), *tafazzin*-knockdown (*Taz*-KD), wildtype (WT).

Subsequently, whole-body glucose homeostasis of 20 and 50 wo WT and *Taz*-KD mice was investigated by measuring plasma glucose, insulin, and glucagon levels during a GTT (**Figure 4.4** and supplements, **Figure 7.4**, protocol description in **Chapter 3.1.4**). The blood glucose levels increased immediately after the IP glucose injection. In 20 wo *Taz*-KD mice of both genders and female WT mice, the blood glucose concentration peaked at around 15 min. For the male WT mice, the values peaked later, at around 30 min. Following the initial rise, the blood glucose levels decreased over time and reached starting values after 120 min for all the groups except the male WT mice. The 20 wo female and male *Taz*-KD mice displayed reduced blood glucose levels at 60 and 120 min after IP injection with glucose when compared to the respective WT group, but only the *Taz*-KD male levels were statistically lower (**Figure 4.4 A**). In addition to the blood glucose levels, the GTT revealed a decrease in plasma insulin levels of *Taz*-KD mice after 6 h fasting (**Figure 4.4 B**). Upon

glucose injection, the fold increase of the plasma insulin levels was higher in *Taz*-KD mice (supplements, **Figure 7.4**), indicating an altered glucose-stimulated insulin response. The plasma glucagon levels of WT and *Taz*-KD mice rose shortly after glucose injection. The rise was followed by a decrease reaching lowest levels at 15 min for WT and at 30 min for *Taz*-KD (**Figure 4.4 C**). Interestingly, in *Taz*-KD mice, the plasma glucagon levels were elevated at 15 min ($p = 0.06$), suggesting an increased glucagon response upon stimulation with glucose. At later time points, the glucagon levels in WT mice continuously increased, but this was less pronounced in *Taz*-KD mice. However, besides different kinetics in plasma glucagon and insulin, no statistically differences were found.

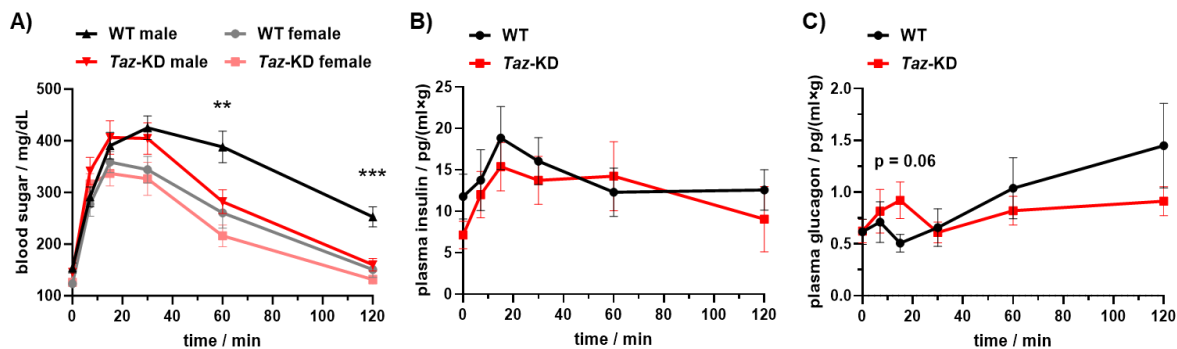


Figure 4.4: Altered whole-body glucose metabolism of *Taz*-KD mice at 20 wo

(A) Quantification of blood glucose levels during GTT. N (WT female) = 15, N (*Taz*-KD female) = 14, N (WT male) = 12, N (*Taz*-KD male) = 14. (B) Quantification of plasma insulin during GTT. Values are normalised against body weight. N (WT) = 7, N (*Taz*-KD) = 8. This Figure is supplemented by data not separated by gender, **Figure 7.4**. Data = mean \pm SEM; N = number of animals; statistical analysis: unpaired *t* test: ** $p < 0.01$, *** $p < 0.001$. Abbreviations: weeks of age (wo), *tafazzin*-knockdown (*Taz*-KD), wildtype (WT), glucose tolerance test (GTT).

In summary, *Taz*-KD mice exhibited altered whole-body glucose metabolism. During GTT, blood glucose levels were reduced, while plasma insulin and glucagon levels were mostly preserved in *Taz*-KD mice, with some slight and non-statistical changes.

4.3 Immunohistochemistry

To understand the cellular basis of the observed whole-body metabolic phenotype in *Taz*-KD mice, pancreatic islet composition and critical pancreatic islet markers for proliferation and apoptosis were investigated using IHC. The pancreatic islet composition was studied on pancreas cryo-slices, and the proliferation and apoptosis stainings were performed on paraffin slices (method description in **Chapter 3.3**).

4.3.1 Pancreatic islet composition

Pancreatic islets consist of various cell types which fulfil separate tasks (explained in **Chapter 1.2.1**). First, the process of staining and imaging of pancreas cryo-slices isolated from C57BL/6N mice was established. The cryo samples were stained against glucagon (α -cells), insulin (β -cells) and somatostatin (δ -cells). The typical distribution for mouse pancreatic isles, where the β - (green) cells dominate the centre, and the α - (red) and δ - (purple) cells are located on the surface layers, was observed (**Figure 4.5**).

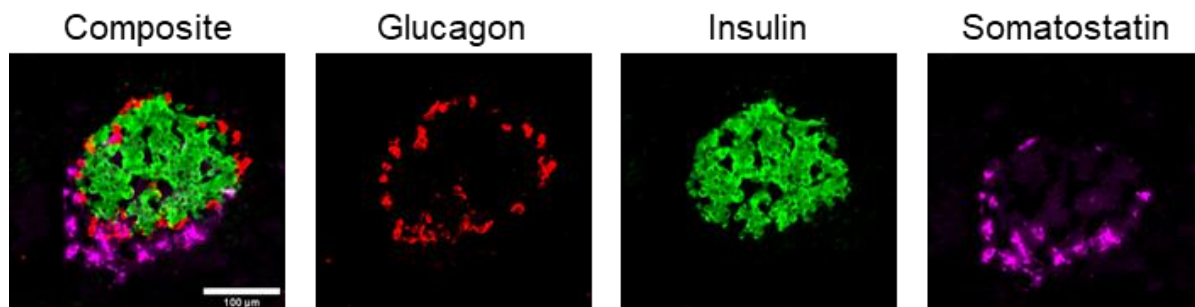


Figure 4.5: Immunohistochemistry for visualising pancreatic α -, β -, and δ -cells

Pancreas cryo-slices from C57BL/6N mice were stained with antibodies against glucagon, insulin, and somatostatin to visualise α -, β - and δ -cells, respectively. The composite image shows the combination of the glucagon, insulin, and somatostatin images. The images were acquired using the Axio Observer 7 microscope with a 20x objective. Scale bar: 100 μ m.

Subsequently, IHC experiments were performed to investigate the composition of shTaz pancreatic islets at 20 wo (**Figure 4.6**). Along with the staining against the cell types, DAPI was added to visualise the nucleus. An increase in the α -cell mass of *Taz*-KD pancreatic islets compared to WT samples was observed. This increase in α -cell number was accompanied by a slight decrease in β -cell number per pancreatic islet area in *Taz*-KD

compared to WT, which was statistically significant when single values of each pancreatic islet were compared (supplements, **Figure 7.5**). The number of δ -cells in *Taz*-KD samples was unchanged compared to WT controls. Cole *et al.*, 2021 also observed an increased α -cell mass in *Taz*-KD pancreatic islets, but only after 10 months of age.⁸² In her study, the α -cell number at 4 months of age showed no difference in *Taz*-KD compared to WT controls.⁸² Moreover, Cole and colleagues did not observe any differences in β -cell numbers for any given age and genotype.⁸²

In summary, *Taz*-KD pancreatic islets showed increased number of α -cells and slightly decreased number of β -cells compared to WT controls. The decrease in β -cell number was significant when single values of each pancreatic islet were compared.

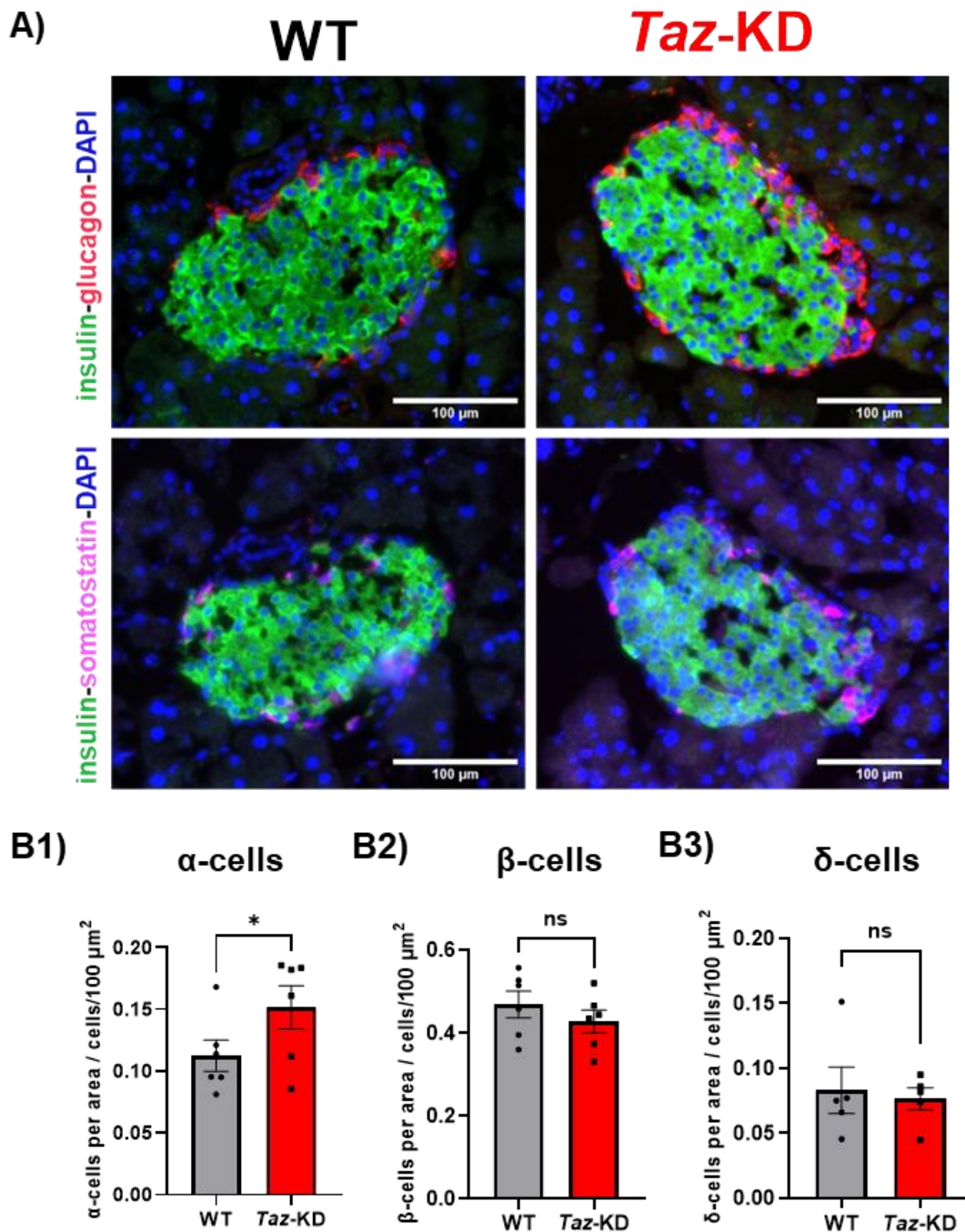


Figure 4.6: More α -cells per area in *Taz-KD* pancreatic islets

(A) Representative IHC images of 20 wo WT and *Taz-KD* pancreatic islets and their stained cell types (red: α -cells, green: β -cells, magenta: δ -cells). The nuclei were stained with DAPI (blue). The glucagon- and somatostatin-insulin double stainings for each genotype represent the same pancreatic islet in a different section cutting depth. Scale bar: 100 μm . The images were acquired using the Axio Observer 7 microscope with a 20x objective. **(B)** Quantitative analysis of α - (B1), β - (B2) and δ - (B3) cell number per pancreatic islet area. $N = 6$. Data = mean \pm SEM; N = number of animals; statistical analysis: unpaired t test: * $p < 0.05$, ns: $p > 0.05$. Abbreviations: immunohistochemistry (IHC), weeks of age (wo), *tafazzin*-knockdown (*Taz-KD*), wildtype (WT).

4.3.2 Proliferation and apoptosis markers

Alterations in pancreatic islet composition are often accompanied by differences in pancreatic islet proliferation or apoptosis levels.¹ Therefore, paraffin slices of 20 wo shTaz mice were stained against the proliferation marker Ki67 and apoptosis marker cleaved caspase-3. To acquire cell type-specific information about Ki67 and cleaved caspase-3 positive cells, an additional glucagon staining was added. No difference was observed in Ki67 or cleaved caspase-3 staining in α - or β -cells among the genotypes (**Figure 4.7**). Therefore, the higher α -cell number of *Taz*-KD mice did not result from increased α -cell proliferation or decreased apoptosis.

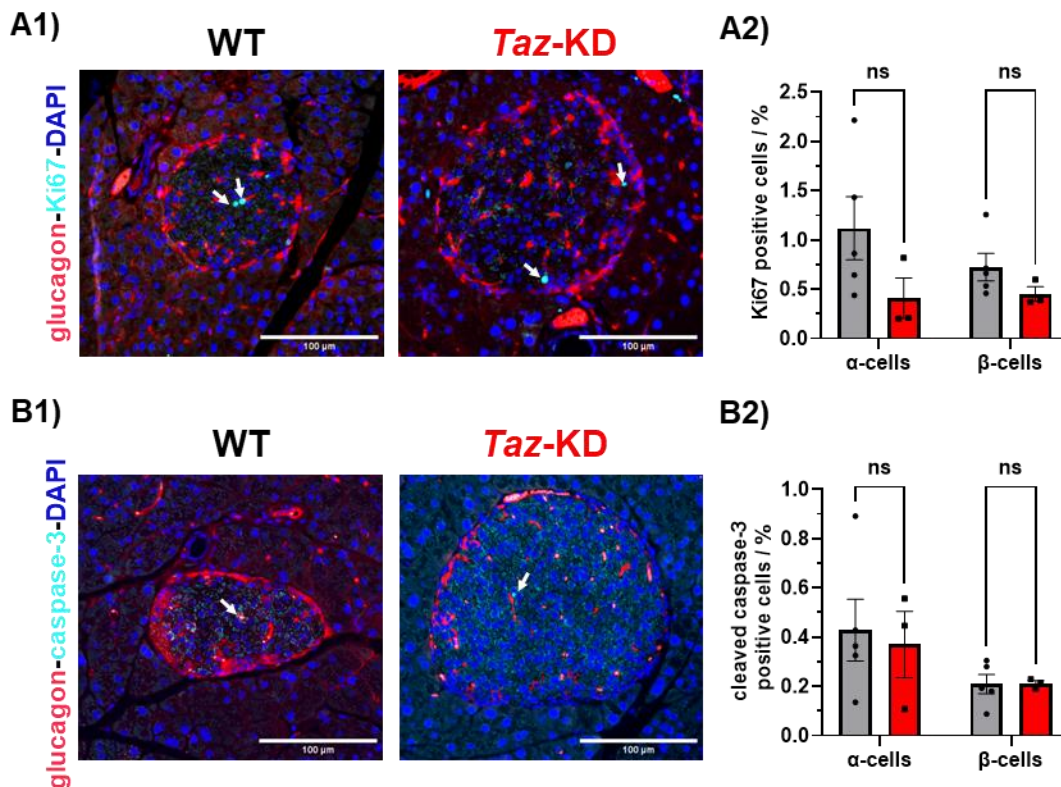


Figure 4.7: The number of Ki67 and cleaved caspase-3 positive cells are unchanged in *Taz*-KD pancreatic islets

(A) (A1) Representative IHC images of proliferation marker Ki67 and glucagon double-immunostaining with DAPI (blue) of 20 wo WT and *Taz*-KD pancreatic islets. Scale bar: 100 μ m. (A2) ImageJ analysis of Ki67 positive cells in α - and β -cells counted with DAPI and normalised to total cell number. N (WT) = 5, N (*Taz*-KD) = 3. (B) Representative images of apoptosis marker cleaved caspase-3 (cyan) and glucagon (red) double-staining with DAPI (blue) of 20 wo WT and *Taz*-KD pancreatic islets. Scale bar: 100 μ m. (B2) ImageJ analysis of cleaved caspase-3 positive cells in α - and β -cells counted with DAPI and normalised to total cell number, N (WT) = 5, N (*Taz*-KD) = 3. Data = mean \pm SEM; N = number of animals; statistical analysis: unpaired *t* test: ns: $p > 0.05$. Abbreviations: immunohistochemistry (IHC), weeks of age (wo), *tafazzin*-knockdown (*Taz*-KD), wildtype (WT).

Additionally, the critical β -cell specific transcription factor, PDX1, was investigated. However, no difference was found among the genotypes (supplements, **Figure 7.6**).

In summary, the levels of cleaved caspase-3, Ki-67 positive α - and β -cells were similar in 20 wt WT and *Taz*-KD pancreatic islets.

4.4 Investigation of pancreatic islet function in *Taz*-KD

The whole-body metabolism and islet composition described in the previous Chapters revealed a unique phenotype with improved glucose tolerance and enhanced α -cell mass in *Taz*-KD mice. These findings might affect islet functionality and *vice versa*. Therefore, the functionality of *Taz*-KD pancreatic islets was investigated in detail. Due to the main task of pancreatic islets to respond to glucose and secrete hormones, this result Chapter is structured according to the steps of the GSIS and glucagon secretion (reviewed in **Chapter 1.2.2**). First, glycolysis was investigated, and NAD(P)H levels were measured. Then, mitochondrial function was evaluated by measuring OCR and mitochondrial membrane potential. The resulting ATP levels from glycolysis and OXPHOS were assessed before Ca^{2+} handling in the cytosol, ER and mitochondria was measured. Ultimately, insulin and glucagon secretion were compared for WT and *Taz*-KD pancreatic islets. Additionally, possible pH changes were investigated, which is another critical indicator of the metabolic state of the cells.

4.4.1 Glycolysis as the first step of glucose metabolism

Upon stimulation with glucose, the first steps in pancreatic islet metabolism are the uptake and phosphorylation of glucose (**Figure 4.8**). Those processes are facilitated by glucose transporters (mostly GLUT2 in β -cells) and hexokinases (mostly glucokinase (Gck) in β -cells). This initiates glucose metabolism, which leads to the production of G6P that can enter the PPP via G6PDH, or the production of F6P that continues in glycolysis, ultimately producing two pyruvate molecules.

Several assays were performed to analyse crucial steps of the initial glucose metabolism (method description in **Chapters 3.7.1** and **3.7.2**). The analysed checkpoints are highlighted with a red star in **Figure 4.8 A**. An increased glucose uptake in *Taz*-KD pancreatic islets compared to WT was observed (**Figure 4.8 B1**). However, this increase was not associated

with a significant rise in protein levels of the primary β -cell glucose transporter GLUT2 (**Figure 4.8 B2**). A representative WB of GLUT2 and the paired analysis can be found in the supplements (supplements, **Figure 7.7**). Other protein transporters may be responsible for the observed phenotype (further discussed in **Chapter 5.2**). No differences in Gck and G6PDH activity between WT and *Taz*-KD pancreatic islets were observed in the conducted experiments (**Figure 4.8 C, D**).

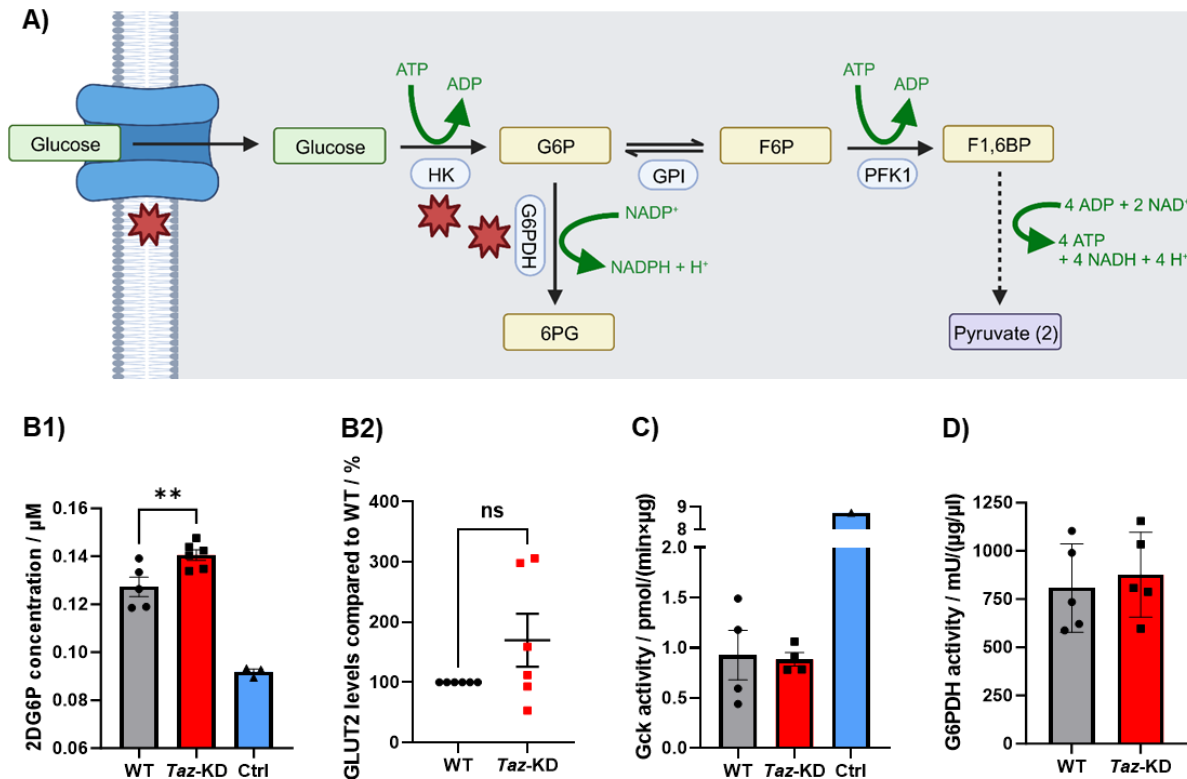


Figure 4.8: Increased glucose uptake independent of GLUT2 in *Taz*-KD pancreatic islets

(A) Scheme of initial glucose metabolism. The red stars highlight the analysed reaction steps in the first steps of the glucose metabolism pathway. After glucose uptake and phosphorylation, G6P either follows the glycolysis pathway catalysed by GPI or G6P enters the pentose phosphate pathway via G6PDH. **(B)** (B1) Glucose uptake using the Glucose Uptake-Glo™ assay and (B2) WB analysis of GLUT2 analysed from 20 wt WT and *Taz*-KD pancreatic islets. The 2DG6P concentration is proportional to the level of glucose uptake into the cell. Pancreatic islet samples without 2DG loading were used as a negative control (blue). The representative WB gel and the paired analysis can be found in the supplements (**Figure 7.7**). N = 6. **(C)** Quantification of Gck activity from 20 wt WT and *Taz*-KD pancreatic islets. The positive control (blue) was isolated Gck protein provided by the kit. N = 4. **(D)** Quantification of G6PDH activity from 20 wt WT and *Taz*-KD pancreatic islets. N = 5. Data = mean ± SEM; N = number of animals; statistical analysis: unpaired *t* test: **p < 0.01, ns: p > 0.05. Abbreviations: Glucokinase (Gck), glucose-6-phosphate isomerase (GPI), hexokinase (HK), glucose-6-phosphate (G6P), 6-phosphogluconolactone (6PG), fructose-6-phosphate (F6P), 2-deoxy-D-glucose (2DG), 2-deoxy-D-glucose-6-phosphate (2DG6P), glucose-6-phosphate dehydrogenase (G6PDH), western blot (WB). (A) was created with BioRender.com.

Measurement of NAD(P)H levels using autofluorescence

NADH is an essential coenzyme for the cellular metabolism process. Its phosphorylated form NADPH plays an equally important role in the cell by catalysing redox processes as the major reducing equivalent (redox regulations are further investigated in **Chapter 4.5**). The concentration of the reduced forms of both redox couples, NADH and NADPH (NAD(P)H), can semi-quantitatively but not specifically be measured with the analysis of the cellular autofluorescence intensity (method description in **Chapter 3.8.2**). The autofluorescence measurement in **Figure 4.9** showed that in WT and *Taz*-KD pancreatic islets, the NAD(P)H levels rose upon stimulation with glucose and decreased after the addition of CCCP. When normalised to CCCP (25 μ M), *Taz*-KD pancreatic islets exhibited higher levels of NAD(P)H in low (2 mM) and high (20 mM) glucose conditions compared to WT (**Figure 4.9 A**). The increased NAD(P)H levels were also observed in long-term (19 h) incubation with 10 mM glucose at 37 °C and 5% CO₂ and when area under the curve (AUC) was calculated (**Figure 4.9 B, C**).

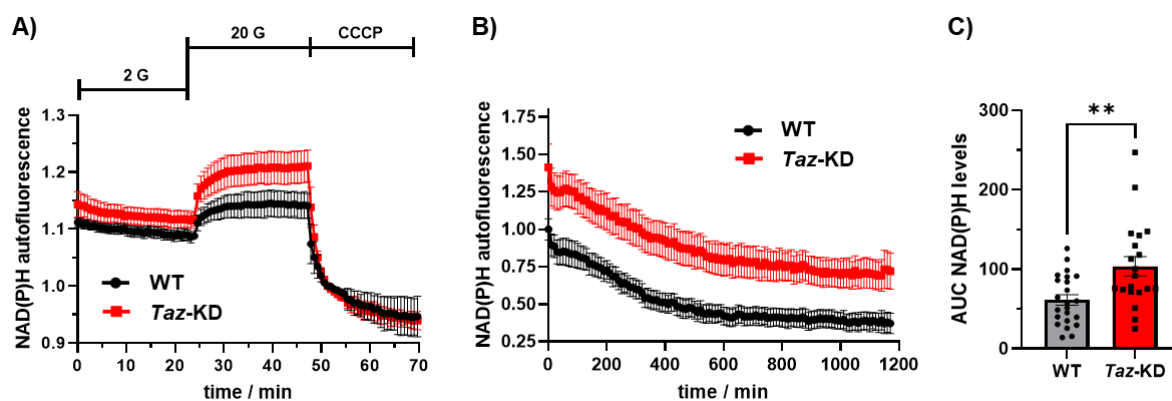


Figure 4.9: Increased NAD(P)H levels in *Taz*-KD pancreatic islets

(**A**) NAD(P)H levels of 20 wo WT and *Taz*-KD pancreatic islets in 2 and 20 mM glucose measured via autofluorescence and normalised to CCCP (25 μ M). N (WT) = 4, N (*Taz*-KD) = 6. (**B**) NAD(P)H levels of WT and *Taz*-KD pancreatic islets in 10 mM glucose measured for 19 h. n (WT) = 23, n (*Taz*-KD) = 20, from 8 animals. (**C**) AUC analysis of NAD(P)H levels in 10 mM glucose measured for 19 h. n (WT) = 23, n (*Taz*-KD) = 20, from 8 animals. Data = mean \pm SEM; N = number of animals; statistical analysis: unpaired *t* test: ***p* < 0.01. Abbreviations: weeks of age (wo), *tafazzin*-knockdown (*Taz*-KD), wildtype (WT), area under the curve (AUC).

In summary, *Taz*-KD pancreatic islets exhibited increased glucose uptake and elevated levels of NAD(P)H compared to WT. However, critical enzymes of the glucose metabolism, like Gck and G6PDH were not upregulated in *Taz*-KD pancreatic islets.

4.4.2 Oxygen consumption rate and mitochondrial membrane potential

The pyruvate generated by glycolysis is transported into the mitochondria where it fuels the OXPHOS to generate ATP. A Seahorse XFe96 Analyser was used to measure the OCR of isolated pancreatic islets. Mitochondrial membrane potential was also measured to further evaluate mitochondrial function.

Mitochondrial stress test using Seahorse XFe 96 analyser

Initially, a mitochondrial stress test with control islets isolated from C57Bl6/N mice was performed to optimise the protocol, including finding the ideal islet number per well, inhibitor concentrations and incubation times. This was especially important in the Seahorse experiments as there are only a few experiments on intact pancreatic islets published (studies from: Taddeo *et al.* 2018, Rocha *et al.* 2024)^{303,358}, and a substantial number of shTaz animals are required for each experiment (1500 – 1800 pancreatic islets from 8 – 9 animals for one spheroid plate). The OCR kinetics followed the predicted curve from the literature described in **Chapter 3.8.3**, and the OCR increased with a rising number of islets per well (**Figure 4.10 A**). Interestingly, even single large islets could be measured, which has also been observed by another group before.³⁵⁸ Although the OCR levels with 20 islets were higher than with 10 islets, it was technically challenging to fit 20 islets into the detent in the wells of the spheroid plate, which is highlighted in **Figure 4.10 B** where 15 pancreatic islets were placed inside the well. The probability of lost or moved islets was higher (not quantified) in the measurement with 20 islets. Based on the OCR curves and the size of the detent in the wells, 15 islets per well were used for the shTaz experiments.

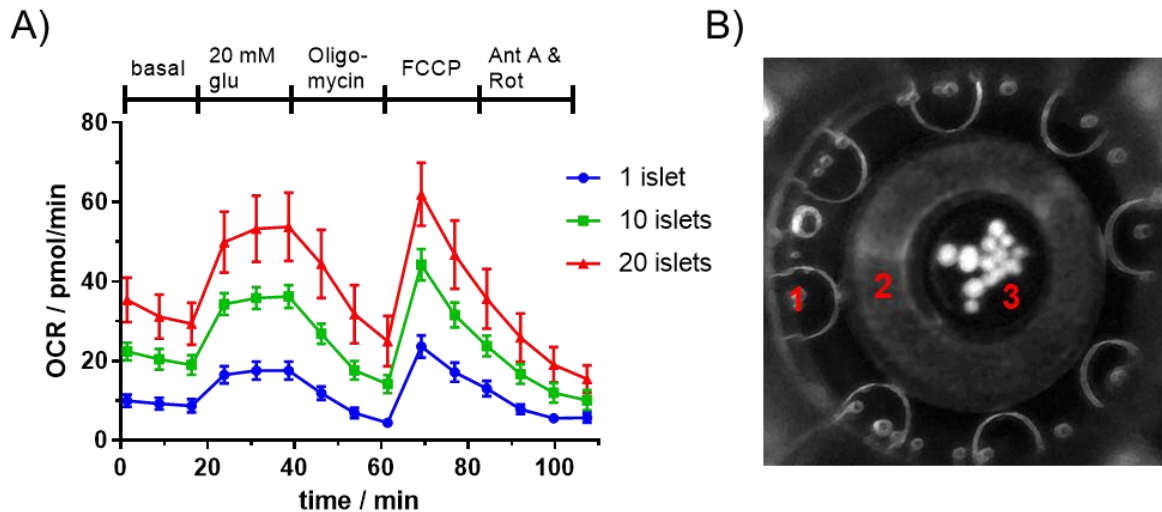


Figure 4.10: Establishing the OCR measurement of pancreatic islets using Seahorse analyser

(A) Mitochondrial stress test protocol for different amounts of C57BL/6N mouse pancreatic islets per well, starting from 2.8 mM glucose and increasing to 20 mM glucose. N = 3 (B) Spheroid plate well construction with 15 pancreatic islets. 1: vents for media diffusion 2: zoning for samples 3: surface for samples. Data = mean \pm SEM; N = number of animals; Abbreviations: weeks of age (wo), *tafazzin*-knockdown (*Taz*-KD), wildtype (WT), oxygen consumption rate (OCR).

After establishing the experimental conditions, a mitochondrial stress test on intact pancreatic islets from 20 wo WT and *Taz*-KD shTaz mice was performed (Figure 4.11). The OCR was measured over time in three glucose concentrations (2.8, 10 and 20 mM). The acquired OCR values were used to calculate and quantify various metabolic parameters, including non-mitochondrial and basal respiration, ATP production, acute glucose response, spare respiratory (SRC), maximum respiration and proton leak (described in Chapter 3.8.3 and illustrated in Figure 3.11).

The basal and non-mitochondrial respiration of WT and *Taz*-KD were similar in both genotypes (Figure 4.11 B1, B2). Furthermore, the OCR curves and metabolic parameters under stimulation with 10 or 20 mM glucose were similar for 20 wo WT and *Taz*-KD pancreatic islets (Figure 4.11 A2, A3, B3, C1, C2, C3). Interestingly, in low glucose concentrations (2.8 mM), increased OCR levels in the kinetic curves of *Taz*-KD pancreatic islets compared to WT were observed (Figure 4.11 A1). While ATP production was unchanged in low glucose, the response to glucose, spare respiratory capacity (SRC), proton leak and maximum respiration were amplified under low glucose conditions in *Taz*-KD pancreatic islets (Figure 4.11 and supplements, Figure 7.8).

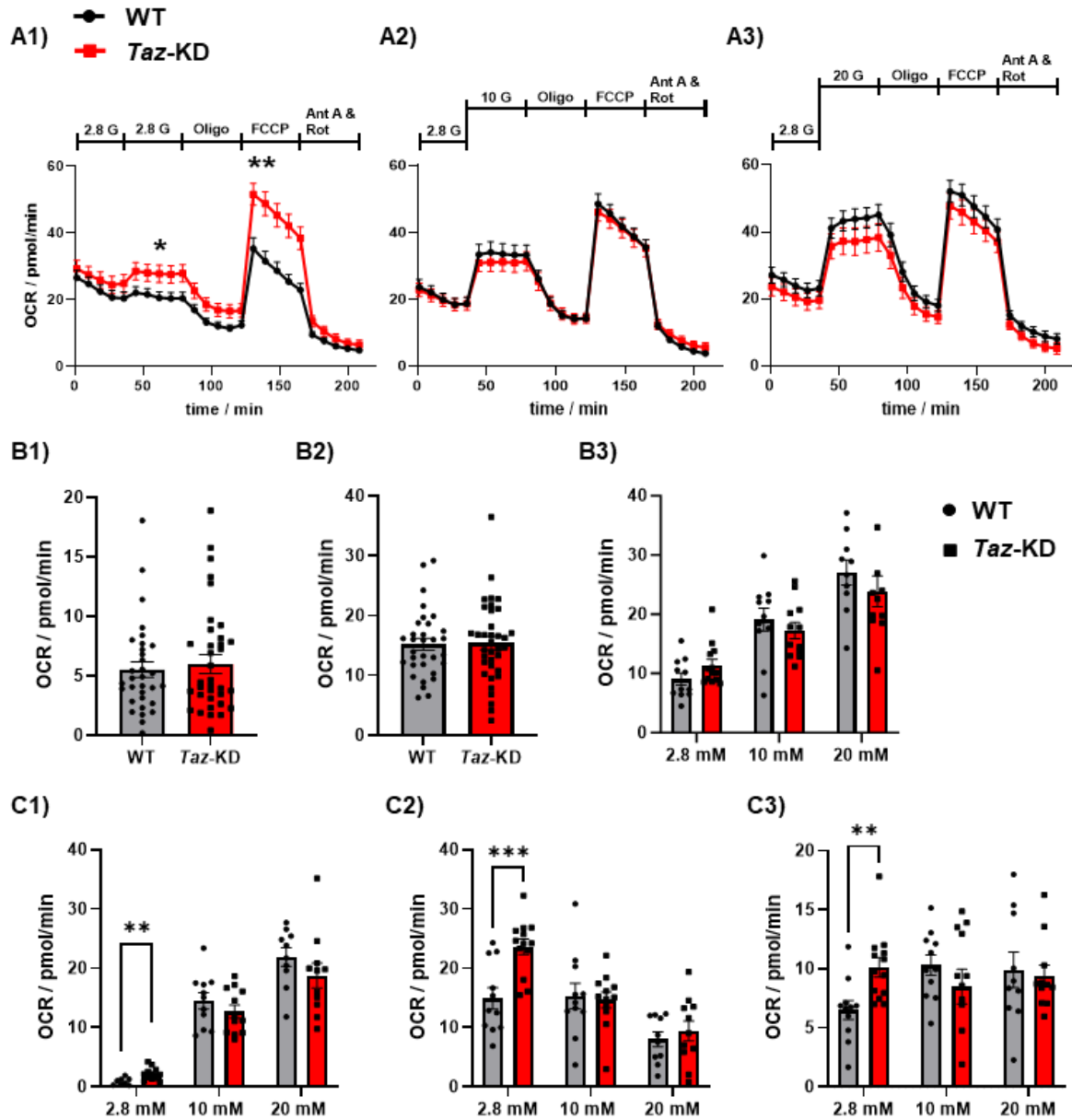


Figure 4.11: Increased SRC and proton leak in low glucose of *Taz*-KD pancreatic islets

(A) The OCR over time of 20 wo WT and *Taz*-KD pancreatic islets at 2.8 mM (A1), 10 mM (A2) and 20 mM (A3) glucose concentration followed by the addition of several inhibitors of the respiratory chain complexes. n (WT) = 11, n (*Taz*-KD) = 13. (B) Quantification of non-mitochondrial (B1) and basal respiration (B2). ATP production (B3) is separated by glucose concentration. n (WT) = 11, n (*Taz*-KD) = 13. (C) Quantification of response to glucose (C1), SRC (C2), and proton leak (C3) separated by glucose concentration. n (WT) = 11, n (*Taz*-KD) = 13; n number of experiments include N (WT) = 5 and N (*Taz*-KD) = 4; Data = mean \pm SEM; n = number of experiments; N = number of animals; statistical analysis: unpaired t test: * p < 0.05, ** p < 0.01, *** p < 0.001. Abbreviations: weeks of age (wo), *tafazzin*-knockdown (*Taz*-KD), wildtype (WT), spare respiratory capacity (SRC), oxygen consumption rate (OCR), oligomycin (Oligo), rotenone (Rot), antimycin A (Ant A).

Mitochondrial nutrient dependencies and capacities using Seahorse XFe96 analyser

To explore the possibility of a metabolic shift from glucose to other nutrients (amino acids or fatty acids) in the cellular metabolism of *Taz*-KD pancreatic islets, a Seahorse XF Mito Fuel Flex Test Kit was performed (method description in **Chapter 3.8.3** and illustrated in **Figure 3.11**).

Therefore, the OCR over time of 20 wt WT and *Taz*-KD pancreatic islets in the presence or absence of metabolic inhibitors was measured and normalised to the baseline to test nutrient dependencies and capacities (**Figure 4.12**). Normalisation was performed on the second value of the baseline, because in all the conditions, the values drop from the first to the second point and then start to stabilise. This initial drop might be due to the moving of the islets or the equilibration of the setup. The OCR of the baseline in Seahorse XF RPMI medium supplemented among others with 10 mM glucose was similar for both genotypes. After the baseline, inhibition of glutamine conversion with BPTES, fatty acid oxidation with etomoxir, and glucose metabolism with UK5099 was investigated. Only the blockage of glucose metabolism reduced the OCR, and this occurred to a similar extent in WT and *Taz*-KD pancreatic islets (**Figure 4.12**). Therefore, the calculated pathway dependencies (**equation: (eq. 1)**) for glutamine and long-chain fatty acid oxidation were found to be 0% for both genotypes (**Table 4.1**). The glucose oxidation dependency was above 100% due to a slight increase in OCR after injection of the inhibitors etomoxir and BPTES (**Figure 4.12** and **Table 4.1**). The OCR rise after adding BPTES was significantly higher in *Taz*-KD compared to the WT pancreatic islets (**Figure 4.12 A1**). The corresponding ECAR curves following the same protocol are displayed in the supplements and no difference in ECAR among the genotypes was found (supplements, **Figure 7.12**).

After testing nutrient dependencies, oligomycin and FCCP were injected to evaluate the responsiveness of the pancreatic islets in the experiment. The fact that all OCR curves showed a clear drop after oligomycin and an increase after FCCP confirms that the islets responded well, and the OCR measured was related to the mitochondria, as the levels after oligomycin reflect the non-mitochondrial OCR.

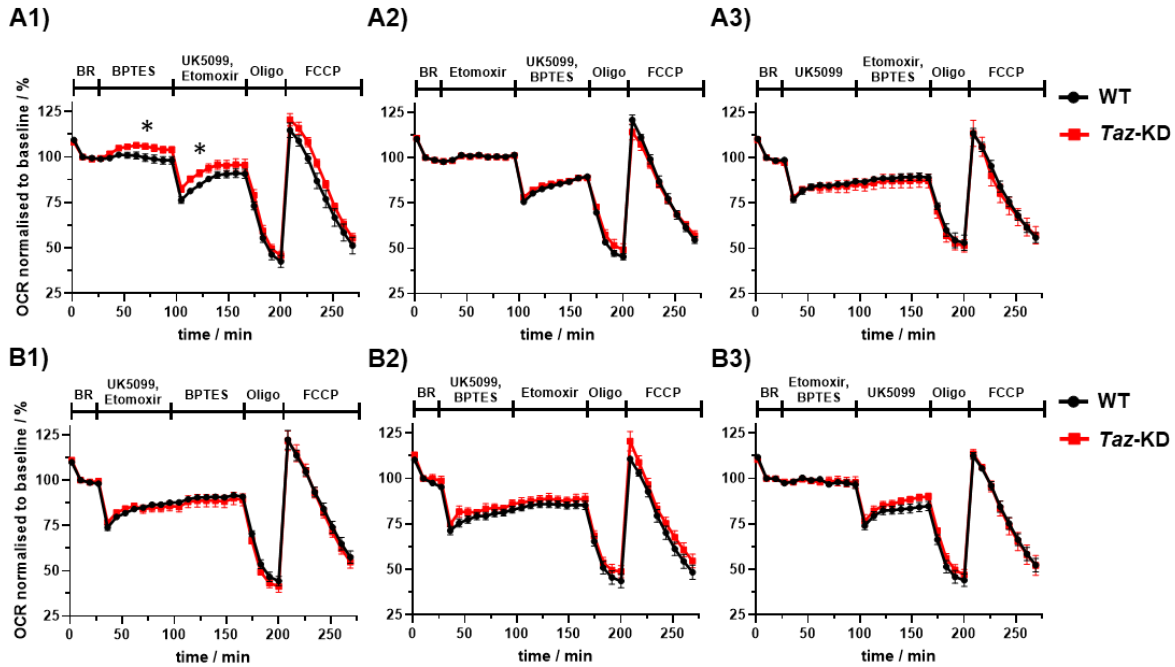


Figure 4.12: No differences in nutrient dependency of *Taz*-KD pancreatic islets

(A) Nutrient dependency test of 20 wo WT and *Taz*-KD pancreatic islets, assessing glutamine (A1), fatty acids (A2) and glucose (A3) oxidation pathways. N (WT) = 6, N (*Taz*-KD) = 4. (B) Nutrient capacity test of 20 wo WT and *Taz*-KD pancreatic islets, assessing glutamine (B1), fatty acids (B2) and glucose (B3) oxidation pathway. N (WT) = 6, N (*Taz*-KD) = 4. Data = mean \pm SEM; N = number of animals; statistical analysis: unpaired *t* test: **p* < 0.05. Abbreviations: weeks of age (wo), *tafazzin*-knockdown (*Taz*-KD), wildtype (WT), oxygen consumption rate (OCR), basal respiration (BR), oligomycin (Oligo).

Table 4.1: Fuel oxidation and pathway dependencies

The pathway dependencies were calculated according to (eq. 1).

Pathway	Group	Dependency / % (mean)	SEM / %
Glucose oxidation	WT	135.36	16.13
	<i>Taz</i> -KD	142.48	18.87
Glutamine oxidation	WT	0	0
	<i>Taz</i> -KD	0	0
Long-chain fatty acid oxidation	WT	0	0
	<i>Taz</i> -KD	0	0

Mitochondrial membrane potential using TMRM

In order to evaluate mitochondrial function, it is useful to examine changes in mitochondrial membrane potential. Therefore, the dye TMRM with a quenching mode setup was used (description in **Chapter 3.8.1**) in whole pancreatic islets to study the mitochondrial membrane potential of 20 wo WT and *Taz*-KD pancreatic islets. The experiments, depicted in **Figure 4.13**, were normalised to the baseline in KHB with 2 mM glucose. After changing to 20 mM glucose, the TMRM signal intensity dropped due to hyperpolarisation of the mitochondrial matrix, which led to an accumulation of TMRM molecules and resulted in fluorescent quenching. Subsequent addition of CCCP released the TMRM molecules by uncoupling the mitochondrial membrane potential. No difference of mitochondrial membrane potential for *Taz*-KD compared to WT pancreatic islets was observed in 2 mM glucose, upon stimulation with 20 mM glucose, or after the addition of 25 μ M of CCCP.

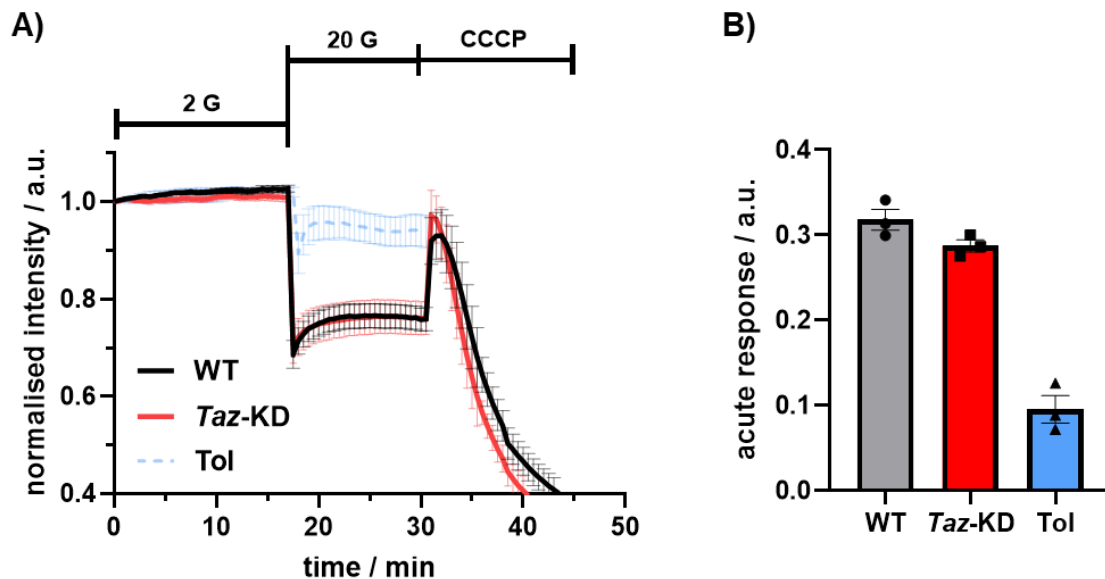


Figure 4.13: Mitochondrial membrane potential was unchanged in *Taz*-KD pancreatic islets

(A) Mitochondrial membrane potential of 20 wo WT and *Taz*-KD pancreatic islets measured with the dye TMRM in quenching mode. After an initial baseline with 2 mM glucose KHB, the glucose level was increased to 20 mM glucose. 25 mM CCCP (final concentration) was added in the end of the experiment to release the TMRM molecules inside the mitochondria. In the Ctrl group, 100 μ M of tolbutamide instead of glucose was added to the samples. N = 3. **(B)** Acute response (calculated delta start to maximal decrease in TMRM intensity) to 20 mM glucose or 100 μ M tolbutamide of 20 wo WT and *Taz*-KD pancreatic islets. N = 3, Data = mean \pm SEM; N = number of animals. Abbreviations: weeks of age (wo), *tafazzin*-knockdown (*Taz*-KD), wildtype (WT), tolbutamide (Tol).

Control experiments using the K⁺ channel blocker tolbutamide were conducted to distinguish changes at the plasma membrane potential from the changes observed at the mitochondrial membrane potential. Tolbutamide acts independently from mitochondrial metabolism and causes depolarisation at the plasma membrane.³⁷³ The addition of 100 μ M tolbutamide instead of 20 mM glucose led to a minor response of the TMRM signal, which indicates that TMRM monitored specifically the changes at the mitochondrial membrane potential and not at the plasma membrane potential (**Figure 4.13**). In summary, mitochondrial functionality in different glucose conditions assessed by OCR and mitochondrial membrane potential was preserved in *Taz*-KD pancreatic islets. Under low glucose conditions, *Taz*-KD showed higher SRC and proton leak than pancreatic islets.

4.4.3 ATP production

The OXPHOS of the mitochondria is the main ATP production centre inside the cell. Therefore, measuring ATP levels is a valuable indicator of mitochondrial functionality and cell viability. Furthermore, in pancreatic islet cells, the cellular (sum of all ATP sources) ATP/ADP ratio determines the state of the ATP-sensitive K_{ATP} channels responsible for membrane depolarisation and the resulting hormone secretion. Although the ATP production was already indirectly measured in the OCR experiments (**Chapter 4.4.2**), due to the particular importance of the cellular ATP availability in pancreatic islet cells, the ATP content was additionally assessed using the luciferase-based CellTiter-Glo[®] assay (method description in **Chapter 3.7.3**). Cellular ATP content of 20 wo WT and *Taz*-KD pancreatic islets were similar when incubated in 10 mM glucose conditions (see pancreatic islet culturing in **Chapter 3.2.1**) for one day after isolation (**Figure 4.14 A**).

Additionally, 20 wo WT and *Taz*-KD pancreatic islets were preincubated with or without different substances, including metabolic and redox inhibitors or stressors (**Figure 4.14 B, C and D**). Interestingly, pre-incubation with substances that affect the cellular redox homeostasis had an impact on ATP levels in *Taz*-KD pancreatic islets compared to WT. While incubation with 10 μ M of the NOX4 inhibitor, GLX, increased the ATP levels, 1 μ M of the thioredoxin reductase inhibitor, auranofin, resulted in slightly diminished (not statistical) ATP levels in *Taz*-KD pancreatic islets (**Figure 4.14 B**). Exposure to increasing exogenous H₂O₂ concentrations (10, 20 and 100 μ M) led to a stepwise decrease of ATP concentrations in both genotypes. Surprisingly, preincubation with the mitochondrial drugs RSV (10 μ M) and SS-31 (100 nM) resulted in decreased ATP levels in *Taz*-KD compared to WT pancreatic islets

(Figure 4.14 C). This might be due to the enhancement of ATP production in WT during treatment with RSV, which was not present in the *Taz*-KD pancreatic islets. Furthermore, incubation under glucolipotoxicity conditions of 20 mM glucose and 100 μ M palmitate (complexed 5:1 in BSA) significantly decreased the ATP levels in WT but not *Taz*-KD pancreatic islets (Figure 4.14 D).

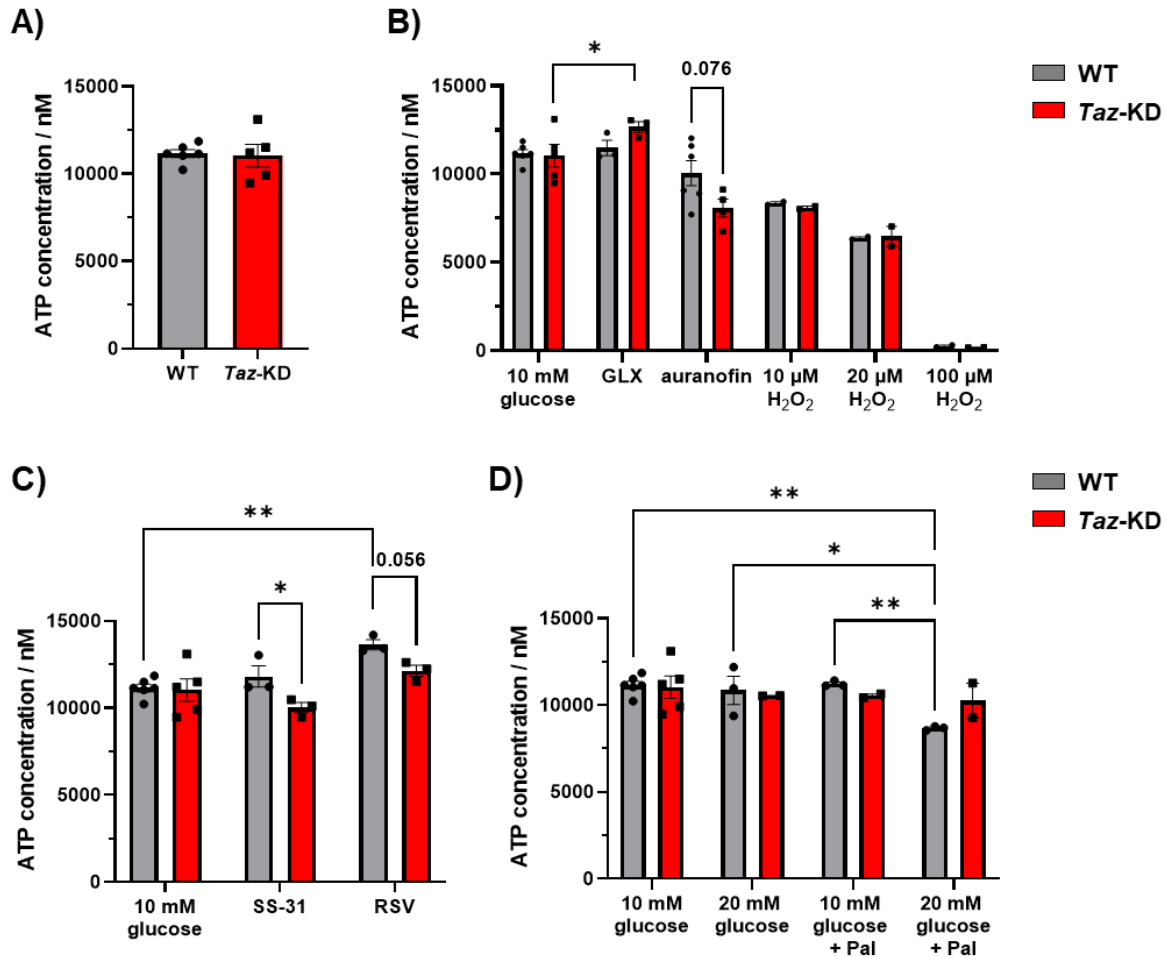


Figure 4.14: Unchanged basal ATP levels of *Taz*-KD pancreatic islets

(A) ATP concentration of 20 wo WT and *Taz*-KD pancreatic islets under standard culturing conditions (10 mM glucose) analysed by the CellTiter-Glo® assay. The ATP levels were used as a reference for the measurements in (B, C and D). N (WT) = 6, N (*Taz*-KD) = 5. (B) ATP levels of 20 wo WT and *Taz*-KD pancreatic islets after 24 h incubation with or without 10 μ M GLX, 1 μ M auranofin, and H_2O_2 (10, 20, 100 μ M). N (GLX) = 3, N (auranofin, WT) = 6, N (auranofin, *Taz*-KD) = 4, N (H_2O_2) = 2. (C) ATP levels of 20 wo WT and *Taz*-KD pancreatic islets after 24 h incubation with or without 100 nM SS-31 and 10 μ M RSV. N = 3 (D) ATP levels of 20 wo WT and *Taz*-KD pancreatic islets after 24 h incubation with 10 mM glucose, 20 mM glucose, 10 mM glucose with 100 μ M palmitate, or 20 mM glucose with 100 μ M palmitate. N (WT) = 3, N (*Taz*-KD) = 2. Data = mean \pm SEM; N = number of animals; statistical analysis: two-way ANOVA: *p < 0.05, **p < 0.01. Abbreviations: weeks of age (wo), *tafazzin*-knockdown (*Taz*-KD), wildtype (WT), GLX351322 (GLX), palmitate (Pal), resveratrol (RSV).

Overall, the ATP levels of WT and *Taz*-KD pancreatic islets were similar in 10 mM glucose, but when challenged with metabolic and redox inhibitors or activators, the resulting ATP content of *Taz*-KD pancreatic islets was less affected compared to that of WT controls. While *Taz*-KD pancreatic islets seem to benefit less from the mitochondrial drugs, they were also less influenced by the deleterious impact of glucolipotoxicity. However, the increase in ATP levels after GLX treatment suggests an involvement of NOX4 in the *Taz*-KD phenotype.

4.4.4 Ca^{2+} handling in *Taz*-KD pancreatic islets

The function of pancreatic islets is highly dependent on tight regulations of the intracellular Ca^{2+} concentrations. Upon stimulation with glucose, cytosolic Ca^{2+} influx triggers the release of insulin vesicles in pancreatic β -cells (further elaborated in **Chapter 1.2.2**).

Cytosolic Ca^{2+} experiments

The intracellular Ca^{2+} concentration of intact and dispersed 20 wt WT and *Taz*-KD pancreatic islets was measured with the ratiometric dye Fura-2 AM (**Figure 4.15**). After recording the baseline with 2 mM glucose KHB for 10 min, a high glucose solution (final concentration 20 mM) was applied. Upon stimulation with glucose, the intracellular Ca^{2+} level dropped due to the previously described activation of the sarcoplasmic/endoplasmic reticulum Ca^{2+} ATPase (SERCA).²⁹¹ After the small initial drop, a cytosolic Ca^{2+} influx increased the monitored Fura-2 AM ratio. At the end of the experiment, a 30 mM KCl solution (positive control) was applied to depolarise the pancreatic islets completely. Although the Ca^{2+} levels in low and high glucose were comparable between both genotypes, in intact *Taz*-KD pancreatic islets, the Ca^{2+} influx occurred significantly earlier (**Figure 4.15 A**). This observation was not connected to a changed steepness of the influx curve. Therefore, the influx process seemed to be preserved among the genotypes, but the upstream triggering process might be altered. In contrast, the dispersed *Taz*-KD pancreatic islet cells did not exhibit a quicker cytosolic Ca^{2+} influx upon stimulation with glucose compared to WT controls (**Figure 4.15 B**).

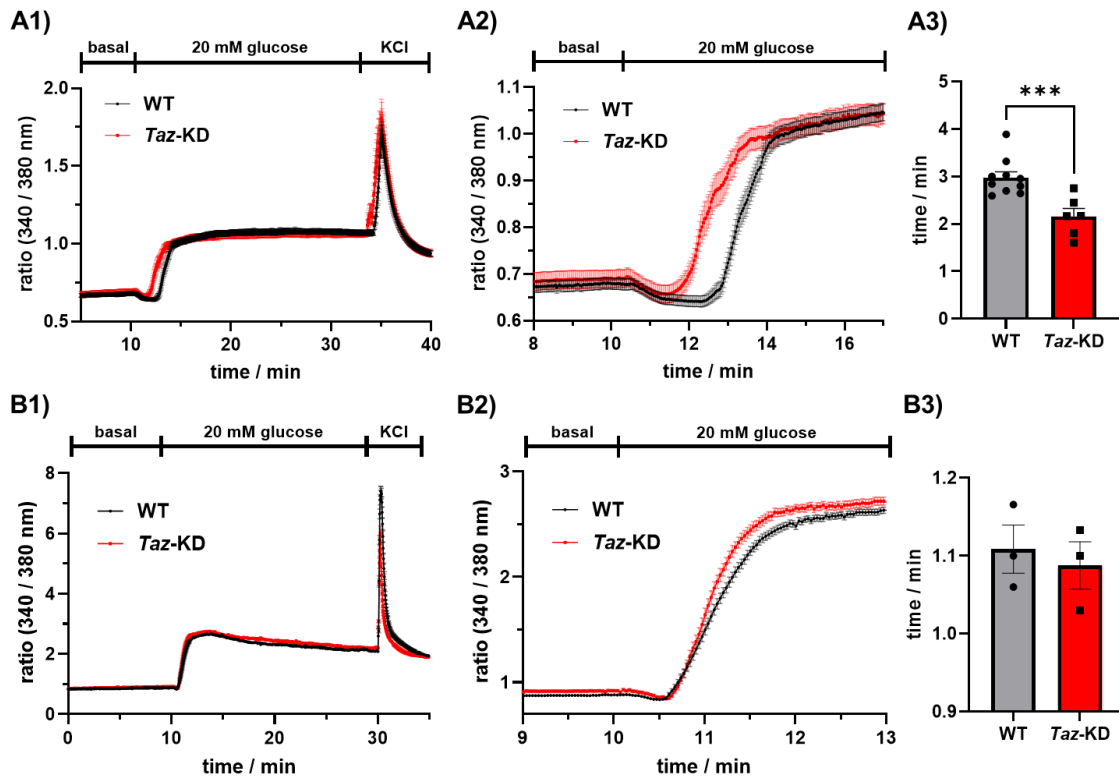


Figure 4.15: Faster cytosolic Ca^{2+} influx in intact but not dispersed *Taz-KD* pancreatic islets

Cytosolic Ca^{2+} levels of intact (A) and dispersed (B) pancreatic islets from 20 wo WT and *Taz-KD* mice using Fura2-AM. (A1, B1) After 10 min of baseline measurement with 2 mM glucose, a high glucose solution (final concentration: 20 mM) was added. An initial decrease of the cytosolic Ca^{2+} levels was followed by an influx of Ca^{2+} into the cell. The Ca^{2+} levels stabilise at around 15 min and in the end a positive control (30 mM KCl) was added. (A2, B2) The graphs represent zoomed versions of (A1, B1) to highlight the time difference of Ca^{2+} influx upon stimulation with glucose in *Taz-KD* compared to WT pancreatic islets. (A3, B3) Quantification of the Ca^{2+} influx time upon glucose stimulation. N (A, WT) = 10, N (A, *Taz-KD*) = 6, N (B) = 3. Data = mean \pm SEM; N = number of animals; statistical analysis: unpaired *t* test: ****p* < 0.001. Abbreviations: weeks of age (wo), *tafazzin*-knockdown (*Taz-KD*), wildtype (WT).

To further investigate this faster cytosolic Ca^{2+} influx phenomenon, glucose and tolbutamide titration experiments of intact 20 wo WT and *Taz-KD* pancreatic islets were conducted (Figure 4.16). Glucose titration experiments were performed using two different sets of measurements. Initially, cytosolic Ca^{2+} influx upon titration of commonly used glucose levels (0.5, 2.8, 5.6, 10 and 20 mM) was investigated (Figure 4.16 A1). The Ca^{2+} dynamics were similar among the genotypes. Subsequently, a finer resolved glucose step size was applied to predict the lowest glucose concentration that leads to a measurable Ca^{2+} influx (Figure 4.16 A2). WT and *Taz-KD* pancreatic islets similarly started to respond to glucose concentrations above 5 mM. The titration experiments with the sulfonylurea drug tolbutamide

(further explained in **Chapter 0**) were performed in 2 mM glucose KHB (**Figure 4.16 B**). *Taz*-KD pancreatic islets exhibited a slight shift towards an earlier Ca^{2+} influx, which was also represented in the enhanced dose-response curve of the tolbutamide and Ca^{2+} correlation. However, the observed effects with tolbutamide were not statistically significant.

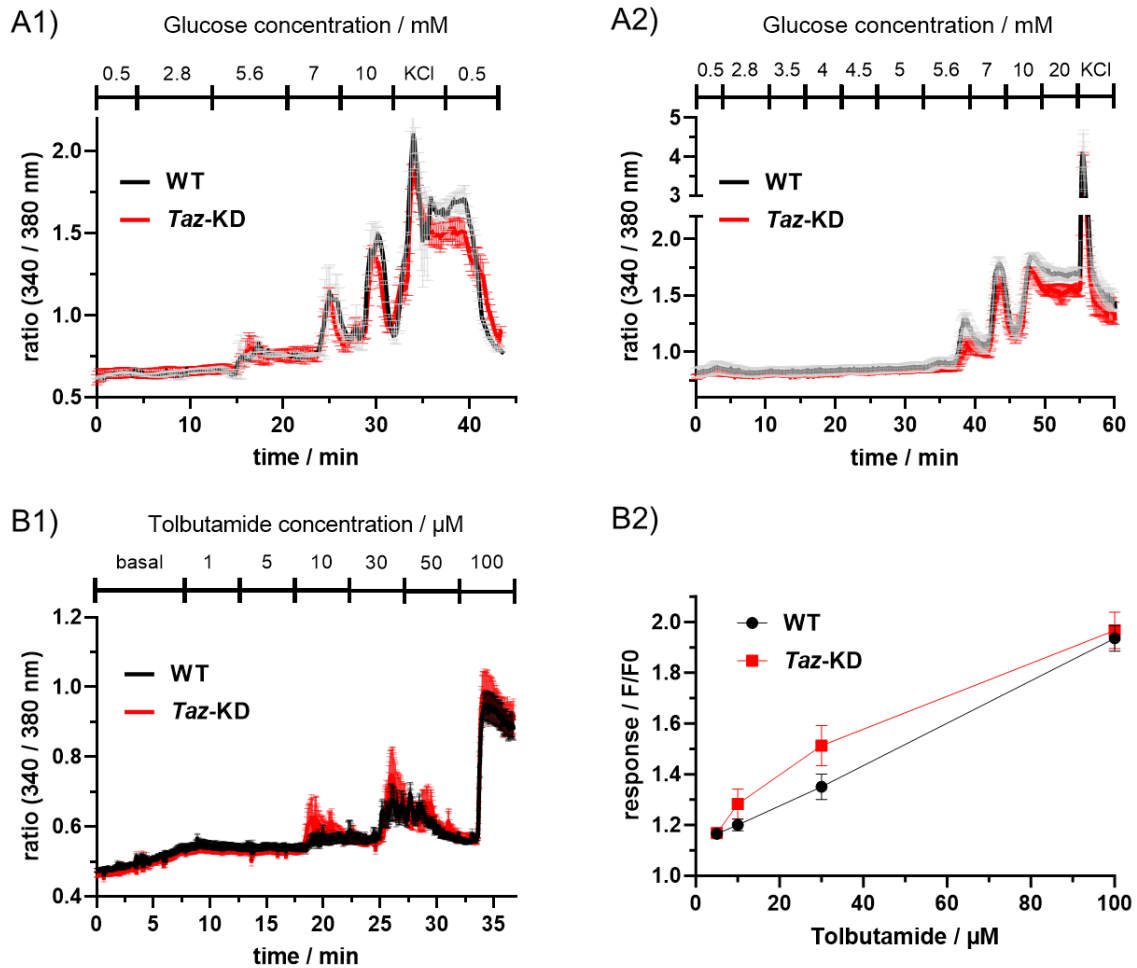


Figure 4.16: Unchanged Ca^{2+} response of *Taz*-KD pancreatic islets titrated with tolbutamide or glucose

(**A**) Glucose titration experiments to stimulate the Ca^{2+} influx into the 20 wo WT and *Taz*-KD pancreatic islets. Glucose was either added in coarse/bigger (A1) or fine/smaller (A2) steps. Ca^{2+} levels were measured with Fura-2 AM. N = 4. (**B**) Representative tolbutamide titration experiment (B1) of whole pancreatic islets and calculated dose-response curve (B2). The dose-response curve is calculated by the change in fluorescence ratio (340 / 380 nm) of the fluorescence ratio (F) to the corresponding tolbutamide concentration divided by the starting fluorescence ratio (F0). Data = mean \pm SEM; N = number of animals. Abbreviations: weeks of age (wo), *tafazzin*-knockdown (*Taz*-KD), wildtype (WT).

ER- and mitochondrial Ca^{2+} experiments

Ca^{2+} dynamics are regulated on different hierarchy scales in the pancreatic islets. From Ca^{2+} response due to inter-islet crosstalk over cytosolic Ca^{2+} influx in hormone secretion to subcellular Ca^{2+} handling.³¹⁴ In the previous Chapters, a different pancreatic islet architecture (more α -cells) and metabolic alterations (increased OCR under low glucose and higher NAD(P)H levels) combined with a quicker cytosolic Ca^{2+} influx in *Taz*-KD compared to WT pancreatic islets were observed. To dive deeper into the Ca^{2+} homeostasis regulation of *Taz*-KD pancreatic islets, Ca^{2+} dynamics in subcellular compartments were analysed. The organelles mitochondria and ER were selected based on their key roles in Ca^{2+} signalling in the process of GSIS.^{174,426} The pancreatic islets had to be dispersed before measuring the subcellular Ca^{2+} dynamics to resolve the organelles under the microscope (method description in **Chapter 3.6**).

Mitochondrial Ca^{2+} levels are pivotal in regulating the TCA cycle and, hence, the ATP output. Therefore, the mitochondrial Ca^{2+} levels inside dispersed pancreatic islet cells from 20 wo WT and *Taz*-KD mice were investigated using the ratiometric Mito-Pericam sensor (**Figure 4.17 A**). A significantly decreased fluorescent intensity ratio (490 / 405 nm) in the *Taz*-KD compared to WT cells was observed at baseline 2 mM glucose, hinting towards decreased mitochondrial Ca^{2+} levels under this condition. However, the normalised to baseline mitochondrial Ca^{2+} dynamics upon glucose and KCl stimulation were similar in WT and *Taz*-KD pancreatic islet cells (**Figure 4.17 A**). The addition of either 20 mM glucose concentration or 30 mM KCl leads to a rise in mitochondrial Ca^{2+} levels similarly in both genotypes. It is important to note that the 490 nm excitation wavelength is known to be pH-sensitive and therefore, the mitochondrial Ca^{2+} dynamics were depicted only with the 405 nm excitation wavelength.²⁶⁴ The full ratiometric (490 / 405 nm) and the non-normalised curves are depicted in the supplements (supplements, **Figure 7.9**).

ER is the main cellular Ca^{2+} store and is directly involved in the process of GSIS. Upon glucose stimulation, SERCA is activated and pumps Ca^{2+} from the cytosol into the ER.²⁹¹ Therefore, ER Ca^{2+} levels in 20 wo WT and *Taz*-KD dispersed pancreatic β -cells in low and high glucose using the ratiometric RIP-D4ER sensor were investigated (**Figure 4.17 B**). The added RIP promoter allowed specific transfection of solely pancreatic β -cells. A trend towards diminished ER Ca^{2+} levels in *Taz*-KD pancreatic β -cells at 2 mM glucose was observed. After the baseline recording, the glucose concentration was raised to 20 mM, which led to an ER Ca^{2+} influx. At the end of the experiment, 1 μM of thapsigargin was added to deplete the ER Ca^{2+} stores. The Ca^{2+} dynamics normalised to baseline were similar in the WT and *Taz*-KD

pancreatic β -cells. The non-normalised curves are depicted in the supplements (supplements, **Figure 7.9**).

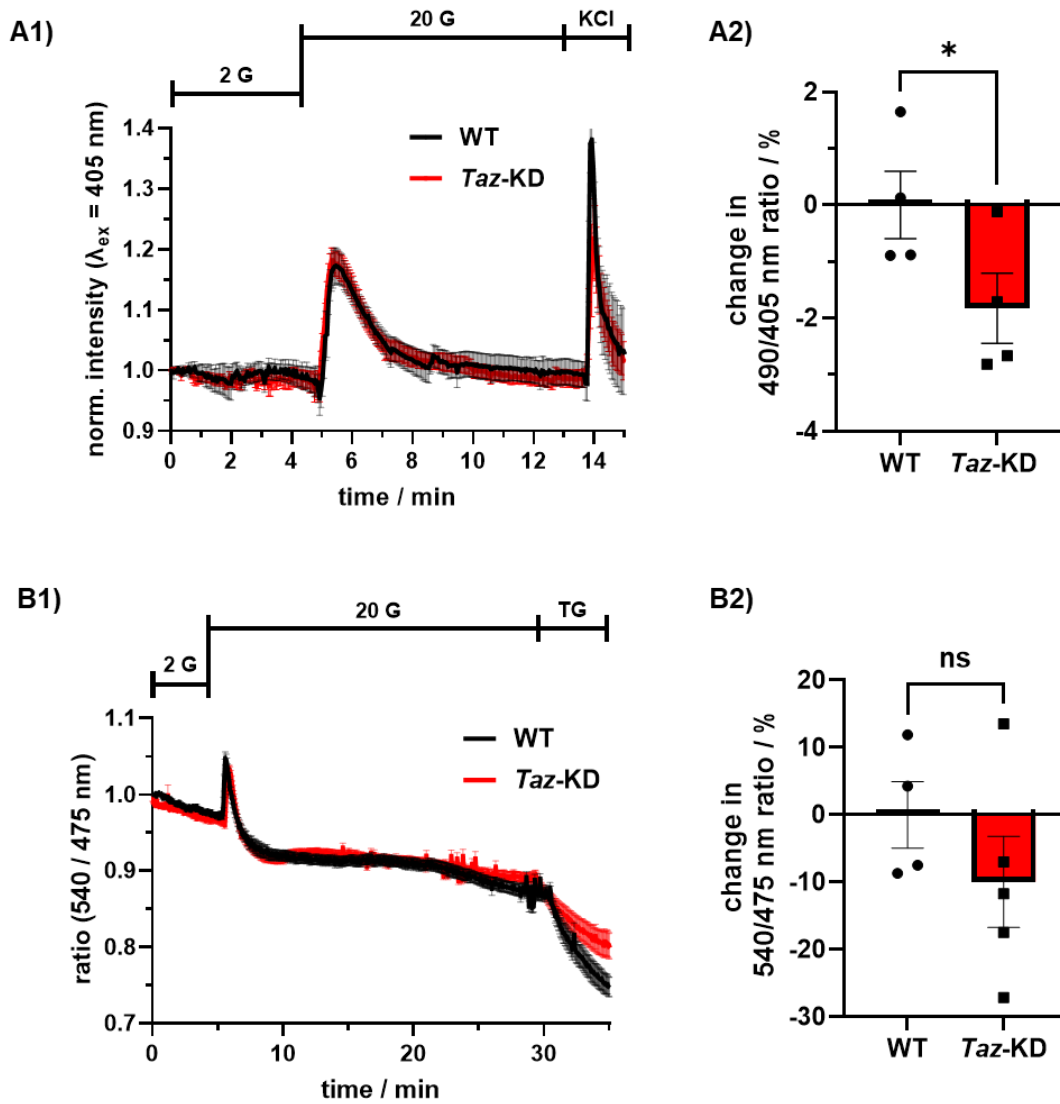


Figure 4.17: Similar mitochondrial and ER Ca^{2+} dynamics of *Taz*-KD pancreatic islets

(A) Mitochondrial Ca^{2+} measurement of 20 wo WT and *Taz*-KD dispersed pancreatic islets transduced with Mito-Pericam. (A1) The kinetic response was measured in the 405 nm excitation window and glucose concentration was increased from 2 to 20 mM before adding 30 mM KCl as a positive control. (A2) The ratio of 490/405 nm at baseline was compared for WT and *Taz*-KD pancreatic islets. N (WT) = 4, N (*Taz*-KD) = 5. (B) (B1) Representative ER Ca^{2+} measurement of 20 wo WT and *Taz*-KD dispersed pancreatic β -cells transduced with RIP-D4ER and normalised to baseline. Glucose concentration was raised from 2 to 20 mM before addition of 1 μM TG to empty the ER Ca^{2+} storage. (B2) Baseline ER Ca^{2+} levels. N (WT) = 4, N (*Taz*-KD) = 5. Data = mean \pm SEM; N = number of animals; statistical analysis: unpaired *t* test: **p* < 0.05, ns: *p* > 0.05. Abbreviations: weeks of age (wo), *tafazzin*-knockdown (*Taz*-KD), wildtype (WT), thapsigargin (TG), rat insulin promoter (RIP).

In summary, *Taz*-KD pancreatic islets displayed an earlier onset of glucose-stimulated Ca^{2+} influx, which was not observed in dispersed *Taz*-KD pancreatic islet cells. The ER- and mitochondrial- Ca^{2+} dynamics of WT and *Taz*-KD pancreatic islet cells were similar.

4.4.5 Insulin and glucagon secretion

The role of the pancreatic islets as an endocrine tissue is to regulate the blood sugar levels by secreting various hormones (introduced in **Chapter 1.2.2**). Insulin and glucagon are arguably the most prominent players in this process, and hence, measuring hormone secretion is key in evaluating pancreatic islet function in health and disease.

Static hormone secretion

Therefore, static insulin and glucagon secretion experiments of whole WT and *Taz*-KD pancreatic islets were performed in various glucose concentrations (0.5, 2.8, 5.6, and 20 mM; **Figure 4.18**). The insulin secretion levels and the insulin content of *Taz*-KD pancreatic islets were unchanged compared to the WT controls (**Figure 4.18 A**). The glucagon secretion was measured with two different approaches (see method **Chapter 3.5**). Interestingly, *Taz*-KD pancreatic islets secreted more glucagon in every glucose condition compared to WT controls (**Figure 4.18 B**). However, it was only significant under very low (0.5 mM) glucose concentrations. Surprisingly, the glucagon content of *Taz*-KD pancreatic islets was only slightly decreased (not significant) compared to WT controls (**Figure 7.10**).

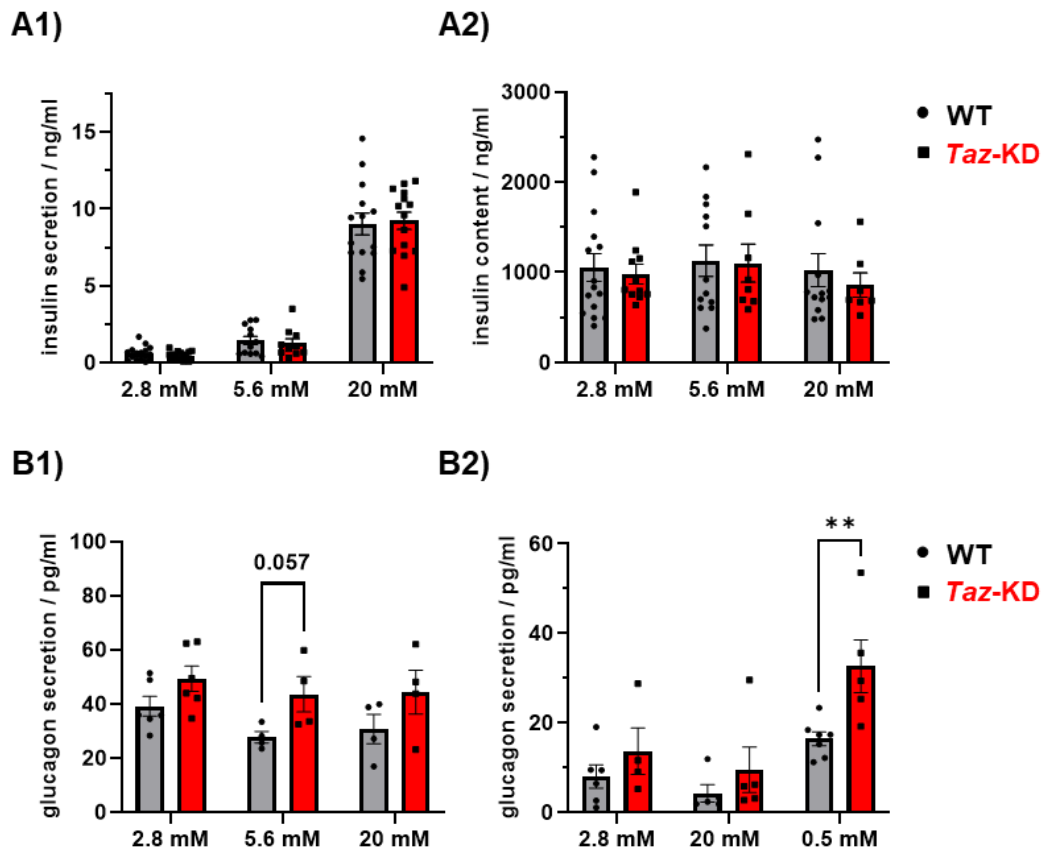


Figure 4.18: Increased glucagon and preserved insulin secretion in *Taz*-KD pancreatic islets

(A) Insulin secretion (A1) and content (A2) measurement of 20 wo WT and *Taz*-KD pancreatic islets using various glucose concentrations (2.8, 5.6, 20 mM). N (WT) = 16, N (*Taz*-KD) = 17. (B) Glucagon secretion of 20 wo WT and *Taz*-KD pancreatic islets measured with two approaches. (B1) The pancreatic islets were pre-treated with high glucose (20 mM) before glucagon secretion incubation. (B2) The pancreatic islets were pre-treated with low glucose (2.8 mM) before glucagon secretion. N (2.8 mM, WT) = 6, N (20 mM, WT) = 5, N (0.5 mM, WT) = 7, N (2.8 mM, *Taz*-KD) = 4, N (20 and 0.5 mM, *Taz*-KD) = 5. Data = mean \pm SEM; N = number of animals; statistical analysis: unpaired *t* test: **p < 0.01. Abbreviations: weeks of age (wo), *tafazzin*-knockdown (*Taz*-KD), wildtype (WT).

Dynamic insulin secretion

To get more insights into the process of GSIS of *Taz*-KD pancreatic islets, the dynamic insulin secretion profile of 20 wo WT and *Taz*-KD pancreatic islets was investigated (Figure 4.19). Unfortunately, the dynamic secretion experiments were not sensitive enough to also measure dynamic glucagon secretion. The biphasic behaviour of the GSIS was preserved in *Taz*-KD pancreatic islets (Figure 4.19 A1). Furthermore, the insulin secretion levels of the first and second phase of GSIS calculated by the AUC were unchanged among the genotypes (Figure 4.19 A2). Interestingly, the first phase of GSIS started slightly earlier (not significant) in

Taz-KD pancreatic islets compared to WT controls (**Figure 4.19 B1**). When normalised to pancreatic islet size instead of DNA content, the peak of the first phase of GSIS was shifted towards earlier time points (**Figure 4.19 B2**). It is important to note that in the dynamic GSIS protocol, the time resolution was in the dimension of minutes, while cytosolic Ca^{2+} levels were imaged every two seconds. (explained in method **Chapters 3.5, 0**). With a *Taz*-KD-mediated effect in the range of a few minutes, the variation makes it difficult to achieve statistically significant results in dynamic GSIS. Therefore, although no statistical difference was observed, the results of the dynamic insulin secretion confirmed the effects of the Ca^{2+} and static insulin measurements.

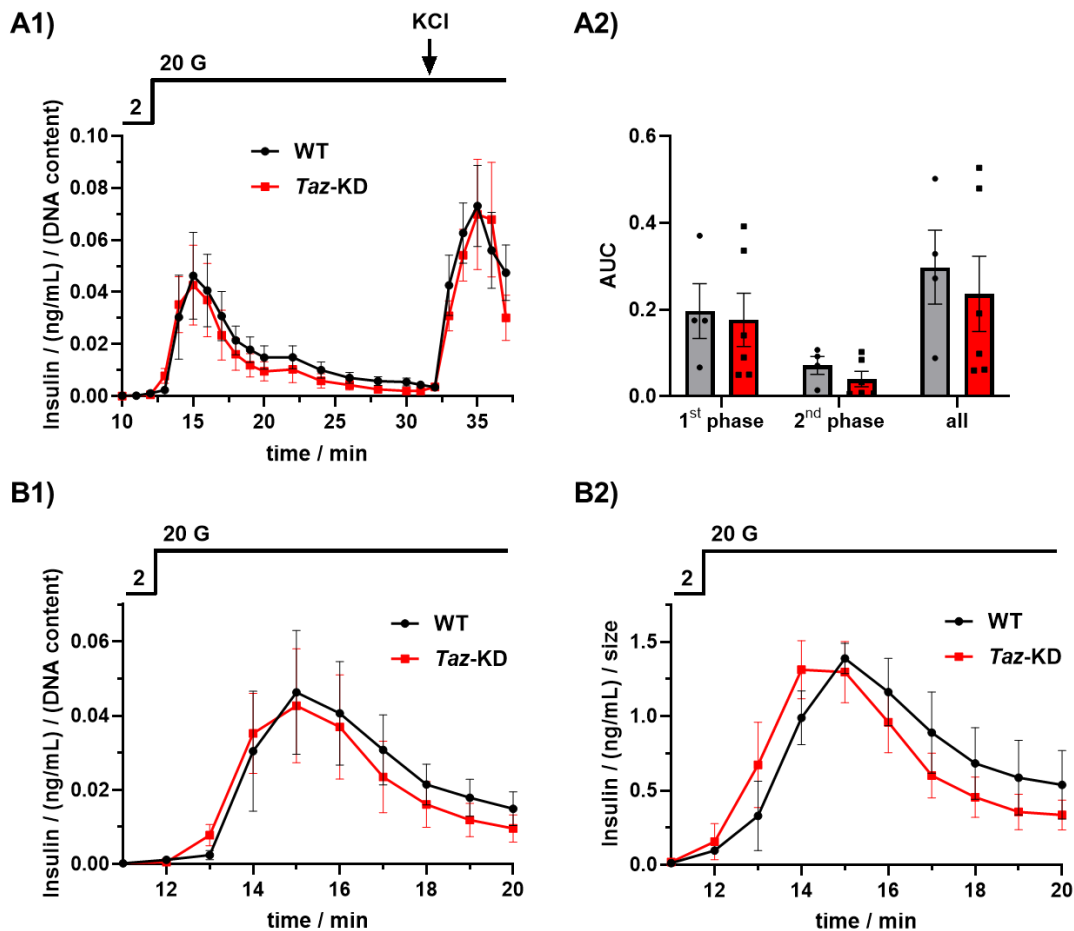


Figure 4.19: Similar dynamics in GSIS of *Taz*-KD pancreatic islets

(A) (A1) Dynamic GSIS of 20 weeks old WT and *Taz*-KD pancreatic islets normalised to DNA content. (A2) AUC quantification of the dynamic GSIS separated in first (10 – 20 min) and second (20 – 31 min) phase of insulin secretion, N (WT) = 4, N (*Taz*-KD) = 6. **(B)** First phase of the dynamic GSIS normalised by DNA content (B1) and islet size (B2). The graph in B1 is a scale-up version of A1 and highlights the slightly faster insulin release in *Taz*-KD pancreatic islets compared to WT control. Normalisation to islets size showed an earlier (not significant) first phase peak of GSIS in *Taz*-KD. N (WT) = 4, N (*Taz*-KD) = 6. Data = mean \pm SEM; N = number of animals. Abbreviations: weeks of age (wo), *tafazzin*-knockdown (*Taz*-KD), wildtype (WT), glucose-stimulated insulin secretion (GSIS), area under the curve (AUC).

In summary, *Taz*-KD pancreatic islets showed enhanced glucagon secretion, while GSIS was preserved compared to WT controls. Additionally, the dynamic insulin secretion tended towards a faster insulin secretion in *Taz*-KD pancreatic islets upon stimulation with glucose.

4.4.6 Extracellular acidification rate and pH measurement

Extracellular acidification rate

Another parameter that was acquired using the Seahorse XFe96 Analyser (additional to the OCR) is the ECAR. The ECAR, measured in mpH per minute, is proportional to the extracellular pH level and reflects changes in mitochondrial metabolism over time. Like the OCR, the ECAR was measured in modified protocols of the Seahorse XF Cell Mito Stress Test Kit (**Figure 4.20** and supplements, **Figure 7.11**) and the Seahorse XF Mito Fuel Flex Test Kit (supplements, **Figure 7.12**) with 20 wt WT and *Taz*-KD pancreatic islets. The ECAR levels rise similarly after the addition of 10 or 20 mM glucose in WT and *Taz*-KD pancreatic islets (supplements, **Figure 7.11**). All the ECAR curves over time, the baseline ECAR levels and the fold change in response to glucose for both Seahorse tests were similar in WT and *Taz*-KD pancreatic islets (**Figure 4.20** and supplements, **Figure 7.11** and **Figure 7.12**). Even under the 2.8 mM low glucose condition, where the OCR levels of WT and *Taz*-KD pancreatic islets differed, the ECAR curves were similar. Interestingly, the ECAR levels drop after adding oligomycin in WT and *Taz*-KD pancreatic islets, which contradicts the widely accepted view that oligomycin leads to cellular acidification.²⁵⁸ An oligomycin-induced drop of the ECAR levels has not been described in other tissues, neither BTHS nor healthy.³⁹ However, another group recently observed the same phenomenon in healthy pseudo Min6 islets.^{75,85}

Cytosolic pH measurements

In addition to measuring the ECAR levels, cytosolic pH measurements in 2 and 20 mM glucose of isolated 20 wt WT and *Taz*-KD pancreatic islets were performed using the pH-sensitive sypHer sensor (**Figure 4.20 B**). The observed changes in the SypHer fluorescent intensity ratio (490 / 400 nm) were in agreement with the ECAR experiments as the SypHer signal increased (higher pH) in 2 mM glucose and decreased (lower pH) in 20 mM glucose. Both WT and *Taz*-KD pancreatic islets showed a similar glucose-stimulated 10% decrease in the Sypher ratio (**Figure 4.20 B2**). Additionally, the SypHer signal increased in the presence of oligomycin and decreased again with FCCP. 30 mM of ammonium chloride was added in the end to have a positive control for the alkalinisation of the cytosol. When *Taz*-KD

pancreatic islets were compared to WT, no differences were observed in the SypHer curve and the response to glucose (**Figure 4.20 B1, B2**).

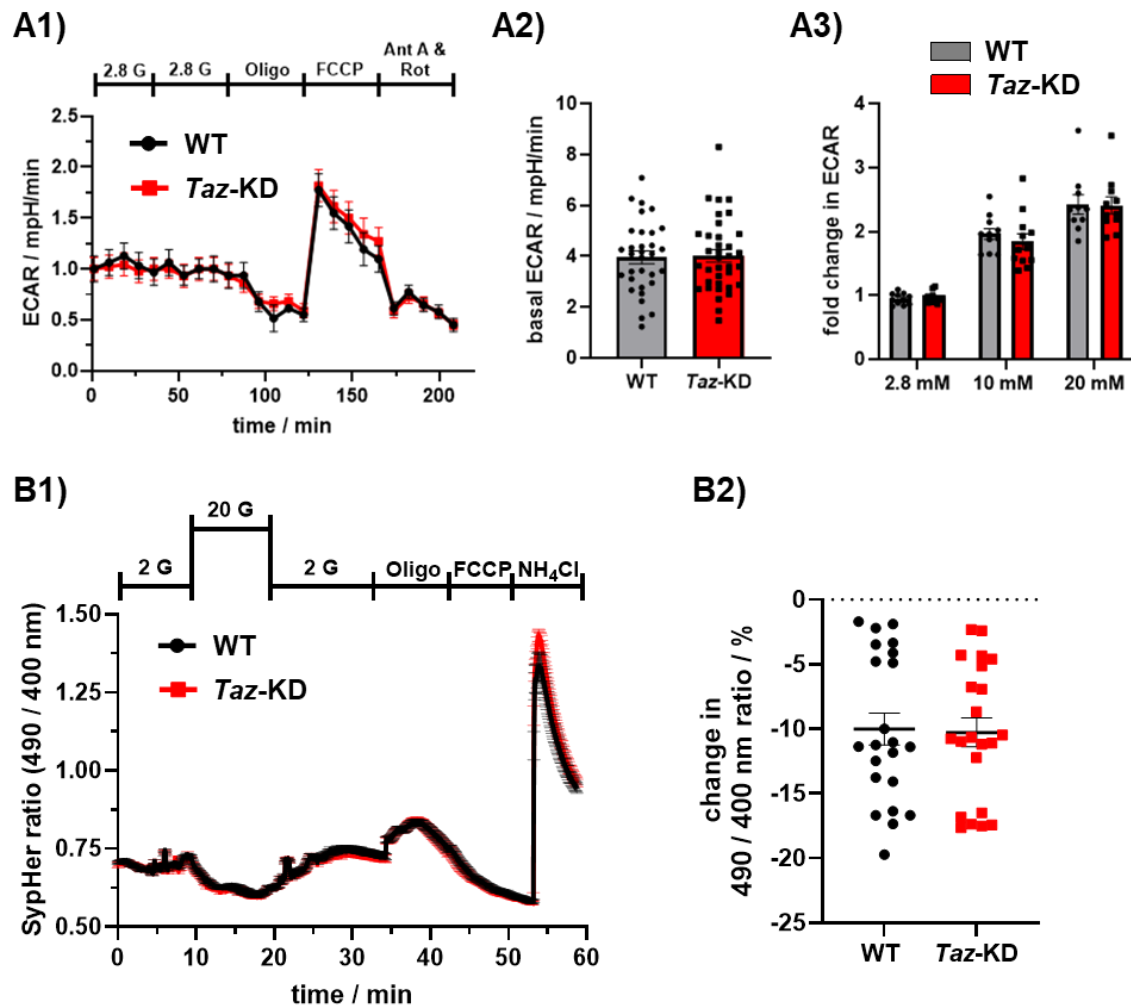


Figure 4.20: Similar acidification levels in *Taz*-KD and WT pancreatic islets

(A) (A1) The ECAR of 20 wo WT and *Taz*-KD pancreatic islets at 2.8 mM glucose. ECAR curves for 10 and 20 mM glucose are provided in the supplements (supplements, **Figure 7.11**). Quantified basal (A2) ECAR levels and ECAR fold change (A3) in response to glucose (2.8 mM, 10 mM and 20 mM) of WT and *Taz*-KD 20 wo pancreatic islets. n (WT) = 11, n (*Taz*-KD) = 13. n number of experiments include N (WT) = 5 and N (*Taz*-KD) = 4. **(B)** (B1) Representative SypHer experiment of 20 wo WT and *Taz*-KD pancreatic islets testing 2 and 20 mM glucose, oligomycin, FCCP and ammonium chloride (NH₄Cl, positive control). (B2) Response to a 20 mM glucose application quantified with the percentage change in SypHer ratio. n (WT) = 7, n (*Taz*-KD) = 6, n = number of experiments include N = 3. Data = mean \pm SEM; N = number of animals. Abbreviations: weeks of age (wo), *tafazzin*-knockdown (*Taz*-KD), wildtype (WT), extracellular acidification rate (ECAR).

In summary, *Taz*-KD pancreatic islets exhibited similar extracellular (ECAR) and cytosolic (SypHer) acidification rate compared to WT controls.

4.5 Redox experiments

The redox state of the cell is a critical regulator and indicator of pancreatic islet functionality in health and disease (introduced in **Chapter 1.2.3**). BTHS was often connected with deterioration in the redox state.²⁸⁷ Increased oxidative stress was considered one of the underlying causes of disease development and progression, as shown in pluripotent stem cell-derived cardiomyocytes.^{230,242} Since BTHS is a mitochondrial disease, the redox analysis in this thesis was focused on alterations in the mitochondrial compartment. In detail, investigations of the mitochondrial redox status in this project were performed with the mitochondrial-targeted mito-roGFP2-Orp1 H_2O_2 sensor. As described in material and methods (**Chapter 3.1.1**), a redox-sensitive BTHS mouse strain was generated, globally expressing the shRNA against *Taz* and the mito-roGFP2-Orp1 biosensor. This mouse strain will be referred to as MiOxTaz. Due to the specific breeding pattern, both genetic inserts were heterozygously expressed. The heterozygous expression of biosensors is known to impact the detection limit and the dynamic range.³⁸⁹

First, the sensitivity of the ratiometric mito-roGFP2-Orp1 biosensor (introduced in **Chapter 3.9**) was tested when it was only heterozygously expressed. In **Figure 4.21**, an H_2O_2 titration experiment in WT MiOxTaz pancreatic islets is displayed. Pancreatic islets were kept for 3 min under baseline conditions (10 mM glucose) with constant peristaltic pump flow of fresh KHB. Afterwards, the H_2O_2 concentration was gradually increased (10, 25, 50 μM), resulting in sensor oxidation. A slight rise was observed at 10 μM of H_2O_2 , which became more pronounced with each following H_2O_2 concentration. Next, the pancreatic islets were perfused again with fresh baseline KHB (without H_2O_2), leading to a reduction of the sensor, demonstrating the reversibility of the roGFP2-Orp1 sensor. Next, the islets were perfused with 100 μM H_2O_2 to achieve maximum oxidation, followed by maximum reduction with 10 mM DTT, a powerful reducing agent. At the end of the experiment, fresh baseline KHB (without H_2O_2) was perfused again to observe the return to baseline and to test the responsiveness after maximum oxidation and reduction.

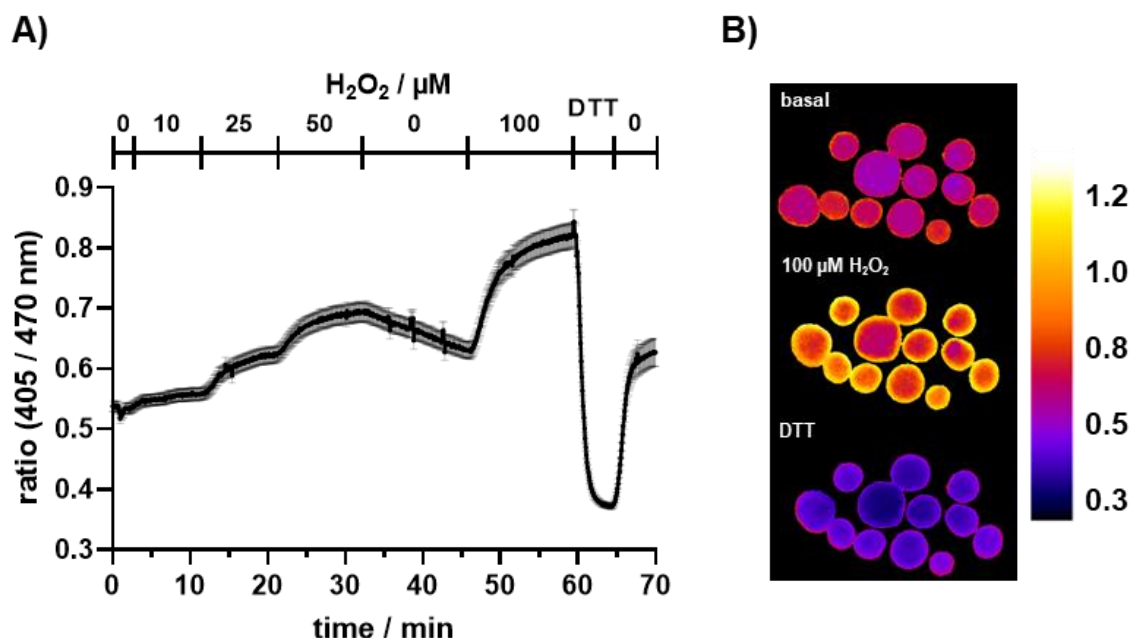


Figure 4.21: H₂O₂ titration of isolated pancreatic islets from WT MiOxTaz mice

(A) Imaging of real-time H₂O₂ (0 – 100 μM) kinetics of isolated pancreatic islets that heterozygously express the mito-roGFP2-Orp1 sensor. Highest oxidation after 100 μM of H₂O₂ and highest reduction after 10 mM DTT, n = 9. (B) Ratiometric images (excitation: 405/470 nm, emission: 500 – 530 nm) images (Lookup table: “Fire”) created with ImageJ and reflect oxidation state at 0 μM (top), 100 μM H₂O₂ (middle) and 10 mM DTT (bottom). Calibration bar (redox state): 0.3 (reduced) to 1.2 (oxidised). Data = mean ± SEM; N = number of animals. Abbreviations: weeks of age (wo), *tafazzin*-knockdown (*Taz*-KD), wildtype (WT), dithiothreitol (DTT).

After verification of a functional and reliable biosensor, several redox experiments using plate reader and microscopy approaches were performed.

4.5.1 Real-time H₂O₂ analysis

Following the real-time kinetics of H₂O₂ over extended periods provides a better representation of the redox state and its changes than simple endpoint measurements. As introduced in **Chapter 3.9** and confirmed in **Figure 4.21**, the measurement of the genetically-encoded mito-roGFP2-Orp1 H₂O₂ biosensor can provide real-time physiological changes in the mitochondrial redox state. Therefore, the mito-roGFP2-Orp1 sensor was used to study the mitochondrial redox kinetics of 20 wo WT and *Taz*-KD pancreatic islets. The redox state was recorded for 19 h at 5% CO₂ and 37°C in a phenol-free islet medium using a Clariostar

plate reader (**Figure 4.22**). The initial H_2O_2 levels in the mitochondria of *Taz*-KD pancreatic islets were higher compared to WT and remained elevated throughout the experiment. However, the H_2O_2 dynamics were similar and gradually increased overnight in both genotypes (**Figure 4.22**). When AUC was calculated, *Taz*-KD pancreatic islets displayed enhanced AUC compared to WT controls. Interestingly, the H_2O_2 levels decreased for the first 2 h of the experiment before the H_2O_2 levels increased over the remaining experiment time. The H_2O_2 experiments were measured in parallel to NAD(P)H measurements that showed the opposite trend (**Figure 4.9 B**). The initial decrease was probably due to the settling of the pancreatic islets after being selected and transferred for the experiment (“stress”). Subsequently, the close proximity of the pancreatic islets in the Clariostar (25 islets in each U-bottom well) likely created hypoxic stress conditions, resulting in oxidation of the mitochondrial redox state over time.

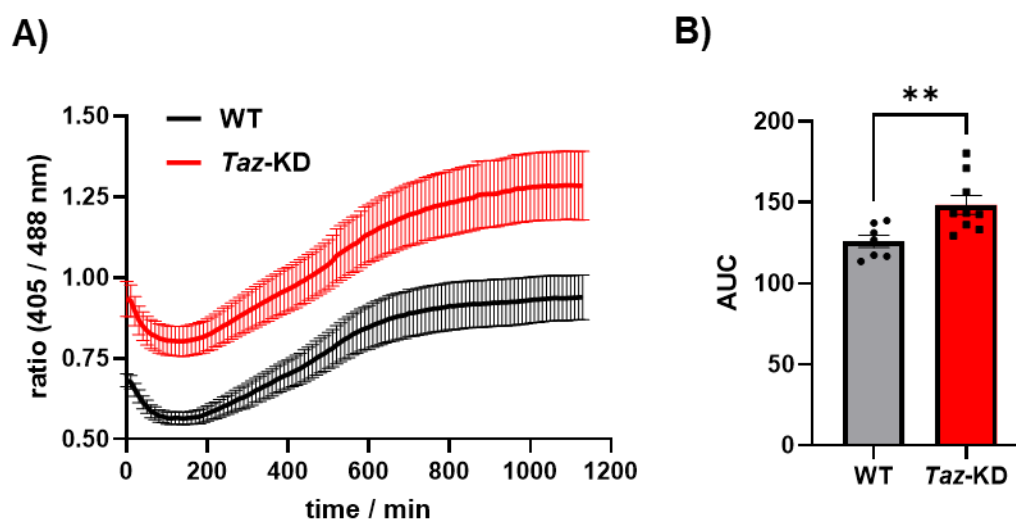


Figure 4.22: Increased basal H_2O_2 levels but similar kinetics in *Taz*-KD pancreatic islets

(A) H_2O_2 kinetics of 20 wo WT and *Taz*-KD pancreatic islets measured with a plate reader in standard pancreatic islet culturing conditions (RPMI 1640 medium, 5% CO_2 and 37 °C). The excitation ratio of mito-roGFP2-Orp1 represents the redox state. Increase in ratio (405 / 488 nm) is proportional to a rise in the H_2O_2 levels. (B) Quantification of the AUC of the H_2O_2 kinetics over 19 h. n (WT) = 7, n (*Taz*-KD) = 9, both from 5 animals. Data = mean \pm SEM; n = number of experiments; statistical analysis: unpaired t test: ** p < 0.01. Abbreviations: weeks of age (wo), *tafazzin*-knockdown (*Taz*-KD), wildtype (WT), area under the curve (AUC).

To pinpoint the sources of mitochondrial H_2O_2 in *Taz*-KD pancreatic islets, NADPH oxidase (NOX) inhibitors were tested. NOX enzymes are prominent $\text{O}_2^{\cdot -}$ and H_2O_2 sources and are highly expressed in pancreatic islets (introduced in **Chapter 1.2.3**).³⁸⁷ Specific inhibition of NOX4 with GLX351322 (GLX) led to a decrease in *Taz*-KD but not WT redox state (**Figure**

4.23). Throughout the experiment, the oxidation state of *Taz*-KD pancreatic islets treated with GLX recovered to WT levels. After 9 h, the H_2O_2 levels of *Taz*-KD were indistinguishable from the WT control (**Figure 4.23 A**). Interestingly, treatment with the NOX2 inhibitor, GSK2795039 (GSK), did not result in a reduction of the *Taz*-KD redox state, which suggests that the NOX2-mediated H_2O_2 production of WT and *Taz*-KD pancreatic islets was similar under the tested conditions (supplements, **Figure 7.14**).

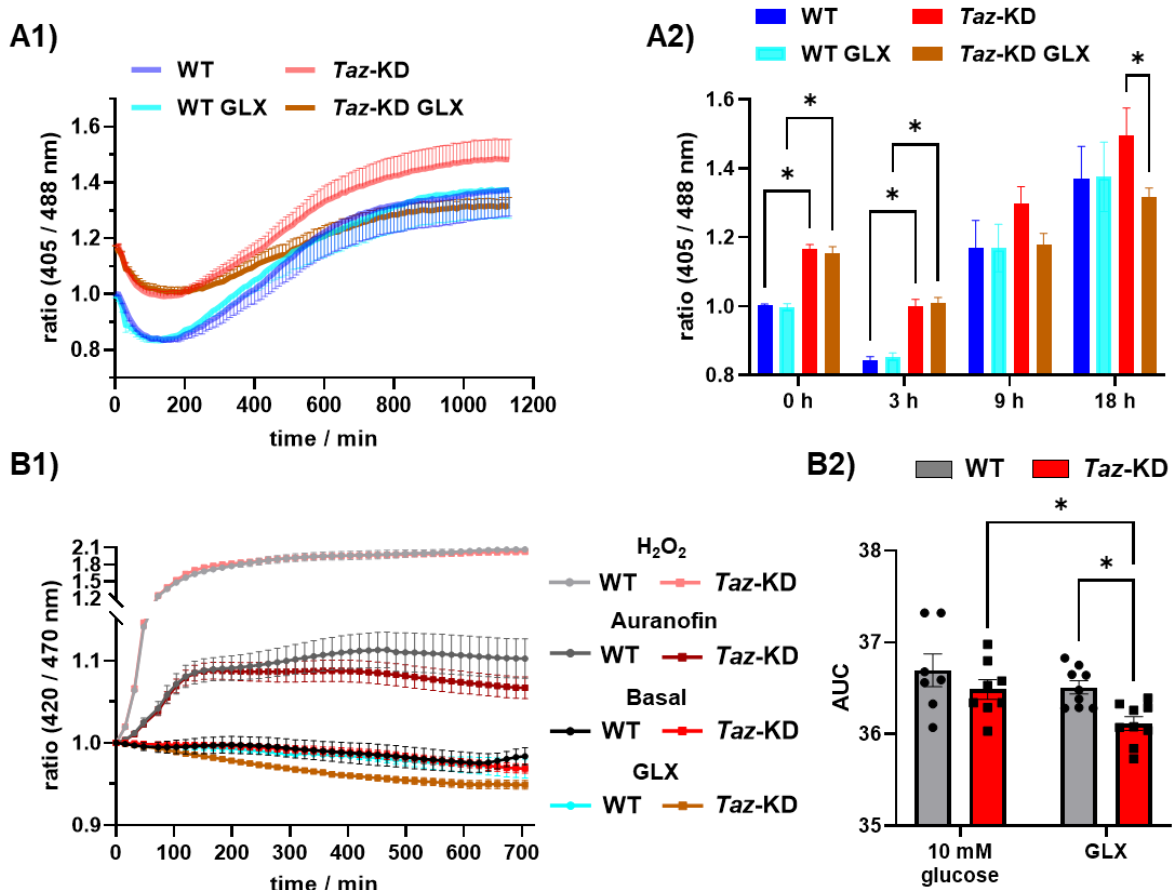


Figure 4.23: GLX decreased the redox state of *Taz*-KD pancreatic islets

(A) (A1) H_2O_2 kinetics of 20 wo WT and *Taz*-KD pancreatic islets measured with a plate reader in presence or absence of the NOX4 inhibitor, GLX. (A2) Quantification of ratio values at certain time points (0, 3, 9 and 18 h). N = 5. **(B)** (B1) H_2O_2 kinetics of 20 wo WT and *Taz*-KD pancreatic islets measured with a CD7 automated imaging system and normalised to baseline. After baseline measurement, 100 μM H_2O_2 , 1 μM auranofin, 10 μM GLX or a water control (with 0.01% DMSO) were added to the respective wells. (B2) Quantification of AUC of the H_2O_2 kinetics in presence or absence of GLX. N = 5. Data = mean \pm SEM; N = number of animals; statistical analysis: two-way ANOVA: * $p < 0.05$. Abbreviations: weeks of age (wo), *tafazzin*-knockdown (*Taz*-KD), wildtype (WT), GLX351322 (GLX).

To measure the redox state with a higher resolution and to avoid the oxidative stress that occurs in the plate reader experiments, the CD7, which is an automated live-cell imaging

system, was used to confirm and expand the results from the plate reader. During 12 h imaging, the redox state normalised to the baseline of WT and *Taz*-KD pancreatic islets remained stable. The addition of the exogenous stressors 1 μ M auranofin or 100 μ M H₂O₂ resulted in oxidation of the roGFP2-Orp1 sensor, which was similar for both genotypes. H₂O₂ enters the pancreatic islet cells via aquaporins and either directly oxidises the mito-roGFP2-Orp1 sensor or via secondary mitochondrial ROS activation. Auranofin is a cytosolic and mitochondrial TrxR inhibitor, hence causing H₂O₂ concentration to increase due to diminished degradation processes. In line with the previous plate reader observation, GLX caused a reduction of solely the *Taz*-KD redox state, which was significant when AUC was calculated (**Figure 4.23 B**).

In summary, in comparison to WT controls, *Taz*-KD pancreatic islets displayed increased basal H₂O₂ levels but unchanged H₂O₂ kinetics in stressed conditions. Inhibition of NOX4 resulted in diminished H₂O₂ levels of *Taz*-KD pancreatic islets, suggesting an involvement of NOX4 in the *Taz*-KD phenotype.

4.5.2 Redox histology

The critical role of ROS in BTHS disease progression is introduced in **Chapter 1.2.3**. Additionally, the previous Chapter revealed an *ex vivo* phenotype of increased basal ROS that could be reduced with the NOX4 inhibitor GLX. However, the redox state under *ex vivo* conditions might not fully reflect the *in vivo* situation. Therefore, the redox histology technique was applied to measure the *in vivo* redox status of WT and *Taz*-KD heart and pancreatic islets. Most methods rely on organ isolation, culturing and experimental setup before the redox measurement can be performed. These steps, although necessary, can impact the cellular redox status. Therefore, the main advantage of the redox histology technique is that the *in vivo* status is fixed by perfusing the cardio-vascular system with NEM before organ isolation (method description in **Chapter 3.9.2**).¹¹⁸

Redox histology of pancreas tissue

Pancreas cryo-slices of 20 and 50 wo WT and *Taz*-KD MiOxTaz mice were investigated using redox histology (**Figure 4.24**). The pancreatic islets inside the pancreas slices were identified by an insulin staining (method described in **Chapter 3.9.2**). Unlike the *ex vivo* experiments, *Taz*-KD pancreatic islets exhibited a reduced redox state compared to WT controls. The *Taz*-KD pancreatic islets from 20 and 50 wo mice displayed redox values similar to the DTT treated control (mean of around 10% lower ratio values than WT). The discrepancy between

in vivo and *ex vivo* results is consistent to the contradictory findings from the literature in cell lines and animal models and further discussed in **Chapter 5.4**.²⁷⁹

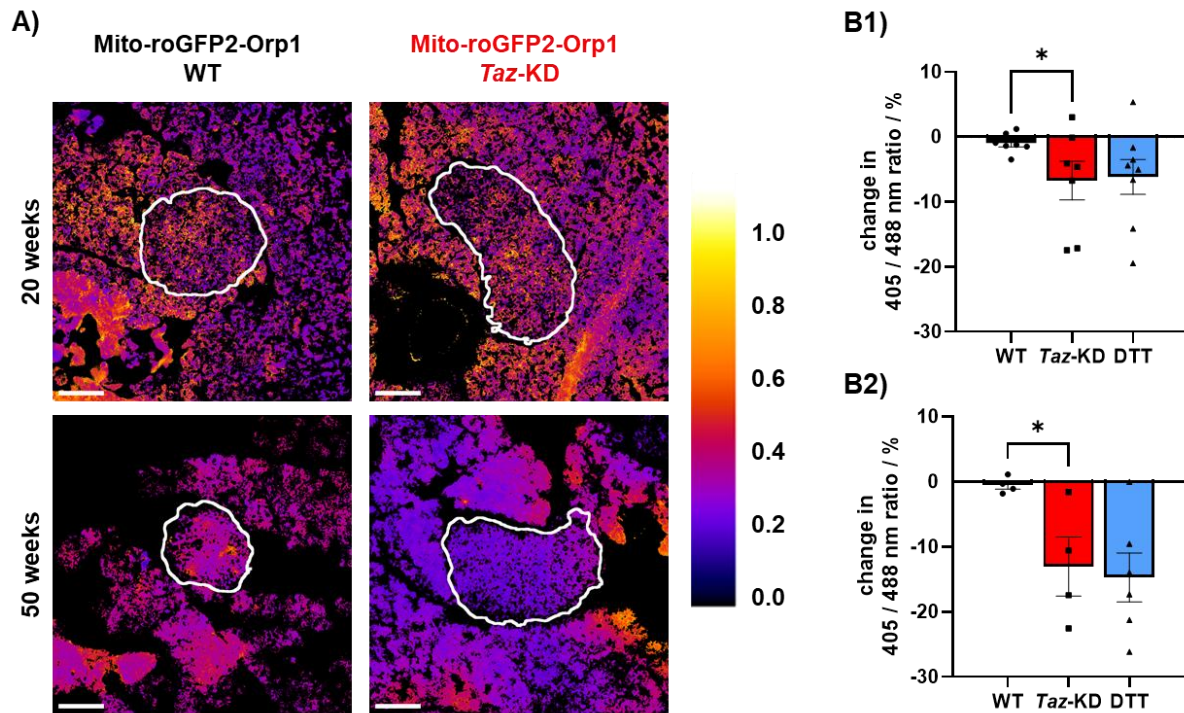


Figure 4.24: Reduced *in vivo* redox state of *Taz*-KD pancreatic islets using redox histology

(A) Representative images of pancreas slices from 20 and 50 wo WT and *Taz*-KD mice displayed in ImageJ “fire mode”. A ratio calibration bar (405 nm / 488 nm) represents the redox state of the tissue. Calibration bar (redox state): 0 (maximal reduction) – 1 (maximal oxidation). The analysed pancreatic islets are marked in white. Scale bar: 100 µm. (B) Quantification of the change in redox state of 20 (B1) and 50 (B2) wo WT and *Taz*-KD pancreatic islets. DTT was used as a reductive control (blue). N (WT, 20 wo) = 7, N (*Taz*-KD, 20 wo) = 7, N (DTT, 20 wo) = 8, N (WT, 50 wo) = 4, N (*Taz*-KD, 50 wo) = 4, N (DTT, 50 wo) = 6. Data = mean ± SEM; N = number of animals; statistical analysis: unpaired *t* test: **p* < 0.05. Abbreviations: weeks of age (wo), *tafazzin*-knockdown (*Taz*-KD), wildtype (WT).

Redox histology of heart tissue

To expand the redox analysis beyond pancreas tissue, redox changes in the heart, the most studied tissue in BTHS models, were investigated. Therefore, heart slices of 20 and 50 wo WT and *Taz*-KD MiOxTaz mice were investigated using redox histology (**Figure 4.25**). Hearts of 20 wo and 50 wo *Taz*-KD displayed a trend towards an around 10% decreased redox state, but unlike in the pancreatic islets, the results were not statistically significant. This data was published in Bertero *et al.*, 2021, *Circulation*.³⁵

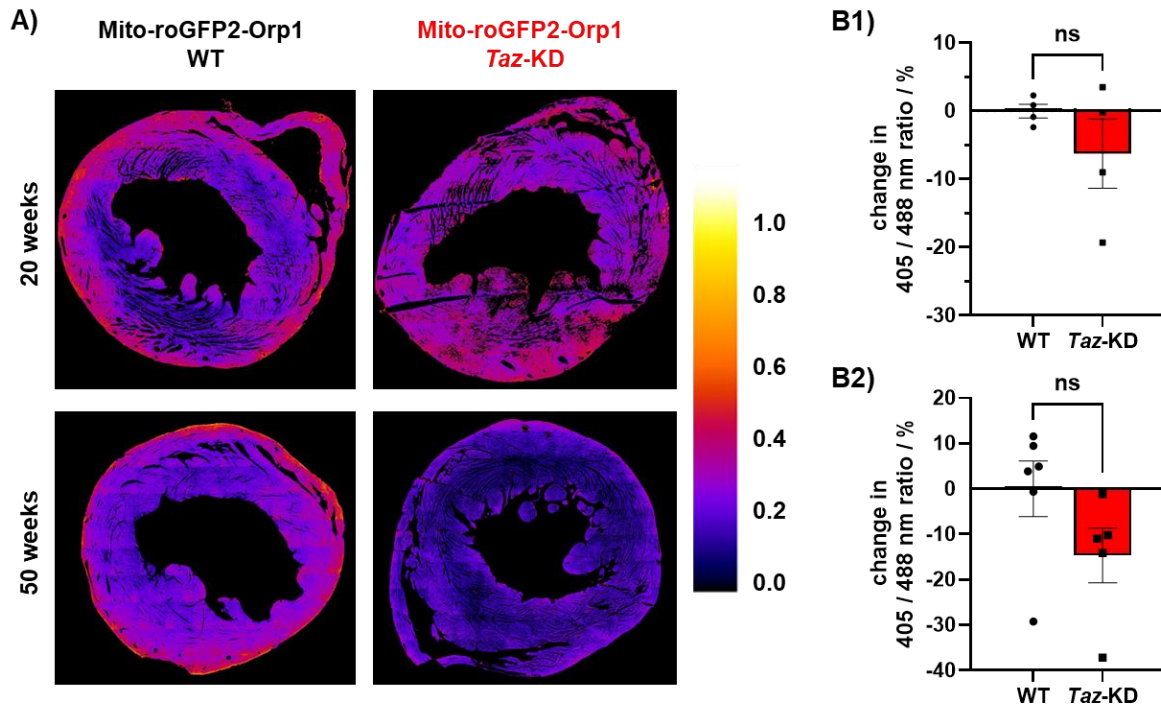


Figure 4.25 Unchanged *in vivo* redox state of *Taz*-KD hearts using redox histology

(A) Representative images of heart slices from 20 and 50 wo WT and *Taz*-KD mice displayed in ImageJ “fire mode”. A ratio calibration bar (405 nm / 488 nm) represents the redox state of the tissue. Calibration bar (redox state): 0 (maximal reduction) – 1 (maximal oxidation). **(B)** Quantification of the change in redox state of 20 (B1) and 50 (B2) wo WT and *Taz*-KD hearts. N (20 wo) = 4, N (WT, 50 wo) = 6, N (*Taz*-KD, 50 wo) = 5. Data = mean ± SEM; N = number of animals; statistical analysis: unpaired *t* test: ns: $p > 0.05$. Abbreviations: weeks of age (wo), *tafazzin*-knockdown (*Taz*-KD), wildtype (WT).

Overall, the *in vivo* redox state measured by redox histology revealed reduced H_2O_2 levels in 20 and 50 wo *Taz*-KD hearts and pancreatic islets compared to WT controls.

4.5.3 Western blot analysis of relevant redox proteins

Biochemical analyses of protein and RNA levels can supplement functional experiments to understand underlying pathways. WB analysis is a semi-quantitative technique to measure protein levels in health and disease. Therefore, several critical proteins that are involved in the cellular redox homeostasis were investigated with WB to check their involvement in the prior described redox phenotype of *Taz*-KD pancreatic islets (**Figure 4.26**). The WB analysis was performed in a paired manner and the variation among the samples is displayed in the supplements. (supplements, **Figure 7.15**). Analysis of the antioxidant enzymes, Prx3, catalase and GPX4 revealed alterations in antioxidative pathways of *Taz*-KD compared to WT pancreatic islets (**Figure 4.26 A**). An increase in mitochondrial peroxiredoxin 3 (Prx3) was observed while catalase showed a reduction in *Taz*-KD. GPX4 protein levels were highly variable, and no clear tendency was visible. WB analysis of NOX4 displayed a trend to higher protein levels in *Taz*-KD but no statistical difference was observed (**Figure 4.26 B**). The stress response protein Nrf2 was unchanged among the genotypes. SOD proteins have a double role in redox processes, as they catalyse the reaction from one highly reactive ROS molecule to another less reactive ROS player (antioxidative and ROS production role). The levels of the mitochondrial localised SOD2 protein were slightly decreased but the N-number was low (N = 2) which limits the statistical power.

Overall, changes in protein levels of some key redox proteins such as catalase and Prx3 suggested an altered redox balance in *Taz*-KD pancreatic islets.

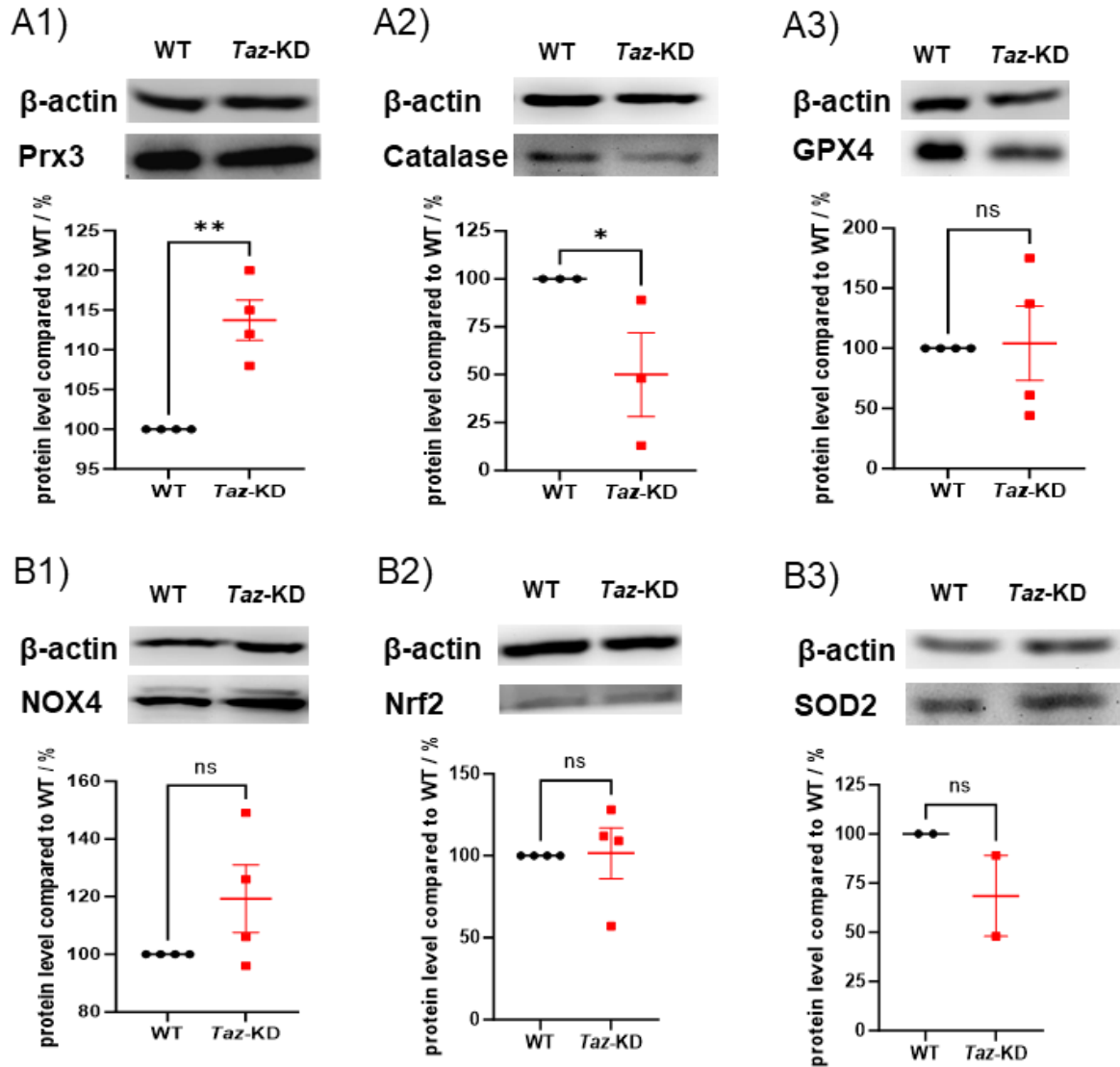


Figure 4.26: Altered redox protein levels of *Taz*-KD pancreatic islets using WB analysis

(A) WB analysis of the antioxidative enzymes: Prx3 at 27 kDa (A1), catalase at 60 kDa (A2) and GPX4 at 22 kDa (A3). Normalised to β-actin at 42 kDa. (B) WB analysis of the ROS production and stress response proteins: NOX4 at 67 kDa (B1), Nrf2 at 110 kDa (B2) and SOD2 at 25 kDa (B3). Normalised to β-actin at 42 kDa. Data = mean ± SEM; N = number of animals; statistical analysis: paired *t* test: **p* < 0.05, ***p* < 0.01, ns: *p* > 0.05. Abbreviations: weeks of age (wo), *tafazzin*-knockdown (*Taz*-KD), wildtype (WT), western blot (WB), reactive oxygen species (ROS).

4.6 Analysis of mitochondrial morphology in *Taz*-KD islets

The ultrastructure of mitochondria can vary considerably depending on the cell's physiological state and is naturally connected to its function.⁴³¹ BTBS samples often show alterations in the mitochondrial structure that have been associated with impaired

mitochondrial function.³⁴ Confocal and STED microscopy were used to investigate the mitochondrial morphology of pancreatic islets. A detailed description of the applied methods can be found in **Chapter 3.10**.

4.6.1 Confocal and STED imaging

The mitochondrial network inside pancreatic islet cells was examined using the mitochondrial matrix marker Mitotracker and the mitochondrial redox-sensor mito-roGFP2-Orp1 (expressed globally in mitochondria of MiOxTaz mice). To increase resolution, confocal imaging using the CD7 confocal mode (description in **Chapter 3.10.2**) was applied instead of wide-field imaging with an epifluorescence microscope in the previous sections. Before imaging, the dispersed pancreatic islet cells isolated from MiOxTaz mice were stained with Mitotracker DeepRed and Hoechst 33342. To establish the method, two representative pancreatic islet cells that were imaged in live mode are shown in **Figure 4.27**. The Hoechst staining revealed the nucleus, while the GFP and Mitotracker staining visualised the mitochondria. However, the GFP and Mitotracker staining did not overlap perfectly. This could be due to several reasons. The imaged cells were alive and moving, and the mitochondrial network might have moved between the different confocal images of each wavelength. Additionally, the confocal alignment for each wavelength might have been suboptimal.

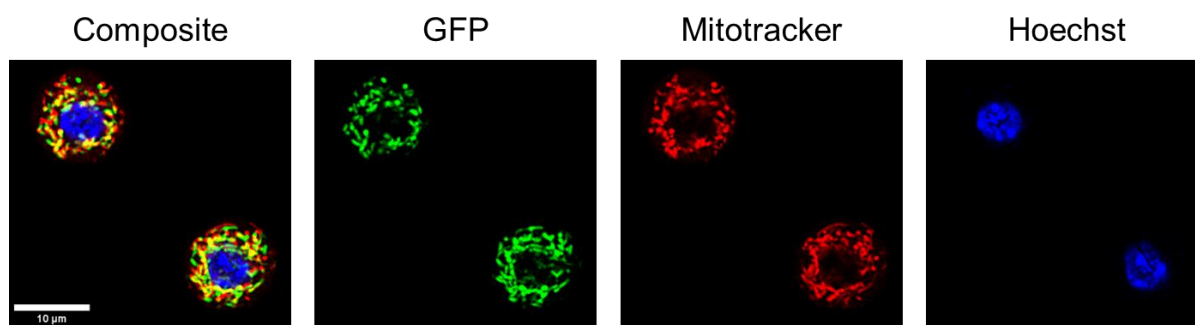


Figure 4.27: Confocal live imaging of two dispersed pancreatic islet cells

The GFP fluorescence originates from the genetically-encoded mito-roGFP2-Orp1 protein. Mitotracker and Hoechst stainings were performed just before live imaging. The GFP and Mitotracker fluorescence visualise the mitochondrial matrix, and the Hoechst dye is localised inside the nucleus. The images are false-coloured according to the emission peak of the dye/chromophore. The composite image shows the combination of the GFP, Mitotracker and Hoechst images. The images were acquired using the CD7 confocal mode with a 50x objective. Scale bar: 10 µm.

Once a mitochondrial imaging protocol using confocal Laser microscopy was established, the mitochondrial volume of 20 wo WT and *Taz*-KD pancreatic islet cells was investigated (**Figure 4.28**). *Taz*-KD dispersed pancreatic islet cells had a significantly higher Mitotracker intensity, normalised to the number of Hoechst nuclei, and compared to the WT cells. In addition to an increased Mitotracker intensity, the roGFP signal showed a tendency (not significant) towards higher levels in the *Taz*-KD pancreatic islet cells. The citrate synthase activity assay normalised to protein content also confirmed the finding of increased mitochondrial volume in *Taz*-KD pancreatic islet cells.

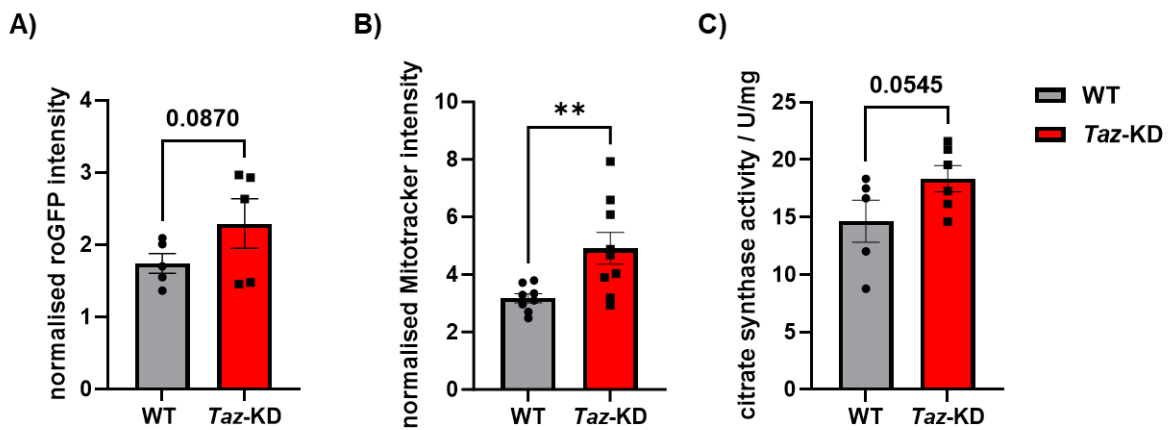


Figure 4.28: Increased mitochondrial volume in *Taz*-KD pancreatic islets

(A) Emission intensity of roGFP from dispersed pancreatic islet cells after excitation at 480 nm. Normalised to Hoechst signal intensity. N = 5. (B) Emission intensity of Mitotracker DeepRed from dispersed pancreatic islet cells after excitation at 480 nm. Normalised to Hoechst signal intensity. N (WT) = 8, N (*Taz*-KD) = 9. (C) Citrate synthase activity assay normalised to total protein content. N (WT) = 5, N (*Taz*-KD) = 6. Data = mean \pm SEM; N = number of animals; statistical analysis: unpaired *t* test: ***p* < 0.01. Abbreviations: weeks of age (wo), *tafazzin*-knockdown (*Taz*-KD), wildtype (WT).

An inverted four-colour STED QuadScan microscope was used to study the mitochondrial network morphology of dispersed pancreatic islet cells in greater detail. After live cell imaging, a 3D morphology analysis of the mitochondrial network was performed on image stacks that were pre-processed with the ImageJ software and rendered with Imaris. The method **Chapter 3.10.2** describes the detailed steps and used parameters. First, the STED imaging was compared to standard confocal imaging. Therefore, pancreatic islet cells dispersed and isolated from sh*Taz* mice were stained with Mitotracker as the genetically-encoded mitochondrial roGFP sensor of the MiOx*Taz* model was overly sensitive to photobleaching. A representative comparison of imaging in STED and confocal mode is presented in **Figure 4.29**. STED imaging resolves the structures with more detail and sharpness. Despite the improvement in resolution with increased sharpness, only parts of the cells or not the full Z-

stack were imaged in STED-mode due to dramatically increased photobleaching and observed changes in mitochondrial morphology after several Z-stacks of imaging in STED mode. Those acquired STED images were used to calculate a correction term for the mitochondrial volume and number. The STED effect's resolution improvement was quantified compared to the standard confocal imaging (**Figure 4.29**). STED mode led to a significantly decreased overall mitochondrial volume by $38.75 \pm 3.86\%$ and an increased mitochondrial number by $30.69 \pm 11.24\%$.

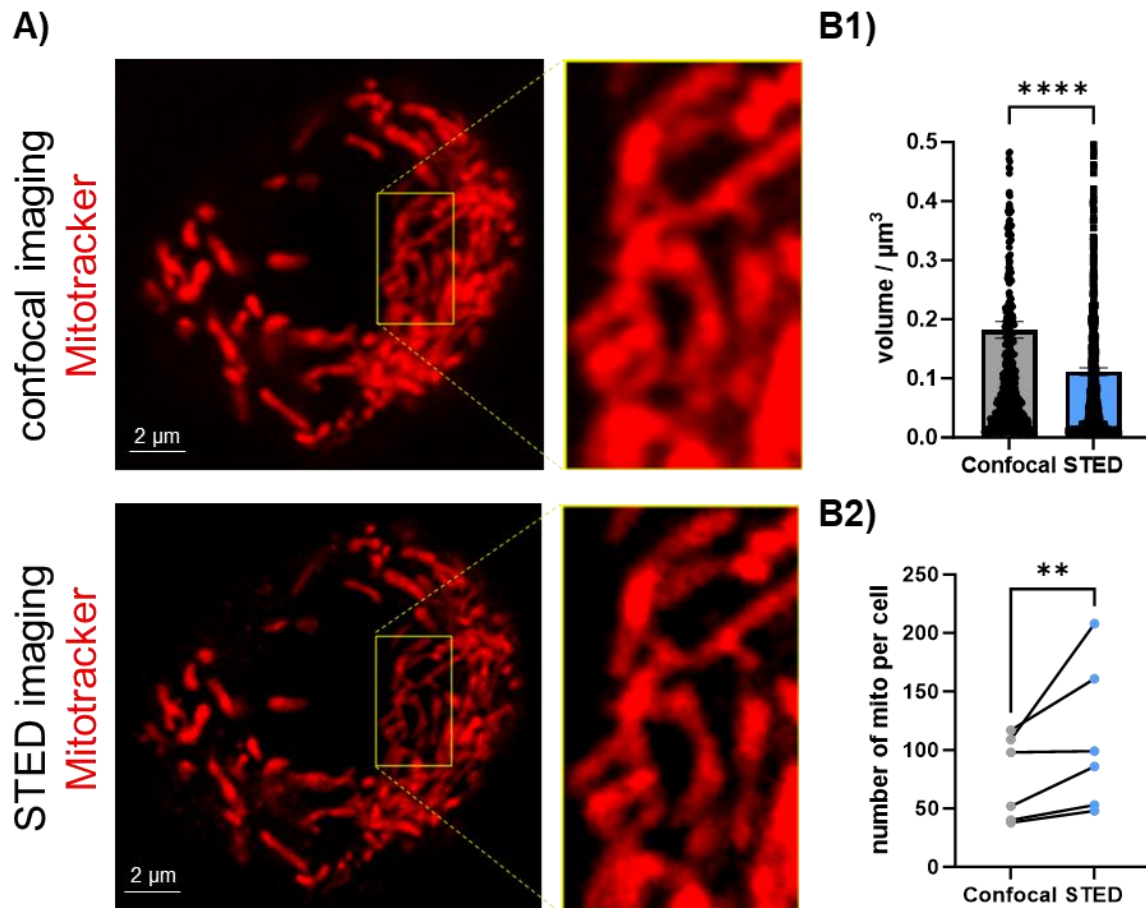


Figure 4.29: Comparison of STED and confocal imaging of pancreatic islet cells

(A) Representative images of a mitochondrial network from a pancreatic islet cell measured in STED and confocal mode. STED mode imaging resolves the structures with greater detail. Scale bar: 2 μm . (B) STED effect leads to a decrease in the observed mitochondrial volume (B1) (displayed comparison per mitochondria) and increased mitochondrial number (B2) (displayed comparison per animal) compared to standard confocal imaging. N = 6. Data = mean \pm SEM; N = number of animals; statistical analysis: unpaired *t* test: ***p* < 0.01, *****p* < 0.0001. Abbreviations: weeks of age (wo), *tafazzin*-knockdown (*Taz*-KD), wildtype (WT), stimulated emission depletion (STED), mitochondria (mito).

Subsequently, confocal and STED microscopy were used to investigate the mitochondrial network of pancreatic islet cells from 20 wt WT and *Taz*-KD shTaz mice. Striking morphological differences in the overall mitochondrial network and the single mitochondria of *Taz*-KD compared to WT pancreatic islet cells were observed (**Figure 4.30**). The mitochondrial network was elongated and superfused in *Taz*-KD samples, highlighted by the representative 3D-rendered Imaris image in **Figure 4.30 A**. Next, the single mitochondria were grouped based on their surface area into three classes: Class A = 0.3 - 3 μm^2 , Class B = 3 - 10 μm^2 , and Class C > 10 μm^2 .

The *Taz*-KD samples displayed an increased number of Class C mitochondria and a decreased number of Class A mitochondria, when compared to WT controls (**Figure 4.30 B**). As the number of Class A mitochondria is much higher than Class C mitochondria regardless of the genotype, an overall reduced total number of mitochondria in *Taz*-KD pancreatic islet cells was observed. A nearest neighbor analysis was also performed to measure mitochondrial density in both genotypes. In line with the increased number of mitochondria, nearby mitochondria were observed at a higher frequency in WT samples. The analysis of single mitochondria revealed an enhanced volume and surface area of *Taz*-KD mitochondria (**Figure 4.30 C**). Additionally, the shape of the single *Taz*-KD mitochondria was more elongated and showed a decreased sphericity compared to WT (**Figure 4.30 C**). A bounding box analysis confirmed the larger size of the *Taz*-KD mitochondria, and showed that the increase was not directed, but instead similar on each axis in 3D dimensions (X, Y and Z) (supplements, **Figure 7.16**). Therefore, the mitochondrial network of *Taz*-KD pancreatic islet cells can be characterised by a decrease in total mitochondrial number due to superfused and elongated single mitochondria leading to an increase in mitochondrial volume compared to WT control cells.

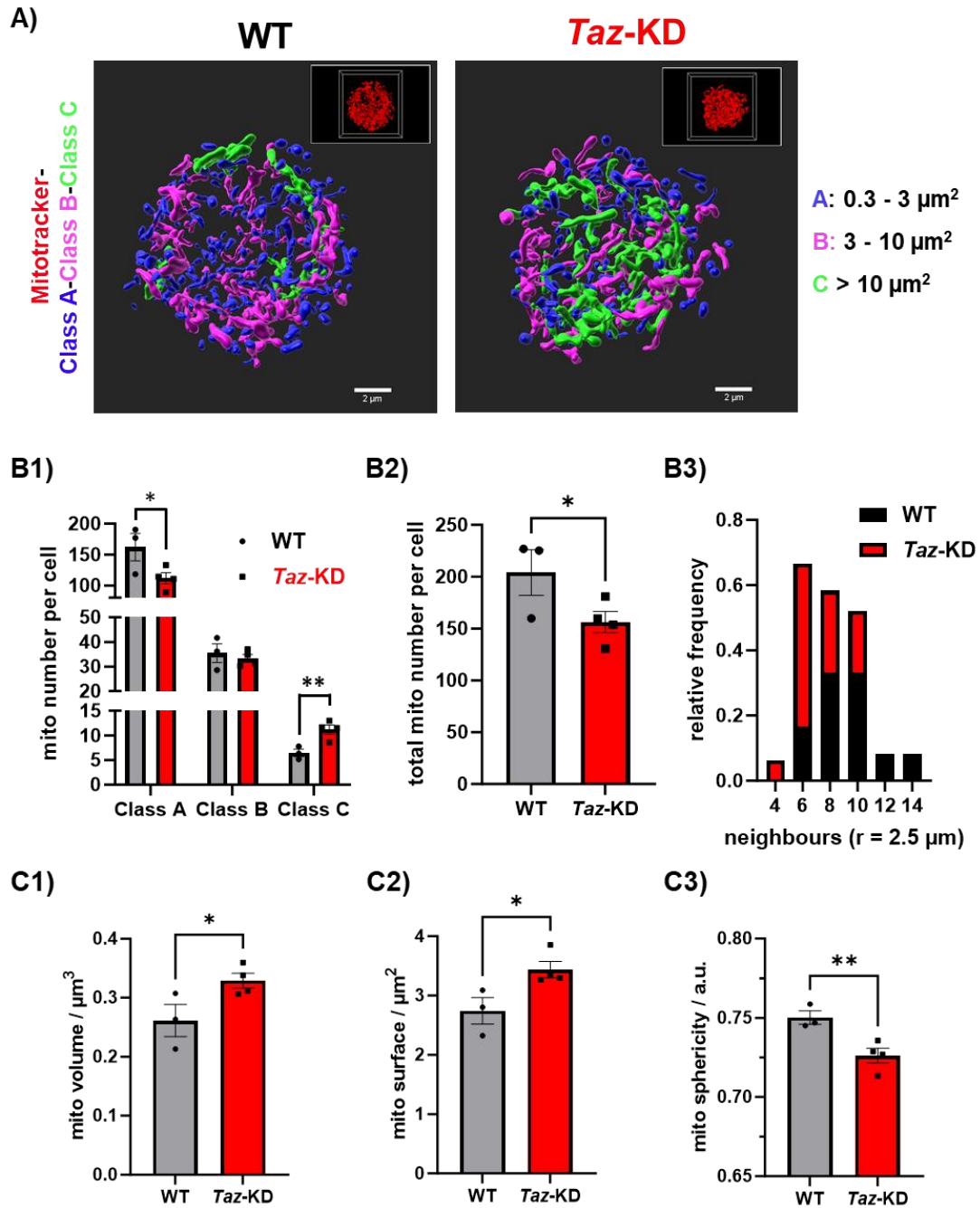


Figure 4.30: More giant and less smaller mitochondria in *Taz*-KD pancreatic islet cells

(A) Representative images of WT and *Taz*-KD mitochondrial network from a pancreatic islet cell. Mitotracker intensity distribution (top right corner) was rendered using Imaris software. Mitochondrial structures were classified according to their surface area: Class A = 0.3 - 3 μm^2 (blue), Class B = 3 - 10 μm^2 (magenta) and Class C > 10 μm^2 (green). Scale bar: 2 μm . (B) Analysis of the mitochondrial network from shTaz pancreatic islet cells: (B1) Mitochondrial number separated by surface classes, (B2) total mitochondrial number, (B3) nearest neighbour analysis for mitochondrial structures in a radius of 2.5 μm . N (WT) = 3, N (*Taz*-KD) = 4. (C) Quantitative analysis of single mitochondria from shTaz pancreatic islet cells: (C1) Mitochondria volume, (C2) surface area (C3) sphericity. N (WT) = 3, N (*Taz*-KD) = 4. Data = mean \pm SEM; N = number of animals; statistical analysis: unpaired *t* test: **p* < 0.05, ***p* < 0.01. Abbreviations: weeks of age (wo), *tafazzin*-knockdown (*Taz*-KD), wildtype (WT), mitochondria (mito).

In summary, standard confocal and STED imaging revealed an increased mitochondrial volume and a rise in single mitochondrion dimensions (surface area and volume) in *Taz*-KD compared to WT pancreatic islet cells.

4.6.2 Western blot analysis of relevant morphology and autophagy proteins

Autophagy plays a central role in intracellular quality control through the degradation and recycling of unnecessary components and damaged organelles. BTHS has been previously linked to defective autophagy, altered mitophagy and impaired quality control.^{77,427} The prior described superfused mitochondrial phenotype with increased mitochondrial volume (**Chapter 4.6.1**) suggests an undelaying impairment in autophagy of *Taz*-KD pancreatic islets. Therefore, autophagy- and morphology-related proteins were investigated to check their involvement in the mitochondrial morphology phenotype of *Taz*-KD pancreatic islets (**Figure 4.31**). Lysosomal-associated membrane protein 1 (LAMP1) levels were upregulated in *Taz*-KD pancreatic islets, whereas the protein levels of LAMP2 were decreased compared to WT controls (**Figure 4.31 A**). The protein levels of autophagy related 7 (Atg7) and the mitophagy-specific PINK1 and Parkin (Prk8) trended towards reduced concentrations in *Taz*-KD pancreatic islets (**Figure 4.31 B**).

Figure 4.31 C shows a representative WB and the linked quantification of LC3B. Although the molecular mass of LC3-2 is higher than that of LC3-1 due to the addition of PE, LC3-2 migrates faster in a WB gel due to its high hydrophobicity. Decreased levels of LC3B-1 and LC3B-2 were observed in *Taz*-KD pancreatic islets. Surprisingly, protein levels of MCUa tended to be increased in *Taz*-KD pancreatic islets which might be connected to the higher mitochondrial volume (described in **Chapter 4.6.1**). This contrasts with previous observations where downregulation of MCU in *Taz*-KD heart tissue was described as one of the key mechanistic changes in BTHS phenotype.¹²⁸ However, the decrease in MCU was found to be highly tissue-specific and less or not at all present in skeletal muscle and brain tissue.⁶¹

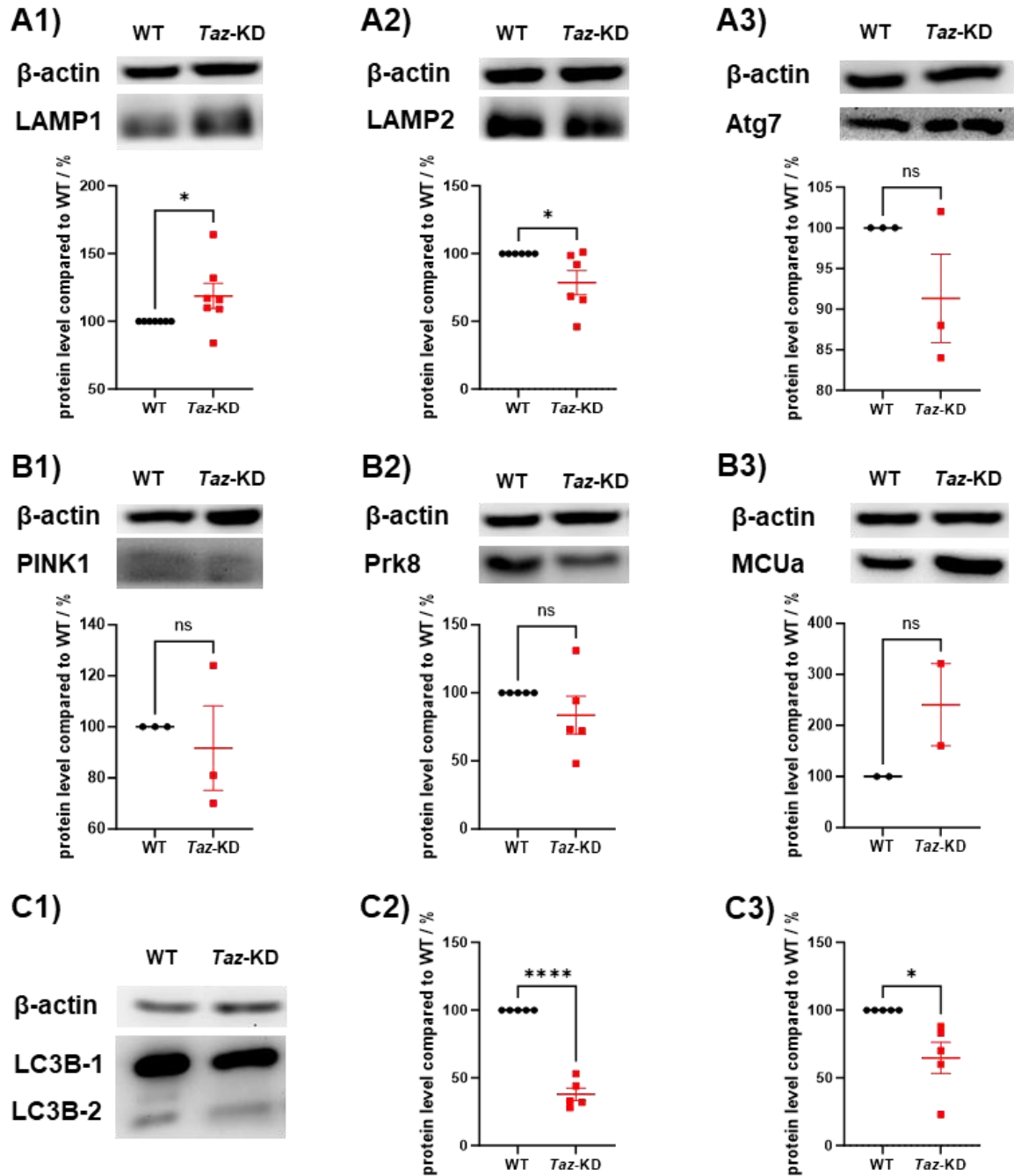


Figure 4.31: WB analysis of morphology- and autophagy-related proteins in *Taz*-KD pancreatic islets

(A) WB analysis of the autophagy proteins: LAMP1 at 120 kDa (A1), LAMP2 at 110 kDa (A2) and Atg7 at 78 kDa (A3). Normalised to β-actin at 42 kDa. (B) WB analysis of PINK1 at 38 kDa (B1), Prk8 at 55 kDa (B2) and MCUa at 30 kDa (B3). Normalised to β-actin at 42 kDa. (C) (C1) Representative LC3B WB gel. WB analysis of LC3B-1 at 16 kDa (C2) and LC3B-2 at 14 kDa (C3). Normalised to β-actin at 42 kDa. N (LAMP1) = 7, N (LAMP2) = 6, N (Atg7) = 3, N (PINK1) = 3, N (Prk8) = 5. N (MCU) = 2, N (LC3B-1/2) = 5. Data = mean ± SEM; N = number of animals; statistical analysis with unpaired *t* test: **p* < 0.05, ***p* < 0.01, ****p* < 0.001, *****p* < 0.0001. Abbreviations: weeks of age (wo), *tafazzin*-knockdown (*Taz*-KD), wildtype (WT), western blot (WB).

Taken together, significant alterations in LAMP1, LAMP2 and LC3B suggest defective autophagy in *Taz*-KD pancreatic islets. Tendencies in Atg7, PINK1 and Prk8 strengthen the assumption of decreased autophagy/mitophagy activity and insufficient mitochondrial quality control in *Taz*-KD pancreatic islets.

4.7 Omics analysis of *Taz*-KD islets

Omics approaches systemically analyse all parts from the respective branch and aim to collectively characterise molecules contributing to the investigated sample's structure, function, and dynamics. They massively contribute to finding mechanisms that underlay pathological alterations.²¹⁰ In this study, lipidomics and bulk mRNA sequencing were performed to study differences in WT and *Taz*-KD pancreatic islets.

4.7.1 Lipidomics

A lipidome analysis of 20 wt WT and *Taz*-KD pancreatic islets was performed in collaboration with the company Lipotype (method **Chapter 3.11**). The effect of *Taz*-KD on the complete lipid profile in pancreatic islet samples was investigated. The resulting CL profile has already been described in the **Chapter 4.1**. In the following paragraphs, the other lipid classes were examined with the focus on some key lipid alterations that occur in *Taz*-KD pancreatic islets.

In **Figure 4.32** the whole lipid class composition (excluding CL) of 20 wt *Taz*-KD and WT pancreatic islets normalised to total lipid content was analysed. *Taz*-KD samples exhibited a downregulation of phosphatidylcholines (PC) and ether-linked lyso-phosphatidylcholines (LPC O-) and an upregulation of lyso-phosphatidyl-glycerols (LPG), phosphatidylethanolamine (PE) and phosphatidylglycerols (PG), when compared to controls.

PG are crucially involved in the biosynthesis of various lipids, especially CL.³³⁸ Like CL, it is a negatively charged phospholipid that is highly specific to the mitochondria. The group of Peter G. Barth observed in BTHS patient samples, that both PG and CL contained decreased levels of linoleic acid (C18:2), which is the dominant acyl chain in mature mammalian CL (forming e.g. CL 72:8).³⁹² Interestingly, the lipid class LPG which is a precursor for PG was also significantly enhanced in *Taz*-KD pancreatic islets, indirectly supporting the hypothesis of increased precursors forms of CL in BTHS. Therefore although, MLCL could not be

measured based on limited sensitivity, upregulations of other CL precursor forms were detected.

The reduction of the amount of the lysoplasmalogen LPC O- in *Taz*-KD pancreatic islets (**Figure 4.32**) was found together with a striking change in acyl chain length and saturation of LPC O- (supplements, **Figure 7.21**). The *Taz*-KD samples of LPC O- had more C16 fatty acid species than WT and none was saturated. The cellular concentrations of lysoplasmalogens, which are precursors to PC O-, are kept relatively low as they can be toxic.⁵¹ Upon enhancement of the plasmalogen biosynthesis, lysoplasmalogens were found in lymphoblasts derived from BTHS patients.⁵⁰ However, the exact biological function of LPC O- remains unknown.

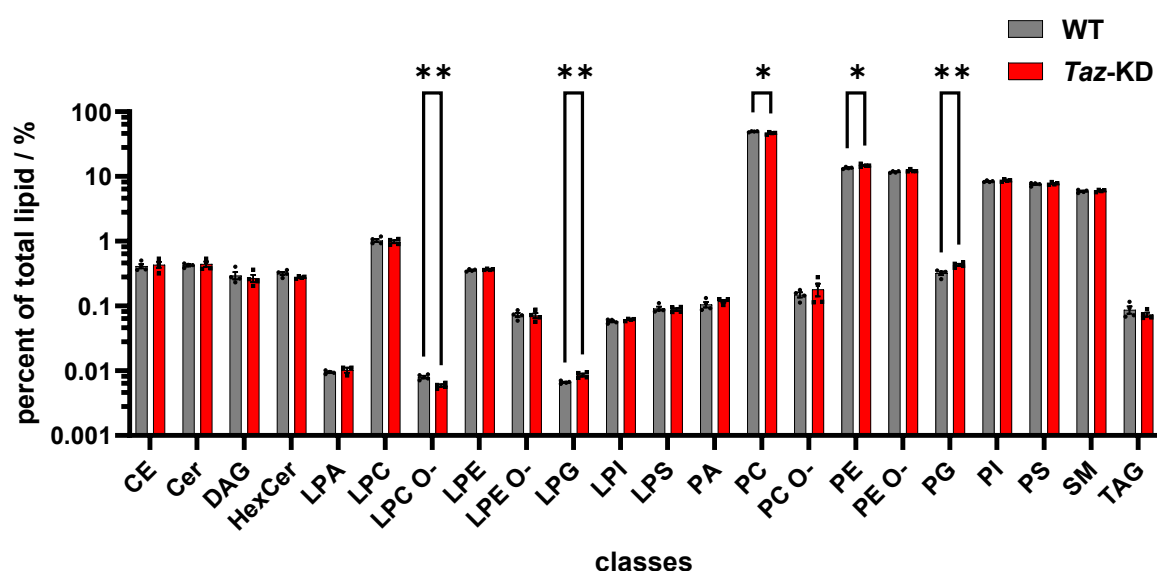


Figure 4.32: Altered lipid class composition in *Taz*-KD pancreatic islets

Lipid class profile of 20 wo WT and *Taz*-KD pancreatic islets. Normalised to percent of total lipid amount and displayed in logarithmic scale. N = 4, Data = mean \pm SEM; Data = mean \pm SEM; statistical analysis: unpaired two-tailed *t* test: **p* < 0.05, ***p* < 0.01. Abbreviations: weeks of age (wo), *tafazzin*-knockdown (*Taz*-KD), wildtype (WT). The abbreviations for each lipid class can be found in the general list of abbreviations.

In addition to the lipid class profile, the single lipid species of all lipid classes were examined (**Figure 4.33**). In **Figure 4.33 A**, the single lipid species are plotted in a volcano diagram based on their fold change and *p* value when *Taz*-KD and WT samples were compared. Although only 10 lipid species were significantly down- and 31 upregulated in *Taz*-KD, several lipid species of the same lipid class cluster on one side of the diagram. The clustering reflects the up- or downregulation of the respective lipid class (**Figure 4.33 B**). All significantly altered

lipid species of *Taz*-KD compared to WT pancreatic islets were displayed in a heatmap in the supplements (supplements, **Figure 7.22**).

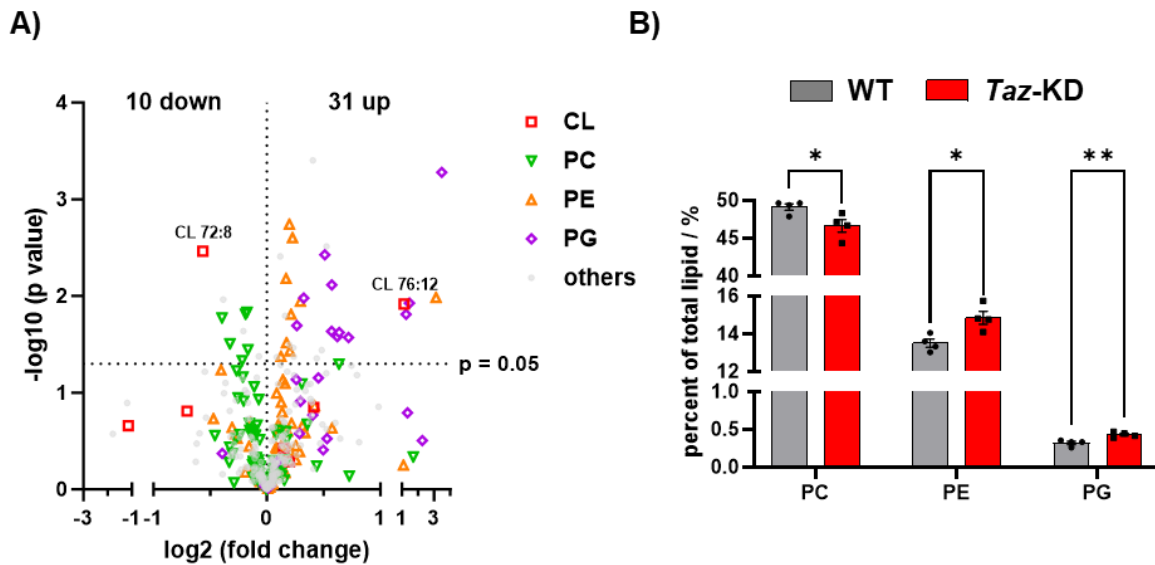


Figure 4.33: Altered lipid species in *Taz*-KD pancreatic islets

(A) Volcano plot of all lipid species of 20 wo WT and *Taz*-KD pancreatic islets normalised to total lipid amount. Statistical analysis showed that 10 lipid species are significantly ($p < 0.05$) down- and 31 are upregulated in *Taz*-KD. The lipid classes CL, PC, PE, and PG are highlighted. **(B)** Alterations in the phospholipids PC, PE and PG of *Taz*-KD compared to WT pancreatic islets normalised to total lipid amount. $N = 4$. Data = mean \pm SEM; N = number of animals; statistical analysis: unpaired two-tailed t test: * $p < 0.05$, ** $p < 0.01$. Abbreviations: weeks of age (wo), *tafazzin*-knockdown (*Taz*-KD), wildtype (WT). The abbreviations for each lipid class can be found in the general list of abbreviations.

In summary, lipidomics profiling revealed several lipid classes, which are closely linked to an impaired *Taz*-mediated CL remodelling, were altered in *Taz*-KD compared to WT pancreatic islets.

4.7.2 RNA sequencing

Whole pancreatic islets bulk mRNA-sequencing was performed to link the observed functional changes and adaptations that are described in the previous Chapters to the underlying pathways and mechanisms. Therefore, the RNA of 20 wo WT and *Taz*-KD pancreatic islets was isolated and sent to the company Novogene for RNA-Seq analysis (methods described in **Chapter 3.12.3**). The RNA-Seq results were compared with gene

ontology (GO) and Reactome pathway databases. In a volcano plot, the significant ($p < 0.05$) upregulation of 98 and downregulation of 66 genes in *Taz*-KD pancreatic islets compared to WT was displayed (**Figure 4.34**). Due to simplicity, not all significantly altered genes and connected pathways were discussed. In **Figure 4.34 A**, the highlighted genes (upregulated: *Entpd4b*, *Rpl30-ps10*, *Pde1c*, *B3gnt9*, *Gnpnat1*, *Galnt17*, *Gcnt7*; down: *Taz*, *Apoe*, *mt-Nd4l*, *Calcoco1*, *Ubc*) are connected to metabolism and autophagy (*Ubc* and *Taz* itself). GO pathways analysis showed that significantly downregulated pathways include purine nucleotide metabolic and biosynthetic processes and regulation of immune response (**Figure 4.34 B**, upper panel). Increased GO pathways included the specifically marked pathways of the *N*-acetyl-glucosamine metabolic process and protein-*O*-linked glycosylation (**Figure 4.34 B**, bottom panel). Reactome pathway analysis confirmed the GO analysis by revealing an enrichment in protein-*O*-linked glycosylation and *O*-linked β -*N*-acetylglucosamine (*O*-GlcNAc) pathways, which are summarised in a schematic **Figure 4.34 C** showing the *O*-GlcNAc pathway. The significantly upregulated genes that encode for *O*-GlcNAcylation are highlighted in purple. Glucose is transformed to fructose-6-phosphate before a glutamine molecule serves as an amide donor by the glutamine-fructose-6-phosphatase transaminase to form glucosamine-6-phosphate which is characterised as the first step of the hexosamine biosynthesis pathway. Subsequently, the GNA1 enzyme (RNA-level upregulation in *Taz*-KD, gene name *GNPNAT1*) uses acetyl-CoA to catalyse the formation of *N*-acetylglucosamine-6-phosphate which is then transformed to UDP-*N*-acetylglucosamine by the addition of UTP in the next two steps. Additionally, heatmaps representing the top 30 down and up differentially expressed genes across the different WT and *Taz*-KD pancreatic islet samples are shown in the supplements (supplements, **Figure 7.23**).

Overall, RNA-Seq revealed several alterations in several critical proteins concerning among others autophagy and metabolism. One of the most striking observations was the upregulation of *O*-GlcNAc, which will be further investigated in the next **Chapter 4.8**.

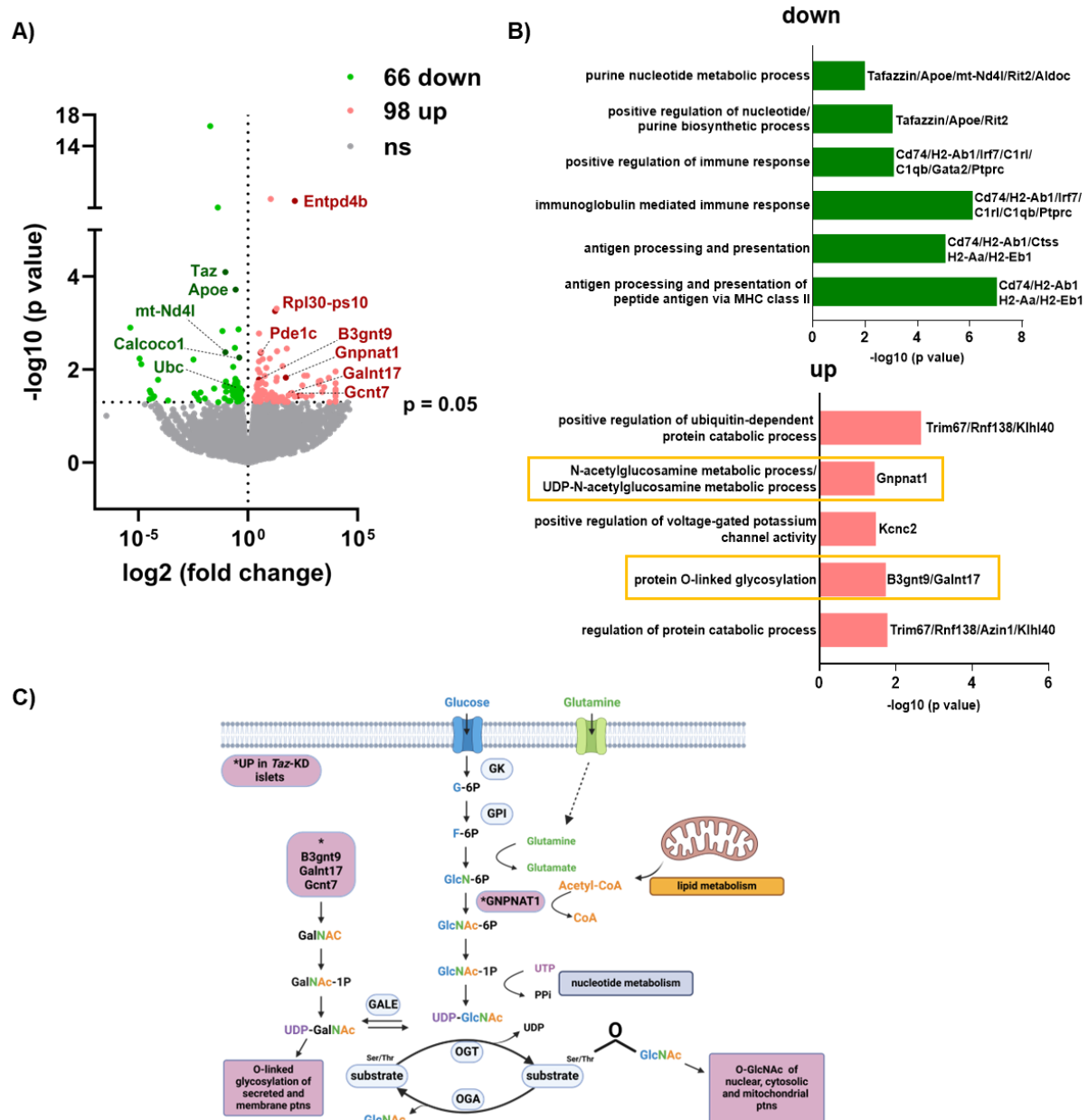


Figure 4.34: Bulk mRNA-sequencing revealed upregulation of O-GlcNAc in *Taz*-KD pancreatic islets

(A) Volcano plot illustrates the upregulation of 98 genes and downregulation of 66 genes ($p > 0.05$) in *Taz*-KD. Selected genes that are significantly altered in *Taz*-KD pancreatic islets are highlighted, $N = 3$. (B) Identified relevant GO pathways with genes that are down- (lower panel) or upregulated (upper panel) in *Taz*-KD. (C) Schematic Figure of the O-GlcNAc pathway, upregulated in Reactome analysis of *Taz*-KD. The proteins and pathways resulting from the upregulated genes in *Taz*-KD are highlighted in purple. Data = mean \pm SEM; N = number of animals; statistical analysis: unpaired two-tailed t test: * $p < 0.05$. Abbreviations: O-linked β -N-acetylglucosamine (O-GlcNAc), weeks of age (wo), *tafazzin*-knockdown (*Taz*-KD), wildtype (WT), gene ontology (GO).

4.8 Post-translational modification: O-Glycosylation

O-linked β -*N*-acetylglucosamine (O-GlcNAc) is a reversible and highly dynamic post-translational modification found on serine and threonine residues of proteins in the nucleus, cytoplasm and mitochondria. This enzymatic modification is described by forming a glycosidic bond between the protein and *N*-acetylglucosamine (GlcNAc).²³² The process of O-GlcNAcylation has particular importance for pancreatic β -cells mass and function.¹²

RNA-Seq analysis from the previous **Chapter 4.7.2** revealed a striking upregulation of O-GlcNAc in the transcriptome of *Taz*-KD compared to WT pancreatic islets. To assess O-GlcNAc on protein level, IHC and WB analysis of 20 wo WT and *Taz*-KD pancreatic islets were performed (**Figure 4.35**). The level of O-GlcNAc protein modification was significantly enhanced in IHC and WB analysis, which might be connected to the increased glucose uptake of *Taz*-KD pancreatic islets.

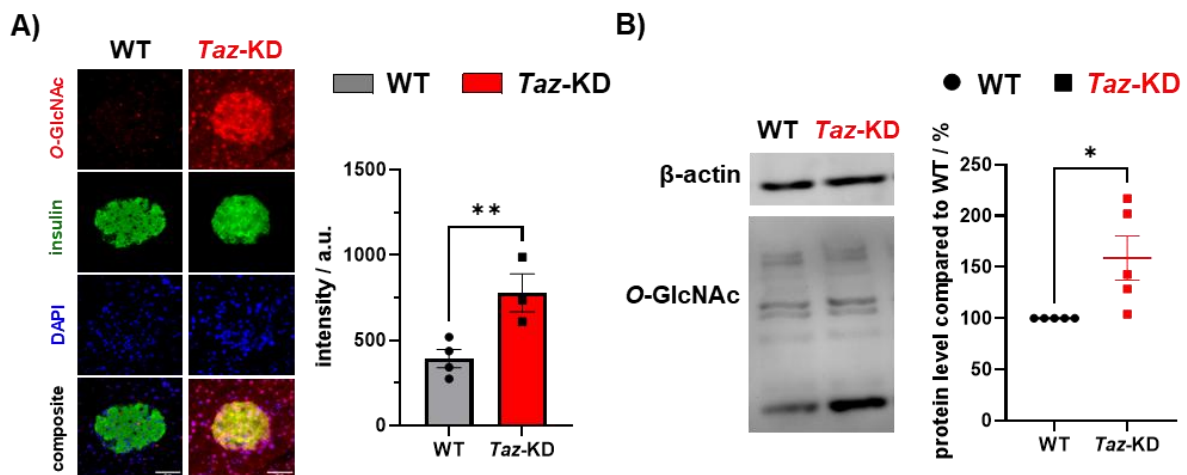


Figure 4.35: Increased O-GlcNAc in IHC and WB analysis of *Taz*-KD pancreatic islets

(A) Representative IHC images (left) and quantification (right) of O-GlcNAc in 20 wo *Taz*-KD and WT pancreatic islets. Scale bar: 50 μ m. N = 5. (B) Representative WB (left) and quantification (right) of O-GlcNAc normalised to β -actin in 20 wo *Taz*-KD and WT pancreatic islets. N = 5. Data = mean \pm SEM; N = number of animals; statistical analysis: unpaired or paired (WB) *t* test: **p* < 0.05, ***p* < 0.01. Abbreviations: O-linked β -*N*-acetylglucosamine (O-GlcNAc), weeks of age (wo), *tafazzin*-knockdown (*Taz*-KD), wildtype (WT), western blot (WB), immunohistochemistry (IHC).

4.9 Direct consequences of *Taz*-KD - *in vitro* model

In the previous Chapters, isolated organs after 20 or 50 weeks of doxy treatment and disease progression were investigated. In the shTaz mouse model, doxy feeding leads to *Taz*-KD, which, together with the doxy diet itself, causes challenges to the organism. Although the resulting cellular modifications (functional and morphological) and systemic effects are crucial to understand the nature of BTHS, they are accumulated consequences of direct *Taz*-KD effects and subsequent adaptation processes. In order to study only the direct effects of *Taz*-KD, a new *in vitro* model was established throughout this thesis and compared to the lifelong doxy feeding model (termed *in vivo* model). In the *in vitro* model, *Taz*-KD was triggered after organ isolation and, hence, right before the experiment (method description in **Chapter 3.1.2**). Therefore, the *in vitro* model allows studying the direct effects of *Taz*-KD independent of long-term adaptations and unwanted doxy feeding side effects.

4.9.1 Characterisation of shTaz - *in vitro* model

First, the efficiency of *in vitro* *Taz*-KD in pancreatic islets was tested using qPCR analysis (**Figure 4.36**, supplements **Figure 7.26**). Application of 1 µg/ml doxy into the culture medium of pancreatic islets was enough to induce a significant reduction of *Taz* RNA levels after 48 h of doxy incubation (**Figure 4.36 A**). Lipidomics profiling revealed that the incubation for 1-week in culture supplemented with doxy caused a significant reduction of total CL levels in both WT and *Taz*-KD pancreatic islets (**Figure 4.36 B**). However, there was no difference between the genotypes. The graphs of the shTaz *in vitro* model were visually separated from the *in vivo* model by using striped pattern but the same color code.

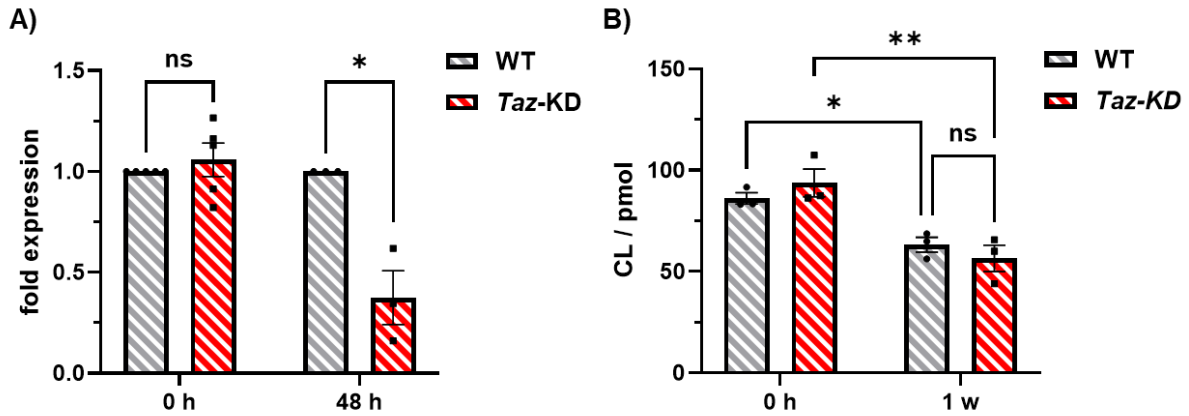


Figure 4.36: *Taz* reduction in the *Taz*-KD pancreatic islets *in vitro* model

(A) RNA levels of *Taz* of WT and *Taz*-KD pancreatic islets after 0 and 48 h of doxy incubation in the culture medium measured by qPCR. N (0 h) = 5, N (48 h) = 3. (B) Total CL levels of WT and *Taz*-KD pancreatic islets after 0 h and 1-week of doxy incubation measured by lipidomic analysis. N = 3. Data = mean \pm SEM; N = number of animals; statistical analysis: unpaired two-tailed (qPCR) *t* test: **p* < 0.05, ***p* < 0.01. Abbreviations: *tafazzin*-knockdown (*Taz*-KD), wildtype (WT), doxycycline (doxy), cardiolipin (CL).

Although the total CL content was not different, the analysed CL species profile was significantly altered in *Taz*-KD pancreatic islets after 1-week incubation of doxy compared to WT (**Figure 4.37**). Several CL species were downregulated in *Taz*-KD (CL 72:6, 72:7, 74:8, 74:9). Interestingly, the most abundant CL 72:8 was not changed compared to WT levels. Additionally, the 1-week incubation in doxy culture medium itself had also dramatic effects on the CL profile in WT and *Taz*-KD from 0 h to 1-week. The complete lipidomics analysis for the other lipid classes of the *in vitro* model is described in **Chapter 4.9.4**. Similar to the CL profile in the *in vivo* model, some replicates had levels close or below the limit of detection and hence, some CL species values in **Figure 4.37** are missing. Also, MLCL, the important precursor form of mature CL, was below the limit of detection as described for the *in vivo* model in **Chapter 4.1**.

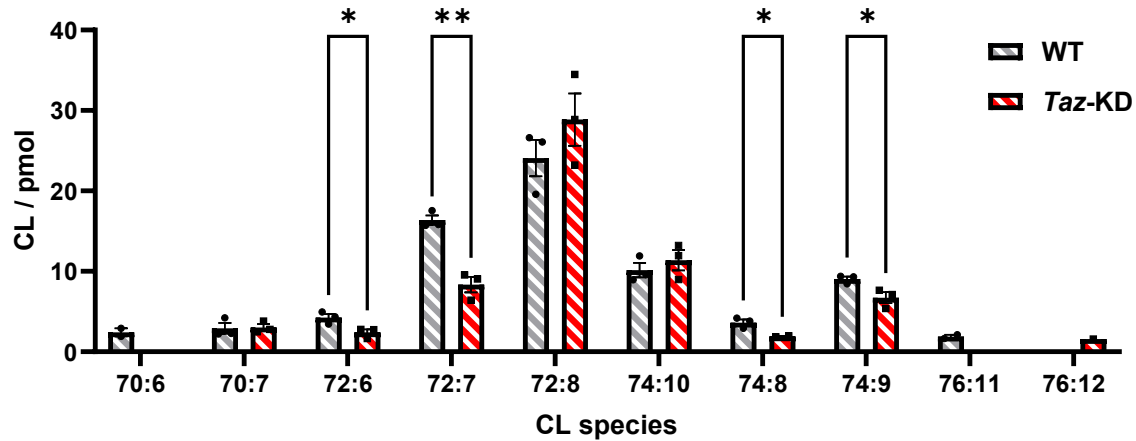


Figure 4.37: Altered CL species profile of *Taz*-KD pancreatic islets of the *in vitro* model

The CL levels (in pmol) of each species after 1-week doxy incubation measured by lipidomics analysis. N = 3, some replicates are missing due to limit of detection. Data = mean \pm SEM; N = number of animals; statistical analysis: unpaired two-tailed *t* test: **p* < 0.05, ***p* < 0.01. Abbreviations: *tafazzin*-knockdown (*Taz*-KD), wildtype (WT), doxycycline (doxy).

4.9.2 Immunohistochemistry - *in vitro* model

After validation of the *in vitro* model by observing the downregulation of *Taz* gene expression and alteration in CL profile, pancreatic islet composition of the *in vitro* model was analysed. Therefore, IHC on isolated pancreatic islets of the 1-week *in vitro* was performed to study the number of pancreatic islets cells according to their cell type. No differences in cell type numbers of α -, β - or δ -cells were observed when comparing WT and *Taz*-KD pancreatic islets after 1-week doxy incubation (**Figure 4.38**). The normalization was performed according to the total islet cell number and not to the area as in the *in vivo* model. This was due to difficulties in separation of the islet's cells and the surrounding tissue in the *in vivo* pancreas cryo-slices. In the paraffin slices of the isolated pancreatic islets, all the counted DAPI spots were well separated from the background and belonged to the imaged pancreatic islet.

In summary, the *in vitro* model, WT and *Taz*-KD pancreatic islets after 1-week of doxy culture showed similar α -, β - or δ -cells numbers.

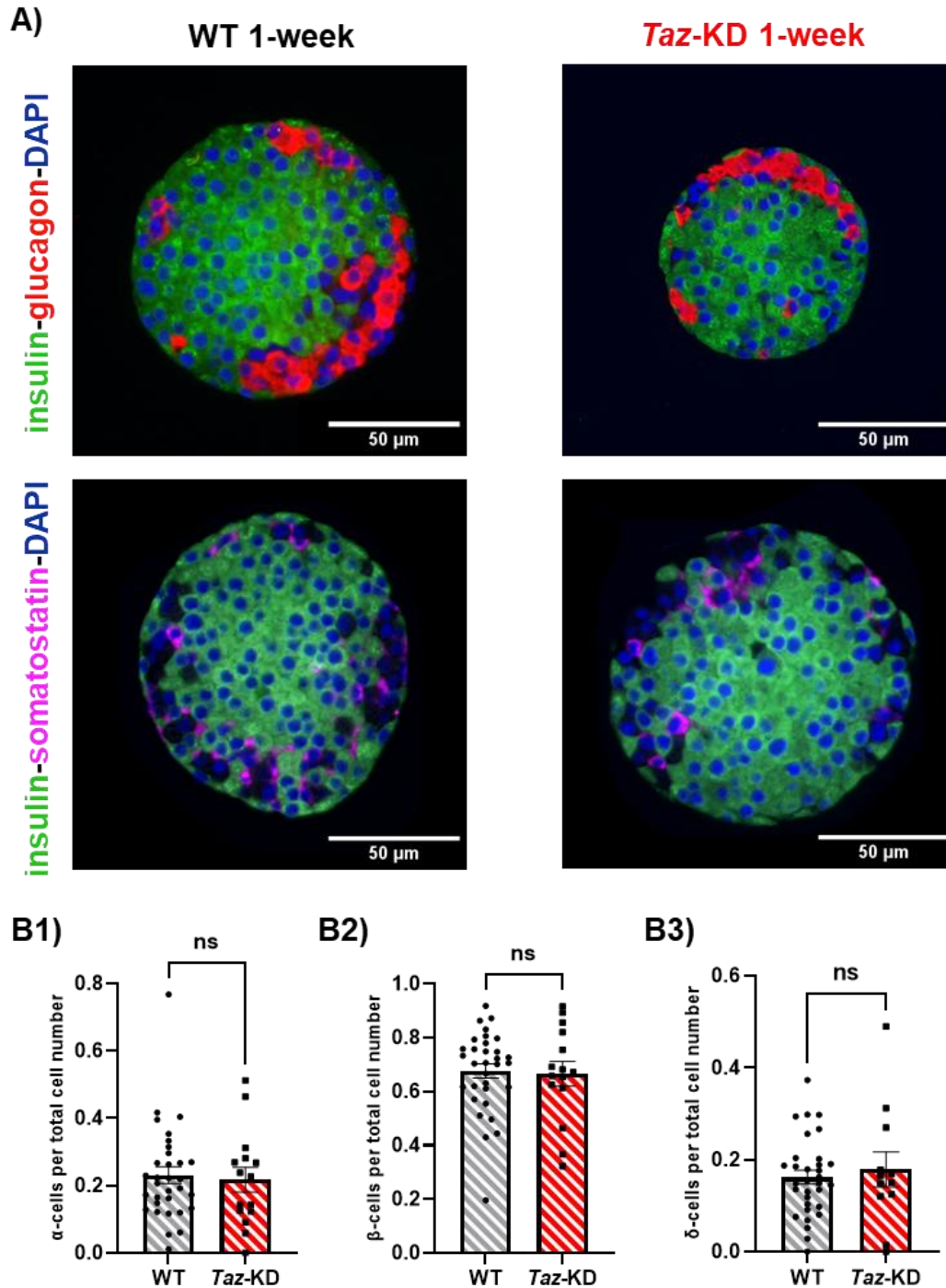


Figure 4.38: Similar pancreatic cell type number of *Taz*-KD *in vitro* model

(A) Representative IHC image of WT and *Taz*-KD pancreatic islets after 1-week doxy culture. Pancreatic islets were stained against insulin (green) - glucagon (red) (top panel) or insulin (green) - somatostatin (magenta) (bottom panel) together with DAPI (blue). Scale bar: 50 μ m. **(B)** Quantitative ImageJ analysis of α - (B1), β - (B2) and δ - (B3) cell number per total islet cells using IHC on paraffin embedded pancreatic islets and counting DAPI spots of WT and *Taz*-KD pancreatic islets of the 1-week *in vitro* model. N = 3. Data = mean \pm SEM; N = number of animals; statistical analysis: unpaired *t* test: ns: *p* > 0.05. Abbreviations: *tafazzin*-knockdown (*Taz*-KD), wildtype (WT), doxycycline (doxy), immunohistochemistry (IHC).

4.9.3 Pancreatic islet function *in vitro* model

The previous Chapter showed that, unlike the *in vivo* model, the pancreatic islet composition of the *in vitro* model was similar for both genotypes. To test if the pancreatic islet function was different in both models, several functional experiments of WT and *Taz*-KD pancreatic islets after 1-week of doxy culture were performed (**Figure 4.39**). To ensure comparability, the functional experiments in the *in vitro* model were conducted in the same manner as the *in vivo* model unless stated otherwise. This allowed for an evaluation of the direct impact of *Taz*-KD on pancreatic islet functionality.

The mitochondrial functionality was assessed by measuring ATP levels of WT and *Taz*-KD pancreatic islets after 1-week of doxy culture. *Taz*-KD pancreatic islets, after 1-week of doxy culture, exhibited decreased ATP levels in 10 mM glucose compared to WT (**Figure 4.39 A**). Cytosolic Ca^{2+} levels in low and high glucose were similar in WT and *Taz*-KD pancreatic islets (**Figure 4.39 B**). Also, the cytosolic Ca^{2+} dynamics upon stimulation with glucose were unchanged. Additionally, the mitochondrial volume measured by Mitotracker intensity normalised to Hoechst was also unchanged among the genotypes (**Figure 4.39 C**). Next, static and dynamic GSIS experiments were performed. *Taz*-KD pancreatic islets display decreased static GSIS in 20 mM glucose and a reduced second phase of GSIS in the dynamic experiments (**Figure 4.39 D, E**). Glucagon secretion in *Taz*-KD pancreatic islets at 0.5 mM glucose tended to be reduced, although not statistically significant (**Figure 4.39 F**).

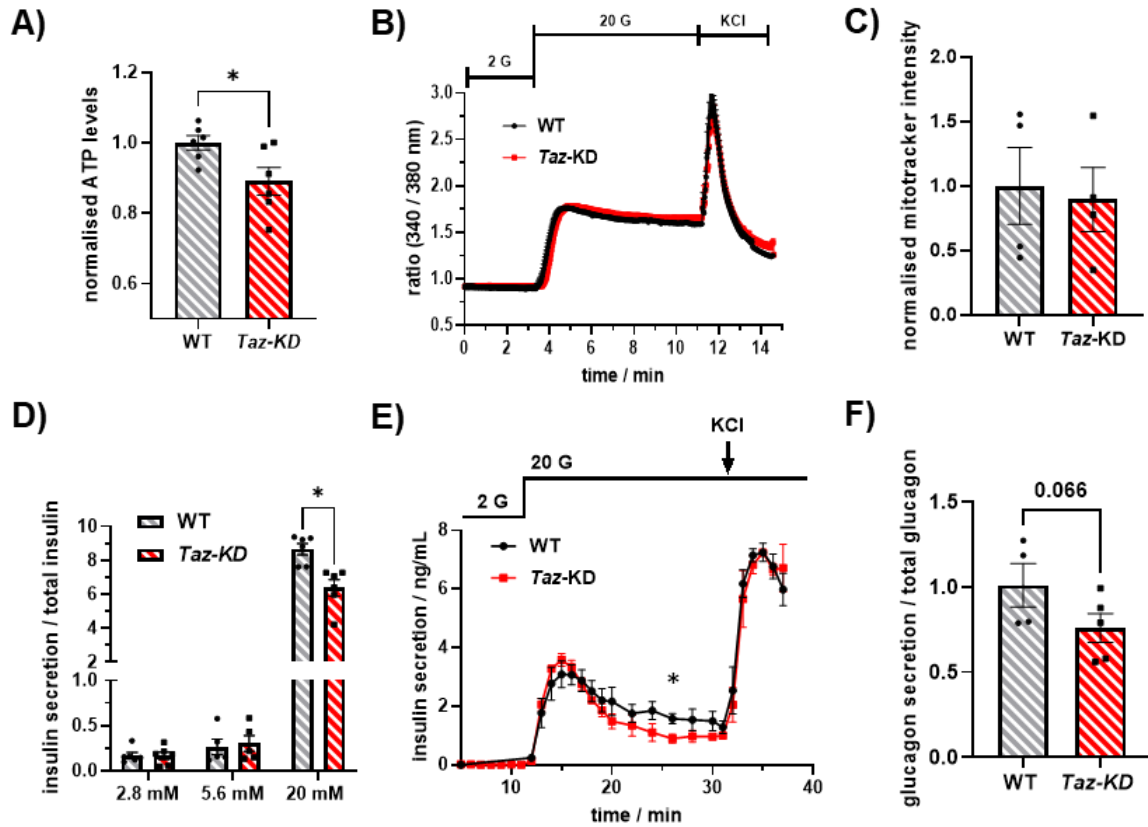


Figure 4.39: Impaired pancreatic islets function in *Taz-KD* *in vitro* model

(A) ATP levels of WT and *Taz-KD* pancreatic islets of 1-week *in vitro* model using the CellTiter-Glo[®] assay and normalised to islet size, N = 6. (B) Cytosolic Ca²⁺ levels of WT and *Taz-KD* pancreatic islets of 1-week *in vitro* model in 2 mM and 20 mM glucose concentration. 30 mM of KCl was added as a positive control, N = 6. (C) Quantification of mitochondrial volume of WT and *Taz-KD* pancreatic islets of 1-week *in vitro* model using MitoTracker Deep Red intensity and DAPI. N = 4. (D) Static GSIS of WT and *Taz-KD* pancreatic islets of 1-week *in vitro* model in 2.8 mM, 5.6 mM or 20 mM glucose, N = 6. (E) Dynamic GSIS of WT and *Taz-KD* pancreatic islets of 1-week *in vitro* model in 2 mM and 20 mM glucose. 30 mM KCl as added as positive control, N = 3. (F) Glucagon secretion of WT and *Taz-KD* pancreatic islets of 1-week *in vitro* model in 0.5 mM glucose, N (WT) = 4, N (*Taz-KD*) = 5. Data = mean \pm SEM; N = number of animals; statistical test: unpaired *t* test: **p* < 0.05. Abbreviations: *tafazzin*-knockdown (*Taz-KD*), wildtype (WT), doxycycline (doxy), glucose-stimulated insulin secretion (GSIS).

In summary, *Taz-KD* pancreatic islets function after 1-week in doxy culture showed impaired pancreatic islet function with decreased ATP levels and defective insulin secretion in high glucose.

4.9.4 Lipidomics - *in vitro* model

The resulting cardiolipin profile of the *in vitro* model has already been described in the **Chapter 4.9.1**. Additionally, the complete lipidome of the *Taz*-KD pancreatic islet 1-week *in vitro* model was examined. First, a principal component (PC) analysis for unaveraged replicates was performed to get an overview of the largest variation in the lipid dataset (**Figure 4.40**). PC allows to reduce the huge number of dimensions (unsupervised) represented by the different lipid species to a few PC. **Figure 4.40 A** displays the PC scores based on the lipid species using the first two principal components (PC 1 on the x-axis and PC 2 on the y-axis). The sample cohort treated with 1-week doxy (WT and *Taz*-KD) showed the largest variation compared to the other samples in the lipid dataset. This suggests that there are major difference resulting out of the 1-week doxy culture. One replicate of the sample cohort *Taz*-KD – 0 h was clearly an outlier and excluded from further lipid analysis. In **Figure 4.40 B**, the fractions of the five main principal components (threshold was set above 5%) were listed.

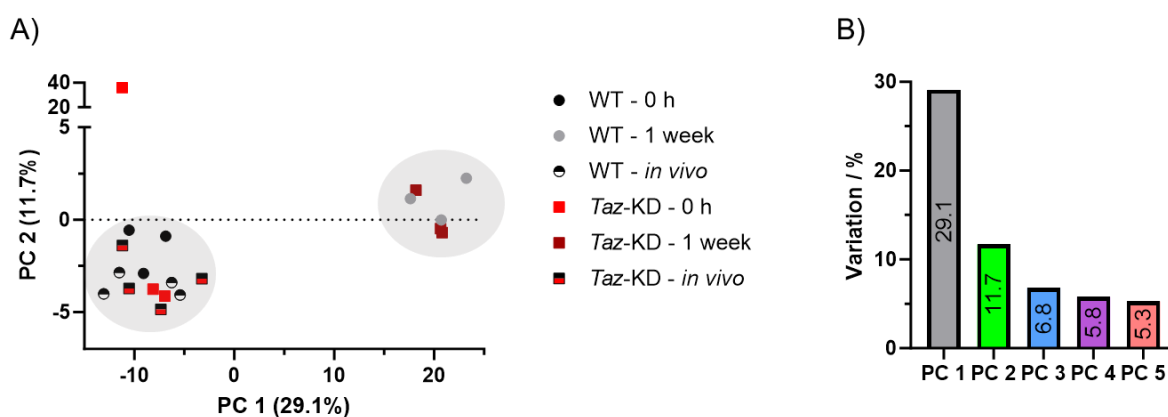


Figure 4.40: PC analysis of shTaz *in vivo* and *in vitro* lipidomic samples

(A) PC scores based on the lipid species. The largest variation in all samples was between the 1-week samples and the other two groups (0 h and *in vivo* model). (B) Variation represented by principal components. PC1 and PC2 display 40.8 % of the variation in samples. Data = mean \pm SEM; N = number of animals; Abbreviations: weeks of age (wo), *tafazzin*-knockdown (*Taz*-KD), wildtype (WT), principal component (PC).

Furthermore, the whole lipid class composition (excluding CL) of *Taz*-KD and WT pancreatic islets *in vitro* model after 1-week doxy culture was analysed and displayed against the total lipid amount per sample (**Figure 4.41**). *Taz*-KD showed a similar profile except for a significant upregulation of ether-linked lyso-phosphatidylcholines (LPC O-). Additionally, the

lipid class profile after 1-week and 0 h doxy culture was also compared to evaluate the effect of pancreatic islet culture on the lipid class composition. As expected from the results of the PC analysis, drastic changes (upregulated CE, PE O-, PG, and downregulated Cer, HexCer, PI) in the lipid class profile after 1-week doxy culturing compared to 0 h (supplements, **Figure 7.20**). These measured alterations heavily depend on the composition of the culturing medium and the incubation time.

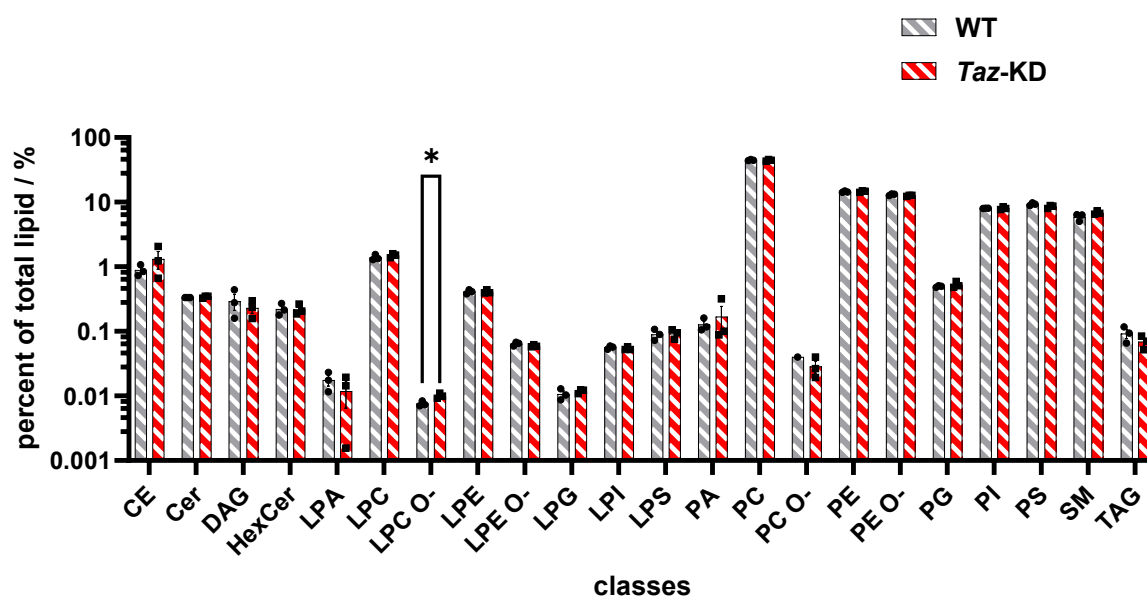


Figure 4.41: Lipid class composition of *Taz*-KD pancreatic islets of the 1-week doxy *in vitro* model

Lipid class profile of WT and *Taz*-KD pancreatic islets. Normalised against total lipid amount and displayed with a logarithmic scale. N (WT 1-week) = 2 - 3, N (*Taz*-KD 1-week) = 3; Data = mean \pm SEM; N = number of animals; statistical analysis: unpaired two-tailed *t* test: **p* < 0.05. Abbreviations: *tafazzin*-knockdown (*Taz*-KD), wildtype (WT), doxycycline (doxy). The abbreviations for each lipid class can be found in the general list of abbreviations.

Notably, the amount of the ether-linked lipid LPC O- was altered in both models, but in opposing directions. The amount of LPC O- was decreased in *Taz*-KD pancreatic islets of the *in vivo* model, but in the 1-week *in vitro* model LPC O- of *Taz*-KD pancreatic islets was elevated.

In summary, the full lipid class profile of the *Taz*-KD pancreatic islets after 1-week of doxy culture was similar to the WT doxy-treated controls. Instead, the lipid profile for both genotypes was drastically influenced by the culture condition itself.

4.9.5 RNA sequencing - *in vitro* model

RNA-Seq was used to link observed functional impairment of *Taz*-KD after 1-week of doxy culture with the involved pathways. Bulk mRNA sequencing revealed the significant upregulation of 137 and downregulation of 315 genes in *Taz*-KD pancreatic islets of the 1-week *in vitro* model (**Figure 4.42**). Therefore, the observed alterations in gene expression were considerably higher in number compared to the *Taz*-KD *in vivo* model (**Figure 4.34**). Genes that are associated with metabolism or glycosylation were highlighted in the Volcano plot (upregulated: *Gt(Rosa)26Sor*, *Rps27rt*, *Adarb2*, *Galnt9*; downregulated: *Taz*, *Fbln2*, *Anxa2*, *Leprotl1*, *Gpx8*, *Atf3*, *Wnt7a*). GO pathways analysis showed that significantly downregulated pathways include organisation of extracellular matrix with the connected cell adhesion, and cell growth. In turn upregulated pathways included several processes involved in DNA packaging and cell cycle, and oligosaccharide metabolism.

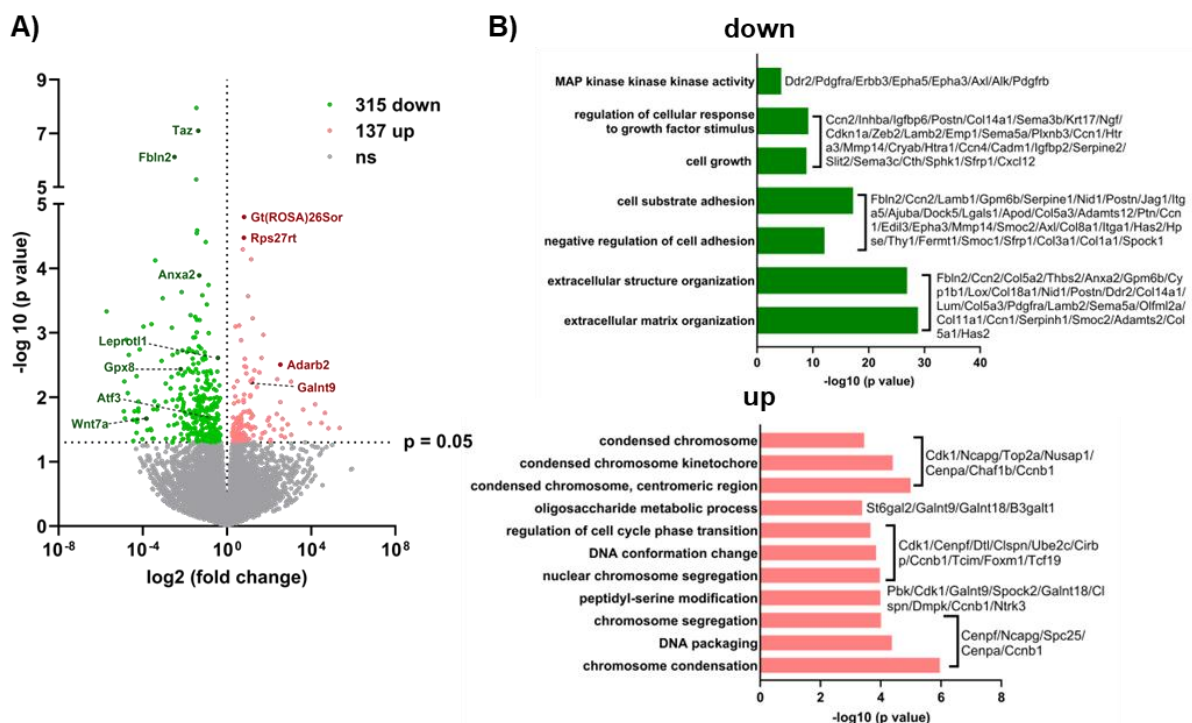


Figure 4.42: RNA-Seq of *Taz*-KD pancreatic islets of the 1-week doxy *in vitro* model

(A) Volcano plot analysis showed downregulation of 137 and upregulation of 315 genes ($p < 0.05$) in *Taz*-KD 1-week *in vitro* model pancreatic islets. Selected genes that are significantly altered in *Taz*-KD pancreatic islets are highlighted, $N = 3$. (B) Relevant GO pathways (left) with genes (right) that are down- (upper panel) or upregulated (lower panel) in *Taz*-KD 1-week *in vitro* model. Data = mean \pm SEM; N = number of animals; statistical analysis: unpaired two-tailed t test: * $p < 0.05$. Abbreviations: *tafazzin*-knockdown (*Taz*-KD), wildtype (WT), doxycycline (doxy).

5 Discussion

As diagnosis and disease management in Barth syndrome (BTHS) have advanced, a growing number of people with BTHS are surviving into adulthood.²⁴⁵ With this rise in life expectancy, it has become increasingly important to understand the metabolic phenotypes of these patients in order to improve their quality of life. BTHS is a mitochondrial disorder known to affect cellular ATP production and Ca^{2+} handling.³⁵ The metabolically active pancreatic islets have high energy demands and rely on functional mitochondria to regulate whole-body blood glucose homeostasis. Moreover, defects in mitochondria have been identified as a central player for the progression of insulin resistance and type 2 diabetes.²¹⁴

In this study, the consequences of *taffazin*-knockdown (*Taz*-KD) and cardiolipin (CL) reduction on pancreatic islet function were investigated in the context of the mitochondrial disorder BTHS. The discussion part is structured into topics that were considered crucial based on the performed experiments. However, some additional findings that do not fit the discussion topics and would thus disrupt the flow of reading were evaluated directly in the respective result Chapter.

5.1 Characterisation of the shTaz mouse model

First, the doxycycline (doxy)-induced shTaz mouse model to achieve *Taz*-KD in pancreatic islets and recapitulate the BTHS phenotype was characterised. The shTaz mice were fed a lifelong, starting during the mother's pregnancy, doxy chow diet (**Figure 3.1**). This approach was crucial for recapitulating the progression and systematic nature of the BTHS disease, similar to the human situation.

The qPCR analysis unveiled a *Taz* downregulation of ~85% in the heart and ~65% in pancreatic islets (**Figure 4.1**). As introduced in **Chapter 1.1.4**, tissue-dependent differences in *Taz*-KD efficiency have been observed before, but the underlying reasons remained elusive. Several transcript variants of the Taz protein are described in the literature, including the full-length transcript variant, variants lacking exons and alternatively spliced mRNA transcript variants.^{172,383} Jagirdar *et al.* re-expressed the full length variant and the enzymatically active variant lacking exon 5, in *tafazzin*-knockout (*Taz*-KO) rat C6 glioma cells. However, only the full length variant fully restored the impaired proliferation rate, indicating that the variants were functionally distinct.²⁵¹ Interestingly, BTHS patients have been found

with a mutation in exon 5.¹³¹ Moreover, Taz isoforms were suggested to have different target sites or substrate specificity, favouring varying remodelling reactions and ultimately leading to the tissue-specific *Taz*-KD phenotypes.¹¹⁴ Therefore, *Taz* splice variants could account for the variation in gene expression and knockdown (KD) efficiency.

The *Taz*-KD efficiency in pancreatic islets was sufficient to trigger CL profile alterations and reduce total CL content (**Figure 4.2**). The most pronounced changes were the reduction in the main CL 72:8 and the connected profile shift towards CL species with longer acyl chains. CL 72:8 accounted for about 60% (WT) and 45% (*Taz*-KD) of all CL species in pancreatic islets. Similarly, previous studies showed that CL 72:8 comprises 60% of all CL in healthy skeletal muscle tissue, whereas 80% in liver and heart tissue.³²⁷ All CL species together encompassed 1.7% (WT) and 1.5% (*Taz*-KD) of all lipids in the pancreatic islets, which is considerably lower than the 10% found in heart tissue. In detail, CL constitutes 15 - 20% of the inner mitochondrial membrane and 10% of total lipids levels in cardiomyocytes.³⁴⁰ The lower CL portion in pancreatic islets might be connected to a lower density of mitochondria compared to heart tissue, but so far, no study has separately tested the lipid composition of mitochondria in pancreatic islets. However, the reduced abundance of CL relative to other lipid classes could impact the tissue-specific severity of the phenotype. Investigations on lipase activity directed toward CL showed that apart from Taz several other enzymes are involved in the cellular CL composition. Yeast with a deletion of the cardiolipin-specific deacylase 1 (CLD1), which is a lipase specifically deacylating palmitoyl acyl chains from CL, displayed a lower degree of unsaturation in CL. Interestingly, a combined deletion of CLD1 and Taz suppressed the accumulation of monolysocardiolipin (MLCL) and the decrease in CL content. However, due to a still changed CL profile the yeast cells did not restore normal growth.³¹ These results indicate that the alteration in CL profile and not the accumulation of MLCL is the primary cause for the cellular BTHS phenotype. Another study assessed the impact of the Ca²⁺-independent phospholipase A2 (iPLA₂) in BTHS. iPLA₂ deletion in *Taz*-KO yeast mutants and inhibition with bromoenol lactone in BTHS lymphoblasts resulted in a decrease of the MLCL/CL ratio which improved electron transport chain (ETC) complexes stability. However, bromoenol lactone treated cells still exhibited an altered CL profile and did not recover respiratory function.^{239,395} On the other hand, a recent article suggested a major role of MLCL in the BTHS pathogenesis due to its interaction with cytochrome c.¹⁹²

Cole and colleagues also investigated the isolated pancreatic islets of *Taz*-KD mice using the same shTaz mouse model with a lifelong doxy diet.⁸² Although their control pancreatic islets exhibited similar CL concentrations (nmol/mg) to our results (detailed comparison in **Chapter 4.1**), many of the other results were contradictory to our results. Most importantly, their samples showed no reduction in CL content, the mice had higher body weight after 50 wo,

and their islets exhibited impaired basal insulin secretion. The functional results of the study by Cole *et al.*, 2021 will be examined in detail in **Chapter 5.2**. In lipidomics, they found a concentration of around 0.1 nmol/mg MLCL and 10 nmol/mg CL in control pancreatic islets, while *Taz*-KD samples had approximately 0.35 nmol/mg MLCL and 13 nmol/mg CL.⁸² This calculates to an apparent increase of around 170% in the MLCL/CL ratio, which is considered a hallmark of BTHS. We could not detect MLCL in any of the pancreatic islet samples investigated. The identification of MLCL failed probably due to a lack of sensitivity in the standard MS approach, and a targeted HPLC-MS/MS might have been necessary.

Instead, our findings demonstrate an upregulation of the lipid classes lyso-phosphatidylglycerol (LPG) and phosphatidylglycerol (PG), key players in the biosynthesis of CL in *Taz*-KD pancreatic islets (**Chapter 4.7.1**). Additionally, the phospholipid classes phosphatidylcholine (PC) and phosphatidylethanolamine (PE), which serve as acyl chain donors for CL remodelling by Taz were found to be altered in *Taz*-KD pancreatic islets. Therefore, the upregulation of phospholipids involved in the biosynthesis of CL (PG and LPG), alterations in the phospholipids participating in Taz-mediated acyl chain transfer (PC and PE), along with the reduction in CL content and changes in CL profile, clearly indicate defective CL biosynthesis and remodelling, even though MLCL could not be detected.

5.2 Pancreatic islet composition and function

The main features of the observed *Taz*-KD phenotype of pancreatic islet function and composition included an earlier onset of Ca^{2+} influx, enhanced α -cell mass, increased glucagon secretion, and preserved insulin secretion.

Ca^{2+} regulation in *Taz*-KD

Ca^{2+} is one of the key intracellular regulators of pancreatic islet function, and its influx triggers the exocytosis of insulin (β -cells) or, together with Na^+ , glucagon (α -cells) granules.¹⁵³ Measurement of cytosolic Ca^{2+} using the ratiometric Fura-2 AM in low and high glucose revealed similar levels in *Taz*-KD and WT pancreatic islets (**Figure 4.15**). Interestingly, *Taz*-KD pancreatic islets exhibited an earlier onset of cytosolic Ca^{2+} influx than WT controls (**Figure 4.15**).

The voltage-gated Ca^{2+} channels mediate the cytosolic Ca^{2+} influx and open upon cellular depolarisation (introduced in **Chapter 1.2.2**). Therefore, the plasma membrane potential was explored by performing tolbutamide titration experiments at low glucose conditions (**Figure**

4.16). The sulfonylureas tolbutamide mimics glucose-stimulated ATP production by closing the K_{ATP} channel independently of metabolism, which allows the study of the direct effects of the plasma membrane potential. Although the dose-response curve of the tolbutamide and Ca^{2+} correlation was slightly enhanced in *Taz*-KD, which suggests a pre-activated state under low glucose conditions, no statistical difference was found among the genotypes (**Figure 4.16**). The hypothesis of plasma membrane potential changes is further supported by the upregulation in the RNA-Seq data of the voltage-gated K^+ channel *Kcnc2* (**Figure 4.34**), which mainly regulates the repolarisation in the pancreatic β -cells and was previously shown to be amplified in pancreatic β -cells with metabolic hyperactivity.^{270,347} However, the levels of K_{ATP} channels that are responsible for the initial depolarisation were most likely not changed, as maximal depolarisation by the addition of KCl was unchanged among the genotypes (**Figure 4.15**). While the levels of the K_{ATP} channels may be similar, their activity could be different in *Taz*-KD. Especially because K_{ATP} channels have been proposed to be redox-sensitive and regulated specifically by NOX4 in pancreatic islets.^{281,418} NOX4 signalling was found to be altered in *Taz*-KD, which could be seen in the slightly increased (not significant) protein levels and the changes in redox state occurring in the presence of the NOX4 inhibitor GLX (**Figure 4.23** and **Figure 4.26**). Furthermore, treatment with GLX elevated ATP levels in *Taz*-KD but not WT pancreatic islets, providing further support for the involvement of NOX4 in the *Taz*-KD phenotype (**Figure 4.14**). In addition to K_{ATP} channel differences, alterations in stability/activity of other proteins involved in the plasma membrane potential or cytosolic Ca^{2+} influx are possible explanations for the observed phenotype. Therefore, the earlier Ca^{2+} influx could also result from potentiated activity of the voltage-gated L-type Ca^{2+} channels mediated via cAMP-dependent phosphorylation.¹⁹⁶ Although cAMP was not monitored in this study, cAMP levels are crucial for proper insulin and glucagon secretion, and further studies could elaborate on cAMP levels in BTHS.⁴²² Of interest, it was speculated that voltage-gated L-type Ca^{2+} channels might be redox-sensitive.¹⁷⁵ Next, the Ca^{2+} release-activated current (CRAC) or transient receptor potential (TRP) channel can influence the GSIS and their involvement in *Taz*-KD phenotype could be tested by using gadolinium, 2-APB or cyclopiazonic acid to inhibit the CRAC channel.^{37,413} Treating *Taz* deficient cells with ouabain to inhibit the Na^+/K^+ ATPase, which helps to maintain the resting potential, could be another exciting future approach.¹⁹³

Furthermore, upstream metabolic differences may be responsible for the observed *Taz*-KD Ca^{2+} phenotype. Supporting this hypothesis is the amplified metabolic activity of *Taz*-KD, as indicated by increased glucose uptake and higher OCR in low glucose conditions (**Figure 4.8** and **Figure 4.11**). The amplified metabolism could result in a faster glucose turnover rate (potential hypermetabolism is further discussed in **Chapter 5.2**). However, there are several

findings that contradict this hypothesis. In glucose titration experiments, both WT and *Taz*-KD pancreatic islets exhibited a similar glucose set point for the initiation of cytosolic Ca^{2+} influx, which was at 5 mM glucose (**Figure 4.16**). An unchanged glucose set point was also reflected by a similar glucokinase (Gck) activity, the glucose sensor within the pancreatic islets, in both WT and *Taz*-KD (**Figure 4.8**). Previous studies showed that heightened Gck activity in pancreatic islets is connected to a lower glucose set point.¹⁹ Additionally, no difference was observed in glucose-6-phosphate dehydrogenase (G6PDH) activity, which is the initial enzyme of the pentose phosphate pathway (PPP) (**Figure 4.8**). G6PDH plays a vital role in metabolic activity and redox homeostasis.¹⁵⁶ Rosa *et al.* demonstrated that overexpression of G6PDH increases NADPH levels, improves whole-body glucose tolerance, and enhances electrical β -cell activity.⁹⁴ To gain a comprehensive understanding of the initial stages of glucose metabolism, future studies should also investigate the activity of the phosphofructokinase, which catalyses the phosphorylation of fructose-6-phosphate and is recognised as the rate-limiting step of glycolysis.⁴¹⁵

Another possible explanation for the *Taz*-KD Ca^{2+} phenotype could be differences in the available ATP pool. It has been shown that mainly glycolysis-derived ATP from pyruvate kinase causes the initial closing of the K_{ATP} channels.²²³ Measurements of ATP levels showed similar basal cellular levels for WT and *Taz*-KD (**Figure 4.14**). Additionally, calculations based on OCR measurements displayed no changes in the mitochondrial ATP level for a specific mitochondrial stress test protocol (**Figure 4.11**). However, it is still plausible that the ATP origin or dynamics might be different among the genotypes, and enhanced glycolysis-derived ATP molecules upon glucose-stimulation would result in a quicker closure of the K_{ATP} channels. Furthermore, the observed increase in the available NAD(P)H pool in *Taz*-KD can be attributed to faster Ca^{2+} dynamics (**Figure 4.9**). A higher NADH pool would promote quicker recruitment of ATP, while NADPH serves as a substrate for NOX4-mediated H_2O_2 production. Both molecules can also be interchanged by the mitochondrial nicotinamide nucleotide transhydrogenase (NNT), which is crucial for metabolism and redox signalling in all cell types.²⁶³ The NNT is the critical genetic difference in the most common mouse background strains C57BL6/N and C57BL6/J. Therefore, genotyping experiments confirmed the NNT expression in all used mice strains (**Figure 3.4**).

To test if the altered Ca^{2+} influx is related to differences in organelle Ca^{2+} levels, mitochondrial and ER Ca^{2+} concentrations were assessed. It has been published that cardiomyocytes of sh*Taz* mice exhibited an impaired mitochondrial Ca^{2+} import, which was due to decreased protein levels of mitochondrial Ca^{2+} uniporter (MCU).^{35,128} The MCU stability was found to be tissue-specific and decreased levels were observed in the heart and to a lesser extent in

skeletal muscle but not in brain tissue.³⁵ In this study, no difference in MCU protein levels was found and the linked mitochondrial Ca^{2+} dynamics were similar in WT and *Taz*-KD pancreatic islets (**Figure 4.31** and **Figure 4.17**). The tissue-specific MCU stability might be explained by differences in cellular CL composition.¹⁴³ It is worth mentioning that the used mitochondrial sensor Mito-Pericam has a relatively low Kd value of 1.7 μM and hence, a high affinity towards Ca^{2+} .²⁶⁰ Although a glucose-induced Ca^{2+} influx was observed, it is not possible to exclude a saturation of the sensor which may cover *Taz*-KD related changes in the mitochondrial Ca^{2+} dynamics. Therefore, other mitochondrial Ca^{2+} transporters could still be involved in the altered cytosolic Ca^{2+} influx in *Taz*-KD. The mitochondrial $\text{Na}^+/\text{Ca}^{2+}$ exchanger (NCLX) and the Ca^{2+} /proton exchanger (LETM1) were shown to impact pancreatic islet function and are involved in mitochondrial Ca^{2+} extrusion and sequestration, respectively.^{10,265} Intriguingly, CL was suggested to participate in NCLX regulation and LETM1 stabilisation as LETM1, which is involved in mitochondrial cristae organisation (further discussed in **Chapter 5.2**) was absent in BTHS patient fibroblasts.^{70,211}

The ER Ca^{2+} regulation orchestrated by the sarcoplasmic/endoplasmic reticulum Ca^{2+} ATPase (SERCA) has enormous implications on pancreatic islet function.⁴²⁵ Ravier and colleagues found that SERCA-mediated Ca^{2+} pumping is responsible for the initial drop in cytosolic Ca^{2+} levels which directly follows the glucose stimulation.²⁹¹ Additionally, the close connection of mitochondria and ER via specialised domains termed mitochondria-associated membranes to ensure the transfer of Ca^{2+} and phospholipids among the organelles, could suggest an involvement of ER in the BTHS phenotype.²⁴² Indeed, a pre-activation of SERCA was recently found in *Taz*-KD cardiomyocytes.³⁵ Therefore, ER Ca^{2+} dynamics were investigated using the probe D4ER. While a slightly decreased (not significant) Ca^{2+} concentration in ER was observed, the ER Ca^{2+} dynamics upon stimulation with glucose were preserved in *Taz*-KD pancreatic islets (**Figure 4.17**).

Apart from intracellular factors contributing to Ca^{2+} homeostasis, intercellular communication among islet cells also regulates Ca^{2+} dynamics and pancreatic islet function. Intercellular communication in pancreatic islets includes autocrine and paracrine signalling, the extracellular matrix, and tight and gap junctions.²⁶² The individual pancreatic islet cells are electrically coupled via gap junctions, and glucose-stimulated depolarisation propagates across the pancreatic islet starting from single hub β -cells.¹⁸² Therefore, the pancreatic islet architecture (introduced in **Chapter 1.2.1**), including the arrangement and number of the different cell types and the mentioned intercellular communication factors could be responsible for the observed changes in *Taz*-KD pancreatic islet function. Therefore, the cytosolic Ca^{2+} dynamics of intact and dispersed pancreatic islet cells were compared (**Figure**

4.15). Surprisingly, the dispersion of *Taz*-KD pancreatic islets before measuring the cytosolic Ca^{2+} levels almost completely recovered the WT Ca^{2+} phenotype. It is important to note that this observation does not automatically exclude all the intracellular factors discussed above, as single β -cells do not respond the same as β -cells part of the pancreatic islet as a functional unit.²⁶² The process of GSIS in dispersed and intact pancreatic islets has some fundamental differences, as some key features are lost in the dispersion process, including diminished electrical activity, decreased dynamic range of insulin secretion, and impaired paracrine signalling.^{262,309} Therefore, the modified GSIS process in dispersed pancreatic islets might not be as strongly affected by *Taz*-KD-mediated intracellular changes. Furthermore, extracellular redox signalling is rarely discussed in the literature but might play a significant role in the pancreatic islet function. NOX enzymes together with the extracellular matrix protein SOD3 can generate H_2O_2 outside the cell which either be taken up by the producing cell, diffuse inside a neighbouring cell, interact with the extracellular matrix (ECM) or oxidise protein in the plasma membrane (introduced in **Chapter 1.2.3**). Post-translational modifications of the ECM by redox reactions have been found to regulate ECM structure and function.³⁰² Additionally, the ECM impacts pancreatic β -cell proliferation and survival.³⁷² Therefore, in the view of increased NOX4-mediated H_2O_2 production, it is conceivable that extracellular H_2O_2 plays a role in the *Taz*-KD phenotype. Future measurements of extracellular H_2O_2 kinetics using sensitive electrochemical approaches can be crucial to test this hypothesis.⁵³

When comparing the Ca^{2+} graphs of intact and dispersed pancreatic islets independent of the described *Taz*-KD differences, a generally faster cytosolic Ca^{2+} influx in dispersed pancreatic islets is observed. This is likely due to the absence of a glucose gradient into the 3D-pancreatic islet tissue. Additionally, the dispersed islets did not exhibit a pronounced initial drop in cytosolic Ca^{2+} levels, which was noticeable in the intact pancreatic islets. Although the dispersed pancreatic islet cells do not accurately represent the functional *in vivo* status in the same way as intact pancreatic islets, they still provide critical information about potential intercellular changes in *Taz*-KD that contribute to the cytosolic Ca^{2+} phenotype.

If the pancreatic islet architecture of WT and *Taz*-KD pancreatic islets is compared, an increased number of α -cells and a slightly reduced number of β -cells were found in *Taz*-KD (**Figure 4.6** and **Figure 7.5**). The higher number of α -cells was accompanied by a significantly increased glucagon secretion as well as a slight enrichment in glucagon content of *Taz*-KD (**Figure 4.18**). Therefore, the differences in cytosolic Ca^{2+} influx might also result from the altered islet architecture and the potentiated glucagon-induced α - to β -cell communication in *Taz*-KD. This would explain why the phenotype was nearly abolished in dispersed pancreatic

islets. Previous studies found that glucagon released from α -cells can stimulate the activity of pancreatic β -cells via glucagon receptors that reside on pancreatic β -cells.^{66,125,168,356} Furthermore, treatment of pancreatic islets with glucagon receptor or glucagon-like peptide-1 receptor (GLP1-R) antagonists abolished first phase of GSIS.⁵⁸ Recently (2024), Suba *et al.* published a study on a newly generated β -cell specific glucagon receptor KO mice (glucagon receptor ^{β -cell^{-/-}}), and its pancreatic islet phenotype.³⁵² They discovered that pancreatic islets from the glucagon receptor ^{β -cell^{-/-}} showed uncoordinated Ca^{2+} waves, and each Ca^{2+} wave had a reduced influx velocity, which impaired GSIS.³⁵² Interestingly, paracrine interactions of glucagon, somatostatin, and insulin were found to fine-tune the glycemic set point, which defines normoglycemia. Glucose levels below or above the glycemic set point lead to glucagon or insulin secretion, respectively.³⁰⁴ Taken together, the altered intra-islet communication via enhanced glucagon secretion is likely one of the main reasons for the observed cytosolic Ca^{2+} phenotype in *Taz*-KD pancreatic islets.

Insulin secretion in *Taz*-KD

The shape and amplitude of the biphasic GSIS curves were similar for both genotypes, with a slightly quicker first phase insulin secretion in *Taz*-KD pancreatic islets (**Figure 4.18** and **Figure 4.19**). The slightly quicker insulin secretion was probably connected to the described faster cytosolic Ca^{2+} influx in *Taz*-KD. It is important to note that the dynamic insulin secretion was measured from pooled samples every one or two minutes, whereas the Ca^{2+} dynamics were imaged every 5 seconds. This might explain why the Ca^{2+} experiments better resolve the time-dependent phenotype. Cole and colleagues also measured *ex vivo* insulin and glucagon secretion of the same shTaz mice model.⁸² They observed a decreased insulin secretion at 2.8 mM glucose, which was unchanged at stimulatory glucose conditions in *Taz*-KD pancreatic islets. This observation was connected to a 58% reduced mitochondrial respiration under low glucose conditions, which was also unchanged at stimulatory conditions in *Taz*-KD pancreatic islets. It remains puzzling why the claimed defective mitochondria in *Taz*-KD pancreatic islets only reduced respiration and insulin secretion under low glucose conditions, where the mitochondria are not challenged. Other studies found the largest differences in OCR when the *Taz*-KD tissue was metabolically challenged. In Bertero *et al.* 2021, *Taz*-KD cardiomyocytes were treated with increasing concentrations of ADP to accelerate the electron flux through the ETC, and only concentrations above 0.3 or 1 mM ADP significantly diminished the measured OCR.³⁵ Another study found no difference in resting metabolism, but a severe deficiency in OCR during exercise when measuring respiration of whole *Taz*-KD mice.²⁸⁵ Furthermore, basal respiration was found to be increased in a BTHS model of induced pluripotent stem cell-derived cardiomyocytes.³⁹⁵ In

this thesis, decreased insulin secretion was only observed for the *in vitro model* at stimulatory conditions of 20 mM glucose (**Figure 4.39**, further discussed in **Chapter 5.6**). However, for the lifelong doxy-fed *Taz*-KD model, no difference in insulin secretion was observed and in low glucose conditions higher OCR was measured (**Figure 4.11**). The higher OCR in low glucose conditions might be connected to the increased number of α -cells, which are known to be still active at low glucose concentrations, likely through fatty acid and amino acid oxidation (further discussed in **Chapter 5.4**).

Islet composition in *Taz*-KD

Although a slight reduction in *Taz*-KD β -cell number was found when single pancreatic islets were compared, the insulin content was similar among the genotypes. This may suggest potential changes in pancreatic islet heterogeneity, indicating the existence of several subpopulations of pancreatic β -cells with varying transcriptional profiles.¹¹ Therefore, some β -cells can have a higher insulin content than others, and some even express α -cell markers.³⁰ Cole *et al.* did not observe differences in β -cell number and insulin content.⁸² As mentioned earlier, they reported a reduced basal insulin secretion. Additionally in their study, similar glucagon secretion was noted for WT and *Taz*-KD, while the glucagon content was strongly decreased in *Taz*-KD pancreatic islets.⁸² The reduction in glucagon content is astonishing, given that, like in this thesis, they found an increased α -cell mass in *Taz*-KD pancreatic islets. They did not elaborate further on this contradiction of increased α -cell mass but decreased glucagon content. Another difference to this thesis is that in Cole *et al.*, the increase in α -cell mass was only present after 10 months of age, and the α -cell number at 4 months of age showed no difference in *Taz*-KD compared to WT controls.⁸² They do not explain the increase in α -cell mass later in the discussion. Possible reasons for the enhanced α -cell mass and the connected increased glucagon content in *Taz*-KD pancreatic islets in this thesis will be discussed in the following paragraphs.

To understand the differences in pancreatic islet composition, the proliferation marker Ki67, the apoptosis marker cleaved caspase-3, and the β -cell specific maturation marker PDX-1 were tested (**Figure 4.7** and **Figure 7.6**). The IHC stainings of Ki67 and cleaved caspase-3 did not reveal differences between the genotypes, and hence, it is unlikely that the islet cell composition phenotype resulted from changes in neogenesis or cell death. During the development of the pancreas, the mature endocrine pancreatic islet cells arise from cell type-specific differentiation driven by complex regulation of various gene expression levels.¹⁷³ PDX-1 plays a crucial role in the β -cell specific maturation process, but the IHC staining levels were similar among the genotypes. However, several other proteins are also involved in this process, and it is still plausible that defects in early pancreas development caused enhanced

α -cell number. One vital component is neurogenin3 (NGN3), as its temporal activation predicts the fate of the endocrine cells. Early activation of NGN3 leads to α -cell differentiation, whereas activation later during the developmental process triggers β - or δ -cell maturation.¹⁷⁹

After the maturation process, the adult pancreatic islets can still change islet cell composition based on functional plasticity and β - to α -cell transdifferentiation.³⁶¹ The β - to α -cell transdifferentiation was previously observed in models of diabetes and insulin resistance.³⁶⁰ However, β - to α -cell transdifferentiation and continuous α -cell proliferation in pancreatic islets was also found independent from diabetes in a subset of young adults.²¹⁸ The pancreatic islet plasticity is based on changes in transcription factors that are induced by environmental cues.⁹³ The environmental factors include metabolic and oxidative stress or alterations in whole-body metabolism.^{124,268} In the context of metabolic and oxidative stress, β -cell dedifferentiation, which includes the loss of several β -cell specific metabolic proteins (among others, insulin, PDX-1, GLUT2 and Gck), is a huge topic in the progression of diabetes.⁴⁰⁶ Considering these previous studies, it is challenging to determine if the *Taz*-KD-mediated changes are directly caused by *Taz*-KD or secondary triggered via systemic glucose alterations. However, based on the minor whole-body glucose changes in *Taz*-KD (further discussed in **Chapter 5.2**), it can be assumed that the pancreatic islet composition is directly influenced by *Taz*-KD. This is possibly due to the stressed conditions of the cells and potential long-term adaptation processes (further discussed in **Chapter 5.7**). Cell-type specific *Taz* expression levels or different *Taz* isoforms in α - or β -cells might be one explanation for the cell-type specific phenotype (further discussed in **Chapter 5.1**).

Glucagon secretion in *Taz*-KD

The amplification of the α -cell mass was accompanied by an increase of glucagon secretion in *Taz*-KD pancreatic islets (**Figure 4.18**). Notably, the glucagon secretion was still enhanced (not significant, $p = 0.08$) after normalisation to the increased glucagon content (**Figure 7.10**). This means that the increased glucagon secretion might be connected to an enhanced α -cell function of *Taz*-KD pancreatic islets. The α -cell function and glucagon secretion can be regulated by several systemic and intracellular factors. While the systemic factors including among others, amino acids, incretins, and ketone bodies are well studied, the intracellular regulators are similar to the exact model of glucagon secretion still vastly elusive. A recurrent regulator is cAMP which has been shown to regulate glucagon secretion via protein kinase A.¹⁶⁷ Future studies should investigate the role of cAMP and protein kinase A in *Taz*-KD. Another possible regulator of glucagon secretion could be the altered plasma and mitochondrial lipid composition in *Taz*-KD (**Figure 4.32**). However, how the lipid composition affects α -cell function is currently unknown. BTHS heart samples perform a metabolic switch

from fatty acid oxidation to glycolysis which in turn increases the circulating levels of non-esterified fatty acids (NEFA).⁷⁵ One interesting thought is that NEFA, which are recently found to be heavily involved in the process of glucagon secretion (introduced in **Chapter 1.2.2**), play a crucial role in the *Taz*-KD glucagon phenotype. NEFA are considered to be the most metabolically active lipids in blood and were found to be significantly upregulated in plasma of BTHS patients (summarised in **Chapter 1.1.2**). Recent findings suggest that α -cells rely on fatty acid oxidation for ATP production at low glucose conditions.⁵⁷ In a condition of increased circulating NEFA and hypoglycemia, one might assume that α -cell activity is enhanced. It is unknown how fatty acid oxidation is regulated in α -cells, but increased fatty acid oxidation in *Taz*-KD α -cells could explain the increase in glucagon secretion. Although, no increase in dependency or capacity of whole pancreatic islets from fatty acid in the seahorse flex test was observed, but the measurements were performed in presence of 10 mM glucose as this was the recommended glucose concentration from the company and to be comparable to the culturing conditions. Recent data showed a significant downregulation of fatty acid oxidation in higher glucose concentrations (from 1 mM to 5 mM).¹⁸ Future experiments of glucagon secretion and seahorse in the presence of carnitine palmitoyltransferase 1 (CPT1) inhibitor, such as etomoxir (described in **Chapter 3.8.3** and **Figure 3.11**) in low glucose conditions would help to investigate the impact of fatty acid oxidation in glucagon secretion of *Taz*-KD pancreatic islets.

The *Taz*-KD induced differences in α -cell number and *ex vivo* glucagon secretion may have major implications on the whole-body phenotype. Although, only tendencies were measured with no significant differences in plasma glucagon or insulin levels in the GTT. Plasma glucagon homeostasis could still be affected by the changed α -cell mass in various conditions, such as with other nutrients (fatty acids or amino acids), circulating hormones like incretins, fasting and neuronal factors.

5.3 Metabolic and whole-body phenotype in BTHS

CL has various tasks in mitochondrial energetics, apoptosis and autophagy.^{2,77} The strong implications on mitochondrial energetics naturally make CL a decisive factor for cell and whole-body metabolism. Along those lines, CL has been associated with diabetes and other metabolic diseases.^{148,400} Another study showed that CL is a hallmark of diabetes progression as alterations in myocardial CL content occurred at the first stages of diabetes.¹⁴⁴ To get more insight into systemic consequences of altered CL profile on the whole-body phenotype,

bodyweight analysis and GTT were performed., and the results were put into perspective with the acquired *ex vivo* measurements. Whole-body analyses provide more comprehensive results than experiments on primary cells or isolated organs. The reason is that the organism is always more than the sum of its single pieces. This is due to inter-organ connection and communication. However, the systemic characteristics can be complex to untangle and different from the results observed on isolated tissues.

The bodyweight of WT and *Taz*-KD mice was evaluated at 10, 20 and 50 wo of doxy diet (**Figure 4.3**). The lower body mass in *Taz*-KD compared to WT mice at 20 and 50 wo is in agreement with previous studies on *Taz*-KD mice and was linked to hypermetabolism due to elevated heat production and increased energy consumption.^{35,81} Additionally, studies in patients have shown that individuals with BTHS are below the 10th percentile for weight at 20 years of age and have a lower fat-free mass combined with a greater insulin-stimulated glucose disposal rate.^{59,301} The improved glucose tolerance seen in the GTT might be linked to the higher glucose disposal rate (**Figure 4.4**). This increased glucose disposal rate might result from the amplified glucose uptake, as observed in 20 wo *Taz*-KD pancreatic islets (**Figure 4.8**). The observation was consistent with previous findings of amplified glucose uptake in other *Taz*-KD tissue.²¹⁵ Furthermore, the glucose utilisation in BTHS patient samples was found to be significantly enhanced.⁶¹ GLUT4, but not GLUT1 was found to be increased in *Taz*-KO mouse embryonic fibroblasts.²¹⁵ In this study, the pancreatic β -cell specific GLUT2 was similar for both phenotypes (**Figure 4.8**). Several studies suggested that GLUT1 might be the primary glucose transporter in pancreatic α -cells and ectopic expression of GLUT1 in GLUT2 β -cells could restore GSIS.^{32,150,353} Therefore, GLUT1 levels would be interesting to test in *Taz*-KD pancreatic islets. Furthermore, inhibition of glycolysis using 2-DG is a common tool, but future studies could also investigate more specifically the increased glucose uptake in *Taz*-KD by using phloretin.³⁶⁶ Back to the GTT data, the blood glucose levels of the WT mice did not return to starting values after 120 min which might indicate a start from a developing insulin resistance (**Figure 4.4**). Insulin resistance after 10 months of age using control mice from the same model treated with lifelong doxy or treated with a high-fat diet was previously described.¹⁰⁷ In the mentioned study, the *Taz*-KD mice were protected from the development of insulin resistance during a high-fat diet. In this thesis, the plasma glucagon and insulin levels were not statistically different (**Figure 4.4** and **Figure 7.4**). However, the glucagon response upon stimulation with glucagon was slightly increased ($p = 0.06$) in *Taz*-KD pancreatic islets. So far, no difference in plasma glucagon levels of BTHS patients has been reported. Recently, it has been shown that the most potent nutrient stimuli of glucagon secretion are not glucose levels but instead, amino acids.¹⁴ BTHS patients exhibit altered circulating levels of amino acids with a strikingly common decrease in arginine

(introduced in **Chapter 1.1.2**). Also, decreased levels of branched-chain amino acid metabolism have been reported in BTHS and supplementation with amino acids improved the observed phenotype.¹⁶ These alterations in circulating amino acids can influence the plasma glucagon and insulin levels and, hence, need to be considered in diet suggestions. Especially because glucagon was shown to effectively enhance energy expenditure and lower food intake, which would be detrimental as the children already suffer from slow weight gain.⁹ Furthermore, excessive glucagon secretion in *Taz*-KD mice can lead to a potential hyperglucagonemia, which has been shown to play an important role in the pathogenesis of diabetes.⁸⁸

Incretin signalling is another crucial factor in regulating pancreatic islet function and whole-body glucose metabolism. The gastric inhibitory polypeptide receptor (GIPR) and glucagon-like peptide-1 receptor (GLP-1R) are expressed in the pancreatic islets and are directly involved in insulin and glucagon secretion.⁶³ While the GLP-1R is only expressed on β - and δ -cells, GIPR is also expressed on pancreatic α -cells.³³⁶ Despite the low expression GLP1 signalling reduces glucagon secretion by inhibiting voltage-dependent Ca^{2+} channels in α -cells.²⁹⁰ On the other hand, GIP signalling in α -cells potentiates glucagon secretion and regulates insulin secretion by activating paracrine α - to β -cell communication.¹⁰⁸ There is currently no data about incretine signalling in BTHS and future studies should consider possible effects on whole-body glucose homeostasis. In discussing paracrine signalling in general and its implications on BTHS phenotype, one must carefully consider the differences between mice and human pancreatic islets (introduced in **Chapter 1.2.1**). The α - to β -cell communication through which glucagon can stimulate insulin secretion was, to date, mostly described in rodents and might be heavily affected by the islet architecture. One key aspect is the intraislet blood flow, which is traditionally viewed from the core-to-mantle model.⁴⁵ Therefore, the intraislet blood flow would limit the communication between endocrine cells.⁴⁰² However, this dogma seemed to be questioned as several studies reported bidirectional blood flow.⁶² Also the striking plasticity of human islet architecture suggests strong reciprocal paracrine interaction of human pancreatic islet cells.¹⁵⁹ Future studies on human islets must further evaluate the paracrine signalling in human islets and the transferability of paracrine pathways identified in rodents to the human situation.

A major observation throughout this thesis was that several metabolic parameters were amplified in *Taz*-KD pancreatic islets. These include the lean phenotype (**Figure 4.3**), the improved glucose tolerance (**Figure 4.4**), the enhanced glucose uptake (**Figure 4.8**), the higher NAD(P)H levels (**Figure 4.9**), the faster cytosolic Ca^{2+} dynamics (**Figure 4.15**), and the higher SRC in low glucose of *Taz*-KD mice (**Figure 4.11**). Mitochondrial diseases are

often associated with a state termed hypermetabolism.³⁵¹ Many other symptoms of BTHS that are not discussed in this thesis also fit to the description of hypermetabolism, such as fatigue, defective OXPHOS, and excess energy expenditure.¹¹⁵ Patients with mitochondrial diseases are rarely obese, which might be caused by the substantial increase in energetic demand to sustain basic physiological functions.¹⁶³ Therefore, it is crucial that nutritional levels of BTHS patients are properly controlled to be able to compensate for the inefficient energy turnover rate inside their cells (compensatory mechanisms are summarised in **Chapter 5.7**). Furthermore, the observed increase in mitochondrial volume was also found to result from mitochondrial disorders and is predicted to exaggerate metabolic demands even further because of the extensive mitochondrial proteome (**Figure 4.28**).^{160,390}

Hypermetabolism is often associated with a glycolytic shift, which leads to enhanced lactate production.^{318,351} Several BTHS patients showed lactic acidosis, especially during exercise (introduced in **Chapter 1.1.2**). Additionally, a recent study found that lactate can support K_{ATP} channel closure and stimulate oscillations in pancreatic β -cells.¹⁵⁸ To test for increased acidification in *Taz*-KD pancreatic islets, pH measurements using the ratiometric SypHer probe and ECAR levels were evaluated (**Figure 4.20**). Similar acidification levels for WT and *Taz*-KD pancreatic islets were observed. Lactate levels might still play a crucial role in the human BTHS phenotype as lactate accumulation is six-fold higher in humans compared to mouse pancreatic islets.⁸⁹ Furthermore, plasma lactate levels were not measured in this study but could still influence pancreatic islet function. It becomes increasingly apparent that lactate has cell type-specific effects on pancreatic α - or β -cells. The expression of lactate dehydrogenase A is six times higher in pancreatic α - than β -cells.³¹⁹ Moreover, lactate was shown to inhibit glucagon secretion by affecting the plasma membrane potential.⁴²³ Taken together, the measured rise in α -cell mass could be a compensatory pathway of *Taz*-KD mice to diminished α -cell activity and, hence, secondary to increased circulating lactate levels (further discussed in **Chapter 5.7**). Future studies should evaluate the cell type-specific (α -, β - and δ -cells) acidification rate in *Taz*-KD pancreatic islet samples to assess the pH levels more accurately.

Another common symptom of BTHS patients was hypocholesterolemia (**Table 1.2**), which might be connected to an interaction of CL and cholesterol biosynthesis in the human body.²⁵⁶ The rate-limiting cholesterol desmolase enzyme, cytochrome P-450 subfamily A member, is localised in the inner mitochondrial membrane where it can bind to CL and catalyses the oxidative side chain cleavage of cholesterol.²⁷⁶ The interaction of CL and cholesterol desmolase improves substrate binding.²¹⁹ Furthermore, CL synthesis has been found to be required for human cholesterol biosynthesis from palmitate in Hela cells.¹⁴⁷ Also a *Taz*-KD

mice model showed decreased plasma concentrations of very low density lipoprotein triacylglycerols and low density lipoprotein-cholesterol concentration.⁸¹ In *Taz*-KD pancreatic islets in this thesis, similar levels of cholesterol esters (CE) compared to WT controls were found (**Figure 4.32**). Interestingly, RNA-Seq analysis revealed a significant downregulation of ApoE (**Figure 4.34**), which mainly functions in lipoprotein-mediated lipid transport and was found to maintain pancreatic β -cell gene expression.²³⁷ Given the crucial role of cholesterol in keeping metabolic balance via the synthesis of steroid hormones, vitamin D, and bile acids, further highlighted in its importance in the progression of diabetes (increase in low-density-lipoprotein and a decrease in high-density-lipoprotein), future diets should carefully consider cholesterol supplementation.²⁷⁸

Other organs not covered in this thesis may also be crucial in the BTHS phenotype. In the context of metabolic changes, the intestines, liver, adrenal glands, and pancreas are the main players.

5.4 *Taz*-KD mitochondria of pancreatic islet cells

Since CL is exclusively found in the inner mitochondrial membrane (in physiological conditions), the mitochondria are the primarily affected organelles in dysregulated CL remodelling.¹⁰⁴ Additionally, the mitochondrial redox homeostasis was heavily linked to the CL content.²⁷⁵ Therefore, several experiments were performed to evaluate mitochondrial function, morphology, and redox signalling in *Taz*-KD pancreatic islets, which will be discussed in the following paragraphs.

Mitochondrial respiration of *Taz*-KD

The primary function of mitochondria is to provide energy via aerobic respiration. BTHS phenotype is linked to decreased ATP production based on impaired mitochondrial energetics. Another vital function of mitochondria is its role in cellular Ca^{2+} homeostasis which is discussed in the context of *Taz*-KD in **Chapter 5.2**.

Mitochondrial respiration of WT and *Taz*-KD pancreatic islets was evaluated by OCR, mitochondrial membrane potential and ATP levels. In the OCR measurements, higher SRC and proton leakage under low glucose conditions were observed in mitochondria from *Taz*-KD mice (**Figure 4.11**). The increased SRC might be connected to the significantly higher NAD(P)H levels (**Figure 4.9**) because FCCP uncouples the proton gradient and, hence, the SRC reflects the ability of the cells to maximise their OCR. The higher proton leak could be

due to slightly uncoupled respiration in *Taz*-KD, which is likely linked to less efficient respiration and more heat production. A higher proton leak was also previously observed in an induced pluripotent stem cell BTHS model.³⁹⁵ The OCR under higher glucose conditions (10 and 20 mM) were similar among the genotypes (**Figure 4.11**). In agreement with the OCR results, mitochondrial membrane potential normalised to the uncoupler CCCP and basal ATP levels were similar in 20 mM *Taz*-KD and WT pancreatic islets (**Figure 4.13** and **Figure 4.14**). It is worth noting that only the ATP levels of the WT group, but not the *Taz*-KD group, increased with the use of mitochondrial drugs (**Figure 4.14**). Previous studies have demonstrated that RSV and SS-31 can enhance mitochondrial function in other tissues.^{64,217} Furthermore, SS-31 was shown to reduce pancreatic islet apoptosis and improve functionality after pancreatic islet transplantation in mice treated twice daily for ten days with SS-31. The inability of *Taz*-KD pancreatic islets to improve upon SS-31 treatment is surprising, given its positive results on cardiac parameters in the patient trial of BTHS.^{161,292,370} This might be due to the mechanism of the protective effects of SS-31 by binding to mature CL. The CL profile of heart tissue and pancreatic islets is different, and compared to the heart, *Taz*-KD pancreatic islets only have slightly reduced CL content, with the main difference being in the CL profile. Moreover, long-term treatment with SS-31 *in vivo* might have a more positive effect on *Taz*-KD mitochondria than only a 24 h treatment *in vitro*.³⁶⁸ RSV is known to upregulate the expression of sirtuins, which can positively affect autophagy and cellular energy metabolism.³⁷⁹ Moreover, sirtuins can influence the mitochondrial morphology and SIRT6 deficiency in pancreatic β -cells led to increased number of damaged mitochondria.^{288,409} However, upregulation of autophagy leading to mitochondrial degradation might not be beneficial for *Taz*-KD pancreatic islets as enhanced mitochondrial volume seems to be a compensatory mechanism in *Taz*-KD that helps to protect the mitochondrial function (further discussed in **Chapter 5.7**). Therefore, RSV might not support adaptation effects and, hence, did not improve mitochondrial functionality in *Taz*-KD pancreatic islets. Furthermore, glucolipotoxicity conditions of 20 mM glucose and 100 μ M palmitate significantly decreased the ATP levels in WT but not *Taz*-KD pancreatic islets (**Figure 4.14**). This might result from hypermetabolism in *Taz*-KD pancreatic islets, increasing the energy demand and, hence, resulting in less accumulating nutrients. This is supported by the observation that the *Taz*-KD mice exhibit a lean phenotype (**Figure 4.3**). A mitochondrial nutrient dependency and capacity test revealed no metabolic shift in *Taz*-KD mitochondria from glucose towards amino acids or fatty acids as nutrient sources (**Figure 4.12**). However, it is important to point out again that the nutrient dependency and capacity test were performed in presence of 10 mM glucose, which might repress other metabolic pathways (further discussed in **Chapter 5.2**). Interestingly, OCR normalised by mitochondrial volume was reduced in *Taz*-KD due to the

increased mitochondrial volume (*Taz*-KD mitochondrial volume was increased by 54.6 %), reflecting a reduced effective OCR per mitochondrion (**Figure 7.13**). Cole *et al.* also measured respiration from isolated *Taz*-KD pancreatic islets but acquired different results.⁸² As elucidated in **Chapter 5.2**, they observed a decreased basal respiration but no differences under stimulating glucose conditions.

Mitochondrial morphology of *Taz*-KD

While mitochondrial fission precedes the turnover of unhealthy or old mitochondria through mitophagy, maintaining a well-connected mitochondrial network by mitochondrial fusion is crucial for exchanging metabolites and substrates and, hence, for optimal metabolic activity.³⁷⁶ Alterations in mitochondrial morphology, including defective cristae formation or mitochondrial dynamics (fission and fusion), are one of the main characteristics of the BTHS phenotype (introduced in **Chapter 1.1.1**).¹⁰⁴ A defect in mitochondrial network structure and dynamics of pancreatic β -cells has been linked to impaired insulin secretion.¹⁹⁰ Furthermore, pancreatic β -cells from diabetic patients were associated with abnormal mitochondrial morphology, indicated by fragmented or swollen mitochondria.²²⁹

There is little literature on mitochondrial network analysis of single pancreatic islet cells. Chaudhry *et al.* created 2020 a pipeline for 3D confocal imaging analysis of mitochondrial networks from pancreatic β -cells using Min6 cells and also the first morphological data on dispersed mouse pancreatic islet cells. Our study was based on the protocol described in Chaudhry *et al.*, and the mitochondrial network of *Taz*-KD pancreatic islet cells was evaluated using the dye Mitotracker (**Figure 4.28**). Mitotracker is a commonly used fluorescent probe to assess mitochondrial volume because it accumulates inside the mitochondria regardless of the mitochondrial membrane potential.⁹⁷ However, it has some limitations as its accumulation was found to be dependent on the cellular redox state, and it may be more prone to target highly active mitochondria.^{261,323} Another popular approach to determine mitochondrial volume is with nonylacridine orange.⁹⁷ Nonylacridine orange was even shown to be independent from mitochondrial and cytosolic ROS, but it binds to cardiolipin which makes it unsuitable for a *Taz*-KD model.²⁰⁰ To account for the limitations of Mitotracker in determining mitochondrial volume, citrate synthase activity was tested (**Figure 4.28**). Citrate synthase is an enzyme of the TCA cycle, and its activity reflects the amount of mitochondrial content, mostly tested in heart and skeletal muscle cells.³³⁹

In the experiments with Mitotracker and the citrate synthase activity assay, an increased mitochondrial volume was observed in *Taz*-KD pancreatic islets. Gonzalvez *et al.* also found an enhanced citrate synthase activity in BTHS cells and, hence, suggested that BTHS cells have a greater mitochondrial volume.¹³² Furthermore, in their study, the respiration and the

ATP/ADP ratio was unchanged in BTHS compared to control samples.¹³² The increased mitochondrial volume might either be caused by an accumulation of old mitochondria, amplified biogenesis of new mitochondria or combination of both. Autophagy, in general, and mitochondria-specific mitophagy are vital regulators of mitochondrial degradation. Therefore, using WB analysis, several autophagy and mitophagy markers were tested in *Taz*-KD pancreatic islets (**Figure 4.31**). A tendency towards reduced Atg7 levels in *Taz*-KD pancreatic islets was observed. Atg7, a key molecule for autophagosome formation, has been linked to the maintenance of islet architecture and insulin secretion.¹⁸⁸ Interestingly, Atg7 deficiency suppressed β -cell proliferation and increased α -cell mass.¹⁵⁷ Furthermore, significantly enhanced levels of LAMP1 and decreased levels of LAMP2 were observed in *Taz*-KD pancreatic islets. It has been shown that LAMP1 and LAMP2 share 37% sequence homology and have similar functions in autophagy and lysosomal biology.^{67,112} LAMP1 deficient mice compensate for the lack of LAMP1 protein by upregulation of LAMP2, suggesting analog functionality.¹³ However, LAMP2 deficiency causes a failure in macroautophagy leading to the multisystem disorder called Danon disease.³¹² Therefore, LAMP1 upregulation can only compensate partly for the loss of LAMP2.¹¹¹ The mitophagy markers PINK1 and Prk8 had slightly reduced levels (not significant) in *Taz*-KD pancreatic islets (**Figure 4.31 B**). Defective mitophagy with altered protein levels in the PINK1/Parkin pathway has been recently observed in heart tissue and isolated mouse embryonic fibroblasts (MEF) from *Taz*-KD mice.⁴²⁷ An important observation was the significant downregulation of LC3B-1 and LC3B-2 in *Taz*-KD pancreatic islets. LC3 has been referred to as a ubiquitin-like protein because it shares structural homology with ubiquitin. Of interest, ubiquitin C, a polyubiquitin precursor, was downregulated in bulk RNA-Seq of *Taz*-KD pancreatic islets (**Figure 4.34**). LC3 is a commonly used marker of autophagy, as it is a crucial protein in the autophagy pathway via autophagy substrate selection and autophagosome biogenesis.²¹³ In the process of autophagy, the cytosolic form of LC3 (LC3B-1) is conjugated with PE to form LC3-PE (LC3B-2). Therefore, the downregulation in LC3B-2 could be partly reflected in the upregulation of PE in *Taz*-KD pancreatic islets (**Figure 4.32**). However, LC3B downregulation can only vaguely indicate decreased autophagy because the marker has some issues in the analysis of autophagy flux. First, LC3B-2 itself is also degraded by autophagy. Second, measurements at certain time points do not account for differences in cell cycle state. Third, LC3B-2 tends to be more sensitive than LC3B-1 in WB analysis. To account for those limitations, future studies should include a lysosomal protease inhibitor and measure LC3B levels in the presence and absence of the inhibitor.²⁵⁴

In general, the lipid composition is crucial for initiating and regulating autophagy/mitophagy processes. While PE was upregulated, the phospholipid PC was downregulated in *Taz*-KD

pancreatic islets (**Figure 4.32**). As described in the introduction **Chapter 1.1.1**, the two most abundant phospholipid classes, PC and PE, can be used by Taz as acyl chain donors for CL remodelling. Therefore, a defect in the acyltransferase Taz might affect the levels and molecular composition of both phospholipids. Alterations in PC and PE levels are connected to defects in mitochondrial energetics, integrity and morphology.^{187,333} Similar to our results, the group of Balážová observed increased levels of PE and decreased levels of PC when Taz was absent, and PG was upregulated in the BTHS *pgc1Δtaz1Δ* yeast strain. In addition to that the species profiles of PE, PC and PG were altered but MLCL were unchanged in *Taz* deficiency.¹⁹⁷ In the study from Lu *et al.*, they found differences in length and saturation of acyl chains of PC and PE in the *taz*^{TALEN} mammalian cell model.²³³ Additionally, the species profiles of PC and PE but not the overall amount was identified to be different in heart, skeletal muscle and lymphoblasts from BTHS patients.^{328,410} Moreover, the crucial phospholipid PG which is a precursor form of CL (further described in **Chapter 4.7.1**) was upregulated in *Taz*-KD pancreatic islets (**Figure 4.32**). A recent study showed that the *Taz* deficient mammalian cell line *taz*^{TALEN} (TALEN-mediated genome editing within *Taz* exon 1) displays an increased abundance of PG compared to the control cells.²³³ Increased levels of PG were found to influence mitochondrial morphology and function.²⁸³ Furthermore, it has been suggested that the low content of PG in yeast might limit the power of yeast BTHS models, as CL and PG interplay might be necessary to mimic the complex human BTHS phenotype.¹⁹⁷ Interestingly, also in yeast, accumulation of PG at normal CL led to a more fragmented mitochondrial network. Instead, accumulation of PG in the absence of CL led to superfusion of mitochondria.²⁸³ These previous observations in yeast are in agreement with our observation as the analysis of the mitochondrial network revealed a superfusion of single mitochondria, which was reflected in a higher abundance of giant mitochondria and lower levels of small mitochondria in *Taz*-KD (**Figure 4.30**). Also, lower levels of CL and higher levels of PG were observed in *Taz*-KD pancreatic islets. Additionally, PG was shown to be able to substitute some of the functions of CL.¹⁷⁷ This might be one explanation for the mild phenotype with preserved insulin secretion in *Taz*-KD pancreatic islets and could be one of the compensatory mechanisms, which are summarised in **Chapter 5.7**. In line with this hypothesis is that high PG content correlates with an increased OCR, reported by Pokorna *et al.* and is also observed in this thesis under low glucose conditions with *Taz*-KD pancreatic islets.²⁸³

Moreover, increased mitochondrial fusion was previously observed in BTHS patient cells and connected to an upregulation of the cristae regulator OPA1.⁷⁰ The mechanistic insights about OPA1 and its activity dependency on CL have been recently elegantly described.³⁹¹ Furthermore, the scaffolding complex prohibitin was suggested to interact with CL and was shown to be upregulated in BTHS patient cells.^{70,299} Several other proteins, including MICOS,

Mitofusin1 and Mitofusin2, involved in the mitochondrial morphology and cristae formation have been shown to interact with CL (introduced in **Chapter 1.1.1**). On the other hand, Zhang *et al.* found more fragmented mitochondria in *Taz*-KD of MEF.⁴²⁷ Therefore, it becomes apparent that Taz-mediated remodelling is important for the execution of mitophagy, and mitochondrial morphology is heavily affected in models of BTHS. However, the exact affected process (fission or fusion) and the resulting consequence (hyperfusion or fragmentation) seem to be tissue-specific, which can be well explained by the tissue-specific differences in mitochondria themselves.

Alterations in mitochondrial morphology have huge implications on mitochondrial functionality.^{119,120} Based on the literature analysis, it appears that changes in mitochondrial morphology are a double-edged sword. On one side, enhanced mitochondrial fusion was attributed to increased OXPHOS, higher NAD⁺ production and less dependency on glycolysis.^{44,252} Moreover, parallel analysis of cell cycle and mitochondrial morphology revealed that mitochondria become transiently hyperfused at the G1–S transition, making them highly metabolically active by producing more ATP than in other cell cycle stages.²⁵³ On the other hand, excessive mitochondrial fusion caused by mutations in the mitochondrial fission protein, SLC25A46, was instead linked with decreased OXPHOS and reduced cell proliferation.⁴³⁴ However, the turning point at which OXPHOS improvement transitions to deterioration seems yet to be defined, possibly tissue-specific and influenced by environmental factors.

Mitochondrial redox homeostasis in *Taz*-KD

ROS are inevitably generated during aerobic metabolism, and excessive ROS production leads to oxidative damage. However, they also exert vital roles in the regulation and adaptation of the cellular metabolic state (introduced in **Chapter 1.2.3**).²⁵⁹ BTHS was massively associated with perturbations in the mitochondrial and cellular redox homeostasis.²³⁰ Therefore, in the past, antioxidants like coenzyme Q10 and vitamin E that reduce oxidative stress were considered to support mitochondrial health and alleviate the BTHS phenotype (Barth syndrome Foundation recommendations of medications for Barth syndrome patients).³⁵⁷

Due to its characteristics, H₂O₂ is likely the key ROS signalling molecule in the cell (explained in **Chapter 1.2.3**). Therefore, mitochondrial H₂O₂ levels of *Taz*-KD pancreatic islets were evaluated *ex vivo* (**Figure 4.22**) and *in vivo* (**Figure 4.24**) using the genetically encoded mito-roGFP2-Orp1 sensor. Whereas the *ex vivo* experiments revealed increased basal oxidation of *Taz*-KD pancreatic islets, the *in vivo* studies exhibited a reduced redox state compared to WT controls. Notably, the H₂O₂ kinetics, when normalised to starting levels, were similar

among the genotypes (**Figure 4.23**). Interestingly, this obvious discrepancy between the *ex vivo* and *in vivo* situation agrees with the contradictory findings from previous studies where increased ROS was found in most BTHS cell line models and isolated patient samples.^{279,324} In contrast, animal models (including our group and collaborators) do not exhibit redox changes.^{35,130} This discrepancy between *in vivo* and *in vitro* results can be explained by several factors. For the purpose of comparability, the performed *ex vivo* of primary tissue will be grouped with previous *in vitro* measurements, as the environmental conditions are similar in the two approaches. A key factor in the discussion *in vivo* or *in vitro*, is the difference in oxygen partial pressure. Tissues under *in vivo* conditions experience a much lower oxygen pressure (around 1 kPa) compared to atmospheric conditions (around 20 kPa), present in the *in vitro* experiments.¹⁹⁹ Culturing in atmospheric conditions is common practice but is termed hyperoxia by some scientists and was associated with stress response activation via Nrf2.³⁹⁹ Additionally, the higher oxygen pressure leads to higher substrate availability for NOX-mediated ROS production, which would fit the observed increased NOX4-mediated mitochondrial H₂O₂ production and slightly increased (not significant) NOX4 protein levels in *Taz*-KD pancreatic islets (**Figure 4.23** and **Figure 4.26**). Supporting this hypothesis, NOX4 was found to be present in the mitochondrial membrane.³⁸⁴ However, NOX4 was described as constitutively active and not regulated by substrate supply.³⁸⁷ Another crucial difference between *in vivo* and *in vitro* is that adaptation processes are usually much more robustly present in complex systems like a whole-body metabolism compared to isolated cells (adaptation processes are summarised in **Chapter 5.7**). This leads to the assumption that the *in vivo* pancreatic islets can compensate systematically. In support of this hypothesis, when stress was mimicked by blocking the Trx system by adding auranofin, the *Taz*-KD pancreatic islets tended to produce less ATP than WT controls (**Figure 4.14**). Therefore, the pancreatic islets may attempt to compensate for the consequences of the defective CL composition, which might be easier achieved *in vivo* than *in vitro*. Still, in situations with increased stress, the compensatory mechanisms might also collapse *in vivo*. This hypothesis could be tested by applying redox histology after starvation, exercise or any other challenging situation for the mice. For BTHS patients this means that they should pay special attention or implement additional measures (such as medications or relaxation breaks) when in stressful situations. Another possibility for the increased basal H₂O₂ in *Taz*-KD levels is oxidative stress generated during the pancreatic islet isolation procedure (described in **Chapter 3.2.1**), which might differ for WT and *Taz*-KD pancreatic islets. The variability could result from physical differences in pancreatic islet integrity or metabolic stress during the stepwise changes in oxygen and nutrient supply in the course of the isolation process.

To extend the redox analysis, WB analysis of crucial redox proteins, including parts of the antioxidative system and ROS production sources, were performed (**Figure 7.15**). Meanwhile, protein levels of Prx3, which is the mitochondrial form of the Prx family, were upregulated, and catalase levels were slightly downregulated. Catalase and Prx3 have different affinities towards H_2O_2 and, hence, act in different cellular H_2O_2 concentrations.^{298,8} Prx proteins have a very high affinity (nM – low μ M range) for H_2O_2 and, thus, are more involved in redox signalling processes.²⁹⁷ In contrast, catalase is more active at high H_2O_2 concentrations (μ M - mM range) to avoid oxidative stress.¹⁴⁹ Interestingly, targeted overexpression of catalase to mitochondria did not result in a rescue of the cardiomyopathy BTHS phenotype.¹⁸⁰ Therefore, the increased protein levels of Prx3 and also NOX4 in *Taz*-KD pancreatic islets indicate that amplified redox signaling and not oxidative stress might play an important role in BTHS phenotype.

Overall, although interesting, the differences in basal H_2O_2 were minor, not present *in vivo* due to the mentioned reasons, and most importantly, H_2O_2 kinetics were similar in both genotypes. Therefore, oxidative stress was not considered a major driver of the *Taz*-KD phenotype in pancreatic islets. However, amplified NOX4-mediated redox processes could have direct implications on pancreatic islet function which were further discussed in **Chapter 5.2**.

5.5 O-GlcNAc in *Taz*-KD pancreatic islets

Post-translational modifications of proteins offer the possibility to quickly adapt to changing environmental conditions with relatively few cellular resources and without major changes in RNA expression or protein composition.²⁹³ The post-translational glycosylation O-GlcNAcylation is highly dynamic, unlike other glycosylation pathways, that form rather rigid, branched glycan structures. The O-GlcNAcylation is regulated mainly by the O-GlcNAc transferase (OGT) and O-GlcNAcase (OGA), which add or remove GlcNAc to the protein residue, respectively (pathway is described in **Chapter 4.7.2**). Against the traditional view that glycosylation appears mostly on extracellular proteins, O-GlcNAc modifications occur on proteins localised in the cytoplasm, nucleus, and mitochondria.⁶⁹ Additionally, O-GlcNAc modifications are of particular importance for pancreatic islets due to their role in nutrient sensing.¹⁷⁸

When RNA levels of WT and *Taz*-KD pancreatic islets were compared using Reactome analysis of bulk mRNA-Seq, the O-GlcNAcylation pathway was significantly enriched in *Taz*-

KD (**Figure 4.34**). Furthermore, the upregulated genes encoding this hexosamine pathway resulted in a higher abundance of O-GlcNAc protein modification, analysed by WB and IHC in *Taz*-KD pancreatic islets (**Figure 4.35**). Therefore, the enhanced O-GlcNAc protein modification might play an important role in the *Taz*-KD phenotype. Interestingly, alterations in O-GlcNAc modifications have been connected to changes in mitochondrial morphology and function.²³⁸ Tan *et al.* found that elevated O-GlcNAcylation levels resulted in elongated mitochondria and increased mitochondrial membrane potential.³⁵⁹ Therefore, the protein modification O-GlcNAc might be the missing link between the metabolic and morphological phenotype of *Taz*-KD pancreatic islets. Previous measurements found similar levels of O-GlcNAc in proteins of *Taz*-KD hearts and *Taz*-KO MEF.²¹⁵ However, pancreatic islets seem to rely more on this pathway compared to most other tissues, which is apparent in the high expression levels of OGT in pancreatic β -cells.¹⁶⁹ Furthermore, the disruption of O-GlcNAcylation resulted in β -cell failure and the development of diabetes.¹² Therefore, the tissue-specific differences of O-GlcNAcylation might be one explanation for the tissue-specific phenotype in mitochondrial morphology (fragmentation or superfusion) of BTHS models. Another indication for the high abundance of O-GlcNAc modification in pancreatic islets was found when the O-GlcNAc intensity measured via IHC of pancreatic islets was compared to the surrounding exocrine tissue (**Figure 7.25**). The intensity of O-GlcNAcylation was significantly increased in endocrine compared to exocrine pancreas. The amplification of O-GlcNAc modifications might be associated with increased glucose uptake observed in *Taz*-KD pancreatic islets because the glucose is distributed into various pathways (**Figure 4.8**).

Alterations in O-GlcNAcylation have various implications on cellular metabolism and have been associated with beneficial as well as deleterious effects. Changes in O-GlcNAcylation have implications for diabetes and diabetic complications.²³⁴ Furthermore, excessive protein modification via O-GlcNAcylation has also been associated with heart failure.³⁷⁸ On the other hand, increased glycosylation in cancer cells gave them an explicit growth advantage by inhibiting phosphofructokinase activity and redirecting glucose through the PPP to produce NADPH.⁴²¹ Moreover, supplementation with D-glucosamine prolonged the life span in *C.elegans* and mice via increasing mitochondrial biogenesis, lowering of blood glucose and enhanced amino-acid catabolism.⁴⁰¹

More specifically for O-GlcNAcylation, an increase in O-GlcNAc protein modification reduced ROS generation and optimised mitochondrial function.¹³⁸ Intriguingly, sustained slight elevation of O-GlcNAc levels on proteins promoted weight loss in mice, and glucose deprivation resulted in upregulation of genes encoding in O-GlcNAc.^{359,364,433} These

characteristics make O-GlcNAcylation, together with the fact that a treatment-induced increase in O-GlcNAc via inhibition of OGA resulted in improvements in mitochondrial function, a crucial target for BTHS disease management. Future studies should investigate the protein levels of OGT and OGA in *Taz*-KD pancreatic islets and study the effects of activation or inhibition of O-GlcNAcylation on BTHS phenotype.

5.6 Comparison shTaz *in vivo* and *in vitro* model

Living organisms constantly adapt to the environment and can cope with several challenges with a broad set of compensatory mechanisms. Cellular adaption processes occur on different timescales, and it is essential to separate immediate consequences of a change in environment from mid- or long-term adaptations in response to the same stimuli. In order to get more insights into the direct effects of *Taz*-KD on pancreatic islet tissue and to account for some of the limitations of the *Taz*-KD model (introduced in **Chapters 1.1.4, 4.9**), a new doxy *in vitro* model was used in this thesis. One fundamental limitation of the *in vivo* model is the lifelong doxy feeding, which was found to have metabolic effects independent from BTHS and puts a substantial burden on the mice.^{162,405} Therefore, in the *in vitro* model, doxy was solely added after pancreatic islet isolation into the culturing medium of WT and *Taz*-KD pancreatic islets (method explained in **Chapter 3.1.2**). In the following paragraphs, the results of the *in vitro* shTaz model, will be compared to those from the *in vivo* shTaz model, which were discussed separately in more detail in **Chapters 5.1 - 5.5**.

The qPCR analysis could confirm *Taz*-KD in the *in vitro* model after 48 h of doxy treatment (**Figure 4.36**). Interestingly, the relative reduction in *Taz* RNA was comparable in both models, which suggested that the efficiency of *Taz*-KD in pancreatic islets was limited by other factors independent of doxy concentration and incubation time. The lipidome of *Taz*-KD pancreatic islets after 1-week of doxy incubation was assessed using lipidomics analysis. Surprisingly, CL content was found to be similar in *Taz*-KD pancreatic islets after 1-week of doxy culture (**Figure 4.36**). This might be due to the long half-life of mature CL (approximately 2 days) compared to other phospholipids.^{412,424} In line with the long half-life of CL, Xu *et al.* found that CL remodelling did not occur continuously but was rather closely coupled to *de novo* biosynthesis.⁴¹² Despite the lack of decreased CL content, several studies previously described that primarily CL profile and not content is decisive for the development of the BTHS phenotype.^{236,237,273} In this study, significant alteration in CL profile of *Taz*-KD pancreatic islets was observed after 1-week of doxy administration (**Figure 4.37**).

Interestingly, the CL profiles of *Taz*-KD *in vivo* and *in vitro* models have not changed in the same way (supplements, **Figure 7.19**). Instead of a decrease in CL 72:8 as seen in the *in vivo* model, the CL species 72:6, 72:7, 74:8, and 74:9 were reduced in the *Taz*-KD *in vitro* model compared to the WT controls. The available lipid environment provided by the medium (*in vitro* model) or the systemic circulation (*in vivo* model) as acyl chain donors for the CL remodelling process is crucial for the constitution of the plasma and mitochondrial membranes.^{241,267} Oemer *et al.* found that the availability of the linoleic acid fraction is reduced in RPMI supplemented with FBS.²⁶⁷ Furthermore, the *in vitro* incubation of primary tissue is known to induce gene expression changes.²¹² This is based on various environmental factors, including oxygen pressure, nutrient availability, and salt concentration, as well as the absence of tissue interconnection.³⁸⁰ In line with these arguments, the 1-week doxy incubation itself reduced total CL content and altered CL profile, independent from the absence or presence of *Taz*-KD (**Figure 4.36** and **Figure 7.19**). Future studies could improve the *Taz*-KD 1-week *in vitro* model by adjusting the lipid composition in the culture medium to better mimic *in vivo* conditions, modulate the CL profile, and study its impact on tissue function.

A PC analysis of the lipidome from all shTaz pancreatic islet samples confirmed the drastic effects of the 1-week culture on the lipid profile (**Figure 4.40**). This underscores the importance of using a proper WT 1-week *in vitro* doxy culture control to assess the impact of *Taz*-KD on pancreatic islets in the *in vitro* model. Furthermore, the full lipidome revealed that *Taz*-KD after 1-week doxy culture had only relatively little effect on the lipid class composition, and only the lysoplasmalogene LPC O- was significantly upregulated (**Figure 4.41**). Conversely, for *Taz*-KD in the *in vivo* model, LPC O- levels were found to be decreased compared to WT (**Figure 4.32**). Interestingly, deeper analysis of LPC O- revealed a changed double bond and carbon length profile in *Taz*-KD pancreatic islets (**Figure 7.21**). Lysoplasmalogens were described as toxic lipid intermediates, so their levels are kept low under physiological conditions.⁴⁸ On the other hand, a previous study found that lysoplasmalogens play a vital role in membrane fluidity.³⁸² Interestingly, lysoplasmalogens synthesis and regulation were found to be dysfunctional in lymphoblasts derived from BTHS patients.^{47,49} Moreover, levels of plasmalogens, which are synthesised out of lysoplasmalogens, were changed in some BTHS models.²⁰⁷ Taken together, these observations and the findings from this thesis suggest a crucial involvement of the lysoplasmalogen LPC O- in Taz-mediated remodelling.

To test if the significant increase in α -cell mass of *Taz*-KD pancreatic islets, which was found *in vivo* (discussed in **Chapter 5.2**), is a direct effect or long-term adaptation of *Taz*-KD on

pancreatic islet biology, pancreatic islet composition after *Taz*-KD 1-week doxy incubation was measured (**Figure 4.38**). The analysis showed no changes in pancreatic α -, β -, or δ -cell numbers using the *Taz*-KD *in vitro* model. This indicated that the increase in α -cell mass is an adaptation process that develops during the disease progression. A key experiment to test this hypothesis would be investigating the islet composition of younger *Taz*-KD mice (e.g. after 10 wo). There are also other explanations for the absence of α -cell mass increase in the *Taz*-KD *in vitro* model. The 1-week incubation time might be simply too short for trans-differentiation events like β - to α -cell differentiation. Although, the trans-differentiation of β - to α -cells has been associated with the pathogenesis of diabetes and pancreatic cancer, the underlying mechanisms and time scales remain mostly unknown.^{374,393} Chung *et al.* studied β - to α -cell trans-differentiated after pancreatic duct ligation combined with alloxan treatment, which destroys most pancreatic β -cells within the mouse. After applying this injury model, they observed a regeneration of β -cells out of remaining and newly formed α -cells, which occurred over the course of two weeks. However, after one week, primarily intermediate cells co-expressing α - and β -cell-specific markers were observed, which only became mature β -cells after two weeks.⁷⁸ Although most studies on islet cell plasticity were performed *in vivo*, Ben-Othman *et al.* managed to observe a significant α - to β -cell trans-differentiation in isolated human pancreatic islets after 14 days of γ -aminobutyric acid *in vitro* treatment.²⁸ However, the *in vivo* surroundings might still be necessary for pancreatic islet cell trans-differentiation in the *Taz*-KD model. For instance, noradrenergic fibers were found to be involved in β -cell (de)differentiation.⁷⁹ Furthermore, in case the increase in *Taz*-KD α -cell mass *in vivo* is connected to a defective pancreas development, where most of the neogenesis of endocrine cells occurs, the *in vitro* model could not replicate this.²⁴³ However, *Taz*-KD and WT's similar pancreatic islet composition after 1-week doxy incubation allowed studying *Taz*-KD direct effects independent of an altered intra-islet communication.

Studying the functionality of *Taz*-KD pancreatic islets after 1-week of doxy culture revealed an impairment in pancreatic islet function (**Figure 4.39**). This was evident by decreased ATP levels and reduced GSIS at 20 mM of glucose in *Taz*-KD pancreatic islets after 1-week doxy incubation. The defective insulin secretion was independent of Ca^{2+} influx and more prominent in the second phase of insulin secretion when amplifying pathways are active (introduced in **Chapter 1.2.2**). Additionally, glucagon secretion at 0.5 mM glucose tended to be reduced in *Taz*-KD pancreatic islets after 1-week of doxy culture. In the *in vivo* model, the amplified glucagon secretion was mainly inferred from the increased α -cell mass and systemic factors, both absent in the *in vitro* model.

This data shows that CL remodelling is directly important for pancreatic islet function and confirms the significance of CL during diabetes development, as it has been shown during diabetic cardiomyopathy.¹⁴² Defective phospholipid remodelling has been previously linked to impaired pancreatic islet function.⁶⁸ In addition to the previously described study from Cole *et al.* (discussed in **Chapter 5.2**), other phospholipid remodelling enzymes, such as phospholipase A and ALCAT1, have been associated with defective insulin secretion.^{185,225} ALCAT1 has been implicated in mitochondrial biogenesis, and inhibition of ALCAT1 restored mitochondrial dynamics after hypoxia.^{176,226} Moreover, overexpression of ALCAT1 caused oxidative stress, leading to mitochondrial fragmentation associated with Mitofusin2 depletion.²²⁶ Interestingly, mitochondrial volume was unchanged among the genotypes after 1-week of doxy incubation (**Figure 4.39**). Therefore, the increase in mitochondrial volume in the *in vivo* model might be a compensatory mechanism to counteract the mitochondrial defect. Collectively, the functional analysis of the *in vitro* model reinforces the idea that *Taz*-KD pancreatic islets *in vivo* compensate for the initial mitochondrial defect seen in the *in vitro* model.

In vitro Taz-KD transcriptomic data showed that genes involved in the regulation of the cell cycle were upregulated, and instead, cell growth was downregulated (**Figure 4.42**). This could be a result of the decreased ATP levels or a direct effect of altered CL profile, as shown by others.⁷² Interestingly, some upregulated genes were also involved in O-glycosylation (e.g. *Galnt9*), as seen in the *in vivo* model. Additionally, extracellular structure and matrix organisation were among the most downregulated pathways in the GO analysis. The stability of the ECM depends on glycosylation processes.⁴¹⁴ Therefore, alterations in glycosylation might impact ECM organisation in *Taz*-KD pancreatic islets after 1-week doxy incubation. In summary, the RNA-Seq results of the *in vitro* model strengthen the assumption that O-glycosylation is a crucial pathway in *Taz*-KD pancreatic islets (discussed for the *in vivo* model in **Chapter 5.5**), and early-stage modulation in the *in vitro* model of *Taz*-KD might be an attempt to rescue cellular function.

One key advantage of this inducible *Taz*-KD *in vitro* model is the flexibility to regulate the *Taz* mRNA levels with the administration of doxy. Future studies could greatly benefit from the described *in vitro* model, which can be used for all tissues that can be cultured for a more extended period of time (above 2 day). As demonstrated for pancreatic islets, *Taz*-KD could already be observed after 48 h in culture with 1 µg/ml doxy (**Figure 4.36**). The concentration of 1 µg/ml doxy was selected based on establishing experiments that showed no effect on pancreatic islet function for this concentration (more details in **Chapter 3.1.2**). However, the development of a change in lipid profile and mitochondrial rearrangement probably takes

longer, and hence, the analysis was performed after the 1-week of doxy treatment. One limitation of the *in vitro* model is the unclear time span for the sequential events that happen after the application of doxy. While *Taz* mRNA may be rapidly reduced, protein levels might take longer to decrease. Only after the protein levels have been effectively reduced can changes in the CL profile occur, which in turn depends on the lipid turnover rates. Once the CL profiles have been altered, it will take an unknown amount of time for a cellular and tissue phenotype to develop. The lack of a specific *Taz* antibody during the project has made it difficult to assess the timeline accurately.

5.7 Pancreatic islet adaption processes

Adaptation during stress is a fundamental cellular ability to deal with changing environmental conditions that threaten the organism's homeostasis.²⁹³ The mitochondrial disorder BTHS is based on a defective CL remodelling pathway, impacting various cellular processes. This is because the composition of the essential phospholipid CL has major roles in cellular energetics, turnover, and signalling (introduced in **Chapter 1.1.1**). The major differences in pancreatic islet function of sh*Taz* *in vivo* and *in vitro* models (discussed in **Chapter 5.6**) underline the significance of adaptative processes. Understanding adaptive processes in pancreatic islets is important for gaining insight into pancreatic islet biology and optimising intervention strategies in pathological conditions. It also aids in diagnosing diseases, particularly in identifying scenarios where cells are still able to combat the disease. For instance, in the early stages of diabetes, pancreatic β -cells adapt to persistent hyperglycemia by enhancing insulin production and secretion.

First, it is important to note that the KD phenotype might be milder than a complete KO. Furthermore, the decrease in *Taz* gene expression in pancreatic islet tissue was less efficient compared to the heart. The varying levels of *Taz* expression can impact how severely each organ is affected by the disease. If the organ is affected to a lesser extent, it can provide room for adaptation processes to occur, making it easier to handle the disease. *Taz* splice variants might be responsible for the tissue-specific KD efficiency (further discussed in **Chapter 5.1**). The loss-of-function mutation R57L and H69Q in humans, which lead to catalytically inactive *Taz*, are well described.²³³ However, some missense mutations in the human *Taz* gene result in mild clinical BTHS symptoms.^{198,317} In particular, several BTHS mutations associated with reported BTHS cases were studied with a 3D molecular docking program. This analysis suggested that mutations outside the conserved HX4D domain (H69,

D74) of the acyltransferase superfamily may lead to a milder phenotype.⁹⁵ Therefore, the shTaz model with partially active Taz-mediated CL remodelling is relatable to some extent to clinical situations. The generation of novel models utilising the CRISPR/Cas method, such as the recently published TAZ^{G197V} mouse model with the missense point mutation G197V (introduced in **Chapter 1.1.4**), which corresponds to a known patient mutation, opens up exciting and more personalised possibilities for future studies.⁷⁵ These new findings can then be compared with previous models, such as the shTaz model for pancreatic islet research used in this thesis.

Throughout this thesis, several possible adaptations and compensatory mechanisms of *Taz*-KD pancreatic islets were described and will be summarised in the following paragraphs (collectively illustrated in **Figure 5.1**).

A key adaptation was the increase in mitochondrial volume of *Taz*-KD pancreatic islet cells (discussed in **Chapter 5.4**). The analogous adaptive pathway is cellular hypertrophy, which describes the increase in cell size and volume in response to a change in environment.^{117,432} Of interest, hyperplasia describes the increase in cell number and the analogous mitochondrial number, was not upregulated in *Taz*-KD pancreatic islet cells. The increase in mitochondrial volume was considered crucial as it was absent in the *Taz*-KD *in vitro* model, which showed an impaired pancreatic islet function. The observed change in the shape of *Taz*-KD mitochondria in the *in vivo* model might be closely linked to a decrease in autophagy. The decrease is indicated by the reduction of certain autophagy and mitophagy markers, such as LC3B and Atg7 (autophagy is further discussed in **Chapter 5.4**). Interestingly, *Taz*-KD affects the mitochondria of various tissues differently. For example, studies have reported fragmentation in heart tissue from *Taz*-KD mice.⁴²⁷ These organelles can have different characteristics in various cell types, including differences in number, shape, and function throughout the body.²⁵⁷ Therefore, the unique adaptive responses in mitochondria could be linked to their tissue-specific differences and should be examined separately.

Another crucial indicator for the metabolic and energetic state of the cell is cellular redox homeostasis. An oxidative environment can trigger the upregulation of antioxidative defense mechanisms.⁴ In *Taz*-KD pancreatic islets, an upregulation of the antioxidative enzyme Prx3 combined with elevated NAD(P)H levels might be responsible for the slightly reduced ROS levels *in vivo*. This adaptive process seems to fail under *ex vivo* conditions as increased basal levels of mitochondrial ROS were observed in *Taz*-KD (discussed in **Chapter 5.4**). Adaptation processes are usually much more robust in complex systems like whole-body metabolism than in isolated cells. This might explain why the *in vivo* pancreas seems able to compensate while the isolated pancreatic islets cannot.

The lipid composition of the mitochondrial membranes is another vital regulator of mitochondrial morphology and function (discussed in **Chapter 5.4**). The upregulation of PE and PG in *Taz*-KD pancreatic islets could be a compensatory mechanism to replace CL functionality. Previous studies have assumed that PG upregulation can partly compensate for the loss of CL.¹⁷⁷ Additionally, the degree of curvature of the cristae shape was described to be achieved by an asymmetric distribution of phospholipids in the inner mitochondrial membrane.¹⁷⁰ PE, similarly to CL, induces negative curvature, and hence, PE and CL are highly concentrated in negatively curved leaflet monolayers.^{295,365} Instead, PC and other phospholipids segregate to the positively curved leaflets.¹⁷⁰ Therefore, the upregulation of PE and downregulation of PC, which was observed in *Taz*-KD pancreatic islets, might maintain the balance in the absence of CL.

The cellular metabolism is constantly adapting to changing environmental conditions. A shift from mitochondrial to more glycolytic ATP production is a fast and efficient way to keep up with the energy demand in challenging or anaerobic conditions.³⁶⁶ The famous Warburg effect is used by cancer cells to boost glycolysis, and hence, increases lactate production.³⁴⁵ Although increased metabolic rates were observed, higher acidification levels were not measured in *Taz*-KD pancreatic islets (discussed in **Chapter 5.3**). Instead, a state of hypermetabolism was suggested in *Taz*-KD pancreatic islets (discussed in **Chapters 5.2, 5.3**). Hypermetabolism has been observed in other mitochondrial disorders, where the increased metabolic rate can reduce life expectancy.³⁵¹ Therefore, affected cells can handle their inefficient machinery as long as enough nutrients are available, but this takes a toll on the cells. Overall, hypermetabolism is likely responsible for the lean body phenotype and the improved glucose tolerance test in the context of BTHS.

Furthermore, the upregulation of α -cell mass and amplified glucagon secretion observed in *Taz*-KD pancreatic islets was suggested to prime the pancreatic β -cells via enhanced paracrine signalling (discussed in **Chapter 5.2**). This was thought to be the primary factor behind the faster cytosolic Ca^{2+} influx in *Taz*-KD pancreatic islets upon glucose stimulation.

Glycosylation, especially O-GlcNAcylation, appears to be relevant for both *in vivo* and *in vitro* models. The enhanced levels of O-GlcNAc protein modification in *Taz*-KD pancreatic islets might link metabolic and mitochondrial morphology phenotype (extensively discussed in **Chapter 5.5**).

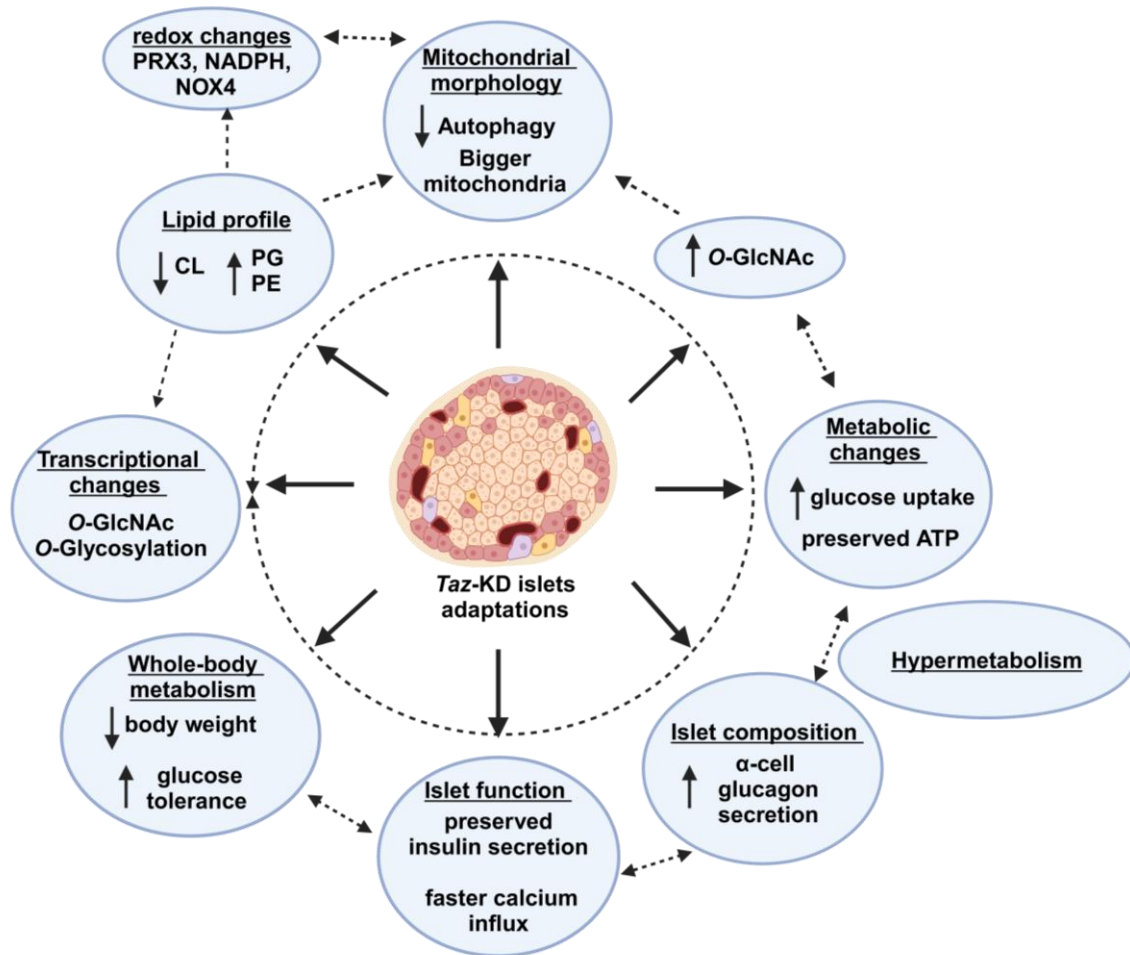


Figure 5.1: *Taz*-KD pancreatic islet adaptation processes

Taz-KD *in vivo* adaptations are linked among each other and work in synergy to compensate for the initial mitochondrial defect, which is observed in the *Taz*-KD *in vitro* model. Created with Biorender.com.

The precise interplay between the compensatory mechanisms remains unknown. The arrows in **Figure 5.1** indicate some of the potential connections between the adaptive processes, but others are also plausible and mentioned throughout the discussion **Chapters 5.1 - 5.7**. The adaptive mechanisms work together to preserve pancreatic islet functionality and, thus, can also provide insight into the cellular state of *Taz*-KD pancreatic islet cells. There may be additional adaptive processes not covered in this thesis that are active and related to observed changes in gene expression from RNA-Seq data. These processes could be explored in future studies.

5.8 Conclusion and outlook

Since mitochondria are present in all cells of the body (except erythrocytes), BTHS affects every cell to some extent.⁸ While most studies primarily focus on the heart, one must also consider other organs and organ communication to understand the full nature of this multisystem disease.²⁷³ This thesis evaluated the consequences of *Taz*-KD on pancreatic islets by addressing five questions formulated at the beginning (**Chapter 1.3**).

1. Does BTHS negatively impact pancreatic islet function?

In vitro *Taz*-KD resulted in a direct effect of CL profile alteration, which impaired GSIS, possibly via the reduced ATP production in high glucose. However, the direct effects of *Taz*-KD were compensated and not manifested in the *in vivo* pancreatic islets, which instead exhibited accelerated cellular metabolism compared to WT.

2. Does BTHS lead to oxidative stress, which contributes to the disease manifestation?

Oxidative stress was not observed *in vivo* in the pancreatic islets and heart tissue of *Taz*-KD mice. However, *ex vivo* measurements of *Taz*-KD pancreatic islets showed increased basal oxidation with NOX4 involved as an H₂O₂ production site. This concludes that redox signalling is altered in *Taz*-KD compared to WT pancreatic islets which did not result in oxidative stress.

3. How do pancreatic islets adapt during the development of BTHS?

Pancreatic islets undergo various adaptive pathways in *Taz*-KD conditions. The most prominent findings in this thesis include increased mitochondrial volume, amplified O-GlcNAcylation, enhanced α -cell mass, and accelerated cellular metabolism compared to WT.

4. Are whole-body metabolism changes in BTHS related to a defect in pancreatic islets?

No significant differences in plasma glucagon or insulin levels were observed in *Taz*-KD. Therefore, the systemic metabolic changes result from other factors, such as glucose clearance due to increased glucose uptake. When other nutrients are present, such as fatty acids or amino acids, or during exercise or fasting, the increased α -cell mass might contribute to the whole-body phenotype.

5. What is the role of CL in pancreatic islet function?

In vivo, CL remodelling in pancreatic islets influences mitochondrial morphology and mitochondrial phospholipid composition. Defective remodelling triggers a vast set of metabolic and morphological adaptations. Furthermore, changes in the CL profile diminished

ATP levels and impaired GSIS, as demonstrated by the *in vitro* model. Thus, the profile of CL plays a crucial role in the function and shape of mitochondria in pancreatic islets.

Outlook

The results of this thesis indicate that *in vivo* *Taz*-KD has a rather mild impact on pancreatic islet functionality. Various adaptive mechanisms come into play and compensate for the, in the *in vitro* model observed, defect in GSIS. Similar compensatory pathways, such as hypermetabolism or increased mitochondrial volume, have already been observed in BTHS samples of other tissues.^{70,248,410} Additionally, individuals with BTHS can display a mild phenotype not only in BTHS but also in other mitochondrial disorders, suggesting that cells are capable of managing slightly dysfunctional mitochondria.^{95,351} The efficient activation of adaptative pathways supplemented with enough nutrients is very important to sustain the compensation for the inefficient energy turnover rate.³⁵¹ It would be interesting to compare the findings from this thesis with the patient's situation to address questions such as whether increased glucagon secretion might contribute to hypoglycemic events in BTHS patients. Furthermore, improved diagnosis and disease management, along with successful heart transplantation, have raised the life expectancy in BTHS patients.⁵ Therefore, long-term dietary considerations become increasingly essential, especially as nowadays the prevalence of type 2 diabetes is rising due to unhealthy diets and sedentary lifestyles.¹⁶⁵ Given that the progression of type 2 diabetes is known to depend on mitochondria, it is crucial to evaluate if patients with mitochondrial disorders such as BTHS might be more susceptible to developing diabetes or other metabolic diseases as they age.²¹⁴

The shTaz model is a common system to study BTHS as it mimics many aspects of the human phenotype. In the introduction, the shTaz mouse model is compared to other animal and cellular models of BTHS (**Chapter 1.1.4**).²⁸⁷ Although this *Taz*-KD model has advantages over other BTHS models, such as yeast, fruit fly, zebrafish or cellular models, newly generated mouse models like *Taz*-KO and TAZ^{G197V} seem to recapitulate the BTHS human pathology in some aspects better than the shTaz system and should be taken into consideration for future studies.^{75,287} Additionally, future studies should also discuss employing a rabbit model of BTHS since the cardiac physiology in rabbits has more characteristics that are similar to humans than mice. In particular, the electrophysiology and Ca²⁺ transport in rabbits recapitulates more the human situation.²⁸² However, for studying the impacts of *Taz* deletion on pancreatic islets, rabbits are suboptimal as they display a similar islet architecture to mice with a β -cell core and α -cell mantle.^{186,349} Therefore, pancreatic islets from humans or nonhuman primates would be best to discuss the effects of *Taz* deletion on paracrine signalling, pancreatic islet plasticity and overall pancreatic islet functionality.

6 References

- 1 **Aamodt, K. I. & Powers, A. C.** Signals in the pancreatic islet microenvironment influence β -cell proliferation. *Diabetes, Obesity and Metabolism* 19, 124-136,(2017).
- 2 **Acehan, D. et al.** Cardiolipin affects the supramolecular organization of ATP synthase in mitochondria. *Biophysical journal* 100, 2184-2192,(2011).
- 3 **Acehan, D. et al.** Cardiac and skeletal muscle defects in a mouse model of human Barth syndrome. *J Biol Chem* 286, 899-908,(2011).
- 4 **Acharya, J. D. & Ghaskadbi, S. S.** Islets and their antioxidant defense. *Islets* 2, 225-235,(2010).
- 5 **Addabbo, F., Montagnani, M. & Goligorsky, M. S.** Mitochondria and reactive oxygen species. *Hypertension* 53, 885-892,(2009).
- 6 **Afzal, N., Lederer, W. J., Jafri, M. S. & Mannella, C. A.** Effect of crista morphology on mitochondrial ATP output: A computational study. *Current research in physiology* 4, 163-176,(2021).
- 7 **Agilent Technologies.** *Seahorse XF Mito Fuel Flex Test Kit User Manual*, <https://www.agilent.com/cs/library/usermanuals/public/XF_Mito_Fuel_Flex_Test_Kit_User_Guide%20old.pdf> (2019).
- 8 **Ahsan, M. K., Lekli, I., Ray, D., Yodoi, J. & Das, D. K.** Redox regulation of cell survival by the thioredoxin superfamily: An implication of redox gene therapy in the heart. *Antioxid Redox Signal* 11, 2741-2758,(2009).
- 9 **Al-Massadi, O., Ferno, J., Dieguez, C., Nogueiras, R. & Quinones, M.** Glucagon control on food intake and energy balance. *Int J Mol Sci* 20, 3905,(2019).
- 10 **Alam, M. R. et al.** Mitochondrial Ca^{2+} uptake 1 (MICU1) and mitochondrial Ca^{2+} uniporter (MCU) contribute to metabolism-secretion coupling in clonal pancreatic β -cells. *J Biol Chem* 287, 34445-34454,(2012).

-
- 11 **Aldous, N., Moin, A. S. M. & Abdelalim, E. M.** Pancreatic β -cell heterogeneity in adult human islets and stem cell-derived islets. *Cell Mol Life Sci* 80, 176,(2023).
- 12 **Alejandro, E. U. et al.** Disruption of O-linked N-acetylglucosamine signaling induces ER stress and β -cell failure *Cell Rep* 13, 2527-2538,(2015).
- 13 **Andrejewski, N. et al.** Normal lysosomal morphology and function in LAMP-1-deficient mice. *J Biol Chem* 274, 12692-12701,(1999).
- 14 **Ang, T., Bruce, C. R. & Kowalski, G. M.** Postprandial aminogenic insulin and glucagon secretion can stimulate glucose flux in humans. *Diabetes* 68, 939-946,(2019).
- 15 **Antón, Z. et al.** Human Atg8-cardiolipin interactions in mitophagy: Specific properties of LC3B, GABARAPL2 and GABARAP. *Autophagy* 12, 2386-2403,(2016).
- 16 **Antunes, D. et al.** Overexpression of branched-chain amino acid aminotransferases rescues the growth defects of cells lacking the Barth syndrome-related gene TAZ1. *J Mol Med (Berl)* 97, 269-279,(2019).
- 17 **Arkhammar, P. O., Terry, B. R., Kofod, H. & Thastrup, O.** Pancreatic islets cultured on extracellular matrix: An excellent preparation for microfluorometry. *Methods in cell science* 19, 255-268,(1998).
- 18 **Armour, S. L. et al.** Glucose controls glucagon secretion by regulating fatty acid oxidation in pancreatic α -cells. *Diabetes* 72, 1446-1459,(2023).
- 19 **Ashcroft, F. M., Lloyd, M. & Haythorne, E. A.** Glucokinase activity in diabetes: Too much of a good thing? *Trends in Endocrinology & Metabolism* 34, 119-130,(2023).
- 20 **Audoze-Chaud, J.** *Direct effects of tafazzin knockdown on pancreatic islets function*. Bachelor thesis, Saarland University, (2021).
- 21 **Ban, T., Heymann, J. A., Song, Z., Hinshaw, J. E. & Chan, D. C.** OPA1 disease alleles causing dominant optic atrophy have defects in cardiolipin-stimulated GTP hydrolysis and membrane tubulation. *Human molecular genetics* 19, 2113-2122,(2010).

-
- 22 **Barrett, K. E., Brooks, H. L., Boitano, S. & Barman, S. M.** *Ganong's review of medical physiology*. 23rd edition edn, (McGraw-Hill, 2010).
- 23 **Barth, P. et al.** An X-linked mitochondrial disease affecting cardiac muscle, skeletal muscle and neutrophil leucocytes. *J Neurol Sci* 62, 327-355,(1983).
- 24 **Basco, D. et al.** α -cell glucokinase suppresses glucose-regulated glucagon secretion. *Nat Commun* 9, 546,(2018).
- 25 **Bath, A. et al.** Barth Syndrome: Psychosocial impact and quality of life assessment. *J Cardiovasc Dev Dis* 9,(2022).
- 26 **Becker & Hickl.** *Metabolic imaging by NAD(P)H and FAD FLIM*, <<https://www.becker-hickl.com/applications/metabolic-imaging/>> (2024).
- 27 **Beltrán-Heredia, E. et al.** Membrane curvature induces cardiolipin sorting. *Communications biology* 2, 225,(2019).
- 28 **Ben-Othman, N. et al.** Long-term GABA administration induces α -cell-mediated β -like-cell neogenesis. *Cell* 168, 73-85 e11,(2017).
- 29 **Benninger, R. K. & Piston, D. W.** Cellular communication and heterogeneity in pancreatic islet insulin secretion dynamics. *Trends in Endocrinology & Metabolism* 25, 399-406,(2014).
- 30 **Benninger, R. K. P. & Kravets, V.** The physiological role of β -cell heterogeneity in pancreatic islet function. *Nat Rev Endocrinol* 18, 9-22,(2022).
- 31 **Beranek, A. et al.** Identification of a cardiolipin-specific phospholipase encoded by the gene CLD1 (YGR110W) in yeast. *J Biol Chem* 284, 11572-11578,(2009).
- 32 **Berger, C. & Zdzienlo, D.** Glucose transporters in pancreatic islets. *Pflugers Arch* 472, 1249-1272,(2020).
- 33 **Bertero, E. & Maack, C.** Calcium signaling and reactive oxygen species in mitochondria. *Circulation research* 122, 1460-1478,(2018).

-
- 34 **Bertero, E., Kutschka, I., Maack, C. & Dudek, J.** Cardiolipin remodeling in Barth syndrome and other hereditary cardiomyopathies. *Biochim Biophys Acta Mol Basis Dis* 1866, 165803,(2020).
- 35 **Bertero, E. et al.** Loss of mitochondrial Ca^{2+} uniporter limits inotropic reserve and provides trigger and substrate for arrhythmias in Barth syndrome cardiomyopathy. *Circulation* 144, 1694-1713,(2021).
- 36 **Bertero, E.** *Mechano-energetic uncoupling in Barth syndrome cardiomyopathy*. Doctoral thesis, University of Würzburg, (2022).
- 37 **Bertram, R. et al.** A role for calcium release-activated current (CRAC) in cholinergic modulation of electrical activity in pancreatic β -cells. *Biophysical Journal* 68, 2323-2332,(1995).
- 38 **Bione, S. et al.** A novel X-linked gene, *G4.5*. is responsible for Barth syndrome. *Nat Genet* 12, 385-389,(1996).
- 39 **Birk, A. V. et al.** The mitochondrial-targeted compound SS-31 re-energizes ischemic mitochondria by interacting with cardiolipin. *J Am Soc Nephrol* 24, 1250-1261,(2013).
- 40 **Bittel, A. J. et al.** Reduced muscle strength in Barth syndrome may be improved by resistance exercise training: A pilot study. *JIMD Rep* 41, 63-72,(2018).
- 41 **Blom, H. & Brismar, H.** STED microscopy: Increased resolution for medical research? *Journal of internal medicine* 276, 560-578,(2014).
- 42 **Blum, B. et al.** Functional β -cell maturation is marked by an increased glucose threshold and by expression of urocortin 3. *Nat Biotechnol* 30, 261-264,(2012).
- 43 **Bohnert, K. L. et al.** Resistance exercise training with protein supplementation improves skeletal muscle strength and improves quality of life in late adolescents and young adults with Barth syndrome: A pilot study. *JIMD Rep* 62, 74-84,(2021).
- 44 **Bonnay, F. et al.** Oxidative metabolism drives immortalization of neural stem cells during tumorigenesis. *Cell* 182, 1490-1507 e1419,(2020).

-
- 45 **Bonner-Weir, S. & Orci, L.** New perspectives on the microvasculature of the islets of Langerhans in the rat. *Diabetes* 31, 883-889,(1982).
- 46 **Bortolotti, M., Polito, L., Battelli, M. G. & Bolognesi, A.** Xanthine oxidoreductase: One enzyme for multiple physiological tasks. *Redox Biol* 41, 101882,(2021).
- 47 **Bozelli, J. C., Jr., Lu, D., Atilla-Gokcumen, G. E. & Epand, R. M.** Promotion of plasmalogen biosynthesis reverse lipid changes in a Barth syndrome cell model. *Biochim Biophys Acta Mol Cell Biol Lipids* 1865, 158677,(2020).
- 48 **Bozelli, J. C., Jr., Azher, S. & Epand, R. M.** Plasmalogens and chronic inflammatory diseases. *Frontiers in Physiology* 12, 730829,(2021).
- 49 **Bozelli, J. C., Jr. & Epand, R. M.** Interplay between cardiolipin and plasmalogens in Barth syndrome. *J Inherit Metab Dis* 45, 99-110,(2022).
- 50 **Bozelli Jr, J. C., Lu, D., Atilla-Gokcumen, G. E. & Epand, R. M.** Promotion of plasmalogen biosynthesis reverse lipid changes in a Barth syndrome cell model. *Biochim Biophys Acta Mol Cell Biol Lipids* 1865, 158677,(2020).
- 51 **Bozelli Jr, J. C. & Epand, R. M.** Interplay between cardiolipin and plasmalogens in Barth syndrome. *J Inherit Metab Dis* 45, 99-110,(2022).
- 52 **Bozem, M. & Henquin, J. C.** Glucose modulation of spike activity independently from changes in slow waves of membrane potential in mouse β -cells. *Pflugers Arch* 413, 147-152,(1988).
- 53 **Bozem, M. et al.** Electrochemical quantification of extracellular local H_2O_2 kinetics originating from single cells. *Antioxid Redox Signal* 29, 501-517,(2018).
- 54 **Bradley, R. M., Stark, K. D. & Duncan, R. E.** Influence of tissue, diet, and enzymatic remodeling on cardiolipin fatty acyl profile. *Molecular nutrition & food research* 60, 1804-1818,(2016).
- 55 **Brand, R. M. et al.** Targeting mitochondrial oxidative stress to mitigate UV-induced skin damage. *Frontiers in Pharmacology* 9, 920,(2018).

-
- 56 **Breschi, A., Gingeras, T. R. & Guigó, R.** Comparative transcriptomics in human and mouse. *Nat Rev Genet* 18, 425-440,(2017).
- 57 **Briant, L. J. B. et al.** CPT1a-dependent long-chain fatty acid oxidation contributes to maintaining glucagon secretion from pancreatic islets. *Cell Rep* 23, 3300-3311,(2018).
- 58 **Cabrera, O. et al.** Intra-islet glucagon confers β -cell glucose competence for first-phase insulin secretion and favors GLP-1R stimulation by exogenous glucagon. *J Biol Chem* 298,(2022).
- 59 **Cade, W. T. et al.** Substrate metabolism during basal and hyperinsulinemic conditions in adolescents and young-adults with Barth syndrome. *J Inherit Metab Dis* 36, 91-101,(2013).
- 60 **Cade, W. T. et al.** Blunted fat oxidation upon submaximal exercise is partially compensated by enhanced glucose metabolism in children, adolescents, and young adults with Barth syndrome. *J Inherit Metab Dis* 42, 480-493,(2019).
- 61 **Cade, W. T. et al.** Myocardial glucose and fatty acid metabolism is altered and associated with lower cardiac function in young adults with Barth syndrome. *Journal of Nuclear Cardiology* 28, 1649-1659,(2021).
- 62 **Caicedo, A., Huising, M. O. & Wess, J.** An intraislet paracrine signaling pathway that enables glucagon to stimulate pancreatic β -cells. *Diabetes* 72, 1748-1750,(2023).
- 63 **Campbell, J. E. et al.** GIPR/GLP-1R dual agonist therapies for diabetes and weight loss-chemistry, physiology, and clinical applications. *Cell Metab* 35, 1519-1529,(2023).
- 64 **Campbell, M. D. et al.** Improving mitochondrial function with SS-31 reverses age-related redox stress and improves exercise tolerance in aged mice. *Free Radic Biol Med* 134, 268-281,(2019).
- 65 **Cao, J., Liu, Y., Lockwood, J., Burn, P. & Shi, Y.** A novel cardiolipin-remodeling pathway revealed by a gene encoding an endoplasmic reticulum-associated acyl-CoA:lysocardiolipin acyltransferase (ALCAT1) in mouse. *J Biol Chem* 279, 31727-31734,(2004).

-
- 66 **Capozzi, M. E., D'Alessio, D. A. & Campbell, J. E.** The past, present, and future physiology and pharmacology of glucagon. *Cell Metab* 34, 1654-1674,(2022).
- 67 **Cenacchi, G. et al.** Danon disease: Review of natural history and recent advances. *Neuropathology and Applied Neurobiology* 46, 303-322,(2020).
- 68 **Chang, W., Hatch, G. M., Wang, Y., Yu, F. & Wang, M.** The relationship between phospholipids and insulin resistance: From clinical to experimental studies. *J Cell Mol Med* 23, 702-710,(2019).
- 69 **Chatham, J. C., Zhang, J. & Wende, A. R.** Role of O-linked *N*-acetylglucosamine protein modification in cellular (patho)physiology. *Physiol Rev* 101, 427-493,(2021).
- 70 **Chatzisprou, I. A. et al.** Barth syndrome cells display widespread remodeling of mitochondrial complexes without affecting metabolic flux distribution. *Biochim Biophys Acta Mol Basis Dis* 1864, 3650-3658,(2018).
- 71 **Chen, J. J. & Yu, B. P.** Alterations in mitochondrial membrane fluidity by lipid peroxidation products. *Free Radic Biol Med* 17, 411-418,(1994).
- 72 **Chen, S., Liu, D., Finley, R. L., Jr. & Greenberg, M. L.** Loss of mitochondrial DNA in the yeast cardiolipin synthase *crd1* mutant leads to up-regulation of the protein kinase Swe1p that regulates the G2/M transition. *J Biol Chem* 285, 10397-10407,(2010).
- 73 **Cheng-Xue, R. et al.** Tolbutamide controls glucagon release from mouse islets differently than glucose: Involvement of K_{ATP} channels from both α -cells and δ -cells. *Diabetes* 62, 1612-1622,(2013).
- 74 **Choi, S.-Y. et al.** A common lipid links Mfn-mediated mitochondrial fusion and SNARE-regulated exocytosis. *Nat Cell Biol* 8, 1255-1262,(2006).
- 75 **Chowdhury, A. et al.** Metabolic switch from fatty acid oxidation to glycolysis in knock-in mouse model of Barth syndrome. *EMBO Mol Med*, e17399,(2023).
- 76 **Christodoulou, J. et al.** Barth syndrome: Clinical observations and genetic linkage studies. *Am J Med Genet A* 50, 255-264,(1994).

-
- 77 **Chu, C. T. et al.** Cardiolipin externalization to the outer mitochondrial membrane acts as an elimination signal for mitophagy in neuronal cells. *Nat Cell Biol* 15, 1197-1205,(2013).
- 78 **Chung, C. H., Hao, E., Piran, R., Keinan, E. & Levine, F.** Pancreatic β -cell neogenesis by direct conversion from mature α -cells. *Stem Cells* 28, 1630-1638,(2010).
- 79 **Cinti, F. et al.** Noradrenergic fibers are associated with β -cell dedifferentiation and impaired β -cell function in humans. *Metabolism* 114, 154414,(2021).
- 80 **Clarke, S. L. et al.** Barth syndrome. *Orphanet J Rare Dis* 8, 1-17,(2013).
- 81 **Cole, L. K. et al.** Impaired cardiolipin biosynthesis prevents hepatic steatosis and diet-induced obesity. *Diabetes* 65, 3289-3300,(2016).
- 82 **Cole, L. K. et al.** *Tafazzin* deficiency reduces basal insulin secretion and mitochondrial function in pancreatic islets from male mice. *Endocrinology* 162, 1–15,(2021).
- 83 **Coman, D., Yapfite-Lee, J. & Boneh, A.** New indications and controversies in arginine therapy. *Clin Nutr* 27, 489-496,(2008).
- 84 **Corey, R. A., Harrison, N., Stansfeld, P. J., Sansom, M. S. & Duncan, A. L.** Cardiolipin, and not monolysocardiolipin, preferentially binds to the interface of complexes III and IV. *Chemical Science* 13, 13489-13498,(2022).
- 85 **Cornell, D. et al.** Pseudoislet aggregation of pancreatic β -cells improves glucose stimulated insulin secretion by altering glucose metabolism and increasing ATP production. *Cells* 11, 2330,(2022).
- 86 **Corrado, M. et al.** Dynamic cardiolipin synthesis is required for CD8⁺ T-cell immunity. *Cell Metab* 32, 981-995. e987,(2020).
- 87 **Cosson, L. et al.** Barth syndrome in a female patient. *Molecular genetics and metabolism* 106, 115-120,(2012).
- 88 **Cryer, P. E.** Minireview: Glucagon in the pathogenesis of hypoglycemia and hyperglycemia in diabetes. *Endocrinology* 153, 1039-1048,(2012).

-
- 89 **Cuozzo, F. et al.** LDHB contributes to the regulation of lactate levels and basal insulin secretion in human pancreatic β -cells. *Cell Rep* 43, 114047,(2024).
- 90 **Dabner, L. et al.** Treatment of Barth syndrome by cardiolipin manipulation (CARDIOMAN) with bezafibrate: Protocol for a randomized placebo-controlled pilot trial conducted in the nationally commissioned Barth syndrome service. *JMIR Res Protoc* 10, e22533,(2021).
- 91 **Dale, D. C. et al.** A randomized controlled phase III trial of recombinant human granulocyte colony-stimulating factor (filgrastim) for treatment of severe chronic neutropenia. *Blood* 81, 2496-2502,(1993).
- 92 **Damschroder, D., Reynolds, C. & Wessells, R.** Drosophila tafazzin mutants have impaired exercise capacity. *Physiological reports* 6, e13604,(2018).
- 93 **Dassaye, R., Naidoo, S. & Cerf, M. E.** Transcription factor regulation of pancreatic organogenesis, differentiation and maturation. *Islets* 8, 13-34,(2016).
- 94 **De la Rosa, A. et al.** Overexpression of glucose 6 phosphate dehydrogenase preserves mouse pancreatic β -cells function until late in life. *Free Radical Biology and Medicine* 164, 149-153,(2021).
- 95 **Debnath, S. & Addya, S.** Mis-sense mutations in Tafazzin (TAZ) that escort to mild clinical symptoms of Barth syndrome is owed to the minimal inhibitory effect of the mutations on the enzyme function: *In-silico* evidence. *Interdiscip Sci* 7, 21-35,(2015).
- 96 **Deglasse, J.-P. et al.** Glucose acutely reduces cytosolic and mitochondrial H_2O_2 in rat pancreatic β -cells. *Antioxid Redox Signal* 30, 297-313,(2019).
- 97 **Doherty, E. & Perl, A.** Measurement of mitochondrial mass by flow cytometry during oxidative stress. *Reactive oxygen species (Apex, NC)* 4, 275,(2017).
- 98 **Donati, M. A. et al.** Barth syndrome presenting with acute metabolic decompensation in the neonatal period. *J Inherit Metab Dis* 29, 684-684,(2006).
- 99 **Dowhan, W.** Molecular basis for membrane phospholipid diversity: Why are there so many lipids? *Annual review of biochemistry* 66, 199-232,(1997).

-
- 100 **Dröse, S., Zwicker, K. & Brandt, U.** Full recovery of the NADH:ubiquinone activity of complex I (NADH:ubiquinone oxidoreductase) from *Yarrowia lipolytica* by the addition of phospholipids. *Biochimica et Biophysica Acta (BBA)-Bioenergetics* 1556, 65-72,(2002).
- 101 **Dudek, J. et al.** Cardiolipin deficiency affects respiratory chain function and organization in an induced pluripotent stem cell model of Barth syndrome. *Stem Cell Res* 11, 806-819,(2013).
- 102 **Dudek, J. et al.** Cardiac-specific succinate dehydrogenase deficiency in Barth syndrome. *EMBO Mol Med* 8, 139-154,(2016).
- 103 **Dudek, J.** Role of cardiolipin in mitochondrial signaling pathways. *Frontiers in Cell and Developmental Biology* 5, 90,(2017).
- 104 **Dudek, J. & Maack, C.** Barth syndrome cardiomyopathy. *Cardiovasc Res* 113, 399-410,(2017).
- 105 **Eble, K. S., Coleman, W. B., Hantgan, R. R. & Cunningham, C. C.** Tightly associated cardiolipin in the bovine heart mitochondrial ATP synthase as analyzed by ³¹P nuclear magnetic resonance spectroscopy. *J Biol Chem* 265, 19434-19440,(1990).
- 106 **Eirin, A. et al.** Restoration of mitochondrial cardiolipin attenuates cardiac damage in swine renovascular hypertension. *J Am Heart Assoc* 5, e003118,(2016).
- 107 **Ejsing, C. S. et al.** Global analysis of the yeast lipidome by quantitative shotgun mass spectrometry. *Proc Natl Acad Sci* 106, 2136-2141,(2009).
- 108 **El, K. et al.** GIP mediates the incretin effect and glucose tolerance by dual actions on α -cells and β -cells. *Science advances* 7, eabf1948,(2021).
- 109 **Elayat, A. A., el-Naggar, M. M. & Tahir, M.** An immunocytochemical and morphometric study of the rat pancreatic islets. *Journal of anatomy* 186, 629,(1995).
- 110 **Elsner, M., Gehrman, W. & Lenzen, S.** Peroxisome-generated hydrogen peroxide as important mediator of lipotoxicity in insulin-producing cells. *Diabetes* 60, 200-208,(2011).

-
- 111 **Endo, Y., Furuta, A. & Nishino, I.** Danon disease: A phenotypic expression of LAMP-2 deficiency. *Acta neuropathologica* 129, 391-398,(2015).
- 112 **Eskelinen, E.-L.** Roles of LAMP-1 and LAMP-2 in lysosome biogenesis and autophagy. *Molecular aspects of medicine* 27, 495-502,(2006).
- 113 **Ferreira, C., Pierre, G., Thompson, R. & Vernon, H.** Barth syndrome.(2020).
- 114 **Ferri, L. et al.** New clinical and molecular insights on Barth syndrome. *Orphanet J Rare Dis* 8, 1-11,(2013).
- 115 **Finsterer, J.** Barth syndrome: Mechanisms and management. *Appl Clin Genet* 12, 95-106,(2019).
- 116 **Francisco, A., Figueira, T. R. & Castilho, R. F.** Mitochondrial NAD(P)⁺ transhydrogenase: From molecular features to physiology and disease. *Antioxid Redox Signal* 36, 864-884,(2022).
- 117 **Frey, N. & Olson, E. N.** Cardiac hypertrophy: The good, the bad, and the ugly. *Annu Rev Physiol* 65, 45-79,(2003).
- 118 **Fujikawa, Y. et al.** Mouse redox histology using genetically encoded probes. *Science signaling* 9, rs1,(2016).
- 119 **Galloway, C. A., Lee, H. & Yoon, Y.** Mitochondrial morphology-emerging role in bioenergetics. *Free Radic Biol Med* 53, 2218-2228,(2012).
- 120 **Galloway, C. A. & Yoon, Y.** Mitochondrial morphology in metabolic diseases. *Antioxid Redox Signal* 19, 415-430,(2013).
- 121 **Gao, X. et al.** Altered cofactor preference of thermostable StDAPDH by a single mutation at K159. *Int J Mol Sci* 21,(2020).
- 122 **Garlid, A. O. et al.** TAZ encodes tafazzin, a transacylase essential for cardiolipin formation and central to the etiology of Barth syndrome. *Gene* 726, 144148,(2020).
- 123 **Gaspard, G. J. & McMaster, C. R.** Cardiolipin metabolism and its causal role in the etiology of the inherited cardiomyopathy Barth syndrome. *Chemistry and physics of lipids* 193, 1-10,(2015).

-
- 134 **Graham, K. L. et al.** Isolation and culture of the islets of Langerhans from mouse pancreas. *Bio-protocol* 6, e1840-e1840,(2016).
- 135 **Greenwell, A. A., Tabatabaei Dakhili, S. A. & Ussher, J. R.** Myocardial disturbances of intermediary metabolism in Barth syndrome. *Frontiers in Cardiovascular Medicine* 9, 981972,(2022).
- 136 **Greotti, E., Wong, A., Pozzan, T., Pendin, D. & Pizzo, P.** Characterization of the ER-targeted low affinity Ca^{2+} probe D4ER. *Sensors* 16, 1419,(2016).
- 137 **Gromada, J., Chabosseau, P. & Rutter, G. A.** The α -cell in diabetes mellitus. *Nat Rev Endocrinol* 14, 694-704,(2018).
- 138 **Groves, J. A., Lee, A., Yildirim, G. & Zachara, N. E.** Dynamic O-GlcNAcylation and its roles in the cellular stress response and homeostasis. *Cell Stress Chaperones* 18, 535-558,(2013).
- 139 **Gulaboski, R., Mirčeski, V., Kappl, R., Hoth, M. & Bozem, M.** Quantification of hydrogen peroxide by electrochemical methods and electron spin resonance spectroscopy. *Journal of The Electrochemical Society* 166, G82,(2019).
- 140 **Habegger, K. M. et al.** The metabolic actions of glucagon revisited. *Nat Rev Endocrinol* 6, 689-697,(2010).
- 141 **Hædersdal, S., Andersen, A., Knop, F. K. & Vilsbøll, T.** Revisiting the role of glucagon in health, diabetes mellitus and other metabolic diseases. *Nat Rev Endocrinol* 19, 321-335,(2023).
- 142 **Han, X. et al.** Shotgun lipidomics identifies cardiolipin depletion in diabetic myocardium linking altered substrate utilization with mitochondrial dysfunction. *Biochemistry* 44, 16684-16694,(2005).
- 143 **Han, X., Yang, K., Yang, J., Cheng, H. & Gross, R. W.** Shotgun lipidomics of cardiolipin molecular species in lipid extracts of biological samples. *J Lipid Res* 47, 864-879,(2006).
- 144 **Han, X. et al.** Alterations in myocardial cardiolipin content and composition occur at the very earliest stages of diabetes: A shotgun lipidomics study. *Biochemistry* 46, 6417-6428,(2007).

-
- 145 **Hao, Y. et al.** ALCAT1-mediated abnormal cardiolipin remodelling promotes mitochondrial injury in podocytes in diabetic kidney disease. *Cell Commun Signal* 22, 26,(2024).
- 146 **Hasan, S. S. et al.** Endothelial Notch signaling controls insulin transport in muscle. *EMBO Mol Med* 12, e09271,(2020).
- 147 **Hauff, K. D., Choi, S. Y., Frohman, M. A. & Hatch, G. M.** Cardiolipin synthesis is required to support human cholesterol biosynthesis from palmitate upon serum removal in Hela cells. *Can J Physiol Pharmacol* 87, 813-820,(2009).
- 148 **He, Q. & Han, X.** Cardiolipin remodeling in diabetic heart. *Chem Phys Lipids* 179, 75-81,(2014).
- 149 **Heck, D. E., Shakarjian, M., Kim, H. D., Laskin, J. D. & Vetrano, A. M.** Mechanisms of oxidant generation by catalase. *Ann N Y Acad Sci* 1203, 120-125,(2010).
- 150 **Heimberg, H., De Vos, A., Pipeleers, D., Thorens, B. & Schuit, F.** Differences in glucose transporter gene expression between rat pancreatic α - and β -cells are correlated to differences in glucose transport but not in glucose utilization. *J Biol Chem* 270, 8971-8975,(1995).
- 151 **Henquin, J.-C.** Regulation of insulin secretion: A matter of phase control and amplitude modulation. *Diabetologia* 52, 739-751,(2009).
- 152 **Henquin, J.-C.** The dual control of insulin secretion by glucose involves triggering and amplifying pathways in β -cells. *Diabetes research and clinical practice* 93, S27-S31,(2011).
- 153 **Herchuelz, A. & Malaisse, W.** Regulation of calcium fluxes in pancreatic islets: dissociation between calcium and insulin release. *The Journal of Physiology* 283, 409-424,(1978).
- 154 **Herzog, R. et al.** A novel informatics concept for high-throughput shotgun lipidomics based on the molecular fragmentation query language. *Genome biology* 12, 1-25,(2011).

-
- 155 **Herzog, R. et al.** LipidXplorer: A software for consensual cross-platform lipidomics. *PloS one* 7, e29851,(2012).
- 156 **Heymann, A. D., Cohen, Y. & Chodick, G.** Glucose-6-phosphate dehydrogenase deficiency and type 2 diabetes. *Diabetes care* 35, e58-e58,(2012).
- 157 **Himuro, M. et al.** Cellular autophagy in α -cells plays a role in the maintenance of islet architecture. *Journal of the Endocrine Society* 3, 1979-1992,(2019).
- 158 **Ho, T., Potapenko, E., Davis, D. B. & Merrins, M. J.** A plasma membrane-associated glycolytic metabolon is functionally coupled to K_{ATP} channels in pancreatic α - and β -cells from humans and mice. *Cell Rep* 42, 112394,(2023).
- 159 **Hoang, D. T. et al.** A conserved rule for pancreatic islet organization. *PLoS One* 9, e110384,(2014).
- 160 **Hoitzing, H. et al.** Energetic costs of cellular and therapeutic control of stochastic mitochondrial DNA populations. *PLoS Comput Biol* 15, e1007023,(2019).
- 161 **Hornby, B. et al.** Natural history comparison study to assess the efficacy of elamipretide in patients with Barth syndrome. *Orphanet J Rare Dis* 17, 336,(2022).
- 162 **Hou, X. et al.** Testosterone disruptor effect and gut microbiome perturbation in mice: early life exposure to doxycycline. *Chemosphere* 222, 722-731,(2019).
- 163 **Hou, Y. et al.** Appendicular skeletal muscle mass: a more sensitive biomarker of disease severity than BMI in adults with mitochondrial diseases. *PLoS One* 14, e0219628,(2019).
- 164 **Houtkooper, R. & Vaz, F.** Cardiolipin, the heart of mitochondrial metabolism. *Cellular and Molecular Life Sciences* 65, 2493-2506,(2008).
- 165 **Hu, F. B.** Globalization of diabetes: The role of diet, lifestyle, and genes. *Diabetes Care* 34, 1249-1257,(2011).

-
- 166 **Huang, Y. et al.** The PPAR pan-agonist bezafibrate ameliorates cardiomyopathy in a mouse model of Barth syndrome. *Orphanet J Rare Dis* 12, 1-9,(2017).
- 167 **Hughes, J. W., Ustione, A., Lavagnino, Z. & Piston, D. W.** Regulation of islet glucagon secretion: Beyond calcium. *Diabetes Obes Metab* 20 Suppl 2, 127-136,(2018).
- 168 **Huising, M. O.** Paracrine regulation of insulin secretion. *Diabetologia* 63, 2057-2063,(2020).
- 169 **Ida, S. et al.** Diverse metabolic effects of O-GlcNAcylation in the pancreas but limited effects in insulin-sensitive organs in mice. *Diabetologia* 60, 1761-1769,(2017).
- 170 **Ikon, N. & Ryan, R. O.** Cardiolipin and mitochondrial cristae organization. *Biochim Biophys Acta Biomembr* 1859, 1156-1163,(2017).
- 171 **Ino, T. et al.** Dilated cardiomyopathy with neutropenia, short stature, and abnormal carnitine metabolism. *The Journal of pediatrics* 113, 511-514,(1988).
- 172 **Jagirdar, G. et al.** Re-expression of tafazzin isoforms in TAZ-deficient C6 glioma cells restores cardiolipin composition but not proliferation rate and alterations in gene expression. *Frontiers in Genetics* 13, 931017,(2022).
- 173 **Jennings, R. E., Scharfmann, R. & Staels, W.** Transcription factors that shape the mammalian pancreas. *Diabetologia* 63, 1974-1980,(2020).
- 174 **Jezek, P., Holendova, B., Jaburek, M., Dlaskova, A. & Plecita-Hlavata, L.** Contribution of mitochondria to insulin secretion by various secretagogues. *Antioxid Redox Signal* 36, 920-952,(2022).
- 175 **Ježek, P. et al.** The pancreatic β -cell: The perfect redox system. *Antioxidants* 10, 197,(2021).
- 176 **Jia, D. et al.** Cardiolipin remodeling by ALCAT1 links hypoxia to coronary artery disease by promoting mitochondrial dysfunction. *Mol Ther* 29, 3498-3511,(2021).

- 177 **Jiang, F. et al.** Absence of cardiolipin in the *crd1* null mutant results in decreased mitochondrial membrane potential and reduced mitochondrial function. *J Biol Chem* 275, 22387-22394,(2000).
- 178 **Jo, S. et al.** Pancreatic β -cell hyper-O-GlcNAcylation leads to impaired glucose homeostasis *in vivo*. *Frontiers in Endocrinology* 13, 1040014,(2022).
- 179 **Johansson, K. A. et al.** Temporal control of neurogenin3 activity in pancreas progenitors reveals competence windows for the generation of different endocrine cell types. *Developmental cell* 12, 457-465,(2007).
- 180 **Johnson, J. M. et al.** Targeted overexpression of catalase to mitochondria does not prevent cardioskeletal myopathy in Barth syndrome. *Journal of molecular and cellular cardiology* 121, 94-102,(2018).
- 181 **Johnston, J. et al.** Mutation characterization and genotype-phenotype correlation in Barth syndrome. *Am J Hum Genet* 61, 1053-1058,(1997).
- 182 **Johnston, N. R. et al.** β -cell hubs dictate pancreatic islet responses to glucose. *Cell Metab* 24, 389-401,(2016).
- 183 **Jonas, J.-C. et al.** Glucose regulation of islet stress responses and β -cell failure in type 2 diabetes. *Diabetes, obesity and metabolism* 11, 65-81,(2009).
- 184 **Jones, D. E., Klacking, E. & Ryan, R. O.** Inborn errors of metabolism associated with 3-methylglutaconic aciduria. *Clinica Chimica Acta* 522, 96-104,(2021).
- 185 **Jones, P. M., Burns, C. J., Belin, V. D., Roderigo-Milne, H. M. & Persaud, S. J.** The role of cytosolic phospholipase A(2) in insulin secretion. *Diabetes* 53 Suppl 1, S172-178,(2004).
- 186 **Jorns, A., Barklage, E. & Grube, D.** Heterogeneities of the islets in the rabbit pancreas and the problem of "paracrine" regulation of islet cells. *Anat Embryol (Berl)* 178, 297-307,(1988).
- 187 **Joshi, A. S., Thompson, M. N., Fei, N., Hüttemann, M. & Greenberg, M. L.** Cardiolipin and mitochondrial phosphatidylethanolamine have overlapping functions in mitochondrial fusion in *Saccharomyces cerevisiae*. *J Biol Chem* 287, 17589-17597,(2012).

-
- 188 **Jung, H. S. et al.** Loss of autophagy diminishes pancreatic β -cell mass and function with resultant hyperglycemia. *Cell Metab* 8, 318-324,(2008).
- 189 **Justice, M. J. & Dhillon, P.** Vol. 9 101-103 (The Company of Biologists Ltd, 2016).
- 190 **Kabra, U. D. & Jastroch, M.** Mitochondrial Dynamics and Insulin Secretion. *Int J Mol Sci* 24,(2023).
- 191 **Kagan, V. E. et al.** Cytochrome c acts as a cardiolipin oxygenase required for release of proapoptotic factors. *Nat Chem Biol* 1, 223-232,(2005).
- 192 **Kagan, V. E. et al.** Anomalous peroxidase activity of cytochrome c is the primary pathogenic target in Barth syndrome. *Nat Metab* 5, 2184-2205,(2023).
- 193 **Kajikawa, M. et al.** Ouabain suppresses glucose-induced mitochondrial ATP production and insulin release by generating reactive oxygen species in pancreatic islets. *Diabetes* 51, 2522-2529,(2002).
- 194 **Kalwat, M. A. & Cobb, M. H.** Mechanisms of the amplifying pathway of insulin secretion in the β -cell. *Pharmacology & therapeutics* 179, 17-30,(2017).
- 195 **Kang, S.-L., Forsey, J., Dudley, D., Steward, C. G. & Tsai-Goodman, B.** Clinical characteristics and outcomes of cardiomyopathy in Barth syndrome: the UK experience. *Pediatric cardiology* 37, 167-176,(2016).
- 196 **Kanno, T., Suga, S., Wu, J., Kimura, M. & Wakui, M.** Intracellular cAMP potentiates voltage-dependent activation of L-type Ca^{2+} channels in rat islet β -cells. *Pflügers Archiv* 435, 578-580,(1998).
- 197 **Káňovičová, P. et al.** Blocking phosphatidylglycerol degradation in yeast defective in cardiolipin remodeling results in a new model of the Barth syndrome cellular phenotype. *J Biol Chem* 298,(2022).
- 198 **Karkucinska-Wieckowska, A. et al.** Left ventricular noncompaction (LVNC) and low mitochondrial membrane potential are specific for Barth syndrome. *J Inherit Metab Dis* 36, 929-937,(2013).

-
- 199 **Keeley, T. P. & Mann, G. E.** Defining physiological normoxia for improved translation of cell physiology to animal models and humans. *Physiol Rev* 99, 161-234,(2019).
- 200 **Keij, J. F., Bell-Prince, C. & Steinkamp, J. A.** Staining of mitochondrial membranes with 10-nonyl acridine orange, MitoFluor Green, and MitoTracker Green is affected by mitochondrial membrane potential altering drugs. *Cytometry* 39, 203-210,(2000).
- 201 **Kelley, R. I. et al.** X-linked dilated cardiomyopathy with neutropenia, growth retardation, and 3-methylglutaconic aciduria. *The Journal of pediatrics* 119, 738-747,(1991).
- 202 **Khuchua, Z., Yue, Z., Batts, L. & Strauss, A. W.** A zebrafish model of human Barth syndrome reveals the essential role of tafazzin in cardiac development and function. *Circulation research* 99, 201-208,(2006).
- 203 **Khuchua, Z., Glukhov, A. I., Strauss, A. W. & Javadov, S.** Elucidating the beneficial role of PPAR agonists in cardiac diseases. *Int J Mol Sci* 19,(2018).
- 204 **Kim, A. et al.** Islet architecture: A comparative study. *Islets* 1, 129-136,(2009).
- 205 **Kim, A. Y., Vernon, H., Manuel, R., Almuqbil, M. & Hornby, B.** Quality of life in Barth syndrome. *Ther Adv Rare Dis* 3, 26330040221093743,(2022).
- 206 **Kimura, T. et al.** Substantial decrease in plasmalogen in the heart associated with *tafazzin* deficiency. *Biochemistry* 57, 2162-2175,(2018).
- 207 **Kimura, T. et al.** Plasmalogen loss caused by remodeling deficiency in mitochondria. *Life Sci Alliance* 2,(2019).
- 208 **Koga, Y. et al.** MELAS and L-arginine therapy. *Mitochondrion* 7, 133-139,(2007).
- 209 **Kok, F. O. et al.** Reverse genetic screening reveals poor correlation between morpholino-induced and mutant phenotypes in zebrafish. *Developmental cell* 32, 97-108,(2015).

-
- 210 **Kolker, E. et al.** Toward more transparent and reproducible omics studies through a common metadata checklist and data publications. *OMICS* 18, 10-14,(2014).
- 211 **Kostic, M., Katoshevski, T. & Sekler, I.** Allosteric regulation of NCLX by mitochondrial membrane potential links the metabolic state and Ca^{2+} signaling in mitochondria. *Cell Rep* 25, 3465-3475. e3464,(2018).
- 212 **Kraffe, E., Soudant, P., Marty, Y., Kervarec, N. & Jehan, P.** Evidence of a tetradocosahexaenoic cardiolipin in some marine bivalves. *Lipids* 37, 507-514,(2002).
- 213 **Kraft, L. J., Nguyen, T. A., Vogel, S. S. & Kenworthy, A. K.** Size, stoichiometry, and organization of soluble LC3-associated complexes. *Autophagy* 10, 861-877,(2014).
- 214 **Krako Jakovljevic, N. et al.** Targeting mitochondria in diabetes. *Int J Mol Sci* 22, 6642,(2021).
- 215 **Kutschka, I. et al.** Activation of the integrated stress response rewires cardiac metabolism in Barth syndrome. *Basic Res Cardiol* 118, 47,(2023).
- 216 **Lacombe, M.-L. et al.** Interaction of NDPK-D with cardiolipin-containing membranes: Structural basis and implications for mitochondrial physiology. *Biochimie* 91, 779-783,(2009).
- 217 **Lagouge, M. et al.** Resveratrol improves mitochondrial function and protects against metabolic disease by activating SIRT1 and PGC-1 α . *Cell* 127, 1109-1122,(2006).
- 218 **Lam, C. J., Cox, A. R., Jacobson, D. R., Rankin, M. M. & Kushner, J. A.** Highly proliferative α -cell-related islet endocrine cells in human pancreata. *Diabetes* 67, 674-686,(2018).
- 219 **Lambeth, J. D.** Cytochrome P-450_{sc}: Cardiolipin as an effector of activity of a mitochondrial cytochrome P-450. *J Biol Chem* 256, 4757-4762,(1981).
- 220 **Lenzen, S.** Oxidative stress: The vulnerable β -cell. *Biochemical Society Transactions* 36, 343-347,(2008).

-
- 221 **Leung, P. S. & Ip, S. P.** Pancreatic acinar cell: Its role in acute pancreatitis. *Int J Biochem Cell Biol* 38, 1024-1030,(2006).
- 222 **Leung, Y. M. et al.** Electrophysiological characterization of pancreatic islet cells in the mouse insulin promoter-green fluorescent protein mouse. *Endocrinology* 146, 4766-4775,(2005).
- 223 **Lewandowski, S. L. et al.** Pyruvate kinase controls signal strength in the insulin secretory pathway. *Cell Metab* 32, 736-750. e735,(2020).
- 224 **Li, D.-S., Yuan, Y.-H., Tu, H.-J., Liang, Q.-L. & Dai, L.-J.** A protocol for islet isolation from mouse pancreas. *Nat Protoc* 4, 1649-1652,(2009).
- 225 **Li, J. et al.** Cardiolipin remodeling by ALCAT1 links oxidative stress and mitochondrial dysfunction to obesity. *Cell Metab* 12, 154-165,(2010).
- 226 **Li, J. et al.** Lysocardiolipin acyltransferase 1 (ALCAT1) controls mitochondrial DNA fidelity and biogenesis through modulation of MFN2 expression. *Proc Natl Acad Sci* 109, 6975-6980,(2012).
- 227 **Li, Y. et al.** Cardiolipin-induced activation of pyruvate dehydrogenase links mitochondrial lipid biosynthesis to TCA cycle function. *J Biol Chem* 294, 11568-11578,(2019).
- 228 **Li, Y. et al.** Favorable outcomes after heart transplantation in Barth syndrome. *The Journal of Heart and Lung Transplantation* 40, 1191-1198,(2021).
- 229 **Liesa, M., Palacin, M. & Zorzano, A.** Mitochondrial dynamics in mammalian health and disease. *Physiol Rev* 89, 799-845,(2009).
- 230 **Liu, X. et al.** Increased reactive oxygen species–mediated Ca²⁺/calmodulin-dependent protein kinase II activation contributes to calcium handling abnormalities and impaired contraction in Barth syndrome. *Circulation* 143, 1894-1911,(2021).
- 231 **Lou, W. et al.** Loss of tafazzin results in decreased myoblast differentiation in C2C12 cells: A myoblast model of Barth syndrome and cardiolipin deficiency. *Biochim Biophys Acta Mol Cell Biol Lipids* 1863, 857-865,(2018).

- 232 **Lu, Q., Zhang, X., Liang, T. & Bai, X.** O-GlcNAcylation: An important post-translational modification and a potential therapeutic target for cancer therapy. *Mol Med* 28, 115,(2022).
- 233 **Lu, Y.-W. et al.** Defining functional classes of Barth syndrome mutation in humans. *Human molecular genetics* 25, 1754-1770,(2016).
- 234 **Ma, J. & Hart, G. W.** Protein O-GlcNAcylation in diabetes and diabetic complications. *Expert Rev Proteomics* 10, 365-380,(2013).
- 235 **MacDonald, P. E. & Rorsman, P.** Metabolic messengers: Glucagon. *Nat Metab* 5, 186-192,(2023).
- 236 **Maechler, P.** Mitochondrial function and insulin secretion. *Molecular and cellular endocrinology* 379, 12-18,(2013).
- 237 **Mahmoud, A. I. et al.** Apolipoprotein E is a pancreatic extracellular factor that maintains mature β -cell gene expression. *PLoS One* 13, e0204595,(2018).
- 238 **Makino, A. et al.** Regulation of mitochondrial morphology and function by O-GlcNAcylation in neonatal cardiac myocytes. *Am J Physiol Regul Integr Comp Physiol* 300, R1296-R1302,(2011).
- 239 **Malhotra, A., Xu, Y., Ren, M. & Schlame, M.** Formation of molecular species of mitochondrial cardiolipin. 1. A novel transacylation mechanism to shuttle fatty acids between sn-1 and sn-2 positions of multiple phospholipid species. *Biochim Biophys Acta Mol Cell Biol Lipids* 1791, 314-320,(2009).
- 240 **Malhotra, K. et al.** Cardiolipin mediates membrane and channel interactions of the mitochondrial TIM23 protein import complex receptor Tim50. *Sci Adv* 3, e1700532,(2017).
- 241 **Mandal, M. K., Saikia, P., Chanu, N. K. & Chaurasia, N.** Modulation of lipid content and lipid profile by supplementation of iron, zinc, and molybdenum in indigenous microalgae. *Environ Sci Pollut Res Int* 26, 20815-20828,(2019).
- 242 **Marchi, S., Patergnani, S. & Pinton, P.** The endoplasmic reticulum–mitochondria connection: One touch, multiple functions. *Biochimica et Biophysica Acta (BBA)-Bioenergetics* 1837, 461-469,(2014).

-
- 243 **Marquez-Aguirre, A. L., Canales-Aguirre, A. A., Padilla-Camberos, E., Esquivel-Solis, H. & Diaz-Martinez, N. E.** Development of the endocrine pancreas and novel strategies for β -cell mass restoration and diabetes therapy. *Braz J Med Biol Res* 48, 765-776,(2015).
- 244 **Maruszczak, K. et al.** Arginine-induced glucagon secretion and glucagon-induced enhancement of amino acid catabolism are not influenced by ambient glucose levels in mice. *Am J Physiol Endocrinol Metab* 323, E207-E214,(2022).
- 245 **Mazar, I. et al.** Understanding the life experience of Barth syndrome from the perspective of adults: A qualitative one-on-one interview study. *Orphanet J Rare Dis* 14, 1-8,(2019).
- 246 **McCulloch, L. J. et al.** GLUT2 (SLC2A2) is not the principal glucose transporter in human pancreatic β -cells: Implications for understanding genetic association signals at this locus. *Molecular genetics and metabolism* 104, 648-653,(2011).
- 247 **Mejia, E. M., Nguyen, H. & Hatch, G. M.** Mammalian cardiolipin biosynthesis. *Chemistry and physics of lipids* 179, 11-16,(2014).
- 248 **Mejia, E. M. et al.** Glucose uptake and triacylglycerol synthesis are increased in Barth syndrome lymphoblasts. *Lipids* 52, 161-165,(2017).
- 249 **Melo, E. P. et al.** TriPer, an optical probe tuned to the endoplasmic reticulum tracks changes in luminal H_2O_2 . *BMC biology* 15, 1-15,(2017).
- 250 **Meloni, A., DeYoung, M., Lowe, C. & Parkes, D.** GLP-1 receptor activated insulin secretion from pancreatic β -cells: Mechanism and glucose dependence. *Diabetes, Obesity and Metabolism* 15, 15-27,(2013).
- 251 **Miller, P. C., Ren, M., Schlame, M., Toth, M. J. & Phoon, C. K.** A Bayesian analysis to determine the prevalence of Barth syndrome in the pediatric population. *The Journal of Pediatrics* 217, 139-144,(2020).
- 252 **Mishra, P. & Chan, D. C.** Metabolic regulation of mitochondrial dynamics. *J Cell Biol* 212, 379-387,(2016).

-
- 253 **Mitra, K., Wunder, C., Roysam, B., Lin, G. & Lippincott-Schwartz, J. A** hyperfused mitochondrial state achieved at G1-S regulates cyclin E buildup and entry into S phase. *Proc Natl Acad Sci* 106, 11960-11965,(2009).
- 254 **Mizushima, N. & Yoshimori, T.** How to interpret LC3 immunoblotting. *Autophagy* 3, 542-545,(2007).
- 255 **Moede, T., Leibiger, I. B. & Berggren, P.-O.** α -cell regulation of β -cell function. *Diabetologia* 63, 2064-2075,(2020).
- 256 **Montero, J. et al.** Cholesterol and peroxidized cardiolipin in mitochondrial membrane properties, permeabilization and cell death. *Biochim Biophys Acta* 1797, 1217-1224,(2010).
- 257 **Monzel, A. S., Enriquez, J. A. & Picard, M.** Multifaceted mitochondria: moving mitochondrial science beyond function and dysfunction. *Nat Metab* 5, 546-562,(2023).
- 258 **Mookerjee, S. A., Goncalves, R. L., Gerencser, A. A., Nicholls, D. G. & Brand, M. D.** The contributions of respiration and glycolysis to extracellular acid production. *Biochimica et Biophysica Acta (BBA)-Bioenergetics* 1847, 171-181,(2015).
- 259 **Murphy, M. P. et al.** Unraveling the biological roles of reactive oxygen species. *Cell Metab* 13, 361-366,(2011).
- 260 **Nagai, T., Sawano, A., Park, E. S. & Miyawaki, A.** Circularly permuted green fluorescent proteins engineered to sense Ca^{2+} . *Proc Natl Acad Sci* 98, 3197-3202,(2001).
- 261 **Neikirk, K. et al.** MitoTracker: A useful tool in need of better alternatives. *Eur J Cell Biol* 102, 151371,(2023).
- 262 **Ng, X. W., Chung, Y. H. & Piston, D. W.** Intercellular communication in the islet of Langerhans in health and disease. *Compr Physiol* 11, 2191-2225,(2021).
- 263 **Nickel, A. G. et al.** Reversal of mitochondrial transhydrogenase causes oxidative stress in heart failure. *Cell Metab* 22, 472-484,(2015).

- 264 **Nita, Il et al.** Pancreatic β -cell Na^+ channels control global Ca^{2+} signaling and oxidative metabolism by inducing Na^+ and Ca^{2+} responses that are propagated into mitochondria. *FASEB J* 28, 3301-3312,(2014).
- 265 **Nita, I. I. et al.** The mitochondrial $\text{Na}^+/\text{Ca}^{2+}$ exchanger upregulates glucose dependent Ca^{2+} signalling linked to insulin secretion.(2012).
- 266 **Noguchi, G. M. & Huising, M. O.** Integrating the inputs that shape pancreatic islet hormone release. *Nat Metab* 1, 1189-1201,(2019).
- 267 **Oemer, G. et al.** Fatty acyl availability modulates cardiolipin composition and alters mitochondrial function in HeLa cells. *J Lipid Res* 62, 100111,(2021).
- 268 **Oguntibeju, O. O.** Type 2 diabetes mellitus, oxidative stress and inflammation: Examining the links. *Int J Physiol Pathophysiol Pharmacol* 11, 45-63,(2019).
- 269 **Ohashi, K., Kawai, S. & Murata, K.** Identification and characterization of a human mitochondrial NAD kinase. *Nat Commun* 3, 1248,(2012).
- 270 **Osipovich, A. B., Stancill, J. S., Cartailier, J.-P., Dudek, K. D. & Magnuson, M. A.** Excitotoxicity and overnutrition additively impair metabolic function and identity of pancreatic β -cells. *Diabetes* 69, 1476-1491,(2020).
- 271 **Oyarbide Cuervas-Mons, U., Kodger, J., del Rio, S., Sandler, Y. & Corey, S. J.** No cardiomyopathy or skeletal muscle weakness in an organismal model of Barth syndrome - is metabolism the basis for its neutropenia? *Blood* 140, 5472-5472,(2022).
- 272 **Pak, V. V. et al.** Ultrasensitive genetically encoded indicator for hydrogen peroxide identifies roles for the oxidant in cell migration and mitochondrial function. *Cell Metab* 31, 642-653. e646,(2020).
- 273 **Pang, J., Bao, Y., Mitchell-Silbaugh, K., Veevers, J. & Fang, X.** Barth syndrome cardiomyopathy: An update. *Genes (Basel)* 13,(2022).
- 274 **Paradies, G., Petrosillo, G., Paradies, V. & Ruggiero, F. M.** Oxidative stress, mitochondrial bioenergetics, and cardiolipin in aging. *Free Radic Biol Med* 48, 1286-1295,(2010).

- 275 **Paradies, G., Paradies, V., Ruggiero, F. M. & Petrosillo, G.** Oxidative stress, cardiolipin and mitochondrial dysfunction in nonalcoholic fatty liver disease. *World J Gastroenterol* 20, 14205-14218,(2014).
- 276 **Pember, S. O., Powell, G. L. & Lambeth, J. D.** Cytochrome P-450_{scc}-phospholipid interactions: Evidence for a cardiolipin binding site and thermodynamics of enzyme interactions with cardiolipin, cholesterol, and adrenodoxin. *J Biol Chem* 258, 3198-3206,(1983).
- 277 **Pereda, J. et al.** Effect of simultaneous inhibition of TNF- α production and xanthine oxidase in experimental acute pancreatitis: The role of mitogen activated protein kinases. *Annals of surgery* 240, 108,(2004).
- 278 **Perego, C. et al.** Cholesterol metabolism, pancreatic β -cell function and diabetes. *Biochim Biophys Acta Mol Basis Dis* 1865, 2149-2156,(2019).
- 279 **Petit, P. X., Ardilla-Osorio, H., Penalvia, L. & Rainey, N. E.** Tafazzin mutation affecting cardiolipin leads to increased mitochondrial superoxide anions and mitophagy inhibition in Barth syndrome. *Cells* 9, 2333,(2020).
- 280 **Phoon, C. K. et al.** Tafazzin knockdown in mice leads to a developmental cardiomyopathy with early diastolic dysfunction preceding myocardial noncompaction. *Journal of the american heart association* 1, e000455,(2012).
- 281 **Plecitá-Hlavatá, L. et al.** Glucose-stimulated insulin secretion fundamentally requires H₂O₂ signaling by NADPH oxidase 4. *Diabetes* 69, 1341-1354,(2020).
- 282 **Pogwizd, S. M. & Bers, D. M.** Rabbit models of heart disease. *Drug Discovery Today: Disease Models* 5, 185-193,(2008).
- 283 **Pokorná, L. et al.** Specific degradation of phosphatidylglycerol is necessary for proper mitochondrial morphology and function. *Biochimica et Biophysica Acta (BBA)-Bioenergetics* 1857, 34-45,(2016).
- 284 **Poux, C., van Rheede, T., Madsen, O. & de Jong, W. W.** Sequence gaps join mice and men: Phylogenetic evidence from deletions in two proteins. *Molecular biology and evolution* 19, 2035-2037,(2002).

- 285 **Powers, C., Huang, Y., Strauss, A. & Khuchua, Z.** Diminished exercise capacity and mitochondrial bc1 complex deficiency in *tafazzin*-knockdown mice. *Frontiers in Physiology* 4, 74,(2013).
- 286 **Potentiometric Probes.** *Classic Slow Dyes for Measuring Membrane Potential in Cells and Mitochondria*, <<https://potentiometricprobes.com/tmre-and-tmm-slow-vsds-for-mitochondria-imaging-and-resting-potential/>> (2024).
- 287 **Pu, W. T.** Experimental models of Barth syndrome. *J Inherit Metab Dis* 45, 72-81,(2022).
- 288 **Qin, K. et al.** SIRT6-mediated transcriptional suppression of Txnip is critical for pancreatic β -cell function and survival in mice. *Diabetologia* 61, 906-918,(2018).
- 289 **Quinlan, C. L. et al.** The 2-oxoacid dehydrogenase complexes in mitochondria can produce superoxide/hydrogen peroxide at much higher rates than complex I. *J Biol Chem* 289, 8312-8325,(2014).
- 290 **Ramracheya, R. et al.** GLP-1 suppresses glucagon secretion in human pancreatic α -cells by inhibition of P/Q-type Ca^{2+} channels. *Physiol Rep* 6, e13852,(2018).
- 291 **Ravier, M. A. et al.** Mechanisms of control of the free Ca^{2+} concentration in the endoplasmic reticulum of mouse pancreatic β -cells: Interplay with cell metabolism and $[\text{Ca}^{2+}]_c$ and role of SERCA2b and SERCA3. *Diabetes* 60, 2533-2545,(2011).
- 292 **Reid Thompson, W. et al.** A phase 2/3 randomized clinical trial followed by an open-label extension to evaluate the effectiveness of elamipretide in Barth syndrome, a genetic disorder of mitochondrial cardiolipin metabolism. *Genet Med* 23, 471-478,(2021).
- 293 **Rein, T.** Post-translational modifications and stress adaptation: The paradigm of FKBP51. *Biochem Soc Trans* 48, 441-449,(2020).
- 294 **Ren, M., Miller, P. C., Schlame, M. & Phoon, C. K.** A critical appraisal of the *tafazzin* knockdown mouse model of Barth syndrome: What have we learned

- about pathogenesis and potential treatments? *Am J Physiol Heart Circ Physiol* 317, H1183-H1193,(2019).
- 295 **Renner, L. D. & Weibel, D. B.** Cardiolipin microdomains localize to negatively curved regions of *Escherichia coli* membranes. *Proc Natl Acad Sci* 108, 6264-6269,(2011).
- 296 **Reynolds, S., Kreider, C. M. & Bendixen, R.** A mixed-methods investigation of sensory response patterns in Barth syndrome: A clinical phenotype? *Am J Med Genet A* 158A, 1647-1653,(2012).
- 297 **Rhee, S. G.** Overview on peroxiredoxin. *Mol Cells* 39, 1-5,(2016).
- 298 **Rhee, S. G., Woo, H. A. & Kang, D.** The role of peroxiredoxins in the transduction of H₂O₂ signals. *Antioxid Redox Signal* 28, 537-557,(2018).
- 299 **Richter-Dennerlein, R. et al.** DNAJC19, a mitochondrial cochaperone associated with cardiomyopathy, forms a complex with prohibitins to regulate cardiolipin remodeling. *Cell Metab* 20, 158-171,(2014).
- 300 **Rigaud, C. et al.** Natural history of Barth syndrome: A national cohort study of 22 patients. *Orphanet J Rare Dis* 8, 1-13,(2013).
- 301 **Roberts, A. E. et al.** The Barth Syndrome Registry: Distinguishing disease characteristics and growth data from a longitudinal study. *Am J Med Genet A* 158A, 2726-2732,(2012).
- 302 **Roberts, D. D.** Extracellular matrix and redox signaling in cellular responses to stress. *Antioxid Redox Signal* 27, 771-773,(2017).
- 303 **Rocha, D. S., Manucci, A. C., Bruni-Cardoso, A., Kowaltowski, A. J. & Vilas-Boas, E. A.** A practical and robust method to evaluate metabolic fluxes in primary pancreatic islets. *Mol Metab* 83, 101922,(2024).
- 304 **Rodriguez-Diaz, R. et al.** Paracrine interactions within the pancreatic islet determine the glycemic set point. *Cell Metab* 27, 549-558. e544,(2018).
- 305 **Rodriguez-Hernandez, A. et al.** Doxycycline prevents preclinical atherosclerosis, pancreatic islet loss and improves insulin secretion after

- glycemic stimulation: Preclinical study in individuals with a high-fat diet. *Biomedicines* 11, 717,(2023).
- 306 **Rok, J. et al.** Cytotoxic and proapoptotic effect of doxycycline – an *in vitro* study on the human skin melanoma cells. *Toxicology in Vitro* 65, 104790,(2020).
- 307 **Roma, L. P. & Jonas, J.-C.** Nutrient metabolism, subcellular redox state, and oxidative stress in pancreatic islets and β -cells. *Journal of molecular biology* 432, 1461-1493,(2020).
- 308 **Rorsman, P. et al.** The cell physiology of biphasic insulin secretion. *Physiology* 15, 72-77,(2000).
- 309 **Rorsman, P., Eliasson, L., Kanno, T., Zhang, Q. & Gopel, S.** Electrophysiology of pancreatic β -cells in intact mouse islets of Langerhans. *Progress in biophysics and molecular biology* 107, 224-235,(2011).
- 310 **Rorsman, P. & Braun, M.** Regulation of insulin secretion in human pancreatic islets. *Annual review of physiology* 75, 155-179,(2013).
- 311 **Rosol, T. J., DeLellis, R. A., Harvey, P. W. & Sutcliffe, C.** Endocrine system. *Haschek and Rousseaux's handbook of toxicologic pathology*, 2391-2492,(2013).
- 312 **Rowland, T. J., Sweet, M. E., Mestroni, L. & Taylor, M. R.** Danon disease - dysregulation of autophagy in a multisystem disorder with cardiomyopathy. *J Cell Sci* 129, 2135-2143,(2016).
- 313 **Rustenbeck, I., Schulze, T., Morsi, M., Alshafei, M. & Panten, U.** What is the metabolic amplification of insulin secretion and is it (still) relevant? *Metabolites* 11, 355,(2021).
- 314 **Rutter, G. A. et al.** Local and regional control of calcium dynamics in the pancreatic islet. *Diabetes Obes Metab* 19 Suppl 1, 30-41,(2017).
- 315 **Sabbah, H. N. et al.** Chronic therapy with elamipretide (MTP-131), a novel mitochondria-targeting peptide, improves left ventricular and mitochondrial function in dogs with advanced heart failure. *Circulation: Heart Failure* 9, e002206,(2016).

- 316 **Sabbah, H. N.** Barth syndrome cardiomyopathy: Targeting the mitochondria with elamipretide. *Heart failure reviews* 26, 237-253,(2021).
- 317 **Sakamoto, O., Kitoh, T., Ohura, T., Ohya, N. & Iinuma, K.** Novel missense mutation (R94S) in the TAZ (G4.5) gene in a Japanese patient with Barth syndrome. *J Hum Genet* 47, 229-231,(2002).
- 318 **Saleem, A. et al.** Polymerase gamma mutator mice rely on increased glycolytic flux for energy production. *Mitochondrion* 21, 19-26,(2015).
- 319 **Sanchez, P. K. M. et al.** LDHA is enriched in human islet α -cells and upregulated in type 2 diabetes. *Biochem Biophys Res Commun* 568, 158-166,(2021).
- 320 **Sandlers, Y. et al.** Metabolomics reveals new mechanisms for pathogenesis in Barth syndrome and introduces novel roles for cardiolipin in cellular function. *PloS one* 11, e0151802,(2016).
- 321 **Santos, L. R. et al.** NNT reverse mode of operation mediates glucose control of mitochondrial NADPH and glutathione redox state in mouse pancreatic β -cells. *Mol Metab* 6, 535-547,(2017).
- 322 **Santos, R. M. et al.** Widespread synchronous $[Ca^{2+}]_i$ oscillations due to bursting electrical activity in single pancreatic islets. *Pflügers Archiv* 418, 417-422,(1991).
- 323 **Sargiacomo, C., Stonehouse, S., Moftakhar, Z., Sotgia, F. & Lisanti, M. P.** MitoTracker Deep Red (MTDR) is a metabolic inhibitor for targeting mitochondria and eradicating cancer stem cells (CSCs), with anti-tumor and anti-metastatic activity *in vivo*. *Frontiers in Oncology* 11, 678343,(2021).
- 324 **Saric, A., Andreau, K., Armand, A.-S., Møller, I. M. & Petit, P. X.** Barth syndrome: From mitochondrial dysfunctions associated with aberrant production of reactive oxygen species to pluripotent stem cell studies. *Frontiers in Genetics* 6, 359,(2016).
- 325 **Scaduto, R. C. & Grotyohann, L. W.** Measurement of mitochondrial membrane potential using fluorescent rhodamine derivatives. *Biophysical journal* 76, 469-477,(1999).

- 326 **Schafer, C. et al.** The effects of PPAR stimulation on cardiac metabolic pathways in Barth syndrome mice. *Frontiers in Pharmacology* 9, 318,(2018).
- 327 **Schlame, M. et al.** Deficiency of tetralinoleoyl-cardiolipin in Barth syndrome. *Annals of neurology* 51, 634-637,(2002).
- 328 **Schlame, M. et al.** Phospholipid abnormalities in children with Barth syndrome. *Journal of the American College of Cardiology* 42, 1994-1999,(2003).
- 329 **Schlame, M.** Cardiolipin remodeling and the function of tafazzin. *Biochim Biophys Acta Mol Cell Biol Lipids* 1831, 582-588,(2013).
- 330 **Schlame, M. & Xu, Y.** The function of tafazzin, a mitochondrial phospholipid–lysophospholipid acyltransferase. *Journal of molecular biology* 432, 5043-5051,(2020).
- 331 **Schlattner, U. et al.** Mitochondrial cardiolipin/phospholipid trafficking: The role of membrane contact site complexes and lipid transfer proteins. *Chemistry and physics of lipids* 179, 32-41,(2014).
- 332 **Schrader, M. & Fahimi, H. D.** Peroxisomes and oxidative stress. *Biochim Biophys Acta Mol Cell Res* 1763, 1755-1766,(2006).
- 333 **Schuler, M.-H., Di Bartolomeo, F., Mårtensson, C. U., Daum, G. & Becker, T.** Phosphatidylcholine affects inner membrane protein translocases of mitochondria. *J Biol Chem* 291, 18718-18729,(2016).
- 334 **Scialò, F., Fernández-Ayala, D. J. & Sanz, A.** Role of mitochondrial reverse electron transport in ROS signaling: Potential roles in health and disease. *Frontiers in Physiology* 8, 428,(2017).
- 335 **Shan, J. et al.** Oxidative stress, autophagy, and apoptosis induced by doxycycline in loach fin cells *in vitro*. *Science of the Total Environment* 839, 156379,(2022).
- 336 **Shilleh, A. H., Vilorio, K., Broichhagen, J., Campbell, J. E. & Hodson, D. J.** GLP1R and GIPR expression and signaling in pancreatic α -cells, β -cells and δ -cells. *Peptides* 175, 171179,(2024).

- 337 **Shim, J.-K. et al.** Etomoxir, a carnitine palmitoyltransferase 1 inhibitor, combined with temozolomide reduces stemness and invasiveness in patient-derived glioblastoma tumorspheres. *Cancer Cell International* 22, 309,(2022).
- 338 **Short, S. A. & White, D. C.** Biosynthesis of cardiolipin from phosphatidylglycerol in *Staphylococcus aureus*. *Journal of bacteriology* 109, 820-826,(1972).
- 339 **Siu, P. M., Donley, D. A., Bryner, R. W. & Alway, S. E.** Citrate synthase expression and enzyme activity after endurance training in cardiac and skeletal muscles. *J Appl Physiol* (1985) 94, 555-560,(2003).
- 340 **Smeir, E. et al.** Depletion of cardiac cardiolipin synthase alters systolic and diastolic function. *Iscience* 24,(2021).
- 341 **Song, M., Kim, S.-H., Im, C. Y. & Hwang, H.-J.** Recent development of small molecule glutaminase inhibitors. *Current topics in medicinal chemistry* 18, 432-443,(2018).
- 342 **Sourdeval, M., Lemaire, C., Brenner, C., Boisivieux-Ulrich, E. & Marano, F.** Mechanisms of doxycycline-induced cytotoxicity on human bronchial epithelial cells. *Frontiers in Bioscience-Landmark* 11, 3036-3048,(2006).
- 343 **Soustek, M. S. et al.** Characterization of a transgenic short hairpin RNA-induced murine model of Tafazzin deficiency. *Human gene therapy* 22, 865-871,(2011).
- 344 **Spencer, C. T. et al.** Cardiac and clinical phenotype in Barth syndrome. *Pediatrics* 118, e337-e346,(2006).
- 345 **Spencer, N. Y. & Stanton, R. C.** The Warburg effect, lactate, and nearly a century of trying to cure cancer. *Semin Nephrol* 39, 380-393,(2019).
- 346 **Stacpoole, P. W.** Lactic acidosis and other mitochondrial disorders. *Metabolism* 46, 306-321,(1997).
- 347 **Stancill, J. S. et al.** Chronic β -cell depolarization impairs β -cell identity by disrupting a network of Ca^{2+} -regulated genes. *Diabetes* 66, 2175-2187,(2017).

- 348 **Stanton, R. C.** Glucose-6-phosphate dehydrogenase, NADPH, and cell survival. *IUBMB life* 64, 362-369,(2012).
- 349 **Steiner, D. J., Kim, A., Miller, K. & Hara, M.** Pancreatic islet plasticity: Interspecies comparison of islet architecture and composition. *Islets* 2, 135-145,(2010).
- 350 **Stepanyants, N. et al.** Cardiolipin's propensity for phase transition and its reorganization by dynamin-related protein 1 form a basis for mitochondrial membrane fission. *Molecular biology of the cell* 26, 3104-3116,(2015).
- 351 **Sturm, G. et al.** OxPhos defects cause hypermetabolism and reduce lifespan in cells and in patients with mitochondrial diseases. *Commun Biol* 6, 22,(2023).
- 352 **Suba, K. et al.** Intra-islet glucagon signalling regulates β -cell connectivity, first-phase insulin secretion and glucose homeostasis. *Mol Metab* 85, 101947,(2024).
- 353 **Suga, T. et al.** SGLT1 in pancreatic α -cells regulates glucagon secretion in mice, possibly explaining the distinct effects of SGLT2 inhibitors on plasma glucagon levels. *Mol Metab* 19, 1-12,(2019).
- 354 **Surma, M. A. et al.** An automated shotgun lipidomics platform for high throughput, comprehensive, and quantitative analysis of blood plasma intact lipids. *European Journal of Lipid Science and Technology* 117, 1540-1549,(2015).
- 355 **Surma, M. A. et al.** Mouse lipidomics reveals inherent flexibility of a mammalian lipidome. *Sci Rep* 11, 19364,(2021).
- 356 **Svendsen, B. et al.** Insulin secretion depends on intra-islet glucagon signaling. *Cell Rep* 25, 1127-1134. e1122,(2018).
- 357 **Barth Syndrome Foundation.** *Medications used in Barth Syndrome*, <https://www.barthsyndrome.org/file_download/inline/9339f952-f5cf-4f51-958a-4c89941b2b04> (2018).

- 358 **Taddeo, E. P. et al.** Individual islet respirometry reveals functional diversity within the islet population of mice and human donors. *Mol Metab* 16, 150-159,(2018).
- 359 **Tan, E. P. et al.** Sustained O-GlcNAcylation reprograms mitochondrial function to regulate energy metabolism. *J Biol Chem* 292, 14940-14962,(2017).
- 360 **Tanday, N., Flatt, P. R., Irwin, N. & Moffett, R. C.** Liraglutide and sitagliptin counter β - to α -cell transdifferentiation in diabetes. *Journal of Endocrinology* 245, 53-64,(2020).
- 361 **Tanday, N., Tarasov, A. I., Moffett, R. C., Flatt, P. R. & Irwin, N.** Pancreatic islet cell plasticity: Pathogenic or therapeutically exploitable? *Diabetes, Obesity and Metabolism* 26, 16-31,(2024).
- 362 **Tang, Y. et al.** Cardiolipin oxidized by ROS from complex II acts as a target of gasdermin D to drive mitochondrial pore and heart dysfunction in endotoxemia. *Cell Rep* 43, 114237,(2024).
- 363 **Taylor, C. et al.** Clinical presentation and natural history of Barth Syndrome: An overview. *J Inherit Metab Dis* 45, 7-16,(2022).
- 364 **Taylor, R. P., Geisler, T. S., Chambers, J. H. & McClain, D. A.** Up-regulation of O-GlcNAc transferase with glucose deprivation in HepG2 cells is mediated by decreased hexosamine pathway flux. *J Biol Chem* 284, 3425-3432,(2009).
- 365 **Teague, W. E., Jr. et al.** Elastic properties of polyunsaturated phosphatidylethanolamines influence rhodopsin function. *Faraday Discuss* 161, 383-395; discussion 419-359,(2013).
- 366 **TeSlaa, T. & Teitell, M. A.** Techniques to monitor glycolysis. *Methods in enzymology* 542, 91-114,(2014).
- 367 **Thermo Fisher Scientific.** *GeneRuler 100 bp DNA Ladder*, <https://assets.thermofisher.com/TFS-Assets/LSG/manuals/MAN0012995_GeneRuler_100bp_DNALadder_50ug_UG.pdf> (2019).

- 368 **Thomas, D. A. et al.** Mitochondrial targeting with antioxidant peptide SS-31 prevents mitochondrial depolarization, reduces islet cell apoptosis, increases islet cell yield, and improves posttransplantation function. *J Am Soc Nephrol* 18, 213-222,(2007).
- 369 **Thompson, R. et al.** Current and future treatment approaches for Barth syndrome. *J Inherit Metab Dis* 45, 17-28,(2022).
- 370 **Thompson, W. R. et al.** Long-term efficacy and safety of elamipretide in patients with Barth syndrome: 168-week open-label extension results of TAZPOWER. *Genet Med*, 101138,(2024).
- 371 **Tomczewski, M. V., Chan, J. Z., Campbell, Z. E., Strathdee, D. & Duncan, R. E.** Phenotypic characterization of male tafazzin-knockout mice at 3, 6, and 12 months of age. *Biomedicines* 11, 638,(2023).
- 372 **Townsend, S. E. & Gannon, M.** Extracellular matrix-associated factors play critical roles in regulating pancreatic β -cell proliferation and survival. *Endocrinology* 160, 1885-1894,(2019).
- 373 **Trube, G., Rorsman, P. & Ohno-Shosaku, T.** Opposite effects of tolbutamide and diazoxide on the ATP-dependent K^+ channel in mouse pancreatic β -cells. *Pflügers Archiv* 407, 493-499,(1986).
- 374 **Tsuchiya, T. et al.** Increased α -cell to β -cell ratio in patients with pancreatic cancer. *Endocr J* 69, 1407-1414,(2022).
- 375 **Turrens, J. F.** Mitochondrial formation of reactive oxygen species. *The Journal of physiology* 552, 335-344,(2003).
- 376 **Twig, G. et al.** Fission and selective fusion govern mitochondrial segregation and elimination by autophagy. *EMBO J* 27, 433-446,(2008).
- 377 **Tyurin, V. et al.** Interactions of cardiolipin and lyso-cardiolipins with cytochrome c and tBid: Conflict or assistance in apoptosis. *Cell Death & Differentiation* 14, 872-875,(2007).
- 378 **Umapathi, P. et al.** Excessive O-GlcNAcylation causes heart failure and sudden death. *Circulation* 143, 1687-1703,(2021).

- 379 **Ungurianu, A., Zanfirescu, A. & Margina, D.** Sirtuins, resveratrol and the intertwining cellular pathways connecting them. *Ageing Res Rev* 88, 101936,(2023).
- 380 **Valdez-Ojeda, R. A., del Rayo Serrano-Vázquez, M. G., Toledano-Thompson, T., Chavarría-Hernández, J. C. & Barahona-Pérez, L. F.** Effect of media composition and culture time on the lipid profile of the green microalga *Coelastrum* sp. and its suitability for biofuel production. *BioEnergy Research* 14, 241-253,(2021).
- 381 **Valianpour, F. et al.** Cardiolipin deficiency in X-linked cardioskeletal myopathy and neutropenia (Barth syndrome, MIM 302060): A study in cultured skin fibroblasts. *J Pediatr* 141, 729-733,(2002).
- 382 **van Wouw, S. A. E. et al.** Sterol-regulated transmembrane protein TMEM86a couples LXR signaling to regulation of lysoplasmalogens in macrophages. *J Lipid Res* 64, 100325,(2023).
- 383 **Vaz, F. M., Houtkooper, R. H., Valianpour, F., Barth, P. G. & Wanders, R. J.** Only one splice variant of the human TAZ gene encodes a functional protein with a role in cardiolipin metabolism. *J Biol Chem* 278, 43089-43094,(2003).
- 384 **Vendrov, A. E. et al.** NOX4 NADPH oxidase-dependent mitochondrial oxidative stress in aging-associated cardiovascular disease. *Antioxid Redox Signal* 23, 1389-1409,(2015).
- 385 **Vernon, H. J., Sandler, Y., McClellan, R. & Kelley, R. I.** Clinical laboratory studies in Barth syndrome. *Molecular genetics and metabolism* 112, 143-147,(2014).
- 386 **Vicidomini, G., Bianchini, P. & Diaspro, A.** STED super-resolved microscopy. *Nat Methods* 15, 173-182,(2018).
- 387 **Vilas-Boas, E. A., Almeida, D. C., Roma, L. P., Ortis, F. & Carpinelli, A. R.** Lipotoxicity and β -cell failure in type 2 diabetes: Oxidative stress linked to NADPH oxidase and ER stress. *Cells* 10, 3328,(2021).

- 388 **Vilas-Boas, E. A. et al.** Early cytokine-induced transient NOX2 activity is ER stress-dependent and impacts β -cell function and survival. *Antioxidants* 10,(2021).
- 389 **Vilas-Boas, E. A. et al.** Transient NADPH oxidase 2-dependent H_2O_2 production drives early palmitate-induced lipotoxicity in pancreatic islets. *Free Radic Biol Med* 162, 1-13,(2021).
- 390 **Vincent, A. E. & Picard, M.** Multilevel heterogeneity of mitochondrial respiratory chain deficiency. *J Pathol* 246, 261-265,(2018).
- 391 **von der Malsburg, A. et al.** Structural mechanism of mitochondrial membrane remodelling by human OPA1. *Nat* 620, 1101-1108,(2023).
- 392 **Vreken, P. et al.** Defective remodeling of cardiolipin and phosphatidylglycerol in Barth syndrome. *Biochem Biophys Res Commun* 279, 378-382,(2000).
- 393 **Wakabayashi, Y. et al.** STAT3 suppression and β -cell ablation enhance α -to- β reprogramming mediated by Pdx1. *Sci Rep* 12, 21419,(2022).
- 394 **Walejko, J. M. et al.** Branched-chain α -ketoacids are preferentially reaminated and activate protein synthesis in the heart. *Nat Commun* 12, 1680,(2021).
- 395 **Wang, G. et al.** Modeling the mitochondrial cardiomyopathy of Barth syndrome with induced pluripotent stem cell and heart-on-chip technologies. *Nat Med* 20, 616-623,(2014).
- 396 **Wang, N. et al.** Low dose doxycycline decreases systemic inflammation and improves glycemic control, lipid profiles, and islet morphology and function in db/db mice. *Sci Rep* 7, 14707,(2017).
- 397 **Wang, S. et al.** AAV gene therapy prevents and reverses heart failure in a murine knockout model of Barth syndrome. *Circulation research* 126, 1024-1039,(2020).
- 398 **Wang, Z. & Thurmond, D. C.** Mechanisms of biphasic insulin-granule exocytosis—roles of the cytoskeleton, small GTPases and SNARE proteins. *Journal of cell science* 122, 893-903,(2009).

- 399 **Warpsinski, G. et al.** Nrf2-regulated redox signaling in brain endothelial cells adapted to physiological oxygen levels: Consequences for sulforaphane mediated protection against hypoxia-reoxygenation. *Redox Biol* 37, 101708,(2020).
- 400 **Wasmus, C. & Dudek, J.** Metabolic alterations caused by defective cardiolipin remodeling in inherited cardiomyopathies. *Life (Basel)* 10,(2020).
- 401 **Weimer, S. et al.** D-Glucosamine supplementation extends life span of nematodes and of ageing mice. *Nat Commun* 5, 3563,(2014).
- 402 **Weir, G. C. & Bonner-Weir, S.** Conflicting views about interactions between pancreatic α -cells and β -cells. *Diabetes* 72, 1741-1747,(2023).
- 403 **Wenning, A. S. et al.** TRP expression pattern and the functional importance of TRPC3 in primary human T-cells. *Biochim Biophys Acta Mol Cell Res* 1813, 412-423,(2011).
- 404 **Wojtovich, A. P., Berry, B. J. & Galkin, A.** Redox signaling through compartmentalization of reactive oxygen species: Implications for health and disease. *Antioxid Redox Signal* 31, 591-593,(2019).
- 405 **Wüst, R. C. et al.** The antibiotic doxycycline impairs cardiac mitochondrial and contractile function. *Int J Mol Sci* 22, 4100,(2021).
- 406 **Xavier, G. D. S. & Rutter, G. A.** Metabolic and functional heterogeneity in pancreatic β -cells. *Journal of molecular biology* 432, 1395-1406,(2020).
- 407 **Xiao, W., Wang, R.-S., Handy, D. E. & Loscalzo, J.** NAD(H) and NADP(H) redox couples and cellular energy metabolism. *Antioxid Redox Signal* 28, 251-272,(2018).
- 408 **Xiao, W. & Loscalzo, J.** Metabolic responses to reductive stress. *Antioxid Redox Signal* 32, 1330-1347,(2020).
- 409 **Xiong, X. et al.** Sirtuin 6 regulates glucose-stimulated insulin secretion in mouse pancreatic β -cells. *Diabetologia* 59, 151-160,(2016).

-
- 410 **Xu, Y., Sutachan, J. J., Plesken, H., Kelley, R. I. & Schlame, M.** Characterization of lymphoblast mitochondria from patients with Barth syndrome. *Laboratory investigation* 85, 823-830,(2005).
- 411 **Xu, Y. et al.** A Drosophila model of Barth syndrome. *Proc Natl Acad Sci* 103, 11584-11588,(2006).
- 412 **Xu, Y. & Schlame, M.** The turnover of glycerol and acyl moieties of cardiolipin. *Chem Phys Lipids* 179, 17-24,(2014).
- 413 **Yamada, H. et al.** Potentiation of glucose-stimulated insulin secretion by the GPR40–PLC–TRPC pathway in pancreatic β -cells. *Sci Rep* 6, 25912,(2016).
- 414 **Yanagishita, M.** Function of proteoglycans in the extracellular matrix. *Acta Pathol Jpn* 43, 283-293,(1993).
- 415 **Yaney, G. C. et al.** Phosphofructokinase isozymes in pancreatic islets and clonal β -cells (INS-1). *Diabetes* 44, 1285-1289,(1995).
- 416 **Yang, C. et al.** Glutamine oxidation maintains the TCA cycle and cell survival during impaired mitochondrial pyruvate transport. *Molecular cell* 56, 414-424,(2014).
- 417 **Yang, Y. et al.** Palmitate lipotoxicity is closely associated with the fatty acid-albumin complexes in BV-2 microglia. *PLoS One* 18, e0281189,(2023).
- 418 **Yasui, S. et al.** Hydrogen peroxide inhibits insulin-induced ATP-sensitive potassium channel activation independent of insulin signaling pathway in cultured vascular smooth muscle cells. *The Journal of Medical Investigation* 59, 36-44,(2012).
- 419 **Ye, C. et al.** Deletion of the cardiolipin-specific phospholipase Cld1 rescues growth and life span defects in the tafazzin mutant: Implications for Barth syndrome. *J Biol Chem* 289, 3114-3125,(2014).
- 420 **Yen, T.-Y. et al.** Acute metabolic decompensation and sudden death in Barth syndrome: Report of a family and a literature review. *European journal of pediatrics* 167, 941-944,(2008).

- 421 **Yi, W. et al.** Phosphofructokinase 1 glycosylation regulates cell growth and metabolism. *Science* 337, 975-980,(2012).
- 422 **Yu, Q., Shuai, H., Ahooghalandari, P., Gylfe, E. & Tengholm, A.** Glucose controls glucagon secretion by directly modulating cAMP in α -cells. *Diabetologia* 62, 1212-1224,(2019).
- 423 **Zaborska, K. E. et al.** Lactate activation of α -cells K_{ATP} channels inhibits glucagon secretion by hyperpolarizing the membrane potential and reducing Ca^{2+} entry. *Mol Metab* 42, 101056,(2020).
- 424 **Zachman, D. K. et al.** The role of calcium-independent phospholipase A2 in cardiolipin remodeling in the spontaneously hypertensive heart failure rat heart. *J Lipid Res* 51, 525-534,(2010).
- 425 **Zhang, I. X., Raghavan, M. & Satin, L. S.** The endoplasmic reticulum and calcium homeostasis in pancreatic β -cells. *Endocrinology* 161, bqz028,(2020).
- 426 **Zhang, I. X., Ren, J., Vadrevu, S., Raghavan, M. & Satin, L. S.** ER stress increases store-operated Ca^{2+} entry (SOCE) and augments basal insulin secretion in pancreatic β -cells. *J Biol Chem* 295, 5685-5700,(2020).
- 427 **Zhang, J., Liu, X., Nie, J. & Shi, Y.** Restoration of mitophagy ameliorates cardiomyopathy in Barth syndrome. *Autophagy* 18, 2134-2149,(2022).
- 428 **Zhang, L. et al.** New insight into the Nox4 subcellular localization in HEK293 cells: First monoclonal antibodies against Nox4. *Biochimie* 93, 457-468,(2011).
- 429 **Zhang, Q. et al.** Role of K_{ATP} channels in glucose-regulated glucagon secretion and impaired counterregulation in type 2 diabetes. *Cell Metab* 18, 871-882,(2013).
- 430 **Zhu, S. et al.** Cardiolipin remodeling defects impair mitochondrial architecture and function in a murine model of Barth syndrome cardiomyopathy. *Circulation: Heart Failure* 14, e008289,(2021).
- 431 **Zick, M., Rabl, R. & Reichert, A. S.** Cristae formation-linking ultrastructure and function of mitochondria. *Biochim Biophys Acta* 1793, 5-19,(2009).

- 432 **Zong, Y. et al.** Mitochondrial dysfunction: Mechanisms and advances in therapy. *Signal Transduct Target Ther* 9, 124,(2024).
- 433 **Zou, L. et al.** Glucose deprivation-induced increase in protein O-GlcNAcylation in cardiomyocytes is calcium-dependent. *J Biol Chem* 287, 34419-34431,(2012).
- 434 **Zou, W. et al.** Nanoscopic quantification of sub-mitochondrial morphology, mitophagy and mitochondrial dynamics in living cells derived from patients with mitochondrial diseases. *J Nanobiotechnology* 19, 136,(2021).

7 Supplements

7.1 Supplementary data and figures

7.1.1 Genotyping

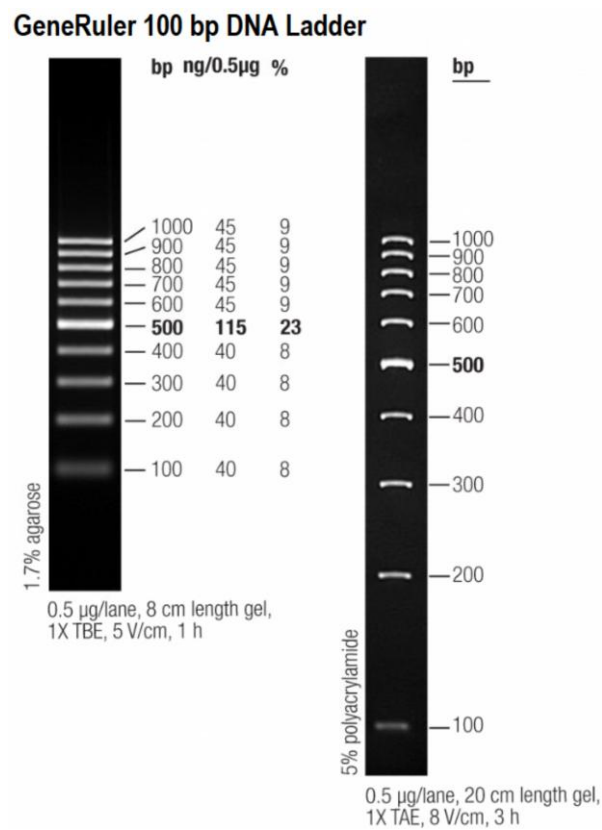


Figure 7.1: GeneRuler 100 bp DNA Ladder

The GeneRuler 100 bp DNA Ladder from Thermo Fisher Scientific was used for the genotyping experiments, depicted in **Figure 3.4**. The Figure was adapted from the Thermo Fisher Scientific website.³⁶⁷

PCR protocols

ShTaz	95 °C 5 min – (95 °C 30 s – 60 °C 30 s – 72 °C 1 min) x40 – 72 °C 10 min
Orp	95 °C 3 min – (95 °C 30 s – 64 °C 30 s – 72 °C 1 min) x20 – (95 °C 30 s – 54 °C 30 s – 72 °C 1 min) x10 – 72 °C 5 min
NNT	95 °C 5 min – (95 °C 1 min – 60 °C 1 min – 72 °C 1 min) x35 – 72 °C 10 min

Primer sequences

Rosa JD 72:	5' CCA TGG AAT TCG AAC GCT GAC GTC 3'
Rosa JD 73:	5' TAT GGG CTA TGA ACT AAT GAC CC 3'
Rosa JD 74:	5' GAG ACT CTG GCT ACT CAT CC 3'
Rosa JD 75:	5' CCT TCA GCA AGA GCT GGG GAC 3'
MS 282:	5' AAA GTC GCT CTG AGT TGT TAT 3'
MS 284:	5' GGA GCG GGA GAA ATG GAT ATG 3'
MS 305:	5' GGG CTA TGA ACT AAT GAC CCC G 3'
E8 for BI/6N:	5' TAT TGG CTA CAC AGA CCT TCC 3'
E8_rev for BI/6N:	5' TGA CGT GAC TCA TTG TAC CA 3'
E6-12 for BI/6J:	5' GTA GGG CCA ACT GTT TCT GC 3'
E6-12_rev for BI/6J:	5' TCC CCT CCC TTC CAT TTA GT 3'

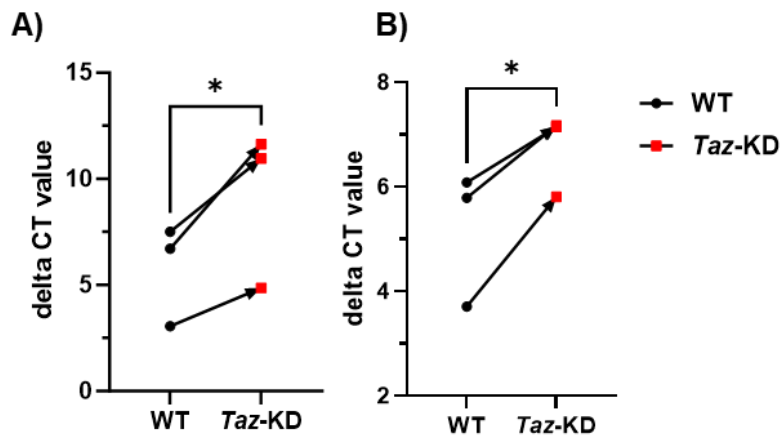
7.1.2 Characterisation of *Taz*-KD in pancreatic islets

Figure 7.2: Pairwise comparison of the delta CT values from *Taz* qPCR experiments

Taz gene expression (linked to **Figure 4.1**) of 20 wo WT and *Taz*-KD heart (A) and pancreatic islets (B) were pairwise compared due to variation among the single values. N = 3, Data = mean \pm SEM; N = number of animals; statistical analysis: paired *t* test: **p* < 0.05. Abbreviations: *tafazzin*-knockdown (*Taz*-KD), wildtype (WT), *tafazzin* (*Taz*), cardiolipin (CL), cycle threshold (CT).

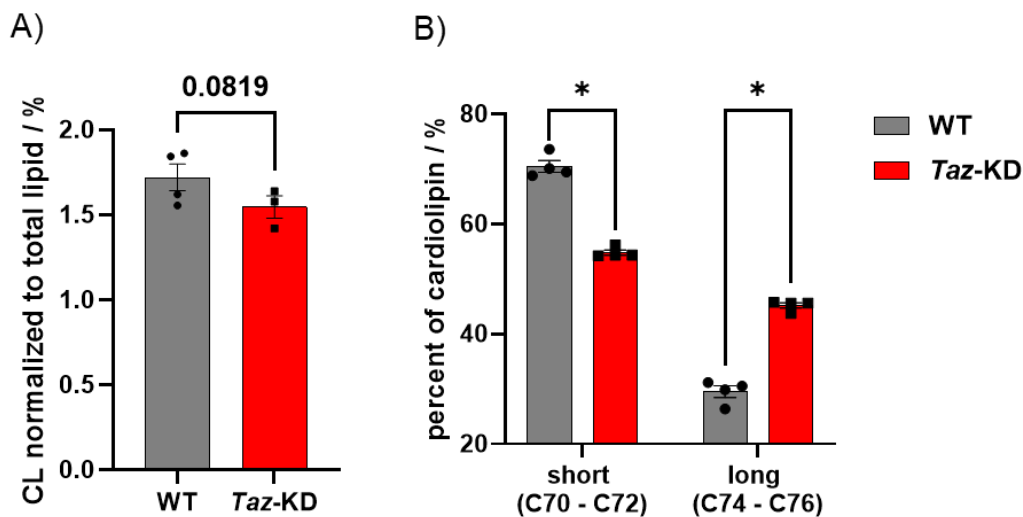


Figure 7.3: CL profile shift towards long acyl chain fatty acids in *Taz*-KD

(A) Total CL levels of 20 wo WT and *Taz*-KD pancreatic islets normalised to the sum of all lipids per sample, N (WT) = 4, N (*Taz*-KD) = 3. (B) Fatty acid composition of CL from 20 wo sh*Taz* pancreatic islets, separated into two groups (fatty acid chain length of 70 – 72 and 74 – 76 carbon atoms). N (WT) = 4, N (*Taz*-KD) = 3. Data = mean \pm SEM; N = number of animals; statistical analysis: unpaired *t*-test (A) or nonparametric Mann-Whitney test (B): statistical analysis: **p* < 0.05. Abbreviations: weeks of age (wo), *tafazzin*-knockdown (*Taz*-KD), wildtype (WT), *tafazzin* (*Taz*), cardiolipin (CL).

7.1.3 Whole-body metabolism

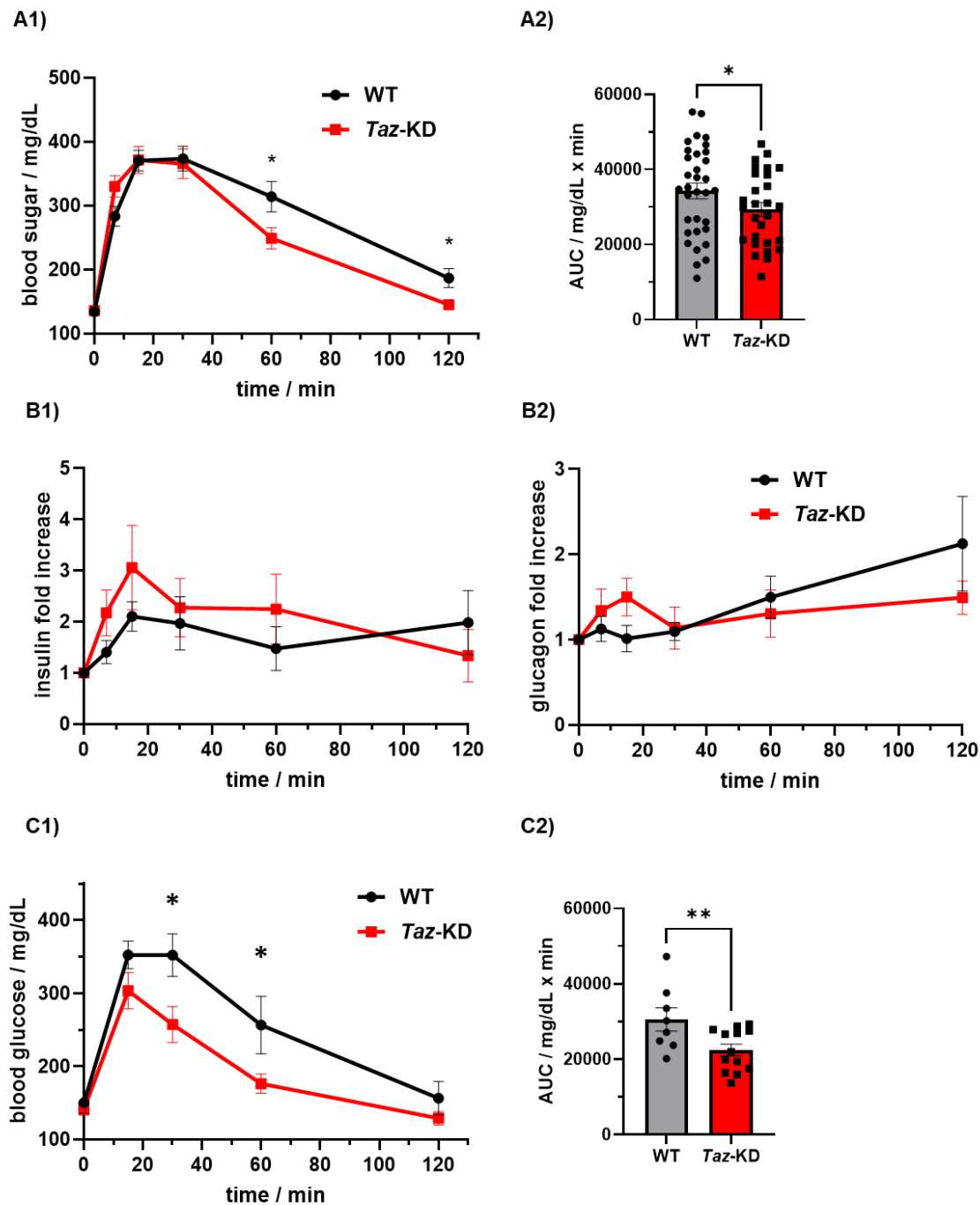


Figure 7.4: Altered whole-body glucose metabolism of *Taz*-KD mice at 20 and 50 weeks of age

(A) (A1) Kinetic and (A2) AUC quantification of blood glucose levels during GTT of 20 weeks WT and *Taz*-KD mice not separated by gender (linked to the **Figure 4.4**). N (WT) = 27, N (*Taz*-KD) = 28. **(B)** Calculation of fold increase of plasma insulin (B1) and glucagon (B2) during GTT. N (WT) = 7, N (*Taz*-KD) = 8. Data = mean \pm SEM; N = number of animals; statistical analysis: paired *t* test: **p* < 0.05. Abbreviations: weeks of age (wo), *tafazzin*-knockdown (*Taz*-KD), wildtype (WT), glucose tolerance test (GTT), area under the curve (AUC).

7.1.4 Immunohistochemistry

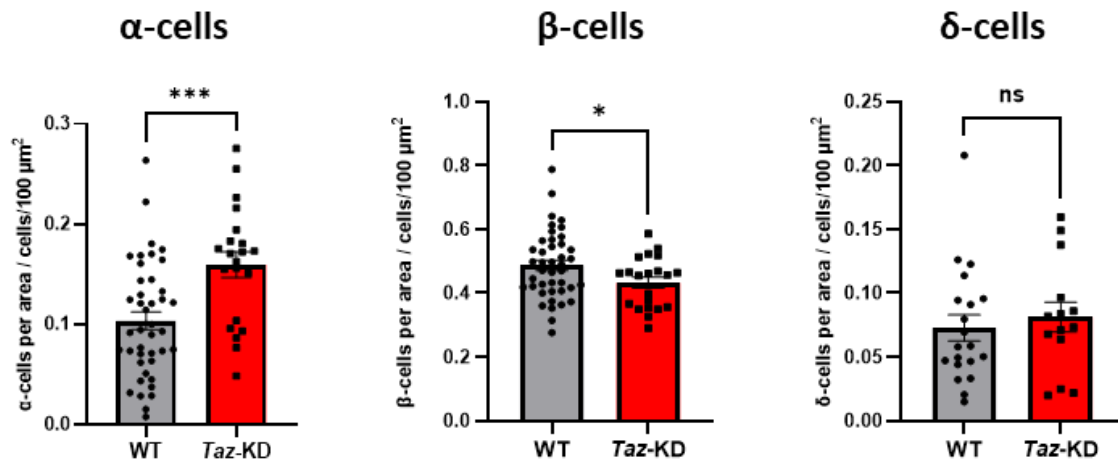


Figure 7.5: Increased α -cell and decreased β -cell number in *Taz*-KD pancreatic islets

Quantitative analysis of 20 wo WT and *Taz*-KD α - (left), β - (middle) and δ - (right) cell type number per pancreatic islet area. n (α -cells, WT) = 42, n (α -cells, *Taz*-KD) = 21, n (β -cells, WT) = 42, n (β -cells, *Taz*-KD) = 21, n (δ -cells, WT) = 20, n (δ -cell, *Taz*-KD) = 14. Data = mean \pm SEM; n = number of pancreatic islets and includes N (number of animals) = 6; statistical analysis: unpaired *t* test: **p* < 0.05, ****p* < 0.001, ns: *p* > 0.05. Abbreviations: weeks of age (wo), *tafazzin*-knockdown (*Taz*-KD), wildtype (WT).

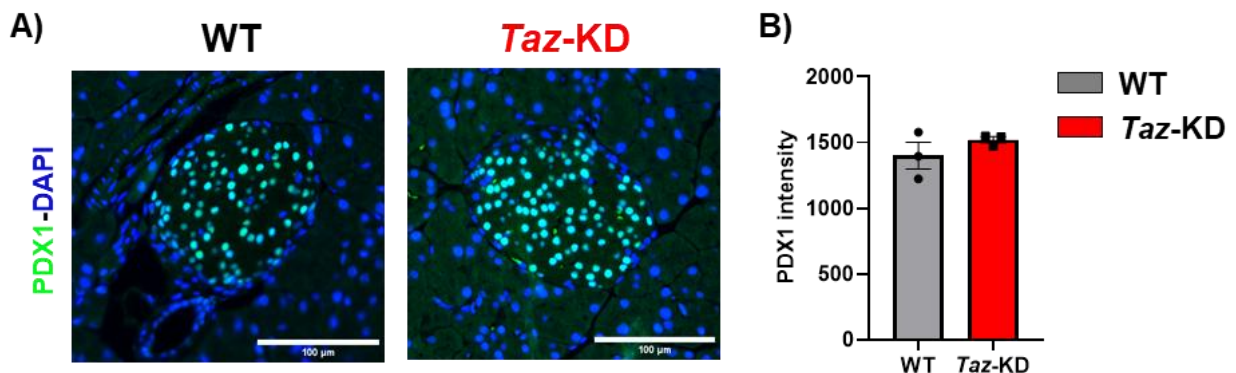


Figure 7.6: Similar PDX1 levels in WT and *Taz*-KD pancreatic islets

(A) Representative IHC images of PDX1 and DAPI staining of 20 wo WT and *Taz*-KD pancreatic islets. Scale bar: 100 μ m (B) Quantification of PDX1 intensity. N = 3. Data = mean \pm SEM; N = number of animals. Abbreviations: weeks of age (wo), *tafazzin*-knockdown (*Taz*-KD), wildtype (WT).

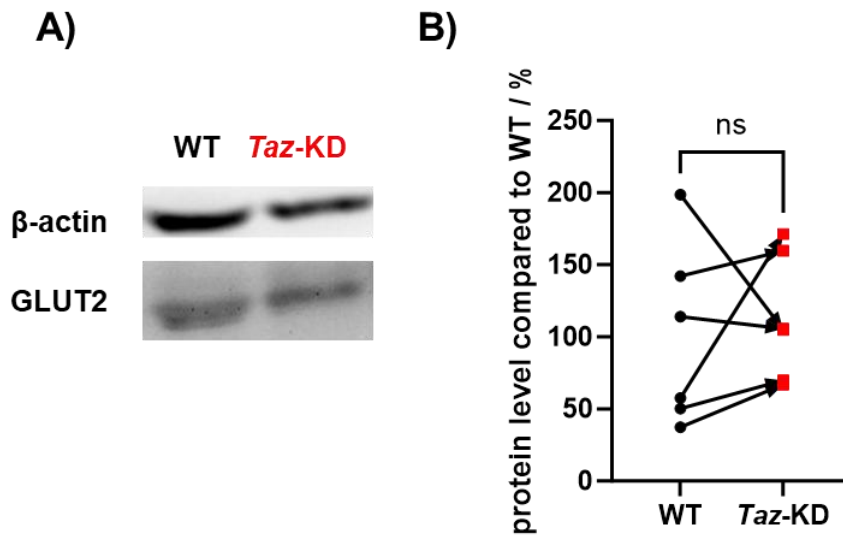
7.1.5 Investigation of pancreatic islet function in *Taz*-KD

Figure 7.7: WB analysis of GLUT2 in 20 wo WT and *Taz*-KD pancreatic islets

(A) Representative WB gel of GLUT2 at 50 kDa. Normalised to β -actin at 42 kDa. (B) Paired analysis of GLUT2 protein levels in 20 wo WT and *Taz*-KD pancreatic islets, N = 6. This Figure supplements the GLUT2 analysis in **Figure 4.8**. N = number of animals; statistical analysis: paired *t* test: ns: $p > 0.05$. Abbreviations: weeks of age (wo), *tafazzin*-knockdown (*Taz*-KD), wildtype (WT), western blot (WB).

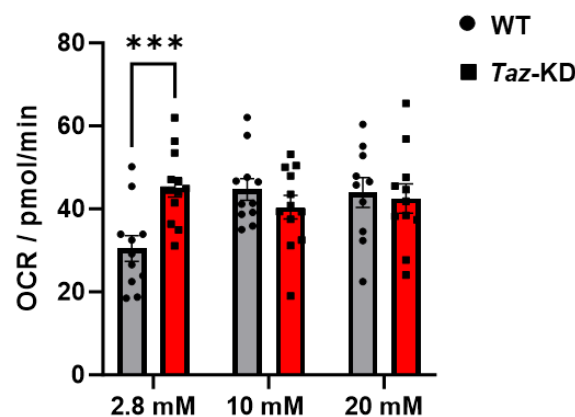


Figure 7.8: Increased maximum respiration of *Taz*-KD pancreatic islets

Quantification of maximum respiration of 20 wo WT and *Taz*-KD pancreatic islets (linked to **Figure 4.11**). n (WT) = 11, n (*Taz*-KD) = 13; n number of experiments include N (WT) = 5 and N (*Taz*-KD) = 4; Data = mean \pm SEM; n = number of experiments; N = number of animals; statistical analysis: unpaired *t* test: *** $p < 0.001$. Abbreviations: weeks of age (wo), *tafazzin*-knockdown (*Taz*-KD), wildtype (WT), western blot (WB).

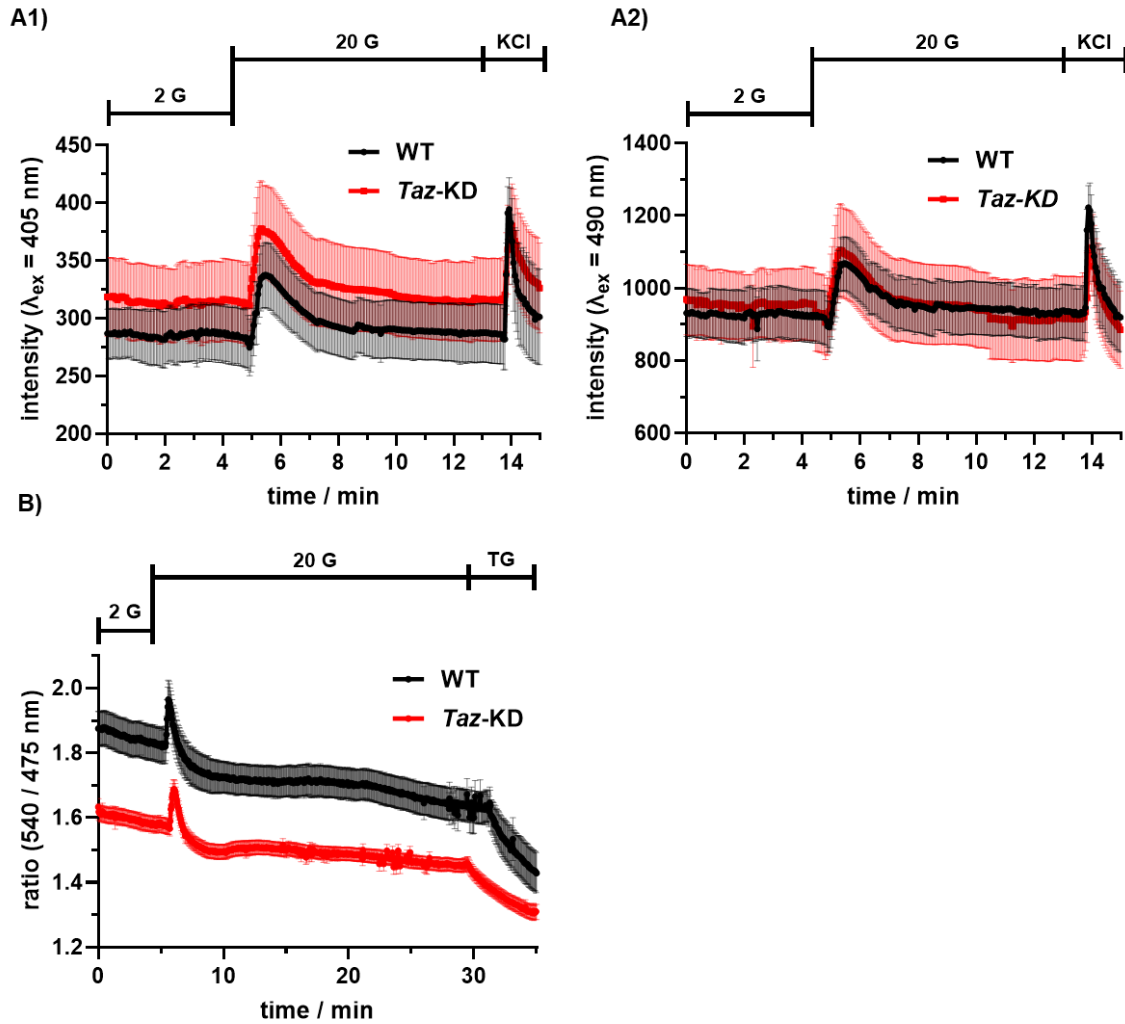


Figure 7.9: Non-normalised mitochondrial- and ER- Ca^{2+} curves of WT and *Taz-KD* pancreatic islet cells

(A) Non-normalised mitochondrial Ca^{2+} measurement of 20 wo WT and *Taz-KD* dispersed pancreatic islets transduced with Mito-Pericam. The kinetic response was measured in the 405 nm (A1) and 490 nm (A2) excitation window and glucose concentration was increased from 2 to 20 mM before adding 30 mM KCl as a positive control). N (WT) = 4, N (*Taz-KD*) = 5. (B) Representative non-normalised ER Ca^{2+} measurement of 20 wo WT and *Taz-KD* dispersed pancreatic β -cells transduced with RIP-D4ER. Glucose concentration was raised from 2 to 20 mM before addition of 1 μM TG to empty the ER Ca^{2+} storage. N (WT) = 4, N (*Taz-KD*) = 5. This figure is linked to **Figure 4.17**. Data = mean \pm SEM; N = number of animals; statistical analysis: unpaired *t* test: **p* < 0.05, ns: *p* > 0.05. Abbreviations: weeks of age (wo), *tafazzin*-knockdown (*Taz-KD*), wildtype (WT), thapsigargin (TG), rat insulin promoter (RIP).

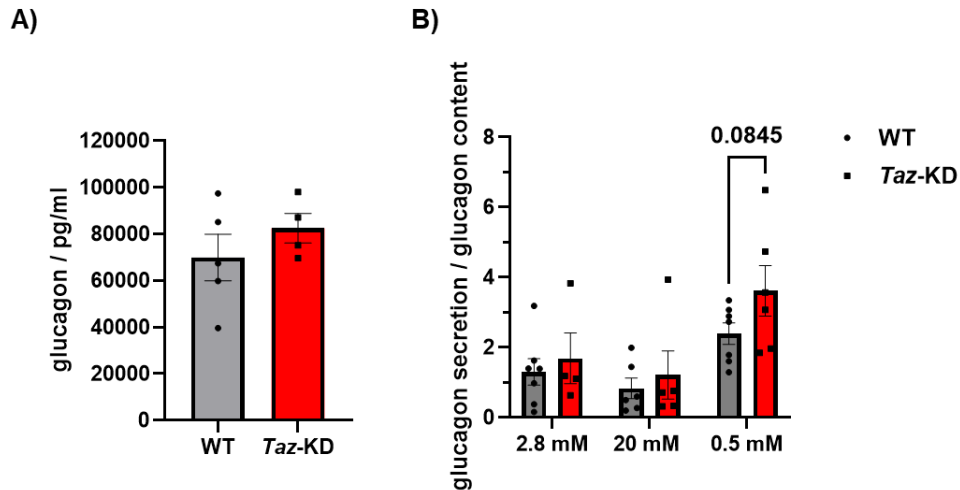


Figure 7.10: Glucagon content and glucagon secretion of *Taz*-KD pancreatic islets

(A) Glucagon content of 20 wo WT and *Taz*-KD pancreatic islets, N (WT) = 5, N (*Taz*-KD) = 4. (B) Glucagon secretion normalised to glucagon content of 20 wo WT and *Taz*-KD pancreatic islets, N (2.8 mM, WT) = 6, N (20 mM, WT) = 5, N (0.5 mM, WT) = 7, N (2.8 mM, *Taz*-KD) = 4, N (20 and 0.5 mM, *Taz*-KD) = 5. Data = mean \pm SEM; N = number of animals; statistical analysis: unpaired *t* test: **p* < 0.05. Abbreviations: weeks of age (wo), *tafazzin*-knockdown (*Taz*-KD), wildtype (WT).

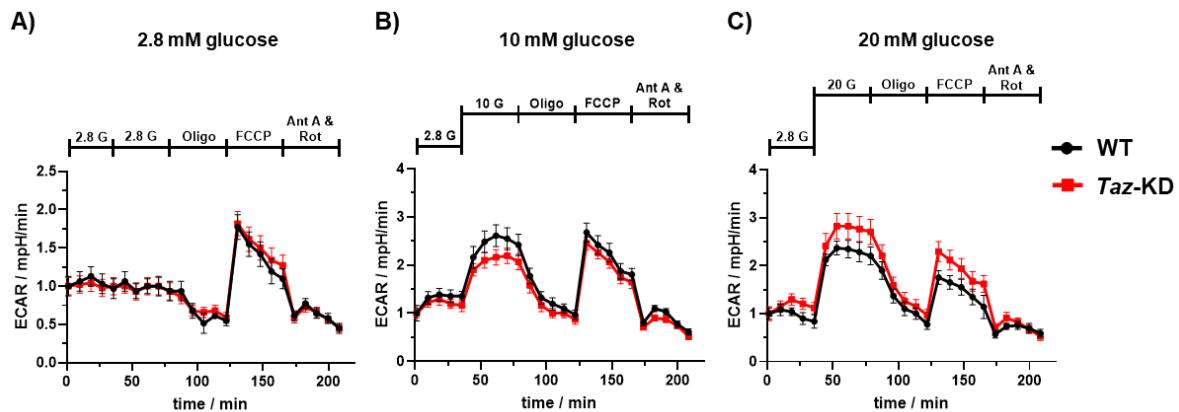


Figure 7.11: ECAR curves using the Seahorse mitochondrial stress test

ECAR curves of 20 wo WT and *Taz*-KD pancreatic islets normalised to baseline in response to 2.8 mM (A), 10 mM (B) and 20 mM (C) glucose stimulation followed by the addition of electron transport chain inhibitors (Oligo, Ant A and Rot) and uncoupler (FCCP) (Figure is linked to **Figure 4.20**) n (WT) = 11, n (*Taz*-KD) = 13. n = number of experiments include N = 3. Data = mean \pm SEM; N = number of animals. Abbreviations: weeks of age (wo), *tafazzin*-knockdown (*Taz*-KD), wildtype (WT), extracellular acidification rate (ECAR).

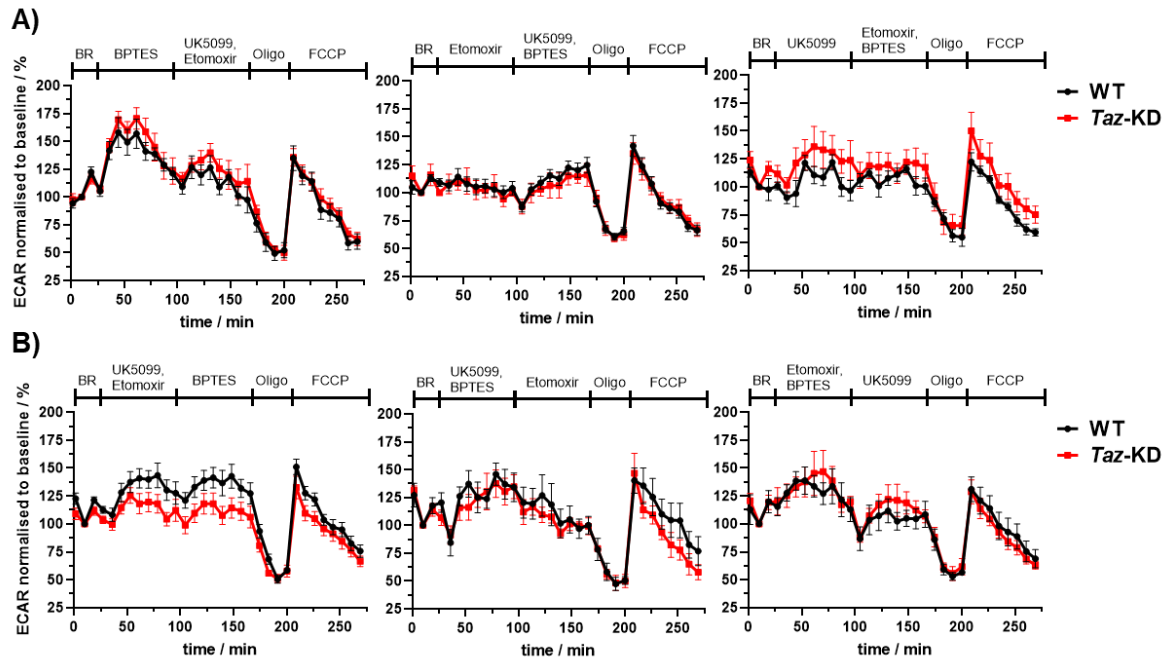


Figure 7.12: ECAR curves using the Seahorse mito fuel flex test

(A) ECAR of the nutrient dependency test of 20 wo WT and *Taz*-KD pancreatic islets, assessing glutamine (left), fatty acids (middle) and glucose (right) oxidation pathways. N (WT) = 6, N (*Taz*-KD) = 4. (B) ECAR of the nutrient capacity test of 20 wo WT and *Taz*-KD pancreatic islets, assessing glutamine (left), fatty acids (middle) and glucose (right) oxidation pathway. N (WT) = 6, N (*Taz*-KD) = 4. This Figure is linked to **Figure 4.11**. Data = mean \pm SEM; N = number of animals. Abbreviations: weeks of age (wo), *tafazzin*-knockdown (*Taz*-KD), wildtype (WT), extracellular acidification rate (ECAR), basal respiration (BR), oligomycin (Oligo).

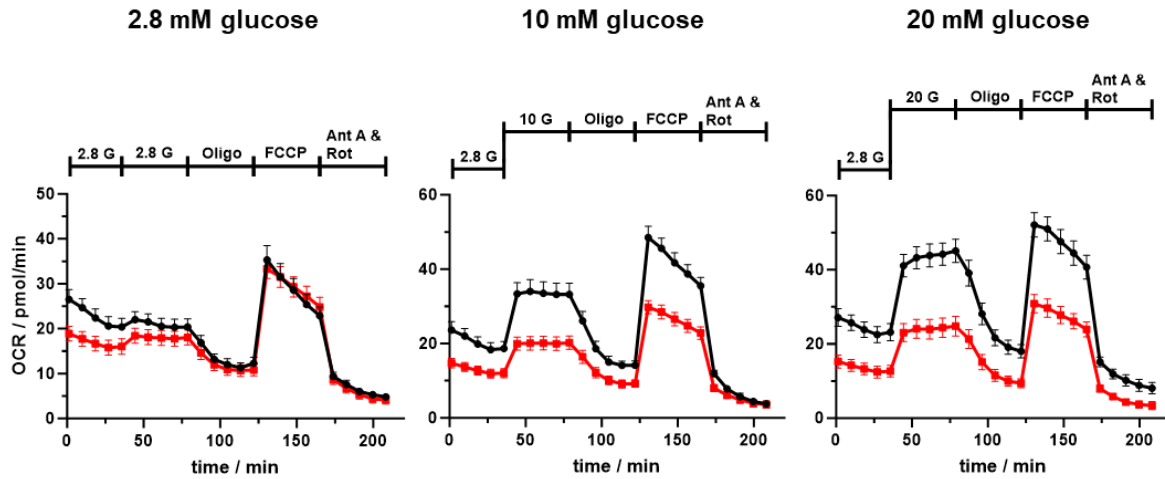


Figure 7.13: Reduced OCR of *Taz*-KD pancreatic islets when normalised to mitochondrial volume

The OCR normalised to mitochondrial volume of 20 wo WT and *Taz*-KD pancreatic islets at 2.8 mM (left), 10 mM (middle) and 20 mM (right) glucose concentration followed by the addition of several inhibitors of the respiratory chain complexes. N (WT) = 5 and N (*Taz*-KD) = 4; N = number of animals; Abbreviations: weeks of age (wo), *tafazzin*-knockdown (*Taz*-KD), wildtype (WT), spare respiratory capacity (SRC), oxygen consumption rate (OCR), oligomycin (Oligo), rotenone (Rot), antimycin A (Ant A).

7.1.6 Redox experiments

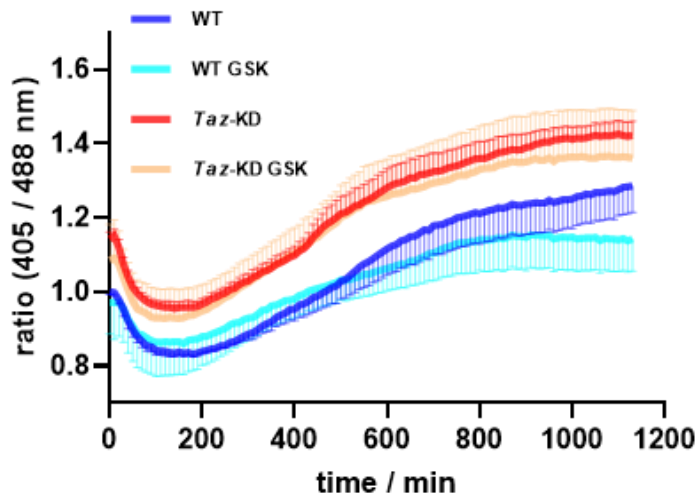


Figure 7.14: Unchanged redox state of *Taz*-KD pancreatic islets treated with GSK

H₂O₂ kinetics of 20 wo WT and *Taz*-KD pancreatic islets measured with a plate reader in presence or absence of 20 μ M NOX2 inhibitor, GSK. The oxidation of the mito-roGFP2-Orp1 sensor is followed over time. N = 5. Data = mean \pm SEM; N = number of animals. Abbreviations: weeks of age (wo), *tafazzin*-knockdown (*Taz*-KD), wildtype (WT), GSK2795039 (GSK).

A paired WB analysis for the redox and autophagy-related proteins was performed as the conditions among the samples varied. In **Figure 7.15** (redox) and **Figure 7.17** (autophagy-related) the sample pairs and their corresponding protein levels normalised to the average WT protein levels are displayed. Additionally, the graph provides the internal variance of the WT samples which is not indicated in the WB experiments of the result part.

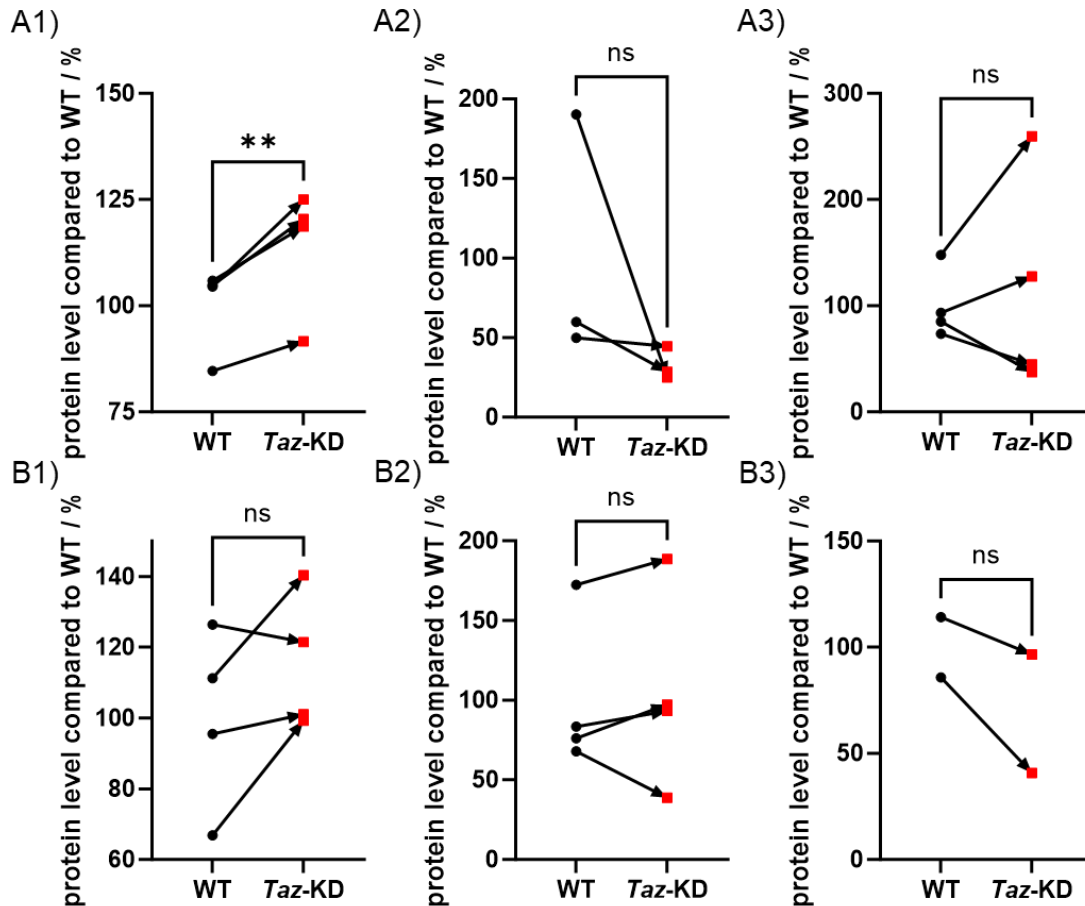


Figure 7.15: WB analysis of redox proteins of WT and Taz-KD pancreatic islets

(A) Pairwise comparison of 20 wo WT and Taz-KD pancreatic islets. WB analysis of the antioxidative enzymes: Prx3 (A1), catalase (A2) and GPX4 (A3). (B) Pairwise comparison of 20 wo WT and Taz-KD pancreatic islets. WB analysis of the ROS production and stress response proteins: NOX4 (B1), Nrf2 (B2) and SOD2 (B3). The Figure is linked to **Figure 4.26**. Data = mean \pm SEM; N = number of animals; statistical analysis: paired *t* test: **p* < 0.05, ***p* < 0.01, ns: *p* > 0.05. Abbreviations: weeks of age (wo), tafazzin-knockdown (Taz-KD), wildtype (WT), western blot (WB), reactive oxygen species (ROS).

7.1.7 Confocal and STED imaging

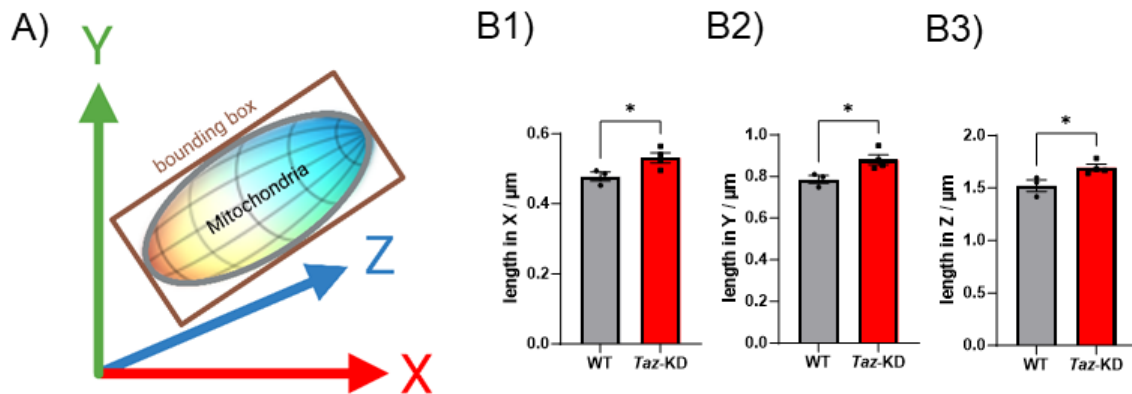


Figure 7.16: Bounding box analysis of the mitochondrial network from *Taz*-KD pancreatic islet cells.

(A) Schematic illustration of object-oriented bounding box analysis in 3D of single mitochondria. (B) Quantitative analysis of bound box analysis of 20 wo WT and *Taz*-KD dispersed pancreatic islet cells. N (WT) = 3, N (*Taz*-KD) = 4. Data = mean \pm SEM; N = number of animals; statistical analysis: unpaired two-tailed *t* test: **p* < 0.05. Abbreviations: weeks of age (wo), *tafazzin*-knockdown (*Taz*-KD), wildtype (WT). (A) was created with Biorender.com.

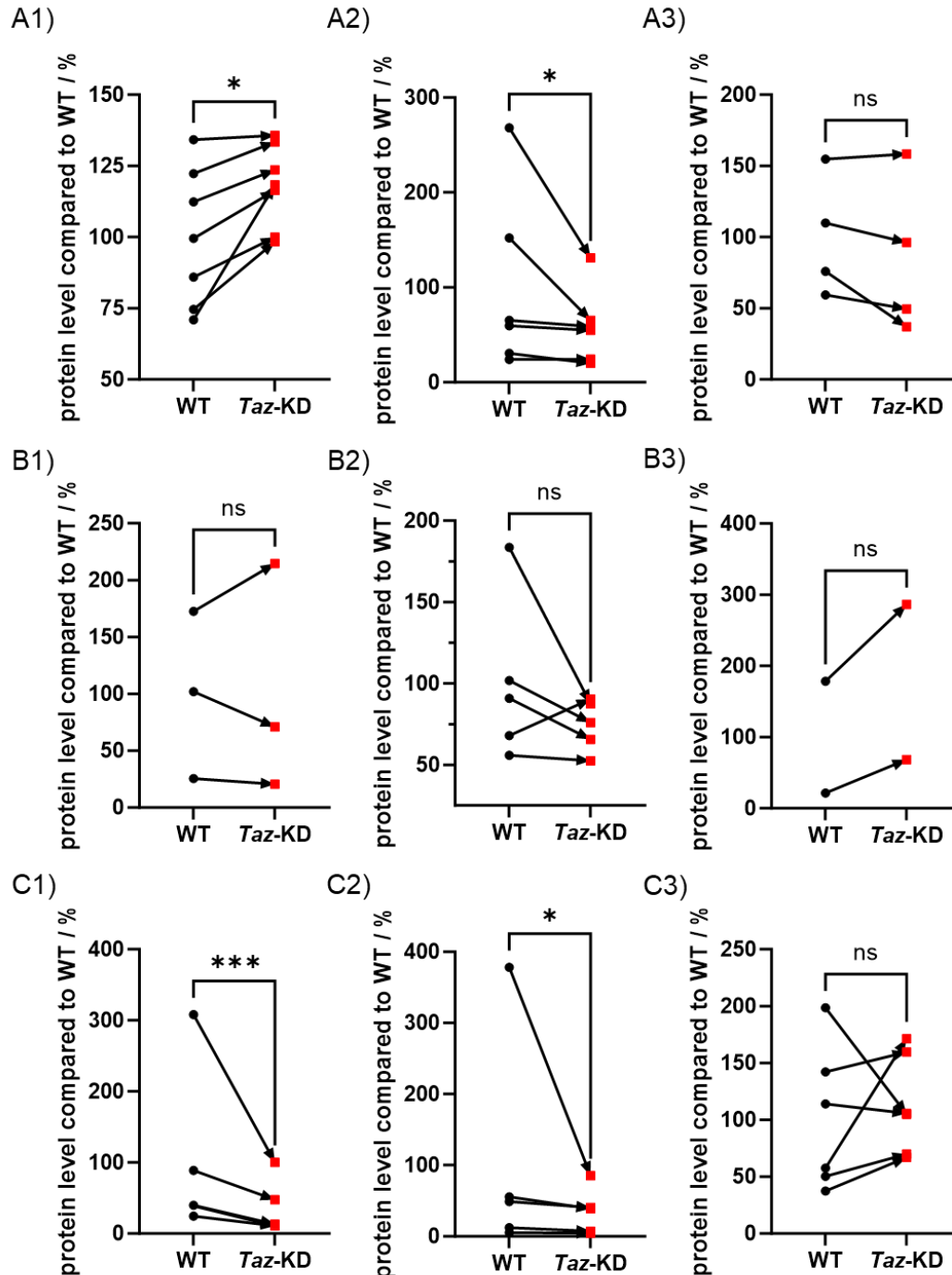


Figure 7.17: WB analysis of autophagy proteins of *Taz*-KD pancreatic islets

(A) Pairwise comparison of 20 wo WT and *Taz*-KD pancreatic islets. WB analysis of the autophagy proteins: LAMP1 (A1), LAMP2 (A2) and Atg7 (A3). (B) Pairwise comparison of 20 wo WT and *Taz*-KD pancreatic islets. WB analysis of PINK1 (B1), Prk8 (B2) and MCUa (B3). (C) Pairwise comparison of 20 wo WT and *Taz*-KD pancreatic islets. WB analysis of LC3B-1 (C1) and LC3B-2 (C2). The Figure is linked to **Figure 4.31**. N (LAMP1) = 7, N (LAMP2) = 6, N (Atg7) = 4, N (PINK1) = 3, N (Prk8) = 5. N (MCU) = 2, N (LC3B-1/2) = 5. Data = mean \pm SEM; N = number of animals; statistical analysis with unpaired *t* test: **p* < 0.05, ***p* < 0.01, ****p* < 0.001, *****p* < 0.0001. Abbreviations: weeks of age (wo), *tafazzin*-knockdown (*Taz*-KD), wildtype (WT), western blot (WB).

7.1.8 Lipidomics

Total lipid amount

The lipidomics samples ranged from 3380 to 6740 pmol, which was according to Lipotype company considered optimal for the performed lipidomics analysis (**Figure 7.18**).

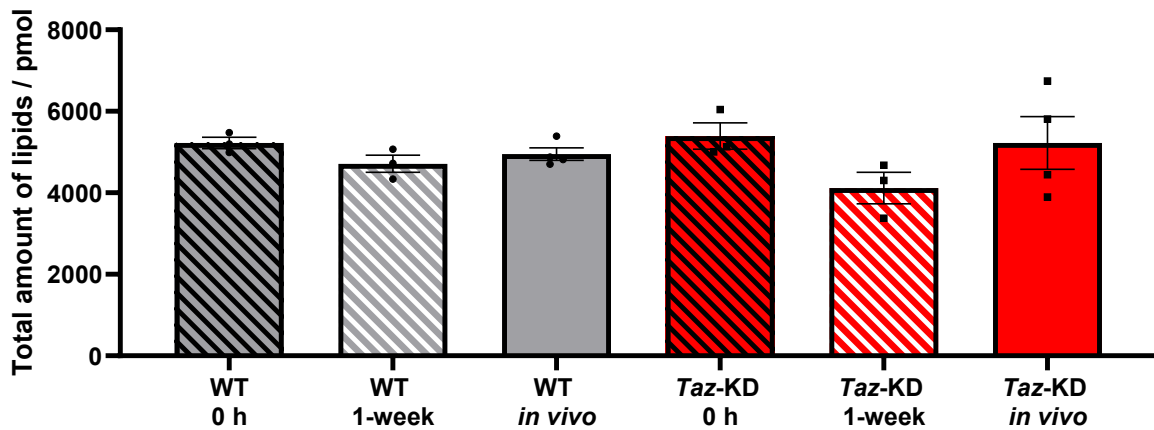


Figure 7.18: Total lipid amount measured in the homogenised pancreatic islet samples

All pancreatic islet samples (*in vivo* and 1-week *in vitro* and 0 h *in vitro*) were tested by Lipotype before lipidomics analysis. Data = mean \pm SEM; N (*in vivo*) = 4, N (*in vitro*) = 3. N = number of animals; Abbreviations: weeks of age (wo), *tafazzin*-knockdown (*Taz*-KD), wildtype (WT), western blot (WB).

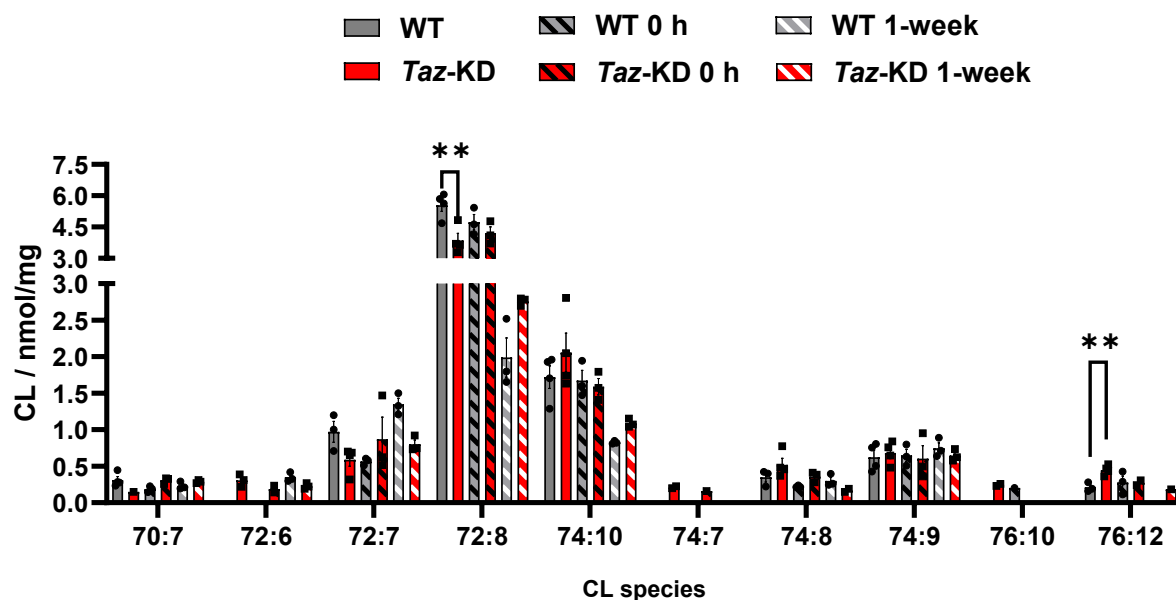


Figure 7.19: CL profiles of *Taz*-KD pancreatic islets of the *in vivo* model, and 0 h and 1-week *in vitro* model

CL species concentration of WT and *Taz*-KD pancreatic from each of the used models (*in vivo*: lifelong doxy diet; *in vitro*: 1-week or 0 h doxy incubation) measured by lipidomics analysis. Normalised to protein content (pmol/mg). N (*in vivo*) = 4, N (*in vitro*) = 3, some replicates are missing due to limit of detection. Data = mean \pm SEM; N = number of animals; statistical analysis comparison WT and *Taz*-KD *in vivo* model: unpaired two-tailed *t* test: ***p* < 0.01. Abbreviations: *tafazzin*-knockdown (*Taz*-KD), wildtype (WT), doxycycline (doxy).

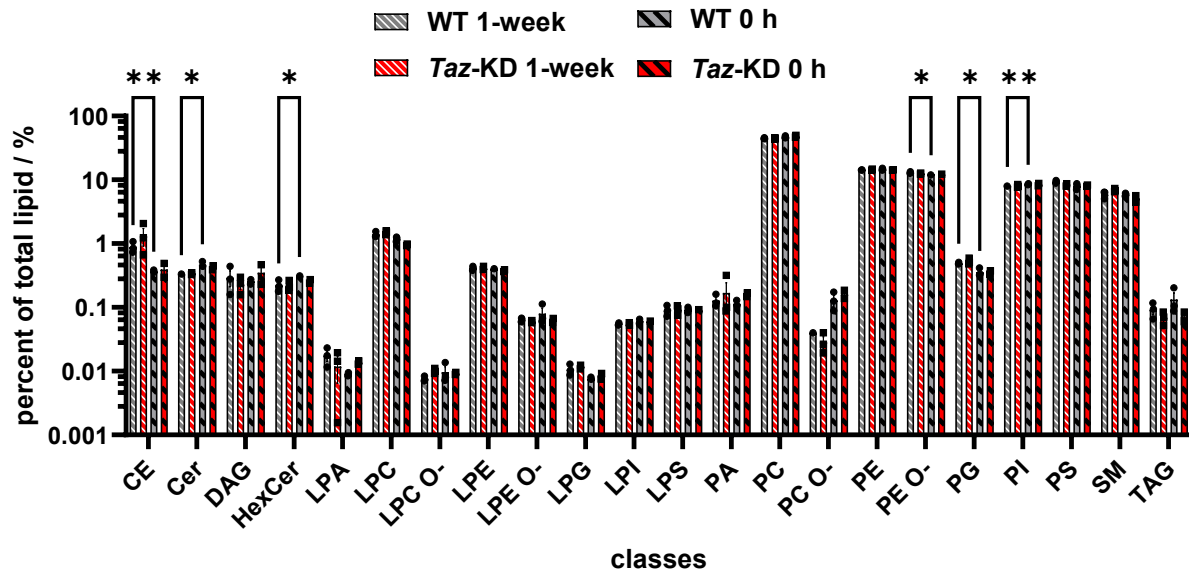


Figure 7.20: Lipid class profile of 0 h and 1-week WT and *Taz*-KD pancreatic islets *in vitro* model

Lipid class profile of WT and *Taz*-KD pancreatic islets of the *in vitro* doxy model. Normalised to total lipid amount and displayed in logarithmic scale. N (WT 0 h) = 3, N (WT 1-week) = 2 - 3, N (*Taz*-KD 0 h) = 2, N (*Taz*-KD 1-week) = 3; Data = mean \pm SEM; N = number of animals; statistical analysis with unpaired two-tailed *t* test comparison of WT 0 h and WT 1-week: **p* < 0.05, ***p* < 0.01. Abbreviations: doxycycline (doxy), *tafazzin*-knockdown (*Taz*-KD), wildtype (WT). The abbreviations for each lipid class can be found in the general list of abbreviations.

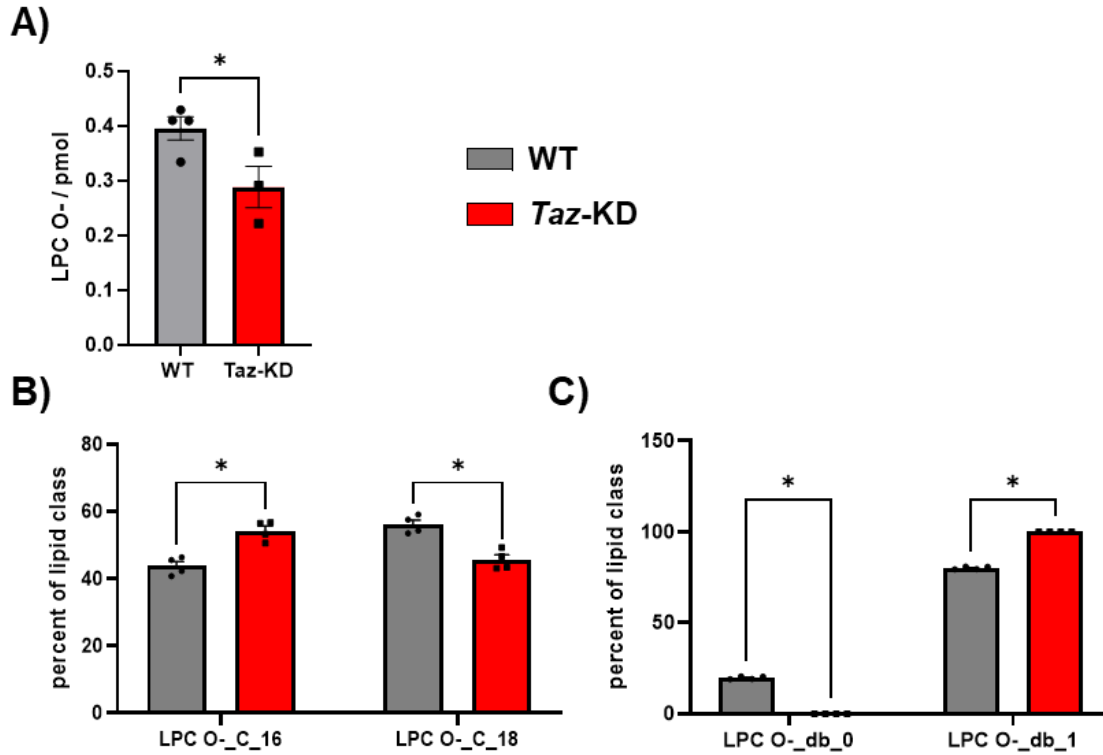


Figure 7.21: Altered levels and profiles of LPC O- in *Taz*-KD pancreatic islets

(A) LPC O- levels in 20 wo WT and *Taz*-KD pancreatic islets, analysed by lipidomics analysis. (B) LPC O- carbon length (C16 or C18) in 20 wo WT and *Taz*-KD pancreatic islets, analysed by lipidomics analysis. (C) LPC O- double bond profile in 20 wo WT and *Taz*-KD pancreatic islets, analysed by lipidomics analysis. No double bonds (db 0) or 1 double bond (db 1). N (WT) = 4, N (*Taz*-KD) = 3. Data = mean \pm SEM; N = number of animals; N = number of animals; statistical analysis: unpaired *t*-test (A) or nonparametric Mann-Whitney test (B,C): statistical analysis: **p* < 0.05. Abbreviations: weeks of age (wo), *tafazzin*-knockdown (*Taz*-KD), wildtype (WT), lyso-phosphatidylcholine-ether (LPC O-).

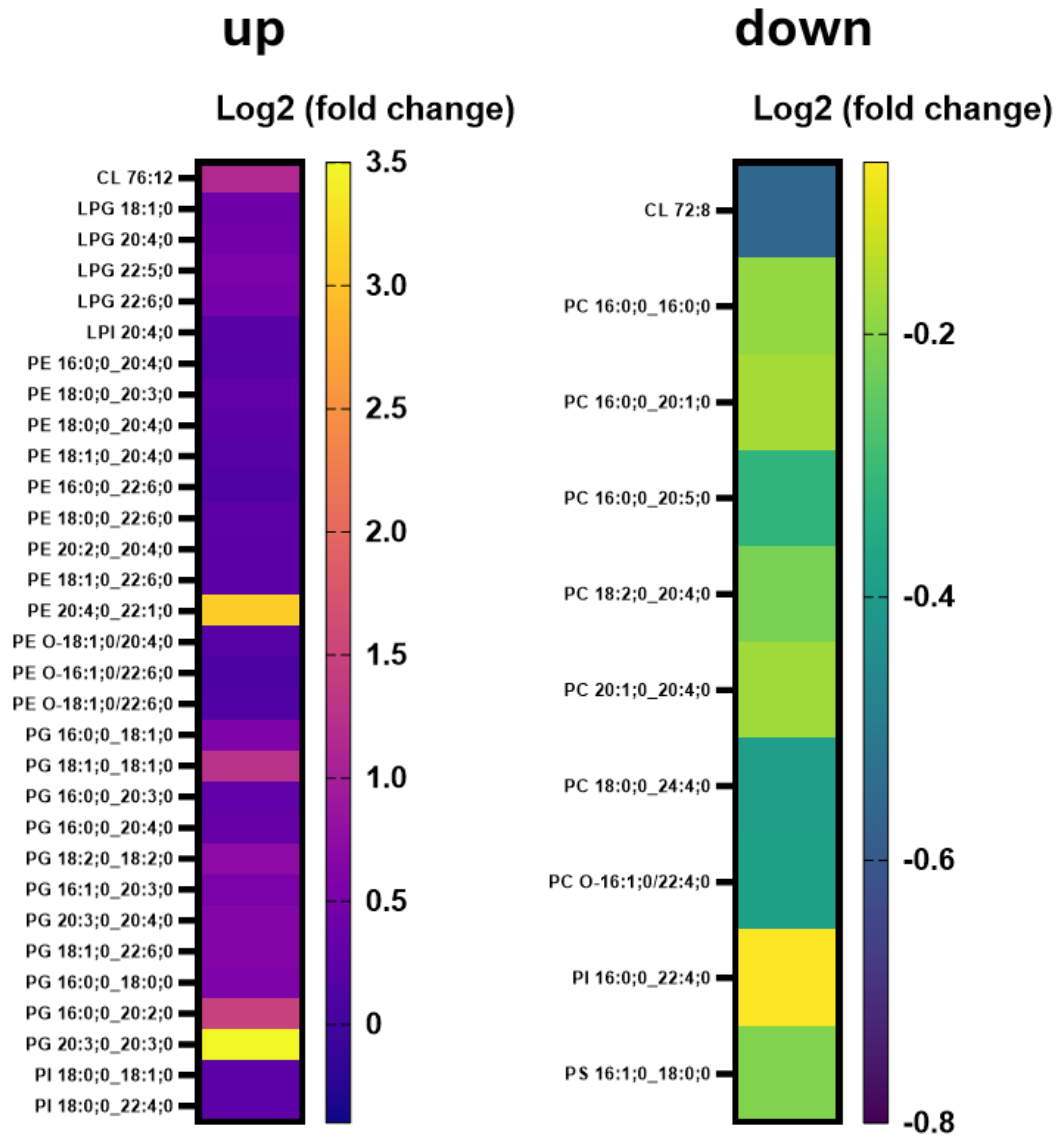


Figure 7.22: Full list of altered lipid species of *Taz*-KD pancreatic islets

All significantly changed lipid species of 20 wo WT and *Taz*-KD pancreatic islets normalised to total lipid amount. This Figure supplements the **Figure 4.33**. The fold change of lipid up- or downregulation are displayed in Log2 colorcode (down: from -1 to 0, green to yellow) (up: from 0 to 3.5, purple to yellow). Abbreviations: weeks of age (wo), *tafazzin*-knockdown (*Taz*-KD), wildtype (WT).

7.1.9 RNA sequencing

Table 7.1: RNA-Seq samples after quality control checkAbbreviations: *tafazzin*-knockdown (*Taz*-KD), wildtype (WT).

Sample description	Sample name	Concentration / ng/μl	Integrity value
WT <i>in vivo</i> model	WT1	213.00	8.8
	WT2	251.00	9
	WT3	132.00	8.5
<i>Taz</i> -KD <i>in vivo</i> model	<i>Taz</i> -KD1	183.00	8.9
	<i>Taz</i> -KD2	171.00	9.2
	<i>Taz</i> -KD3	116.00	8.3
WT <i>in vitro</i> model (1-week)	WT1_1-week	294.00	9
	WT2_1-week	181.00	8
	WT3_1-week	63.00	8
<i>Taz</i> -KD <i>in vitro</i> model (1-week)	<i>Taz</i> -KD1_1-week	198.00	9.2
	<i>Taz</i> -KD2_1-week	280.00	8.2
	<i>Taz</i> -KD3_1-week	107.00	8.4

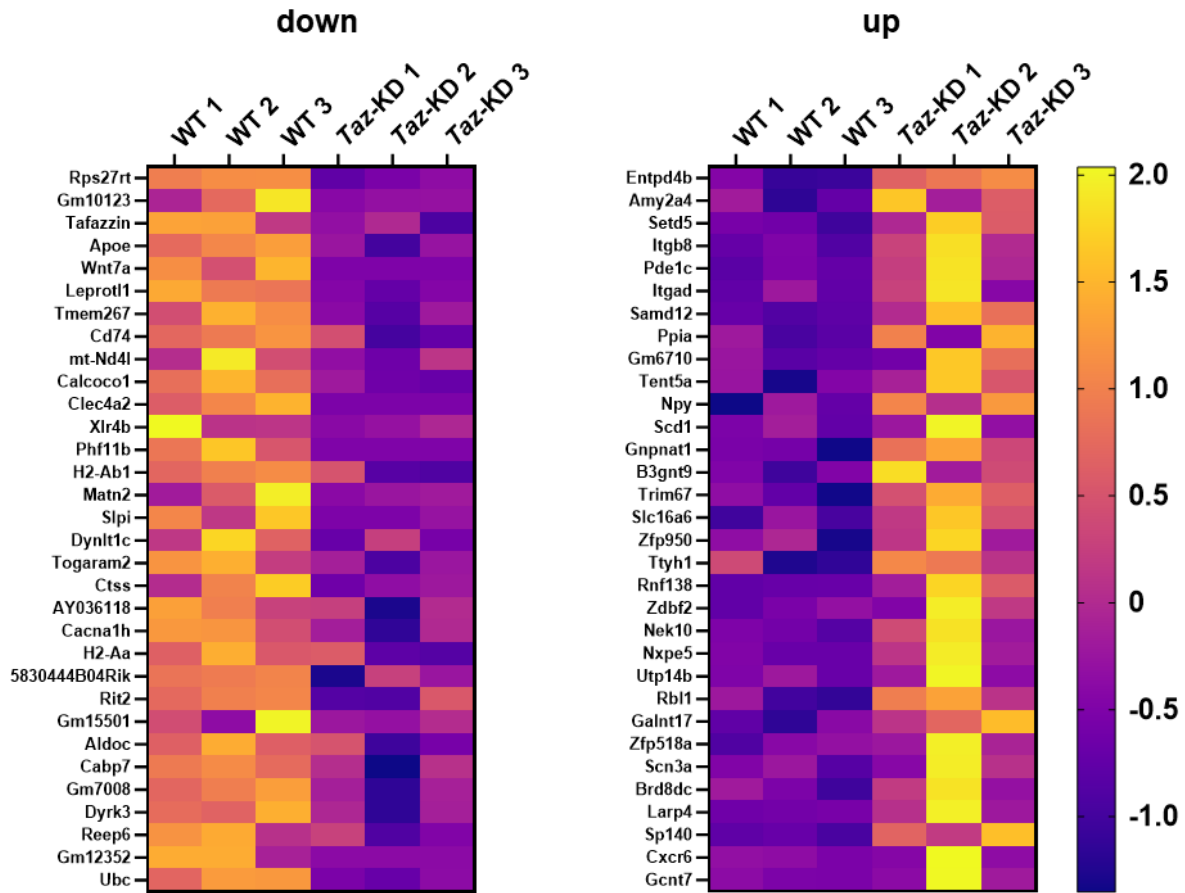


Figure 7.23: Heatmap of the 30 most down- and upregulated genes in *Taz*-KD pancreatic islets

The 30 most significantly changed genes of 20 wo WT and *Taz*-KD pancreatic islets. This Figure supplements **Figure 4.34**. The fold change of gene up- or downregulation is displayed in Log2 colorcode (from -2 to 2, purple to yellow). Abbreviations: weeks of age (wo), *tafazzin*-knockdown (*Taz*-KD), wildtype (WT).

7.1.10 Post-translational modification: O-Glycosylation

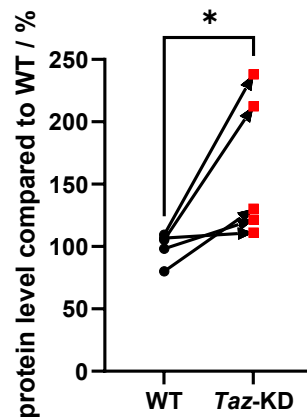


Figure 7.24: WB analysis of O-GlcNAc in 20 wo WT and *Taz*-KD pancreatic islets

Paired analysis of O-GlcNAc WB protein levels in 20 wo WT and *Taz*-KD pancreatic islets. N = 5. This Figure is linked to **Figure 4.35**. Data = mean \pm SEM; N = number of animals; statistical analysis: paired *t* test: **p* < 0.05. Abbreviations: weeks of age (wo), *tafazzin*-knockdown (*Taz*-KD), wildtype (WT), western blot (WB), O-linked β -*N*-acetylglucosamine (O-GlcNAc).

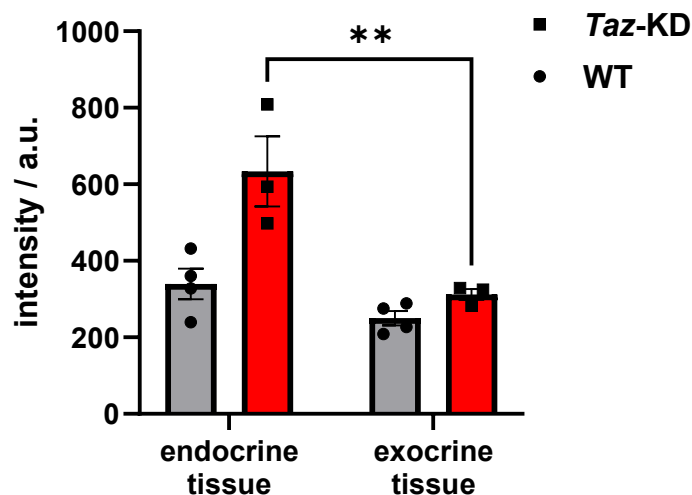


Figure 7.25: Increased endocrine O-GlcNAc modification in *Taz*-KD pancreatic islets

(A) Quantification of O-GlcNAc modification in pancreas endocrine and exocrine tissue of 20 wo *Taz*-KD and WT pancreatic islets. N = 5. This Figure is linked to **Figure 4.35**. Data = mean \pm SEM; N = number of animals; statistical analysis: two-way ANOVA: ***p* < 0.01. Abbreviations: O-linked β -*N*-acetylglucosamine (O-GlcNAc), weeks of age (wo), *tafazzin*-knockdown (*Taz*-KD), wildtype (WT).

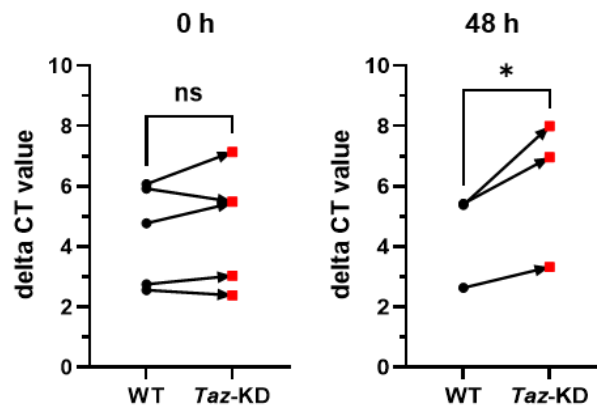
7.1.11 Characterisation of the shTaz *in vitro* model

Figure 7.26: Pairwise comparison of the delta CT values from *Taz* qPCR experiments (*in vitro* model)

Taz gene expression (linked to **Figure 4.36**) of WT and *Taz*-KD pancreatic islets after 0 h (left) and 48 h of doxy culture were pairwise compared due to variation among the single values. N = 3, Data = mean \pm SEM; N = number of animals; statistical analysis: paired *t* test: **p* < 0.05. Abbreviations: *tafazzin*-knockdown (*Taz*-KD), wildtype (WT), *tafazzin* (*Taz*), cardiolipin (CL), cycle threshold (CT).

7.2 List of Figures

Figure 1.1: CL remodelling mediated by the mitochondrial transacylase Taz	3
Figure 1.2: CL supports cristae formation and ETC interaction	4
Figure 1.3: Inducible <i>Taz</i> -KD mouse model via doxy administration	15
Figure 1.4: Pancreas anatomy and islet of Langerhans	19
Figure 1.5: Concept of biphasic insulin secretion and electrical activity of pancreatic β -cells stimulated with glucose	21
Figure 1.6: Schematic illustration of GSIS	23
Figure 1.7: Glucose-mediated glucagon secretion	25
Figure 1.8: Pancreatic α -cell electrical activity	26
Figure 1.9: H_2O_2 production sites in the cell	29
Figure 3.1: Doxy breeding scheme for shTaz mice	44
Figure 3.2: Doxy crossbreeding of shTaz and mito-roGFP2-Orp1 to generate MiOxTaz	45
Figure 3.3: Comparison of the <i>in vivo</i> and <i>in vitro</i> model of <i>Taz</i> -KD	46
Figure 3.4: Genotyping gels of the used mice models	48
Figure 3.5: Experiment timeline of GTT	49
Figure 3.6: Procedure of pancreas perfusion and isolation	50
Figure 3.7: Microscope chamber for Ca^{2+} and dynamic insulin measurements	55
Figure 3.8: Ca^{2+} imaging setup with whole pancreatic islets using Fura-2 AM	57
Figure 3.9: Mechanism of the mitochondrial membrane potential dye TMRM	63
Figure 3.10: NADH/NADPH molecular properties	64
Figure 3.11: Seahorse experiments testing mitochondrial function and nutrient dependencies	65
Figure 3.12: Redox sensing using roGFP2-Orp1	67
Figure 3.13: Comparison of used plate reader and microscope systems	68
Figure 3.14: Redox histology for <i>in vivo</i> redox imaging of pancreatic islets	70
Figure 3.15: STED principle to achieve super-resolution	72
Figure 4.1: <i>Taz</i> and CL reduction in <i>Taz</i> -KD pancreatic islets	80
Figure 4.2: Altered CL species profile in <i>Taz</i> -KD pancreatic islets	81
Figure 4.3: Body weight reduction of <i>Taz</i> -KD mice after 20 and 50 wo	83
Figure 4.4: Altered whole-body glucose metabolism of <i>Taz</i> -KD mice at 20 wo	84
Figure 4.5: Immunohistochemistry for visualising pancreatic α -, β -, and δ -cells	85
Figure 4.6: More α -cells per area in <i>Taz</i> -KD pancreatic islets	87

Figure 4.7: The number of Ki67 and cleaved caspase-3 positive cells are unchanged in <i>Taz</i> -KD pancreatic islets.....	88
Figure 4.8: Increased glucose uptake independent of GLUT2 in <i>Taz</i> -KD pancreatic islets.....	90
Figure 4.9: Increased NAD(P)H levels in <i>Taz</i> -KD pancreatic islets	91
Figure 4.10: Establishing the OCR measurement of pancreatic islets using Seahorse analyser	93
Figure 4.11: Increased SRC and proton leak in low glucose of <i>Taz</i> -KD pancreatic islets	94
Figure 4.12: No differences in nutrient dependency of <i>Taz</i> -KD pancreatic islets.....	96
Figure 4.13: Mitochondrial membrane potential was unchanged in <i>Taz</i> -KD pancreatic islets.....	97
Figure 4.14: Unchanged basal ATP levels of <i>Taz</i> -KD pancreatic islets.....	99
Figure 4.15: Faster cytosolic Ca ²⁺ influx in intact but not dispersed <i>Taz</i> -KD pancreatic islets.....	101
Figure 4.16: Unchanged Ca ²⁺ response of <i>Taz</i> -KD pancreatic islets titrated with tolbutamide or glucose.....	102
Figure 4.17: Similar mitochondrial and ER Ca ²⁺ dynamics of <i>Taz</i> -KD pancreatic islets	104
Figure 4.18: Increased glucagon and preserved insulin secretion in <i>Taz</i> -KD pancreatic islets.....	106
Figure 4.19: Similar dynamics in GSIS of <i>Taz</i> -KD pancreatic islets	107
Figure 4.20: Similar acidification levels in <i>Taz</i> -KD and WT pancreatic islets.....	109
Figure 4.21: H ₂ O ₂ titration of isolated pancreatic islets from WT MiOxTaz mice	111
Figure 4.22: Increased basal H ₂ O ₂ levels but similar kinetics in <i>Taz</i> -KD pancreatic islets	112
Figure 4.23: GLX decreased the redox state of <i>Taz</i> -KD pancreatic islets.....	113
Figure 4.24: Reduced <i>in vivo</i> redox state of <i>Taz</i> -KD pancreatic islets using redox histology.....	115
Figure 4.25 Unchanged <i>in vivo</i> redox state of <i>Taz</i> -KD hearts using redox histology	116
Figure 4.26: Altered redox protein levels of <i>Taz</i> -KD pancreatic islets using WB analysis	118
Figure 4.27: Confocal live imaging of two dispersed pancreatic islet cells	119
Figure 4.28: Increased mitochondrial volume in <i>Taz</i> -KD pancreatic islets	120
Figure 4.29: Comparison of STED and confocal imaging of pancreatic islet cells....	121

Figure 4.30: More giant and less smaller mitochondria in <i>Taz</i> -KD pancreatic islet cells	123
Figure 4.31: WB analysis of morphology- and autophagy-related proteins in <i>Taz</i> -KD pancreatic islets	125
Figure 4.32: Altered lipid class composition in <i>Taz</i> -KD pancreatic islets	127
Figure 4.33: Altered lipid species in <i>Taz</i> -KD pancreatic islets	128
Figure 4.34: Bulk mRNA-sequencing revealed upregulation of <i>O</i> -GlcNAc in <i>Taz</i> -KD pancreatic islets	130
Figure 4.35: Increased <i>O</i> -GlcNAc in IHC and WB analysis of <i>Taz</i> -KD pancreatic islets	131
Figure 4.36: <i>Taz</i> reduction in the <i>Taz</i> -KD pancreatic islets <i>in vitro</i> model	133
Figure 4.37: Altered CL species profile of <i>Taz</i> -KD pancreatic islets of the <i>in vitro</i> model	134
Figure 4.38: Similar pancreatic cell type number of <i>Taz</i> -KD <i>in vitro</i> model	135
Figure 4.39: Impaired pancreatic islets function in <i>Taz</i> -KD <i>in vitro</i> model	137
Figure 4.40: PC analysis of sh <i>Taz</i> <i>in vivo</i> and <i>in vitro</i> lipidomic samples	138
Figure 4.41: Lipid class composition of <i>Taz</i> -KD pancreatic islets of the 1-week doxy <i>in vitro</i> model	139
Figure 4.42: RNA-Seq of <i>Taz</i> -KD pancreatic islets of the 1-week doxy <i>in vitro</i> model	140
Figure 5.1: <i>Taz</i> -KD pancreatic islet adaptation processes	171
Figure 7.1: GeneRuler 100 bp DNA Ladder	215
Figure 7.2: Pairwise comparison of the delta CT values from <i>Taz</i> qPCR experiments	217
Figure 7.3: CL profile shift towards long acyl chain fatty acids in <i>Taz</i> -KD	217
Figure 7.4: Altered whole-body glucose metabolism of <i>Taz</i> -KD mice at 20 and 50 wo	218
Figure 7.5: Increased α -cell and decreased β -cell number in <i>Taz</i> -KD pancreatic islets	219
Figure 7.6: Similar PDX1 levels in WT and <i>Taz</i> -KD pancreatic islets	219
Figure 7.7: WB analysis of GLUT2 in 20 wo WT and <i>Taz</i> -KD pancreatic islets	220
Figure 7.8: Increased maximum respiration of <i>Taz</i> -KD pancreatic islets	220
Figure 7.9: Non-normalised mitochondrial- and ER-Ca ²⁺ curves of WT and <i>Taz</i> -KD pancreatic islet cells	221
Figure 7.10: Glucagon content and glucagon secretion of <i>Taz</i> -KD pancreatic islets	222

Figure 7.11: ECAR curves using the Seahorse mitochondrial stress test.....	222
Figure 7.12: ECAR curves using the Seahorse mito fuel flex test	223
Figure 7.13: Reduced OCR of <i>Taz</i> -KD pancreatic islets when normalised to mitochondrial volume	224
Figure 7.14: Unchanged redox state of <i>Taz</i> -KD pancreatic islets treated with GSK ..	224
Figure 7.15: WB analysis of redox proteins of WT and <i>Taz</i> -KD pancreatic islets.....	225
Figure 7.16: Bounding box analysis of the mitochondrial network from <i>Taz</i> -KD pancreatic islet cells.	226
Figure 7.17: WB analysis of autophagy proteins of <i>Taz</i> -KD pancreatic islets	227
Figure 7.18: Total lipid amount measured in the homogenised pancreatic islet samples	228
Figure 7.19: CL profiles of <i>Taz</i> -KD pancreatic islets of the <i>in vivo</i> model, and 0 h and 1-week <i>in vitro</i> model.....	229
Figure 7.20: Lipid class profile of 0 h and 1-week WT and <i>Taz</i> -KD pancreatic islets <i>in vitro</i> model	230
Figure 7.21: Altered levels and profiles of LPC O- in <i>Taz</i> -KD pancreatic islets	231
Figure 7.22: Full list of altered lipid species of <i>Taz</i> -KD pancreatic islets	232
Figure 7.23: Heatmap of the 30 most down- and upregulated genes in <i>Taz</i> -KD pancreatic islets	234
Figure 7.24: WB analysis of O-GlcNAc in 20 wo WT and <i>Taz</i> -KD pancreatic islets...	235
Figure 7.25: Increased endocrine O-GlcNAc modification in <i>Taz</i> -KD pancreatic islets	235
Figure 7.26: Pairwise comparison of the delta CT values from <i>Taz</i> qPCR experiments (<i>in vitro</i> model)	236

7.3 List of Tables

Table 1.1: Role of CL in mitochondrial functionality	6
Table 1.2: Overview of metabolic alterations in BTHS patients and patient samples ...	7
Table 2.1: Used substances	32
Table 2.2: Used consumables	34
Table 2.3: Used Kits	35
Table 2.4: Krebs-Henseleit buffer (KHB)	36
Table 2.5: Lysis buffer	37
Table 2.6: Islet culture and measurement media	37
Table 2.7: Used devices provided with company name and serial number	38
Table 2.8: Microscope accessories	39
Table 2.9: Used software versions	39
Table 2.10: Used animal preparation equipment	40
Table 2.11: Antibodies used for western blot experiments or immunohistochemistry	40
Table 3.1: Used primers with the predicted product size	47
Table 3.2: Kd values of the used Ca²⁺ sensors	56
Table 3.3: QPCR TaqMan primers	76
Table 4.1: Fuel oxidation and pathway dependencies	96
Table 7.1: RNA-Seq samples after quality control check	233

7.4 Acknowledgements

Throughout my PhD, I was accompanied by many great individuals who all helped me massively during this exciting but challenging period. Unfortunately, I cannot name all of them, but I would like to highlight a few that were of particular importance to this thesis.

First of all, I would like to thank Prof. Dr. Leticia Prates Roma for being an outstanding leader and for the many inspiring suggestions and discussions. Thank you for your constant guidance. Your dedication, support and encouragement over the years were the primary driving force of this project.

Thanks to Markus Hoffmann for being the best lab mate possible. Already, after our experiments together in the Praktikum, I knew we had to do everything to keep this incredible scientist in the lab. A special thanks also to Janina Frisch and Nikolina Mitreska for helping in the lab and simply being amazing people. Actually, this applies to all the members of the highly international Prates Roma Lab. Thank you for creating a perfect working atmosphere and making lab trips, cash nights, “Beat that” games or simply coffee breaks so enjoyable. Also, a big thanks to the technicians in the lab who keep everything running, and for me personally, Sandra Janku, Andrea Armbrüster and Angelique Schniebs helped with all kinds of experiments or other lab issues. I would like to thank Regine Kaleja and Ute Legler for assisting with organisational questions and many friendly conversations.

I would like to thank all the collaborators for all the project input and the opportunities to learn new techniques. A special thanks goes to Monika Bozem for her endless expertise, which helped with planning and analysis, and for proofing this thesis. The experimental surgery, especially Selina, Caroline, and Emmanuel, for great discussions in a relaxed atmosphere and all the excellent collaborations. I would like to thank Vanessa Schmitt for the electron microscopy experiments. Marcel Lauterbach's molecular imaging group allowed me to learn STED microscopy. I am grateful to Yasser Medlej, Tobias Dancker, and Ahmadali Lotfinia for our enjoyable conversations and particularly to Ahmad for our late-night microscopy sessions. I would like to thank Karina von der Malsburg for helping me with the seahorse experiments. I would like to thank Edoardo Bertero and Christoph Maack, who helped me to get a great start on the Barth Syndrome project. Next, I would like to thank Barbara Niemeyer and Markus Hoth and all the members of the biophysics group for inspiring lab meetings and discussions and for creating such a supportive and collaborative environment.

I would also like to thank all my friends outside that lab who always supported me during this PhD. Especially Vincent Mankiewicz and Uli Stock, who were not only best friends but also helped in the project with either lab assistance or ChemDraw introduction, respectively. Also, thanks to my best mate, Vladimir Konchakov, who has always been there for me.

A very special thanks goes to my family. Hans, for his great personality and providing his room when I needed a place. My brother for being an amazing person. My mother for her unlimited support in every situation. My fiancé Claudia for her love and her understanding. Without the constant support of my family, I would not be the person I am today.

7.5 CV: Christopher Carlein (includes the publication list)

Aus datenschutzrechtlichen Gründen wird der Lebenslauf in der elektronischen Fassung der Dissertation nicht veröffentlicht.

Tag der Promotion: 27. März 2025

Dekan: Univ.-Prof. Dr. med. dent. Matthias Hannig

Berichterstatter: Prof. Dr. Leticia Prates Roma

Prof. Dr. Michael Zemlin

Prof. Dr. Jan Riemer